THE UNIVERSITY *of* EDINBURGH

THE UNIVERSITY of EDINBURGH

ELECTROCHEMICAL CHARACTERISATION OF MICROSQUARE NANOBAND EDGE ELECTRODE (MNEE) ARRAYS AND THEIR USE AS BIOSENSORS

AUTHOR: ANDREW PIPER

Thesis submitted for Doctor of Philosophy

University of Edinburgh

Presented 2017

Dedicated in loving memory to my grandparents

Margaret and Stanislaw Adamaszek

Acknowledgements

I would firstly like to thank Prof Andy Mount and Prof Anthony Walton for the opportunity to do this work and the support they have given me throughout. On a similar note I would like to thank Dr Damion Corrigan for his seemingly limitless support and guidance. A special thanks is also extended to Prof Dave Adams and Dr Ben Alston for the hydrogel work done in collaboration with the University of Liverpool. A special thanks is extended to Colin Campbell and Chris Mowat for their support, as well as to Prof Dominic Campopiano who helped me get my first publication and tried to take my head off playing football every Monday.

To the people in the office who put up with me for all these years; Justin Elliott, Simon Reeves, Richard Perry, Charlotte Brady (or Perry depending on when you read this), Kate Fisher, Jamie Marland, Hannah Levene, Ugne Mitrikeviciute, Katie Ember, Ahmet Ucar, Eva Gonzalez-Fernandez, Patrick Thomson, Victoria Price, Martin Ward, Jing Jiang, Lauren Jamieson, Lina Mati, Anna-Maria Maciejuk, Sarah McAughtrie and of course my partner in crime for nearly 9 years now Hannah Johnston. Thank you all for the memories.

To those around the department who would always stop for a quick chat in the corridors, a few beers on a Friday or a game of football; Rachael Fischer, Priyanka Comar, Claire Hobday, Max McMullon, George Murray, Peter Neate, Mark Taylor, Lewis Fenton, Nathan Goodfriend, Chris Mclean, Elvira Bohl, Gareth Williams, John Blackburn, Mary Healy, Ariana Jones and Natalia Brodaczewska, Fergus McWhinnie, John Mallows, Antoine Bader, Amy Challinor and Calum Waterson. Thank you all

To those in the SMC who helped teach me the art of microfabrication; a massive thanks to Ewen Blair, Andrew Bunting, Andreas Tsiamis and Enrico Mastropaolo.

Richard Brewster and Faye Cruickshank, you guys get a paragraph of your own! It's been an adventure and I'm sure it will continue to be in the future. You guys are welcome to visit any time.

I have saved the most important till last, I cannot thank my family enough for their endless support. Especially my parents, David and Diane, who have made countless sacrifices to get me to where I am today; I am eternally grateful. Laura, David, Matthew…you guys played your part! I know that you guys don't understand what it is that I do, but don't worry there are only 3 people named on this page who do.

To anyone who has not been name checked, consider this your acknowledgement.

Declaration of own work

I declare that this thesis is an original report of my research, has been written by me and has not been submitted for any previous degree. The experimental work is almost entirely my own work; the collaborative contributions have been indicated clearly and acknowledged. Due references have been provided on all supporting literatures and resources.

I declare that this thesis was composed by myself, that the work contained herein is my own except where explicitly stated otherwise in the text, and that this work has not been submitted for any other degree or professional qualification.

Signed:

Andrew Piper

Abstract

Nanoelectrodes are defined as electrodes which have a critical dimension on the order of nanometres. Due to their smaller dimensions they have a reduced iR drop and enhanced mass transport, which results in the rapid establishment of an enhanced steady-state diffusion profile and a greater Faradaic current density, along with a smaller relative double layer capacitance, which together give a significantly increased signal to noise ratio compared to macroelectrodes. This potentially makes nanoelectrodes better sensors and analytical tools than macroelectrodes in terms of their having lower limits of detection and faster detection times. However, due to difficulties with fabrication most nanoelectrode designs are highly irreproducible which has inhibited their characterisation and commercial development. The Mount group has previously reported the design, fabrication and characterisation of a novel nanoelectrode design in conjunction with Engineers from the Scottish Microelectronic Centre (SMC). Microsquare Nanoband Edge Electrode arrays (MNEEs) consist of an array of cavities with nanoscale Pt bands (formed by sandwiching the metal between insulating layers) exposed around their perimeter. MNEEs are fabricated using a photolithographic process so can be reproducibly made in large quantities to high fidelity.

The purpose of this work is to develop our understanding of the fundamental electrochemical behaviour of MNEEs for biosensing. First, a quantitative analysis of the cyclic voltammograms (CVs) and Electrochemical Impedance Spectroscopy (EIS) of macroelectrodes, microelectrodes and MNEE are compared and discussed. Second, their fundamental response is compared in terms of their biosensing properties by using a pre-established impedimetric biosensing protocol developed on macroelectrodes. This protocol uses a PNA probe to detect the *mecA* cassette of methicillin resistant *staphylococcus aureus* (MRSA). The procedure has been optimised and compared for macroelectrodes, microelectrodes and MNEE so as to compare their performances as biosensors. It was observed that MNEE's: (a) form thiol films faster than electrodes with larger dimensions, determined by kinetic studies of 6-mercaptohexan-1-ol film formation (b) form films with different packing structures dependant on the electrode bulk to edge ratio (c) can detect the same concentration of target in less time than larger electrodes because of their increased sensitivity. The film packing has also been quantitatively investigated using EIS and it can be seen that films formed n MNEE were better able to incorporate target DNA into their more splayed out structure.

Unique to this project has been the establishment of a protocol to form heterogeneous carbazole-alanine hydrogel matrices on nanoelectrodes, whose polymerisation is initiated by a pH swing at the electrode surface induced by the oxidation of hydroquinone. The gels growth pattern follows the diffusion field at the electrode and can be monitored using EIS. This also gives a measure of the permeability of the gel by fitting to the correct equivalent circuit. The gel structure has been imaged using light microscopy, confocal microscopy and scanning electrochemical microscopy (SEM). The results give a visual demonstration that MNEE has enhanced diffusion at the corners of the cavities, which is in agreement with previously published

simulations, and give evidence as to the onset of hemispherical diffusion and the conditions at which the diffusion field between neighbouring electrodes begin to overlap, a phenomenon which can be observed visually and correlated to changes in the EIS data.

Hydrogels have been grown chronopotentiometrically at different currents and the permittivity (through the diffusion coefficients) has been measured of redox couples through gels grown at different speeds. It was found that the hierarchical structure of the hydrogels can be tuned; potentially opening the door to a new breed of tuneable, biocompatible anti-biofouling matrices on bio-functionalised electrodes. The system was characterised using the same MRSA detection protocol as optimised for the MNEE and the target DNA was found to be able to permeate through the hydrogels and bind to the probe, which resulted in a significant change in impedance.

Contents

1. Introduction

1.1. Motivation

The study of biosensors is a wonderfully diverse and complex field. Utilising a vast array of techniques such as electrochemistry and spectroscopy to detect a variety of biomarkers, such as DNA and proteins, for a multitude of diseases. The ideal biosensor will be quick, easy to use, cheap and able to detect biomarkers of interest at clinically relevant concentrations. There is a drive within the field for *in vivo,* real time diagnostic devices to monitor key indicators in a patient.[1] This has led to the development of so called "smart sensors" like those developed for diabetics that can not only monitor blood glucose levels in real time, but can then trigger the release of insulin at appropriate levels back into the blood stream to keep the patient's blood glucose levels at a uniform concentration.[2] Current treatments, in which larger concentrations of insulin are administered whenever blood glucose levels get too low, result in peaks and troughs in a diabetic's glucose levels which is bad for their general health.[2] This is an ideal system as it allows for the automated release of an appropriate amount of the treatment drug, optimised for the needs of each specific patient, whilst minimising the hassle for the patient; making it more user friendly. It is easy to imagine similar smart devices being used to treat bacterial infections with antibiotics, or targeting cancerous tumours with chemotherapeutics. In effect keeping the blood concentration of drugs above the ED_{50} and below the LD_{50} at all times during a treatment. In order for all these systems to work they need sensors to accurately and reliably provide information as to the disease state of the patient.

As a result of the drive for *in vivo* smart sensors;[3, 4] it is vital that implantable sensors are developed.[5-7] Logically this requires the miniaturisation of the sensors themselves. The move towards nanoscale sensors is therefore inevitable and the benefits of making electrochemical sensors on the nanoscale make electrochemistry the ideal sensing technique.[8-10] It has been reported within the literature that electrochemical sensing on nanoelectrodes offers lower limits of detection and faster detection times than on a macro electrode.[10, 11] It is also preferable for *in vivo* monitoring to use a label free sensing technique as labels can be expensive and must be checked for toxicity.[12-14] One such electrochemical technique is electrochemical impedance spectroscopy (EIS). Often seen as the "dark art" of electrochemistry, EIS is the most sensitive of electrochemical techniques and as such is prone to pick up changes in the experimental system such as slight changes in temperature which makes it very cumbersome to use practically.[15-17]

If EIS were to be used in conjunction with nanoelectrodes the combined sensitivities of the two would theoretically make some of the most sensitive electrochemical biosensors in the world. There is precedent within the literature for achieving femto molar limits of detection using EIS on macro electrodes,[18] hypothetically the combination of EIS and nanoelectrodes will result in even lower limits of detection. Whilst *in vivo* monitoring may be some way off, limited by biofouling and electrode miniaturisation, nanoscale impedance based diagnostic sensors could find uses in the immediate future as *in vitro* sensors for biomarkers present in extremely low concentrations in biological media. One such use would be the detection of foetal biomarkers in a mother's bloodstream.[19, 20] At present amniocentesis is used to test a foetus for a variety of possible genetic mutations such as downs syndrome. Amniocentesis is

a risky and invasive procedure so alternatives would be beneficial. It known that small quantities of the babies' blood cells pass across the placenta into the mother's blood stream.[19, 20] If a sensor was developed with low enough limits of detection capable of measuring foetal blood biomarkers in maternal blood samples then this would be advantageous for pre-natal screening.

The *modus operandi* of electrochemical biosensors can be thought of as following the same general formula. An electrode is functionalised with a probe film which is electrochemically characterised (in terms of its resistivity, conductivity, capacitance, etc.). Biological media containing a target that will specifically interact with the probe molecule in the film in a way that will alter the electrochemistry of said film; either by increasing/decreasing the electrochemical parameter of interest within the system. Thus there are in reality only 3 component parts of a functioning electrochemical biosensor: the electrode, the sensing film and the electrochemical measurement. Each of these components will be discussed in the remainder of this introductory chapter to familiarise the reader with the theory and state of the art for each component at the time of writing.

1.2. Electrodes

Traditional electrochemical techniques were all developed on macro electrodes. In the field of biosensors, these are typically either gold[14, 21] or platinum[22, 23] (other conductive materials on which films can be formed such as silanes[24, 25] and carbon[26, 27] have been widely reported) as these are biocompatible, form strong thiol-metal bonds for probe film formation and are easily mass produced using standard photolithographic techniques. What is particularly important for the successful use of the electrodes as biosensors is that they are uniformly clean and smooth. Any variations in roughness of cleanliness will cause irreproducibility between the sensors.[28] Roughness especially will affect the electrode surface area, which is an important parameter for most electrochemical techniques.[29] Macro electrodes are typically cleaned by polishing with alumina slurries,[28] see chapter 3.2, which scratches the surface and causes roughness. In spite of this macro electrodes are the most commonly used electrodes in the literature; this is due to their ease of fabrication, price and the fact that the fundamental electrochemical properties of macro electrodes are better understood than those of micro and nano electrodes.

There are three main benefits to using nanoelectrodes over conventional macro-electrodes:[30]

1. Smaller electrodes have enhanced mass transport and measure a steady state current.
2. A smaller double layer capacitance combined with enhanced mass transport means that there is a higher faradaic current density and therefore a better signal to noise ratio.
3. Current is proportional to edge length, as the electrodes get smaller we get a proportionally smaller IR drop. This means that the potential being measured is less affected by the current being passed.

When the cell is said to be at a steady state, the capacitance double layer has been set up and the rate of flow of redox agent to the electrode is under diffusional control.[31]

The detailed structure of the electrodes used in this work and their fabrication can be found in chapter 2, in the interest of avoiding repetition these will not be described in detail here. It is the purpose of this introduction merely to give an overview of the benefits of using nanoscale electrodes and familiarising the reader with the current "state of the art". However, a brief overview of the architecture of the nanoscale electrodes is required in order to fully appreciate the remainder of this introduction. The nano electrodes used in this project have been termed Microsquare Nanoband Edge Electrode (MNEE) arrays. They are formed by sandwiching a conductive platinum or gold layer only nano meters high between two insulating layers and etching cavities through the layers to relieve a conductive band running along the walls of the cavities. They are given their nanoscale properties by the height of the band which is typically 10-100nm high. The cavities are reproducibly made using standard photolithographic processes, they range from 10-100µm in diameter or edge length depending on whether they are circles or squares. The structures are hard to describe and are better represented by figure 1.1. the use of nanoelectrode arrays means that the currents are much larger so easier to measure and the average response of all the electrodes in the array is observed which masks possible defects on a few electrodes in the array.

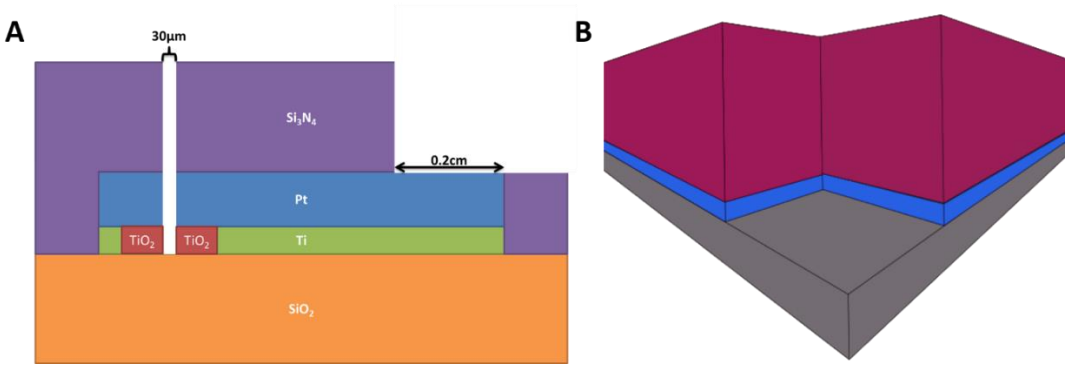

Figure 1.1. NOT TO SCALE. Schematics of the MNEE used in this project. The materials used and dimensions are discussed in detail in chapter 2. (A) shows the vertical architecture of the devices with a Pt band sandwiched between two insulating layers, as well as the etch through the materials. (B) if the reader were to be dropped inside a square cavity and look towards the corner of said cavity they would observe a platinum band (blue) running like cornicing around the wall of said cavity.

The majority of articles in the literature about nanoelectrode biosensing focus on fixing nanoparticles on macroelectrode surfaces for enhancing the sensing performance of macro disk electrodes.[32-35] Another common approach is to electrochemically plate metals, usually gold, for short periods of time in order to "grow" nanoelectrodes.[9-11, 36-38] Another similar approach is to etch electrodes to roughen them and create nanoscale features on the electrode surface.[8] Whilst these techniques have undoubted promise they lack the reproducibility to make commercially viable biosensors. Current reproducible nanoelectrode fabrication methods have broadly been grouped into three classes: metal films whose edge is only exposed to solution, electrochemical etching of metals to create thin cones and the subsequent insulating of all but the tips of the cones and the deposition of metal layers through nanoporous membranes.[22] MNEE arrays fall into the first of these three classes.

1.3. Self-assembling monolayers

The most common method for attaching probe molecules to the electrodes is by the formation of thiolate self-assembling monolayers (SAMs). SAMs are extensively used in the biosensing community as they provide a fast, cheap, easy and efficient route to functionalising noble metal electrode surfaces.[39, 40] It is possible to easily functionalise the tail without disrupting the self-assembly process.[40, 41] The chemistry of SAMs can be divided into two subcategories, the chemistry of the metal-sulfur bond and that between neighbouring alkanethiols in the film.[41, 42] The thiol-metal bond is notoriously strong with a bond dissociation enthalpy of 253.6 ± 14.6 kJ mol^{-1} for gold, similar to those of Au-Au and Pt-Pt which are 226.2 ± 0.5 kJ mol^{-1} and 306.7 ± 1.9 kJ mol^{-1} respectively[43] (no reference could be found with the Pt-S dissociation enthalpy). The formation of the metal thiolate bond formally requires the deprotonation of a thiol, equation 1.1.[44]

$$RSH \rightarrow RS^{-} + H^{+} \qquad \text{(Eqn 1.1)}$$

The Au-S bond is so strong that the thiols can restructure a gold surface by forming clusters around nano-roughened defects in the Au surface layer which are more thermodynamically stable than the Au-Au bonds.[44] Studies carried out by Petrovykh *et al*[45] examine the nature of the sulfur 2p orbital hybridising to Pt after different electrode cleaning and binding protocols using XPS, IR, ellipsometry and contact angle measurements. Three distinct sulfur states were found; they were assigned to a thiolate film, a partially oxidised thiolate film and a third state which was postulated as being one of the following: S bound to Pt bound to an O, S bound to a Pt with a different coordination number, or S adsorbed to Pt as a disulfide.

The interactions between neighbouring thiols in the film are not as strong as the metal-thiol bond. Typically the hydrophobic interactions of the alkyl chains hold neighbouring molecules together,[41] with longer chains forming denser SAMs due to their increased hydrophobicity.[39, 46] Other intermolecular interactions have been proposed to increase the order within the film, such as zwitterionic SAMs, but these were not investigated in this project.[13]

Studies have shown that alkanethiols can be both physisorbed and chemisorbed to the electrode surface, with the ratio between the two dependant on the size of the alkyl chain.[40, 44, 47-49] Non-covalent interactions between the alkanethiol and the metal surface have been observed by using a variety of techniques including ellipsometry[45], XPS[45], IR[42, 45], QCM[42], AFM[48], STM[42], low energy helium diffraction[46] and electrochemistry[41, 50, 51]. These techniques prove that two phases exist in a SAM at thermodynamic equilibrium, with the alkanethiol either “lying down” on the electrode or “standing up” at 30° with respect to the normal of the electrode. The ratio between the two phases is dependent on the electrode topography amongst other factors, with a perfect Au(111) surface reportedly capable of forming a monolayer in only the “standing up” phase.[40, 44, 48-50]

These different phases within the SAM layer are a source of experimental variability and as such there has been much research into the fundamentals of film formation and methodologies to create reproducible alkanethiol monolayers.[13, 41] The SAM structure is hugely dependent on the electrode, with surface roughness and extent of oxidation affecting the nature of the SAM formed.[44, 45]Commonly films are put down in ethanol[40, 45, 49], DMSO[13, 18], water[41, 48, 50] or some mixture of aqueous and organic solvent.[23, 41]

One of the seminal papers within the field was by Poirier[40] in which STM studies of SAM binding kinetics show that there are as many as 6 different phases formed during the formation of a decanethiol monolayer on a Au(111) surface preceding saturation.[40, 49] A brief description of each of these phases is given below.

Figure 1.2 Schematic of the α-phase of alkanethiol film formation. The sulfur head group is represented by the blue disc as it has a variety of possible states, the green arrows represent the ability of the alkanethiol to translocate on the electrode surface.

The first phase (α-phase, figure 1.2) has only been observed using ultra-high vacuum gas phase deposition of thiols. In this phase thiol coverage is very low and the thiols are thought to be able to move around on the metal surface, which shows that the barrier height of a thiol transitioning between neighbouring binding sites must be smaller than kT. Thiols can be thought of as two dimensional gasses in that they are unconstrained in all but one dimension.

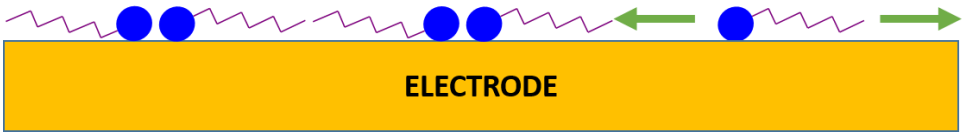

Figure 1.3 Schematic of the β-phase of alkanethiol film formation. The sulfur head group is represented by the blue circle as it could be any of three possible states, the green arrows represent the ability of the alkanethiol to translocate on the electrode surface.

The second phase is the β-phase, figure 1.3, in which the thiol head groups begin to aggregate and form thiolate "islands" on the electrode surface. This process is driven by the hydrophilic head groups and hydrophobic tails aggregating at higher coverage. The size of the alkane side group will determine the amount of hydrophobic interaction and hence the surface coverage at which the β-phase is observed; with longer, more hydrophobic, chains aggregating at lower surface concentrations. For the decanethiol experiments reported, the β-phase was onset when the surface coverage was 26% of the fully saturated film coverage.

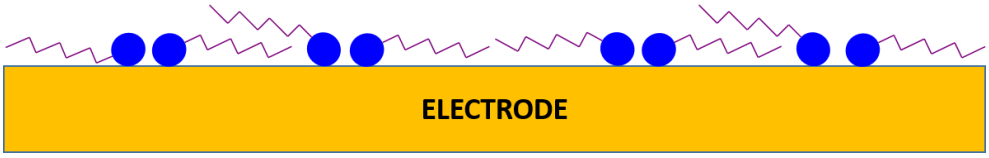

Figure 1.4 Schematic of the χ-phase of alkanethiol film formation. The sulfur head group is represented by the blue circle as its exact state is unknown.

The third phase is the χ-phase, figure 1.4, in which the surface is covered by the combination of thiol head groups and alkane chains. To accommodate further binding as the film continues to saturate the side chains overlap and the film begins to grow in the axis perpendicular to the plane of the electrode. This phase existed between 32-40% of the final saturation coverage of the electrode in the decanethiol experiments performed by Poirier.[40] The χ-phase is a metastable phase, an intermediate combination of the β-phase and δ-phase.

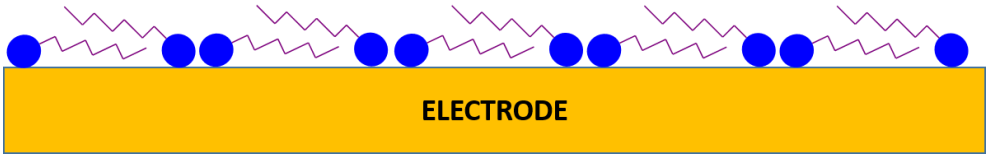

Figure 1.5 Schematic of the δ-phase of alkanethiol film formation. The sulfur head group is represented by the blue circle as its exact state is unknown.

The δ-phase, figure 1.5, occurs next and corresponds to the surface of the electrode being completely covered by the overlapping thiols. This phase is referred to as the interdigitated phase by Poirier and has a two molecule repeating unit of overlapping "islands". Subsequent addition of more alkanethiol will cause a growth of the film perpendicular to the electrode surface.

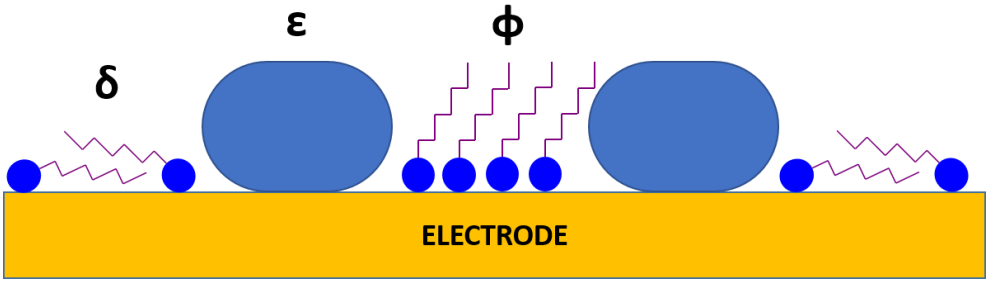

Figure 1.6 Schematic of the ε-phase of alkanethiol film formation. The sulfur head group is represented by the blue circle as its exact state is unknown.

The fifth observed phase is the ε-phase, figure 1.6. This is a very important phase for the comparison of macro and nano electrodes it is found on the boundaries of the ϕ-phase and edges of electrodes. Since the edge to bulk ratio of a nano electrode is different to that of a macro electrode; there will be a higher proportion of this ε-phase on a SAM formed on MNEE. The phase is a highly dynamic region created by the alkanethiol on the edge of a well-structured ϕ-phase region. The alkane chain is free to move in three dimensions in the

volume at the edge of the island/electrode, in effect being limited to one quadrant of a hemisphere with its centre at the metal thiol bond with a radius equal to the persistence length of the alkane chain. In the configuration shown, figure 1.6, where islands of ϕ-phase alkanethiol can move around on the electrode and the ε-phase is not limited to overhanging the edge of the electrode, the alkane chain may be blocking the electrode by "lying down" on the surface held there by the van der Waals forces between electrode and molecule; or "standing up" freeing the space at the electrode, driven by the van der Waals between neighbouring alkanethiol molecules in the ϕ-phase. In reality the alkanethiol is in dynamic motion in the ε-phase constantly switching between the two configurations.

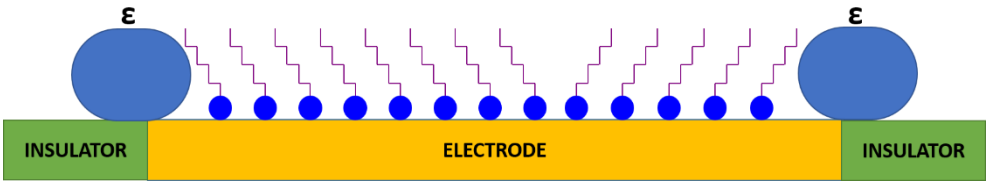

Figure 1.7 Schematic of the ϕ-phase of alkanethiol film formation. The sulfur head group is represented by the blue circle as its exact state is unknown.

The final phase is the afore mentioned ϕ phase, figure 1.7; in which the alkanethiols form well-ordered films with the alkane chain sitting 30° from the normal of the electrode in a close packed resistive structure. This is the monolayer phase that should theoretically have the highest impedance, as it is the most densely packed. There will still be ε-phase thiols at the edges of the electrodes assuming the thiol does not covalently bind to the insulator.

The theory dictates that SAMs formed on macro and nano electrodes will have a different ratio of ε-phase to ϕ-phase probe molecules due to their different bulk to edge ratios which may affect their biosensing performance.

SAMs can either be formed by functionalising the biomolecular probe and creating a SAM directly out of it,[18] or by forming a SAM layer and binding the probe to the SAM through some other chemistry.[13] Both methods allow for any biomolecule to realistically be used as a sensing probe so long as its activity is not compromised during SAM formation i.e. if an antibody were to form a SAM where its active site was held towards the electrode so rendering it unable to bind to the antigen in solution. The general principle of function is that the binding of the probe and target will induce some form of change to the SAM layer, whether that be in terms of its packing density or inherent charge, and that this change will correlate to changes in the electrochemical response of the SAM film.

1.3.1. PNA and DNA probes

In this project only PNA and DNA probes are used. Both of which have 15 base sequences specific for binding the mecA cassette of methicillin resistant *staphylococcus aureus* (MRSA). This biosensing protocol has previously been published by Corrigan *et al*[18] using the PNA probe. PNA is a synthetic probe modelled on DNA but with the phosphate backbone having been replaced by glycine. This removal of a negative charge from the molecule increases binding efficiency with target ssDNA oligomers. There is also a tendancy for ssPNA probe

SAM layers to aggregate and pack more densely than ssDNA probe SAMs due to a lack of electrostatic repulsion between neighbouring probe sequences.[52]

1.4. Electrochemical measurements

1.4.1. Cyclic voltammetry

One of the most frequently used electrochemical techniques is cyclic voltammetry (CV), in which a range of potentials are scanned through and the current measured. In linear sweep voltammetry the potential is scanned in only one direction (i.e. from 0 V → 1 V) whereas in cyclic voltammetry the scan goes back to the start potential (0V → 1V → 0V, for example). The potential time transient for a cyclic voltammogram with two complete cycles is given in figure 1.8.

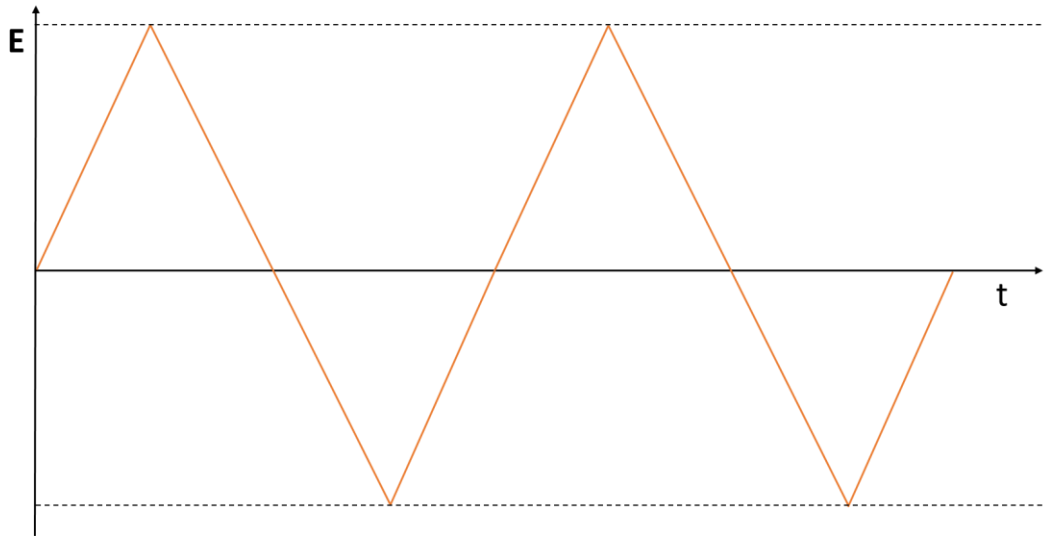

Figure 1.8. A schematic of a typical potential time transient for a cyclic voltammogram going through two full cycles.

A typical CV of a reversible redox couple at a macro electrode has been included in figure 1.10. The basic principle behind cyclic voltammetry is that in order to transfer electrons between the electrode and a redox active species in solution, the right potential must be applied. This is in order to raise the energy of the electrons in the Fermi level of the electrode to a higher energy state than the LUMO of the redox agent for reduction of the redox agent, or conversely to lower the LUMO of the electrode to a state where there is a thermodynamic drive for electron in the HOMO of the redox agent to transfer to the electrode an oxidation reaction. The potential of zero charge is obtained at thermodynamic equilibrium and there is no net transfer of charge between redox agent and electrode. It is important to note that this is an equilibrium and electrons are free to flow between the electrode and redox agent but the forward and reverse reactions are occurring at the same rate and therefore there is no current measured as passing. This is often referred to as the open circuit potential (OCP) as when a three electrode system is set up with a redox agent in solution it will sit at the thermodynamic steady state and the potential across the cell will be a measureable. As the potential in the cell is moved away from the OCP the electrons begin to flow in a particular

direction, from electrode to redox agent as the potential decreases (reduction) and from redox agent to electrode as the potential increases (oxidation). This of course is the very definition of a current and a linear response is normally observed where the rate of electron transfer is proportional to the potential being applied, figure 1.9.

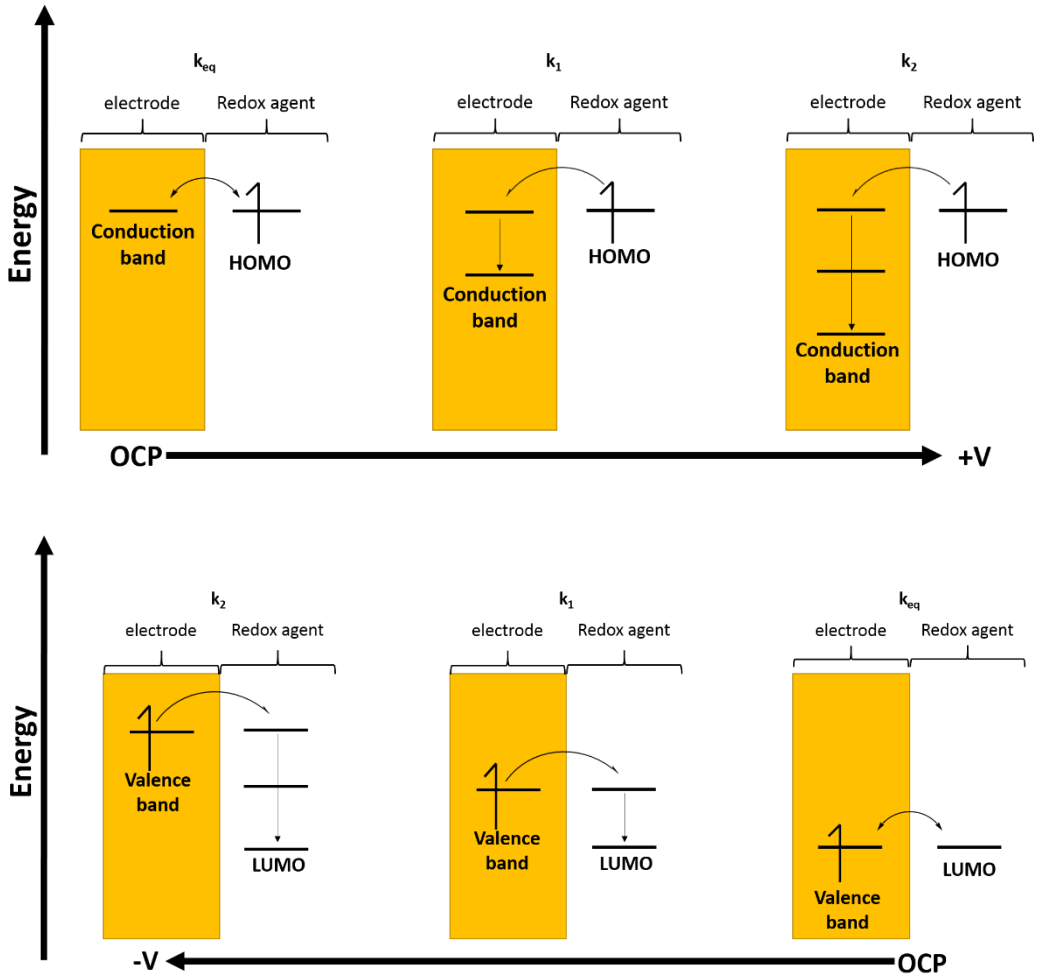

Figure 1.9 Energy diagram showing the difference in electron transfer kinetics as the potential is moved positive and negative of the open circuit potential (OCP). In both cases $k_2 > k_1 > k_{eq}$. The LUMO is the lowest unoccupied molecular orbital and the HOMO is the highest occupied molecular orbital.

At potentials further from the OCP the linearity of this response breaks down, figure 1.10. Peaks are observed in the voltammogram due to the kinetics of electron transfer no longer being the limiting process. At these high potentials electron transfer is so rapid that the limiting factor is the transport of fresh redox agent to and from the electrode surface. Electrons can only transfer over very short distances of < 5 nm.[53] So must be transported from the bulk electrolyte to the electrode surface in order to undergo electron transfer, when the rate of the reaction is limited by the flux of redox agent it is said to be under mass transport control. As the potential continues to increase the current levels off. At these and higher potentials the natural convection within the bulk solution is refreshing the electrode surface with redox agent so a constant current is measured.

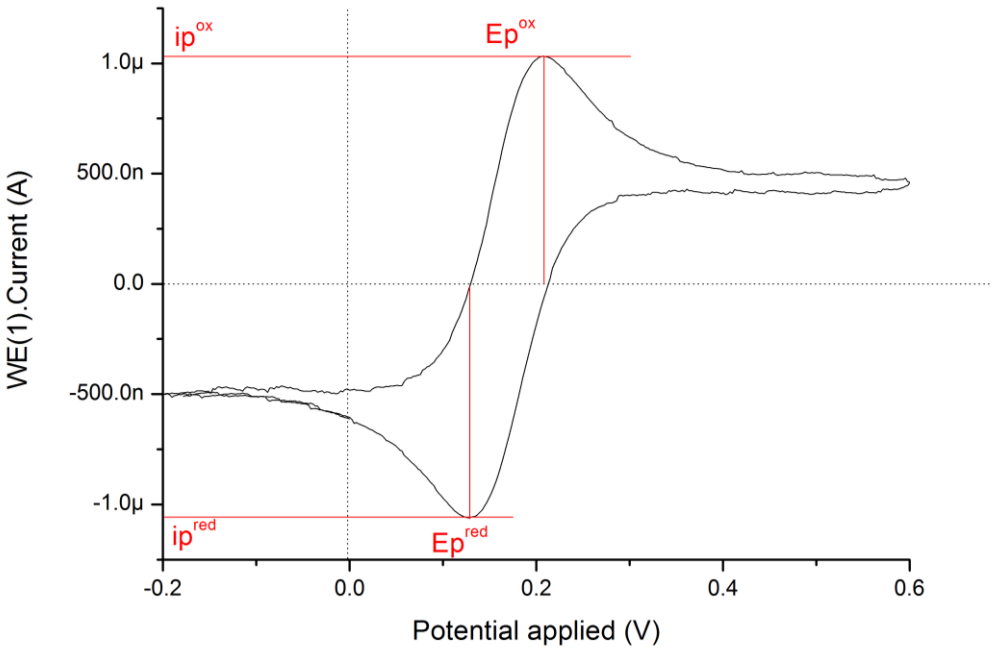

Figure 1.10 The CV wave of 1mM ferri ferrocyanide at a Au macrodisc electrode showing the potential of the oxidation and reduction peaks (+0.20 V and +0.13 V respectively) and the peak currents as well (-1.05 µA and +1.05 µA).

There are many equations used for calculating important experimental factors from a voltammogram. Perhaps the two most important as far as this work is concerned are the Randles'-Sevcik equation, equation 1.2.

$$i_l = 0.4463nFAc_0\left(\frac{nF\nu D}{RT}\right)^{\frac{1}{2}} \qquad \text{(Eqn 1.2)}$$

In which i_l is the diffusion limited current, D, is the diffusion coefficient in m^2s^{-1}, n is the stoichiometric number of electrons being transferred, F is Faraday's constant, A is the surface area of the electrode and c_o is the initial concentration of redox agent.

Equations for calculating the limiting current for micro disk, recessed micro square and recessed nanoband edge electrodes have previously been established and reported. They have been given in equations 1.3-1.5.

Microdisc:

$$i_L = 4nFDcr \qquad \text{(Eqn 1.3)}$$

Microsquare array:

$$i_L = \frac{2.34nFDcr}{1764\ (no.of\ squares\ in\ the\ array)} \qquad \text{(Eqn 1.4)}$$

MNEE array:

$$i_L = \frac{0.956nFDcr}{1764\ (no.of\ squares\ in\ the\ array)} \qquad \text{(Eqn 1.5)}$$

1.4.2. Differential pulse voltammetry

Cyclic voltammetry is not the only voltammetric technique used in this thesis. Differential pulse voltammetry is used occasionally as it makes analysis of the OCP easier as well as being slightly more sensitive than cyclic voltammetry. Rather than scanning the potential linearly a stepwise potential is scanned with the current measured before and after potential steps, figure 1.11.

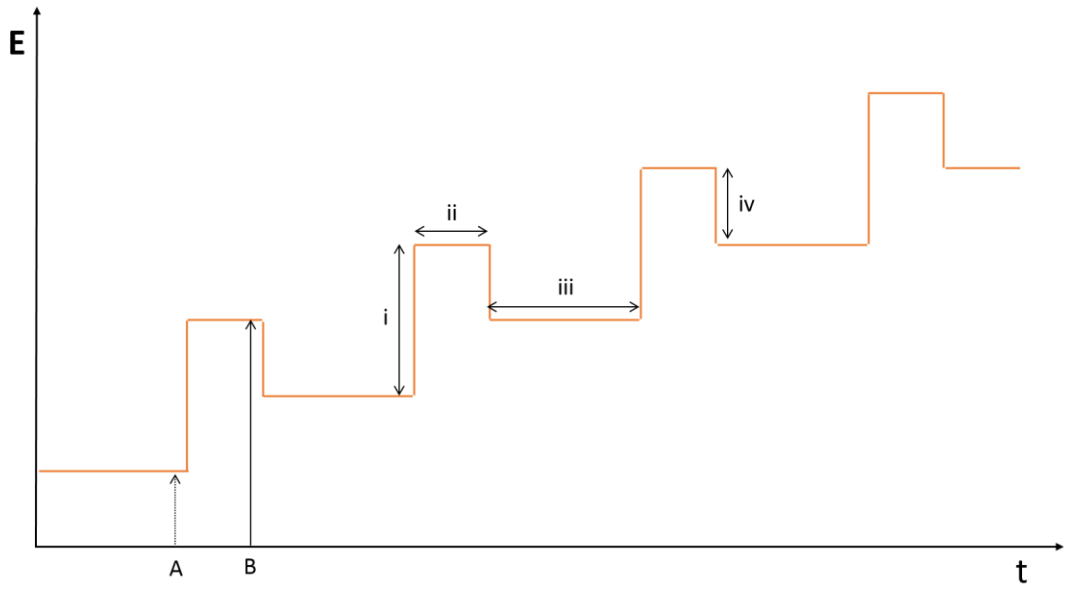

Figure 1.11 Potential time transient of a differential pulse voltammogram (DPV). The current is measured at points (A) and (B) and the difference between them plotted against the base potential. The amplitude of the pulse (i) is tunable but normally 25 mV, the pulse duration (ii) is very short usually 50 ms, the time between pulses (iii) is normally 0.5 seconds and (iv) is the drop potential which is typically half the magnitude of (i).

This measuring of the current before and after potential pulses and plotting of the change in current is where the name differential pulse voltammetry originates. This technique has become fashionable in the field as, despite being more complex than cyclic voltammetry, the data is more user friendly; a layman is better able to appreciate a single peak getting bigger or smaller than a CV where two peaks can smear and become more wavelike. It does however offer less information than cyclic voltammetry so was not used as extensively in this project where the more fundamental information as to electrode processes was sought. The DPV response is typically given in a plot of the change in current (ΔI) vs potential (V), figure 1.12.

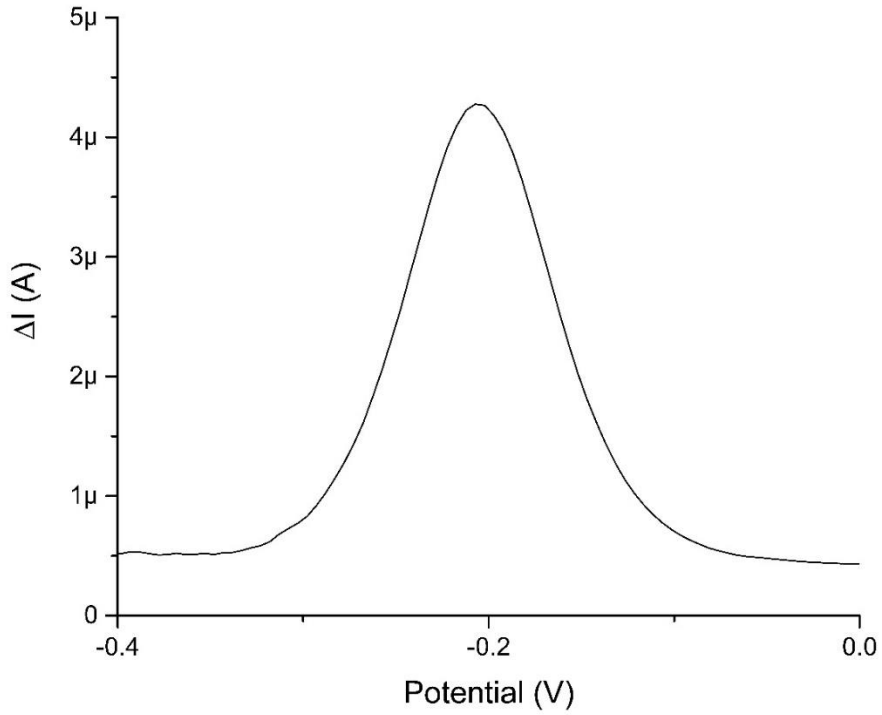

Figure 1.12 Example of a potential vs ΔI plot of the redox wave obtained with a Pt macro electrode in a solution of ruthenium hexamine chloride (1mM) in 1x tris-HCl vs a saturated calomel reference electrode and Pt gauze counter electrode.

1.4.3. Electrochemical impedance spectroscopy (EIS)

Impedance can be thought of as complex plane resistance; where ideal resistance can be described by Ohm's law, equation 1.6.[31]

$$R \equiv \frac{E}{I} \qquad \text{(Eqn 1.6)}$$

Where resistance (R) is equivalent to the voltage (E) divided by the current (I).

For a resistor to be ideal it must meet the following criteria:[16]

- It must follow Ohm's Law at all currents and voltages.
- Resistance does not vary with frequency.
- AC voltage and current signals through a resistor must be in phase with one another.

Complex plane resistance is commonly referred to as impedance (Z) which has greater real world applications.[16, 54] It makes sense to conceptually think of both impedance and resistance as the ability of a circuit to curb the flow of the electrical current. Ohm's law for non-ideal resistors can therefore be re-written for impedances as in equation 1.7.

$$Z = \frac{E}{I} \qquad \text{(Eqn 1.7)}$$

In EIS the cell is held at a DC potential and a small sinusoidal AC potential, typically 0.01 V, is passed across the electrode; and the sinusoidal current signal produced is measured. The applied AC potential is kept small so that the cells response is pseudo-linear, i.e. the current and potential sinusoids will have the same frequency and will only change in amplitude (E_0 and I_0) and phase (Ø), see figure 1.13.[16, 31, 54]

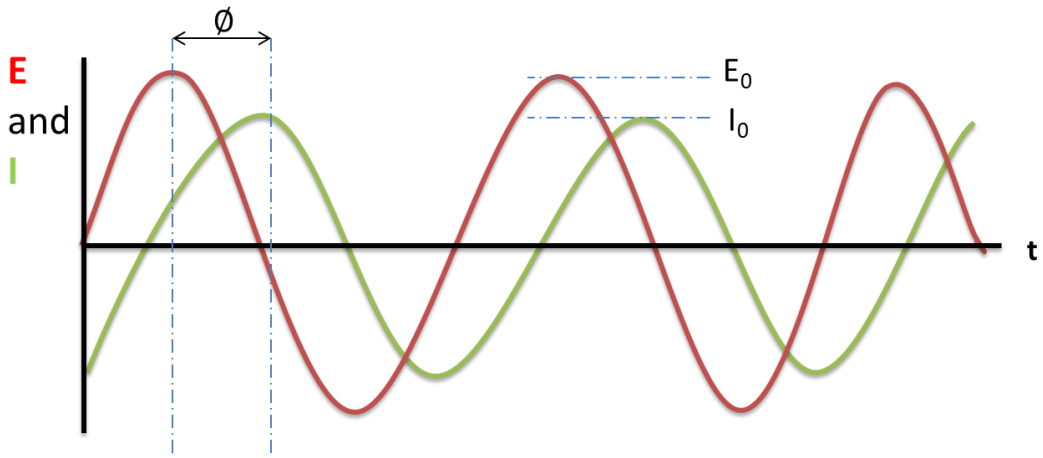

Figure 1.13 The applied sinusoidal potential (red) and measured current sinusoid (green) and how they change in phase (Ø) and amplitude (E_0/I_0).

The potential sinusoid can be expressed by equation 1.8.[16]

$$E_t = E_0 \sin(\omega t) \qquad \text{(Eqn 1.8)}$$

Where E_t is the potential at time *t*, E_0 is the amplitude of the signal and ω is the frequency in radians. In a linear system the current signal can be described by equation 1.9.

$$I_t = I_0 \sin(\omega t + \emptyset) \qquad \text{(Eqn 1.9)}$$

Where I_t is the current at time *t*, I_0 is the amplitude of the signal sinusoid, ω is the frequency in radians and Ø is the change in phase between the applied and measured sinusoids.

Substituting equations 1.8 and 1.9 into equation 1.7 allows the calculation of impedance in terms of amplitude (Z_0) and phase shift (Ø), equation 1.11.[16]

$$Z = \frac{E_t}{I_t} = \frac{E_0 \sin(\omega t)}{I_0 \sin(\omega t + \emptyset)} = Z_0 \frac{\sin(\omega t)}{\sin(\omega t + \emptyset)} \qquad \text{(Eqn 1.10)}$$

Using Euler's formula, equation 1.11, E_t and I_t can be expressed as complex functions, equation 1.12 and 1.13 respectively, and the impedance at a set frequency as a complex number, equation 1.14.[16, 55]

$$\exp(-i\emptyset) = \cos\emptyset - i\sin\emptyset \qquad \text{(Eqn 1.11)}$$

$$E_t = E_0 \exp(-i\omega t) \qquad \text{(Eqn 1.12)}$$

$$I_t = I_0 \exp(-i\omega t + \emptyset) \qquad \text{(Eqn 1.13)}$$

$$Z(\omega) = \frac{E}{I} = Z_0 \exp(i\emptyset) = Z_0(cos\emptyset - isin\emptyset) \qquad \text{(Eqn 1.14)}$$

EIS data is typically analysed and displayed in the form of a Nyquist plot. Each point on a Nyquist plot is the impedance measured at a set frequency. This impedance will consist of

real and imaginary components as shown in equation 8; in a Nyquist plot the real component ($Z_0 cos\emptyset = Z'$) is plotted on the x-axis and the imaginary component ($-Z_0 sin\emptyset = -Z''$) on the y axis, figure 1.14. As stated, an ideal resistor has no frequency dependency so forms a straight vertical line on a Nyquist plot as shown in red on figure 1.14.

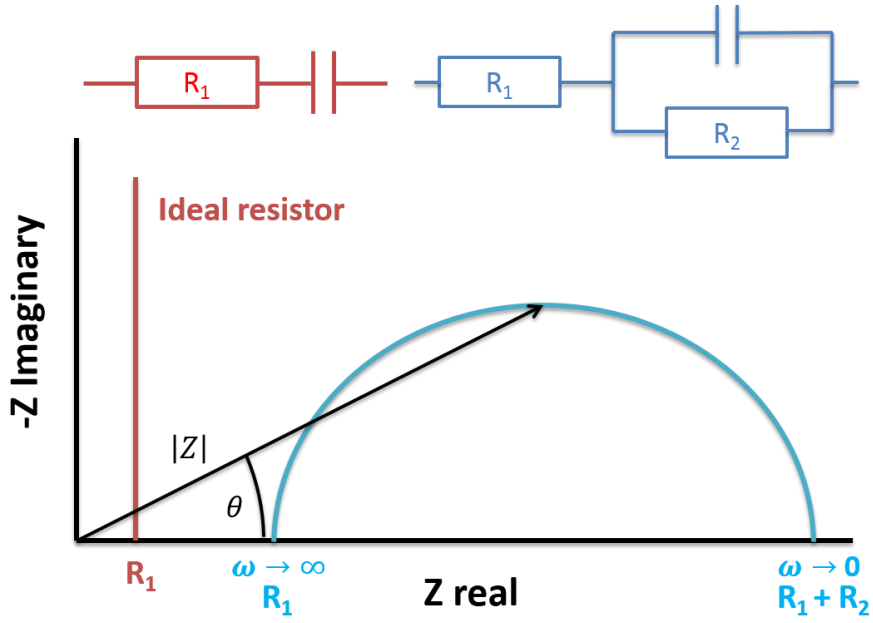

Figure 1.14 Generalised Nyquist plot showing and ideal (red) and non-ideal (blue) resistor with the accompanying circuits they fit too. The impedance at each point on the semicircle can be expressed in terms of magnitude $|\boldsymbol{Z}|$, and phase change ($\emptyset$).

1.4.4. Equivalent circuit representation

For analysis, EIS data must be modelled with an equivalent circuit. This is an electrical circuit with elements used to represent the different physical processes taking place at the electrode, fitting allows the quantification of these different elements and therefore a quantitative analysis of the changes in the system. Examples of this include modelling the resistance of the solution as a resistor, and the capacitance double layer as a capacitor. Before describing the elements that are commonly present in systems it seems prudent at this point to revise the electrical components we can model in the circuit.

1.4.4.1. Resistors (R)

Resistors are circuit elements that limit the flow of current through a circuit. The ability to restrict the flow of current is measured in Ohms. Ideal resistors follow Ohms law, equation 1.6, and can be related to impedance by substituting Z for R, equation 1.7.[16]

1.4.4.2. Capacitors (C)

A capacitor is a component that can store electrical charge, it is comprised of two conducting layers separated by an insulating layer. The units for the amount of charge stored by a capacitor is the Farad, where 1 Farad equates to one coulomb of charge being stored when one volt is applied across the capacitor.[16]

$$Z = \frac{1}{i\omega C} \qquad \text{(Eqn 1.15)}$$

Equation 1.15 is used to fit the capacitance of an impedance spectrum, (Z) is the magnitude between each data point and the origin on the Nyquist plot. Since this magnitude and the frequency of the measurement in radians (ω) is known then the capacitance can be calculated for each frequency sampled. These fitted values are then averaged and a standard deviation quoted as the error in the fit.

A capacitor's impedance decreases as frequency increases, also the measured current sinusoid will be shifted 90° from the applied potential sinusoid when passing through an ideal capacitor.[16] Capacitors are discussed in more detail in the context of the capacitance double layer in section 1.4.6.2.

1.4.4.3. Warburg element (W)

The Warburg element is used to model diffusion of a redox species to the electrode surface when it is the limiting factor in the reaction rate. It manifests itself as a 45° line on a Nyquist plot and varies depending on electrode surface area and diffusion coefficients.[54] Warburg elements give outputs of admittance (Y_0) quantified using equation 1.16 in a similar fashion to the determination of capacitance:

$$Z = \frac{1}{Y_0\sqrt{i\omega}} \qquad \text{(Eqn 1.16)}$$

W is a direct measure of the permittivity of the electrolyte at the electrode solution interface to the redox agent, it sits at a constant angle of 45° when the solution is under convection limited flux of redox agent refreshing the surface at 25 °C. Explaining the nature of a line at 45° to the *x*-axis requires a complex mathematical derivation which is outwith the scope of this work, those interested should consult the textbooks on EIS by Barsoukov.[15] In terms of fitting EIS data, Warburg elements model the data in the same manner as a constant phase element but with a fixed N value of 0.5, see section 1.4.4.d below. The fitting software quotes fits to the Warburg element in units of mho (the SI unit being siemens, S, with 1 Mho = 1 S).

1.4.4.4. Constant phase elements (CPE, Q)

Constant phase elements are a source of controversy within the field, as they fit the data to an equation that does not have a clear theoretical basis. The more parameters to which a circuit is fit the better the fit will be, but the model must still have a physical basis in reality. A justification of why a constant phase element is fitted should be given whenever used. The CPE gives values of admittance in conjunction with an "N" value. A true capacitor will form a perfect semi-circle in an RC circuit as it causes a phase change between the potential and current sinusoids of exactly 90°. An ideal Warburg causes a phase change of 45°, the CPE is able to fit non-ideal values for each of these elements by offsetting the x-axis to which it is fitting. Figure 1.15 depicts this "tilting" of the axis. The offset angle of the new axis and the original axis is given directly by "N". When N = 1 there is no offset and the response is being modelled as an ideal capacitor, i.e. there is a 90° phase change. When N = 0.5 there is a 45° offset and the fit is equivalent to an ideal Warburg element. N = 0 is caused by an ideal resistor, where the signal does not register a positive value on the imaginary axis. Which means that there is no phase change with frequency response, the definition of ideal resistance.

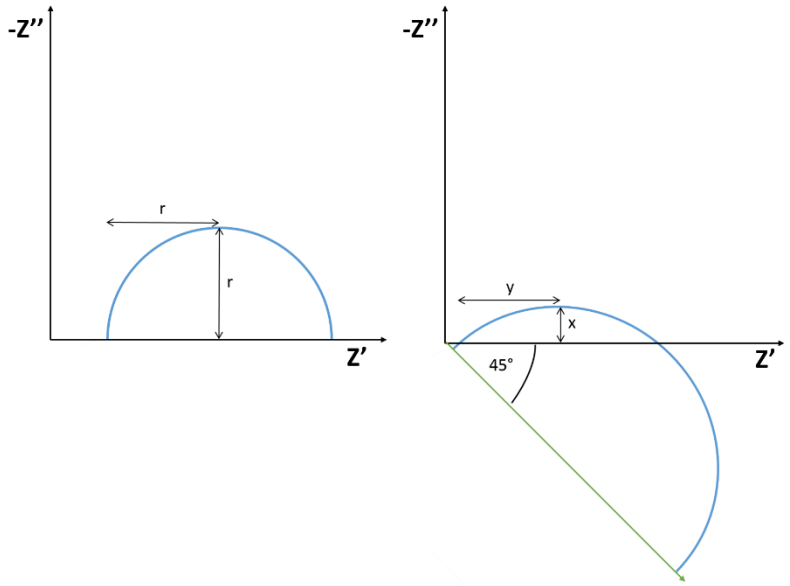

Figure 1.15 Schematic showing how the N value of a constant phase element offsets the x axis and the effect that this has on the observed Nyquist plot.

Some examples of where constant phase elements are used correctly include the fitting of an inhomogeneous film on an electrode where the capacitance double layer is not uniform across the electrode surface.

The equation for fitting the CPE is given below, equation 1.17, it is a modification of the equation 1.15, which is used for fitting capacitors, to include the integer value of N.

$$Z = \frac{1}{Y_0(i\omega)^N} \qquad \text{(Eqn 1.17)}$$

1.4.5. Combinations of circuit elements in series and parallel

Because there are multiple elements in an equivalent circuit it is vital to appreciate the behaviour of resistors and capacitors when in series and parallel with one another and the resulting effect on impedance.

When we have impedances in series the overall impedance of the circuit is the sum of the impedances of the individual circuit elements, equation 1.18:[31, 56, 57]

$$Z_{total} = Z_1 + Z_2 + Z_3 \ldots + Z_n \qquad \text{(Eqn 1.18)}$$

For impedances in parallel the inverse impedance of the cell is equal to the sum of the reciprocals of the individual impedances of each element in the cell, equation 1.19:[16, 31, 57]

$$\frac{1}{Z_{total}} = \frac{1}{Z_1} + \frac{1}{Z_2} + \frac{1}{Z_3} \ldots + \frac{1}{Z_n} \qquad \text{(Eqn 1.19)}$$

For capacitors and Warburg elements the inverse is true as they are both inversely proportional to impedance.

1.4.6. Physical electrochemical elements

It is possible therefore to model the resistive and capacitive behaviours of the physical properties of the cell and quantify them all by fitting to an equivalent circuit; so it is prudent at this point to discuss the typical physical properties that are manifest in the system.

1.4.6.1. Resistance of the solution (R_s)

There is a resistance to passing a current through the solution, this is known as the solution resistance (R_s).[16, 31, 54] A conceptual way of thinking about this is to imagine a single charged particle at a very short distance from the working electrode, at very high frequencies electrode is switching between charge states, changing between negative and positive of the open circuit potential, very rapidly. This causes the particle to vibrate as it is being attracted and repelled by the electric field. As the frequency decreases the particle moves by an increasing amount until a frequency low enough for a build-up of ions at the electrode surface is reached, see figure 1.16.

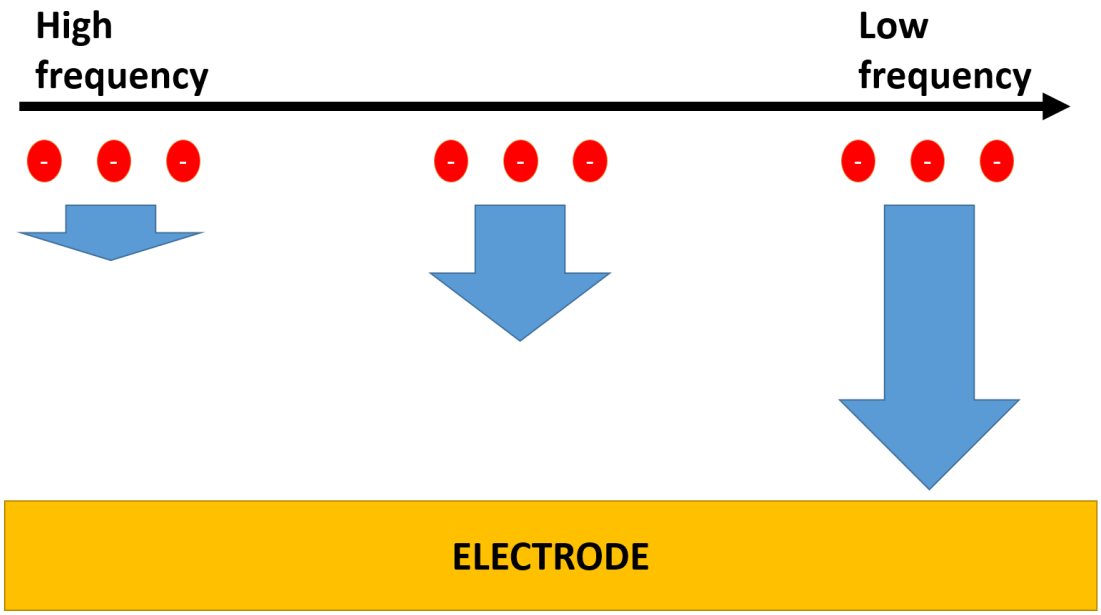

Figure 1.16 Scanning from high to low frequencies the movement of ions in the solution increases until they make contact with the electrode and a signal is observed

This is when we first start to see a change in the impedance of the electrode surface.[16, 54] In this case the highest frequency at which a non-zero response is seen on a Nyquist plot should give the value of R_s, which is a measure of the conductivity of the solution. The resistance of an ionic solution will vary depending on ionic strength, and temperature.[16] The values of R_s are obtained by finding the high frequency x intercept of the fitted semi-circle on a Nyquist plot.

1.4.6.2. Capacitance double layer (C_{dl})

Once ions start to gather at the electrode/solution interface they form a capacitive double layer (C_{dl}). The charge on the electrode causes ions of opposite charge to start to collect at the electrode, but the frequency still exceeds the timescales requires for electron transfer. The separation between the ions in the double layer and the electrode is incredibly small, typically on the scale of angstroms. The separation of charges by an insulator causes a capacitance which is why the double layer is modelled using a capacitor.

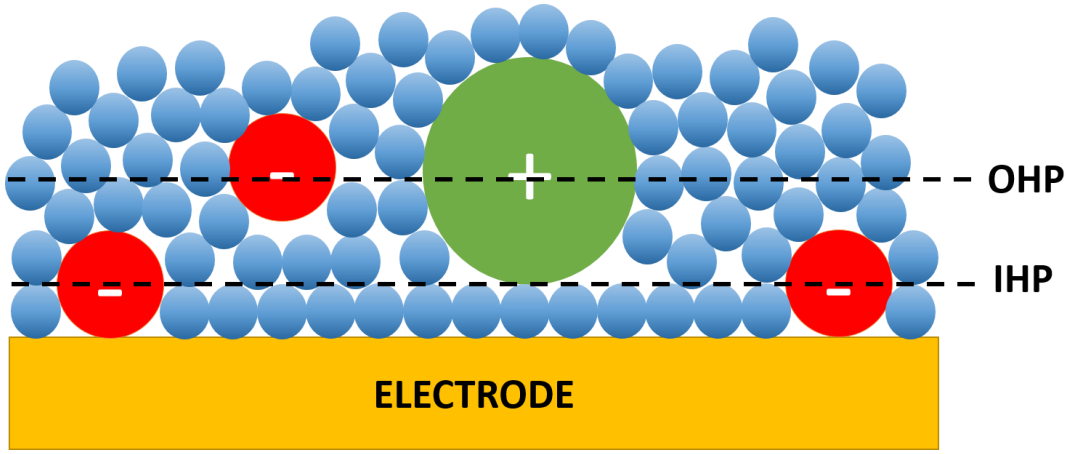

Figure 1.17 Schematic of the double layer at the electrode surface showing the inner and outer Helmholtz planes (IHP and OHP respectively). The anions are coloured red and the cations green with the blue dots representing water molecules.

The magnitude of the C_{dl} is dependent on the potential, the electrolyte, the metal and the electrode area, with typical values between 20-60 μFcm^{-2}.[16, 31] Fouling of the electrode will reduce the number of coordination sites for ions but may introduce a parasitic capacitance.

The earliest attempt to explain the double layer can be credited to Helmholtz (1853).[31, 53] His parallel plate model stipulates that there is free charge on the electrode and charge in the solution. These charges are separated by free space in the region between the electrode and ions. The capacitance of parallel plates can be calculated from equation 1.20 in which the Helmholtz capacitance, C_H, is related to the permittivity of free space, ε_0 (8.8542 ×10^{-12} J^{-1}C^{2}m^{-1}), the dielectric constant of the solvent, ε, the area of the electrode, *A*, and the distance between plates, *d*, which is taken from the radius of the solvated cation.

$$C_H = \frac{\varepsilon_0 \varepsilon A}{d} \qquad \text{(Eqn 1.20)}$$

Since anions are typically smaller and de-solvate to come into contact with the electrode, whereas cations are typically larger and less likely to de-solvate; there are two values of *d* for each system. This gives rise to the inner and outer Helmholtz planes as shown in figure 1.17.

The Helmholtz model fails to describe the effects of changing potential on the size of the double layer or its dependence on ion concentration, which led to the development of the Diffuse-double layer theory of Gouy(1910) and Chapman (1913).[31, 53] Gouy and Chapman independently proposed that there are two forces acting upon the ions in solution, the charge on the electrode and the random thermal motion of the solution, which acts to equalize the charges within the solution. In effect the charge of the electrode causes an

ordered system of layered ions to form, but thermal convection in the solution means that the order in the layers is gradually lost farther away from the electrode surface. The flaw with this model is that it does not correlate with the experimental results; it only agrees with those results obtained in dilute solutions at potentials very close to the point of zero charge.[53]

Finally, there is the Stern model (1924); which combines the Helmholtz and Gouy-Chapman models. The model is that there is a Helmholtz type, compact, double layer immediately at the electrode surface. Beyond this a more diffuse double layer which extends into the bulk solution, see figure 1.18.

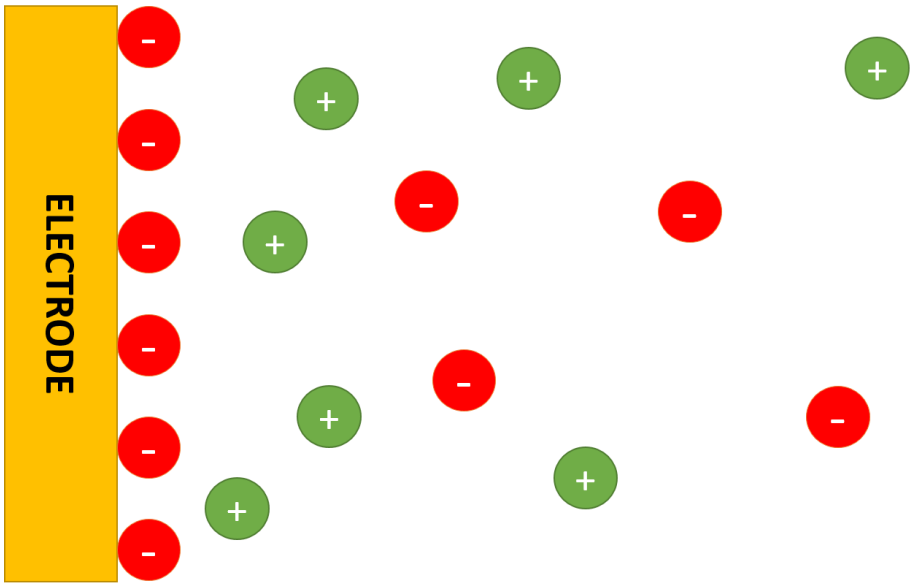

Figure 1.18. Schematic representation of the Stern model of a double layer at an anode.

There have been publications where binding of analytes causes enough of a change in the capacitance double layer that it can be used as a sensing parameter, removing the need for a redox agent in solution, this is commonly referred to as non-faradaic EIS or capacitance spectroscopy.[12, 14, 58]

1.4.6.3. Charge transfer resistance (R_{ct})

The charge transfer resistance is the resistance encountered when transferring an electron from a redox agent to an electrode or vice versa.[31] This charge transfer has a given rate which is dependent on the reaction type, temperature, potential and concentration of redox species.[16] The rate of electron transfer is typically very fast, it is modelled as a resistor as an increase of energy is needed to move an electron in the HOMO of the redox agent to the LUMO of the electrode, or vice versa. The probability of the electron tunnelling between the electrode and a redox agent is dependent on the field at the electrode.[31] This is a thermodynamically controlled process where the rate of electron transfer is dependent on the thermodynamic driving force of the potential drop. The minimum theoretical value of R_{ct} can be related to the area of the electrode by equation 1.21.[30]

$$R_{ct} = \frac{2RT}{n^2F^2c_\infty k^\theta A} \qquad \text{(Eqn 1.21)}$$

Where R and *T* are the gas constant and temperature respectively, F is Faradays constant, *n* is the number of electrons being transferred, c_∞ is the concentration of redox agent in the bulk electrolyte, *A* is the area of the electrode and k^θ is the rate constant for the redox reaction.[30]

1.4.6.4. Warburg diffusion (W)

When the rate of the reaction is controlled by the linear diffusion of redox agent from the bulk solution to the electrode surface, a 45° line is observed in a Nyquist plot. This steady state is set up much faster on smaller electrodes as they have enhanced mass transport. [59] A more detailed explanation of Warburg diffusion is not required for this thesis, it should simply be noted that as stated in section 1.4.4.3, the element is fit as a constant phase element with N=0.5 and models linear diffusion to an electrode surface.

1.4.6.5. Non-linear resistance (R_{nl})

On macro electrodes the majority of redox agent diffuses to the electrode in a linear fashion, so can be fit to a Warburg element at low frequencies. On micro and nano electrodes the majority of signal is no longer coming from the linear diffusion, but rather a hemispherical steady state diffusion profile is formed at low frequencies.[30]

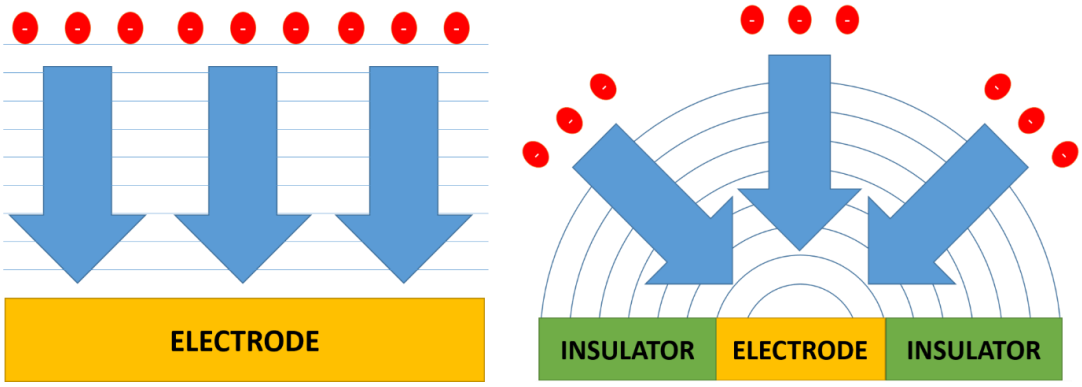

Figure 1.19 (LEFT) The linear diffusion pattern seen over the bulk of an electrode at higher frequencies, which can be fit by a Warburg element. (RIGHT) A hemispherical diffusion pattern formed on smaller electrodes and at lower frequencies, fit by R_{nl}.

At high frequencies the redox agent at the electrode solution interface will undergo redox chemistry, further redox species must diffuse into the Helmholtz plane for electron transfer to occur. Initially there is enough redox agent within the immediate vicinity of the Helmholtz plane to refresh the electrode by diffusing in a linearly to the electrode, which can be modelled by a Warburg element. However, as the depletion zone grows to a similar dimension to the electrode the diffusion profile takes on a hemispherical shape, figure 1.19. On smaller scale electrodes the depletion zone of the same dimensions as the electrode forms much faster/at much higher frequencies, than it would for a larger electrode in the same system. There is an inherent resistance to transporting a redox agent through the depletion zone to the Helmholtz plane, this is modelled as the resistance of non-linear diffusion, R_{nl}. In an ideal system, electrodes of any and all dimensions could theoretically set up a hemispherical diffusion profile. However, natural convection means that R_{nl} cannot be seen for a macro electrode left stationary in solution.[59]

The magnitude of R_{NL} can be theoretically calculated by equation 1.22: [30, 59]

$$R_{nl} = \frac{4NRT}{0.96nF^2c_0DL} \quad \text{(Eqn 1.22)}$$

Where N is the number of squares in the array, R is the universal gas constant, *T* is the temperature, *n* is the number of electrons being transferred, F is Faraday's constant and c_0 is the bulk concentration of redox agent, *D* is the diffusion coefficient and *L* is the length of the squares in the array.

1.4.6.6. Normalising circuit elements

Since electrodes of different dimensions are to be compared throughout this thesis, it is therefore important to be able to normalise data from different sized electrodes.

In equivalent circuits, when considering capacitances, the capacitance (C) can be calculated using equation 1.20. Thus if one assumes the double layer capacitance arises from a simple capacitor (neglecting such effects as the variation of C_{dl} with ionic strength, electrode potential, temperature, ion type, electrode cleanliness and electrode roughness[16]), the response can be normalised by dividing by the geometric area of the electrode.

In contrast, resistances (e.g. the resistance to charge transfer, R_{ct}) have an inverse relationship to the electrode area (see equation 1.21) so all resistance must be normalised by multiplying by the area of the electrode (again ignoring effects that will vary the resistances measured or area of the electrode).

1.4.7. Typical equivalent circuits

There are equivalent circuit to which data can be modelled throughout the literature. What is important when selecting the equivalent circuit to use is to understand the system under investigation and use a circuit that fits all the physical parameters present in said system. For instance, the Randles' circuit, equivalent circuit APP 1.2, is used to model a typical macro electrode response. Where at high frequencies the resistance of the solution will be observed, as the frequency is decreased a capacitance double layer forms. As the frequency is again scanned lower the charge transfer takes place until it becomes diffusion limited, at which point a linear diffusion profile will be present and a Warburg element used to fit the data. Throughout this thesis, different equivalent circuits will be used for different electrodes in different systems. At all times a justification of the choice of equivalent circuit will be provided. To avoid repetition all the equivalent circuits used have been summarised in appendix 1 and will be referred to in the text by their equivalent circuit number as indicated in said appendix.

1.5. Imaging techniques

Throughout this thesis the chips were imaged by optical microscopy, scanning electron microscopy (SEM) and, in chapter 6, confocal microscopy. Light microscopy is a commonly used and well understood technique so will not be explained here, a discussion of confocal microscopy can be found in chapter 6.1.1.3. A brief description of SEM is given below.

1.5.1. Scanning electron microscopy

Scanning electron microscopy (SEM) is a common technique in which the sample is mounted in a chamber that is vacuumed down.[60] The sample is then bombarded with a beam of electrons, focused by a magnetic field, electrons that are scattered back from the sample are collected by a detector and the electrical signal is sent to a video screen.[60] The beam is then scanned across the sample area to obtain an image of the sample. Conventional light microscopes are limited in resolution by the de Broglie wavelength of the light used, in SEMs the typical resolution is limited by the ability to focus the electron beam (rather than the de Broglie wavelength of the electrons which can be as short as 10 pm).[60] Typical resolutions of SEMs are in the region of single nanometres.

Obtaining SEM images of metal samples can be difficult as a large amount of surface charging takes place, the electrons are absorbed by the metal surface and cause the metal to “glow”. This is a result of secondary electron excitation within the sample, the intense brightness of the metals can distort the images collected by this technique, but in this thesis at times provides a clear indication as to the presence or absence of platinum, chapter 2.3.

2. Microfabrication

2.1 Introduction

Previous work published by the Mount group determined a procedure for fabricating microsquare (MS) and microsquare nanoband edge electrodes (MNEE).[22, 30, 59, 61] These electrodes can be made using standard photolithographic procedures by sandwiching a metal between two insulators and etching square cavities 10-100 µm wide through the layers. In the case of MS arrays only the top insulator is etched exposing a metal pad, whereas in the MNEE arrays the cavities are etched right the way through to leave a Pt band running along the cavity wall. The ability to deposit thin films only nano meters thick means that the electrodes on the cavity wall can be typically made 50-100 nm wide, thus having a critical dimension on the nanoscale and exhibiting nanoelectrode responses. A schematic representation of MS arrays and MNEE arrays in given in figure 2.1.

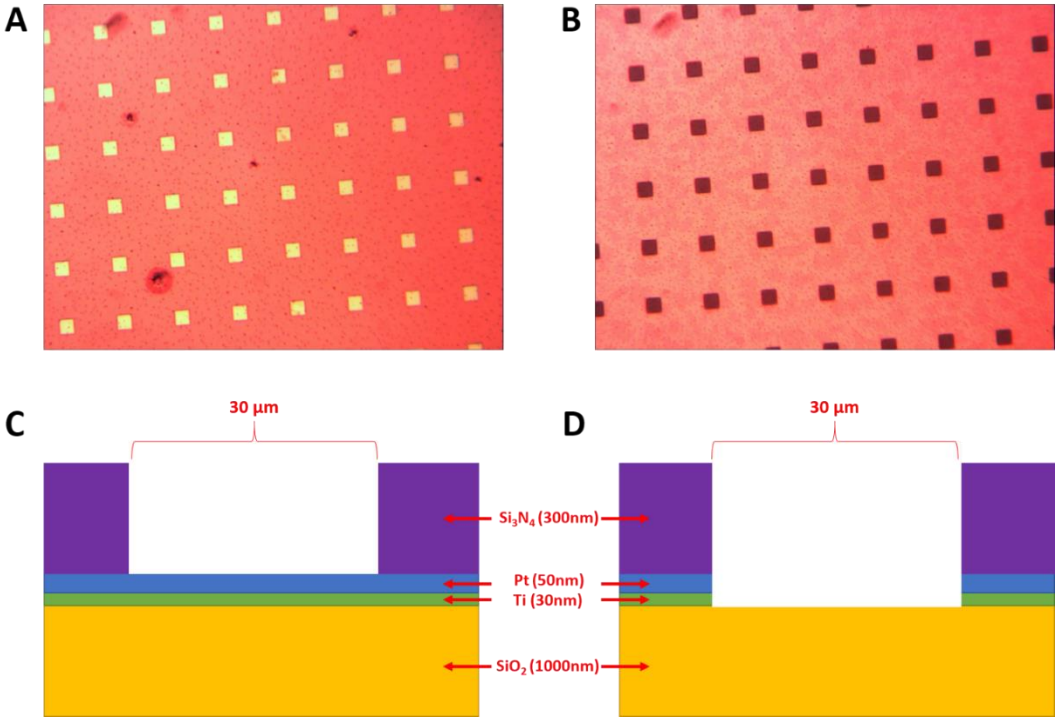

Figure 2.1. Optical images of (A) an MS array and (B) an MNEE array with schematics (C) the cross section of a MS and (D) the MNEE showing the constituent materials in the final devices. Note the thicknesses of the layers in the device have been exaggerated for clarity the target thicknesses have been provided.

At the commencement of this project the run sheet given in appendix 3 was the accepted methodology for fabricating MNEE arrays.[62] However, it was found that further optimisation of the process run sheet was required as it did not yield working electrodes after repeated fabrication attempts. The purpose of this chapter is to outline the afore mentioned optimisations, familiarise the reader as to how the devices were made and inform future researchers how to fabricate the MS and MNEE arrays.

2.2. General background and the original MNEE array fabrication protocol

Microelectrodes were originally fabricated in house at the Scottish Microelectronics Centre (SMC) as per the previously developed run sheet given in appendix 3. The silicon wafers used were 525 µm thick p-type <100> wafers, each with a resistivity of 1-10 Ω cm (IDB technologies) supplied with a 1 µm thick oxide layer, which electrically isolated the silicon semiconductor from the metal. 10-30 nm thick of titanium was first deposited on these 3-inch silicon wafers using an e-beam evaporator, followed by a 50 nm thickness of platinum. The titanium acts as an adhesion layer between the platinum and silicon dioxide,[22, 30, 61, 63]. The individual metals were then patterned to define the metal forming the electrodes, interconnect and contact pads. Figure 2.2 show the Pt metal layout of the twenty devices on a wafer.

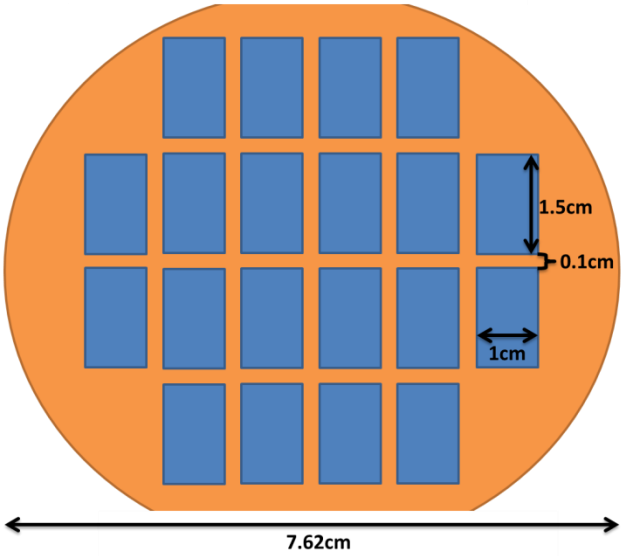

Figure 2.2 Schematic showing the layout of Pt electrode metal patterned to create 20 chips on a 3-inch silicon wafer after patterning.

On top of this platinum layer a 300-500 nm silicon nitride insulating layer was then deposited using low pressure chemical vapour deposition of dichlorosilane and ammonia at 800°C. This resulted in the platinum/titanium metal layers being sandwiched between the two insulators as shown in figure 2.3. The stoichiometry of this nitride layer was controlled by altering the flow rate of ammonia and dichlorosilane fed into the nitride furnace. For the purposes of this research only stoichiometric silicon nitride was formed.

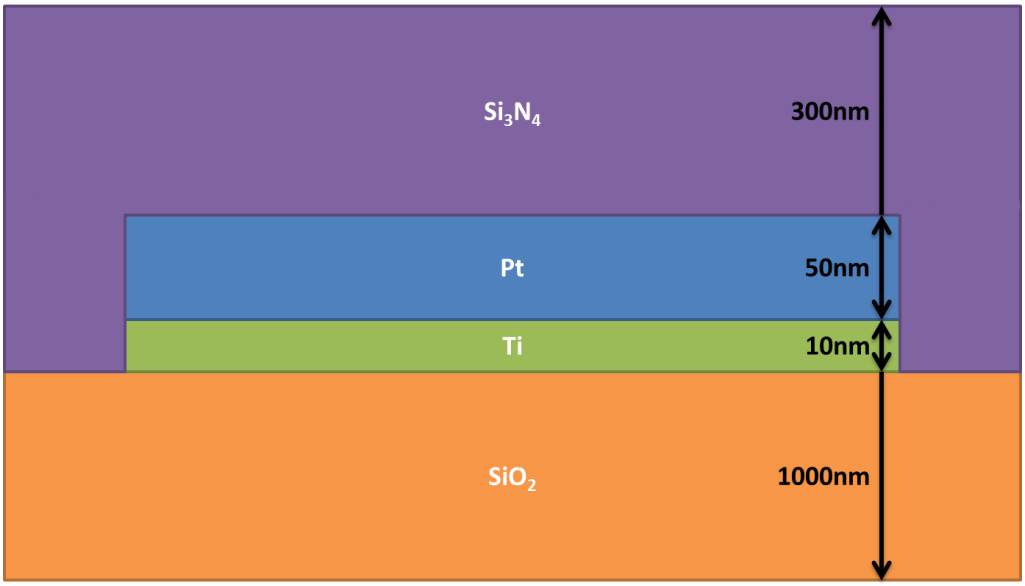

Figure 2.3 A schematic diagram of the vertical layers on the wafer before etching the cavities and/or contact pads.

The next step was to expose the bond pads as shown in figure 2.4. This patterning was produced by photolithography and a CF_4 reactive ion etch (RIE) and a wet etch in $HCl:H_2O:HNO_3$ in a 3:2:1 ratio by volume. The aim was to create a 2mm x 2mm square of exposed Pt in the top corner of each device that acted as the connection point (contact pad) to connect the MNEE electrode array to the potentiostat.

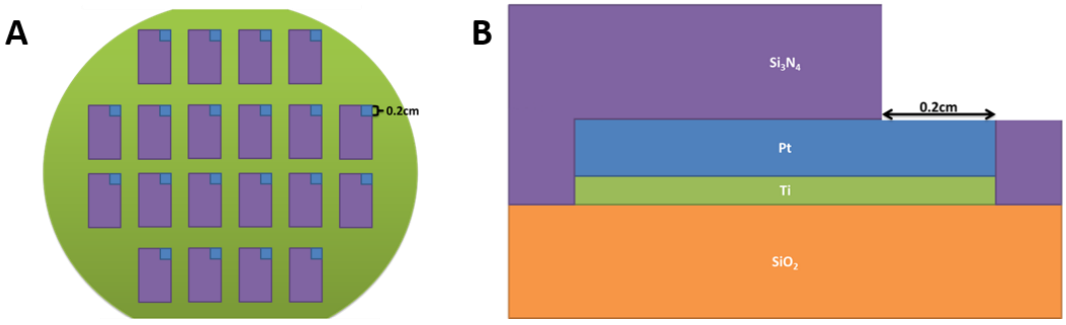

Figure 2.4 (A) Schematic top view of the 3inch wafer with twenty devices each with their 4 mm^2 Pt bond pad. In this diagram purple corresponds to 300 nm of silicon nitride on Pt and green to 300 nm of Si_3N_4 on SiO_2. (B) a cross section of the wafer once the bond pads had been etched into the devices. The colours correspond to those in Fig 2.2

The final step in the fabrication process was to etch an array of square cavities into each device to expose the MNEE array electrodes. These squares have the same edge length within each device, but different edge lengths ranging from 10-100 µm in different devices and were created through the coating of the wafer with photoresist and its selective removal. A mask was used to selectively expose areas to UV light, these exposed areas were then developed and the resulting photoresist pattern used to etch the array. The etch process was performed in three steps; in the first a CF_4 etch removed the Si_3N_4, in the second an Ar milling step removed the Pt and Ti and the third was a wet etch in $HCl:H_2O:HNO_3$ (in a 3:2:1 ratio by volume) to further remove Pt and Ti. The etch rate and etch time of these processes was controlled such that it could be stopped after the CF_4 etch to leave micro

square (MS) platinum array devices, or both steps could be used to produce MNEE devices, with Pt bands around the perimeter of each square cavity. There were two sets of masks used in this project, the first mask gave a variety of different electrode array devices, the areas and spacing's of which are provided in appendix 2; the second set of masks used in this project had a number of devices all consisting of 30 µm x 30 µm edge length square cavities in a square array of 1764 cavities. Adjacent squares were separated by 90µm, thus on any device the occupied area of array was 0.5 cm x 0.5 cm and given the area of each square was 900 μm^2, the total exposed electrode area on the MS array devices was 1.59 $x10^{-6}$ m^2. For the MNEE every cavity had an exposed band electrode area of 4 x 30 µm x 0.05 µm, resulting in a total electrode surface area of 1.06 $x10^{-8}$ m^2 (i.e. 150 times less than the MS array).

The naming protocol for the varied sizes and spacings of squares/cavities is Xµm YD, where X equals the edge length of the squares in the array and Y equals the closest separation between neighbouring squares in the array in multiples of the edge length. Therefore, when Y = 1, the spacing between the neighbouring edges of two adjacent electrodes in the array is the same as the edge length of one of the squares.

Finally, the wafers were coated in a photoresist (SPR350) to protect them from damage during dicing using a "Disco saw".

2.3. Devices from the first batch AP1402

The first batch of devices fabricated by the author (AP1402, the naming follows the order of: initials of author year and month in which fabrication began) showed the presence of a pink residue that fouled the electrode surface. Light microscope images of these devices, figure 2.5.A, and after use in ferri-/ferro-cyanide buffer, figure 2.5.B, suggested that the pink residue was primarily located in the electrode cavities and on the surface of the nitride insulator. This was clearly a problem as the residue was observed to cover the electrode surface and translocate during experiments, introducing irreproducibility between measurements. This contaminant was eventually identified as being residual photoresist SPR350 which was coated on all the electrodes prior to dicing (appendix 3 step 13) to catch any dust or debris thrown up during the dicing step in order to prevent it fouling the electrode. The established microfabrication procedure for removing this resist post dicing was to wash in a stream of first acetone, then isopropan-2-ol (IPA) and then water for 10 seconds each.[64] Clearly this process was inadequate for these devices, which is consistent with the fact that the other photoresist removal steps in appendix 3 require sonication in a resist stripper (ACT, which is a much stronger solvent than acetone) at 50℃ with sonication for 30 minutes.

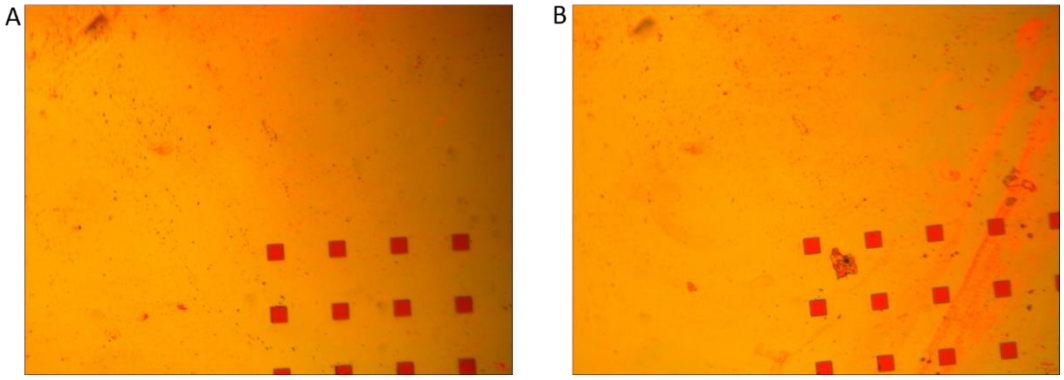

Figure 2.5. A 30µm3D MNEE array under a 10x optical zoom light microscope before (A) and after (B) experiments were run in potassium ferricyande (0.1 mM), potassium ferrocyanide (0.1 mM) in phosphate buffer (10mM) pH 7 (total experimental time was roughly 15 min). As can be seen the pink coloured photoresist is present in the cavities as well as on the insulating layer and the presence of smearing in (B) indicates it is mobile after carrying out the experiments in the buffer.

To try and salvage the electrodes from this batch an attempt was made to remove the resist by sonicating in ACT at 50℃. Half an hour of this treatment was found not to be sufficient to remove the resist, figure 2.6.A, so this was repeated to give a total of 1h sonication figure 2.6.B. Unfortunately, this harsh treatment, whilst removing the photoresist, also led to cracking of the silicon nitride layer, and the exposure and cracking of the platinum layer underneath, thereby breaking the electrode array. The optical images in figure 2.6.B also suggest that even with this, there may still be some unremoved photoresist in the cavities of the electrode. Thus, it was deemed impossible to remove the photoresist without breaking the electrodes and all the devices in this batch had to be written off.

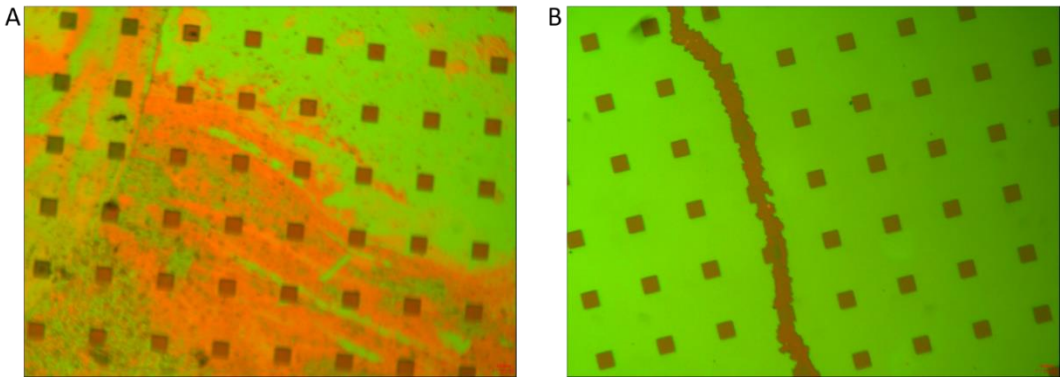

Figure 2.6. light microscope images with a 10x zoom of the 30µm3D MNEE arrays after (A) 15min cleaning in ACT at 50℃ with sonication (B) 1h cleaning in ACT at 50℃ with sonication. There is a gradual removal of the photoresist over time, however with prolonged sonication the array fractured as shown in B.

SEMs were taken of these devices after 1h cleaning, figure 2.7. From these images, it can be seen that the resist had apparently formed small islands that aggregated and remained stuck to the device surface. In all these images there is no platinum band running along the cavity walls. This was attributed to the use of piranha solution in a final attempt to remove the photoresist from the device surface, which was done prior to learning of the damage caused when exposing these electrodes to piranha solution.

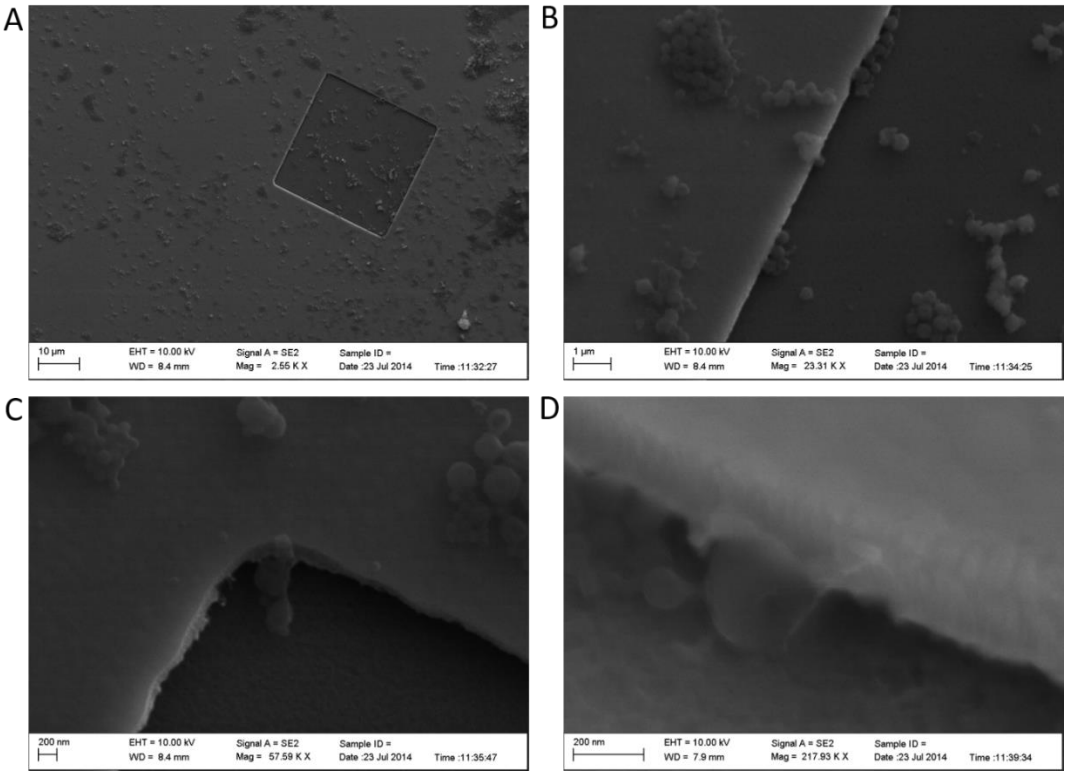

Figure 2.7. SEMs of the MNEE device arrays with photoresist after sonication in ACT for 1 hr at 50℃, and exposure to piranha solution. The insulator deposits are all sub-micron in size.

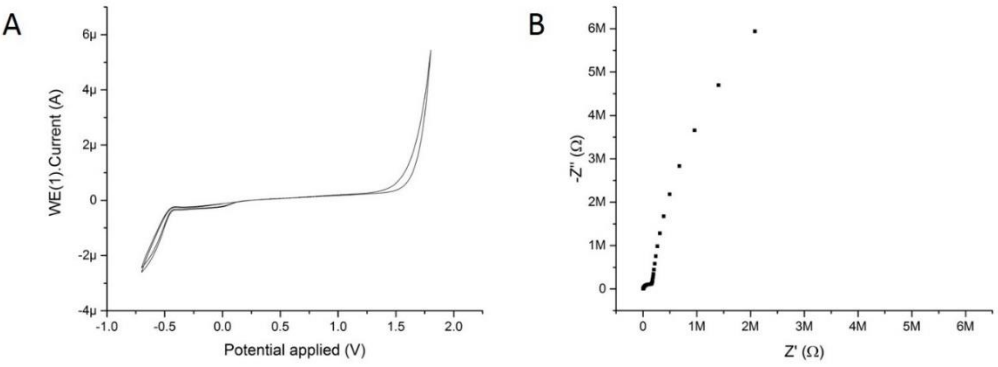

Figure 2.8. (A) The cyclic voltammogram (CV) of a 30µm 3D MNEE array in H_2SO_4 (0.1M) showing a sharp oxidation peak at 1.6V and a wave like Pt oxide reduction at 0.1V that then becomes a hydrogen reduction wave. (B) Nyquist plot recorded at the OCP using ferrocene carboxylic acid in 0.1mM in citrate buffer pH 7. All experiments were carried out using a Pt gauze counter electrode with a saturated calomel reference electrode.

Typical electrochemistry from these devices is given in figure 2.8, in which it should be noted that the CV, figure 2.8.A, has all the features expected from a Pt MNEE array but the currents are too low for an electrode of this geometric surface area in these conditions, likely due to the photoresist passivating a portion of the electrode surface. This decrease in electrode area is also seen in the EIS, figure 2.8.B, which has impedances several orders of magnitude greater than expected, consistent with the reduced currents seen in the CV.

2.4. Investigating the MNEE array dicing and wet etch protocols

The issues with the first batch were addressed as follows in the next batch (AP1405). The first refinement investigated was not using a protective resist for dicing. A new batch was therefore made in which only half of the wafer was coated with protective resist prior to dicing. Also on this wafer the necessity of using a wet etch step was evaluated, as it was thought that the wet etch might be responsible for a further issue, which was that the cavities had roughened edges and the metal looked as though it had been dissolved and re-deposited inside the cavity, figure 2.9. The wet etch step was in addition to the dry etching, and involved putting the wafers in a 3:2:1 mixture by volume of $HCl:H_2O:HNO_3$ at 45°C for 60s.[62] It was interesting that there were also clear signs of uneven topography in figure 2.9.A and 2.9.B, most notably the patchy silicon nitride layer and cavity floor, which were also attributed to uneven etching.

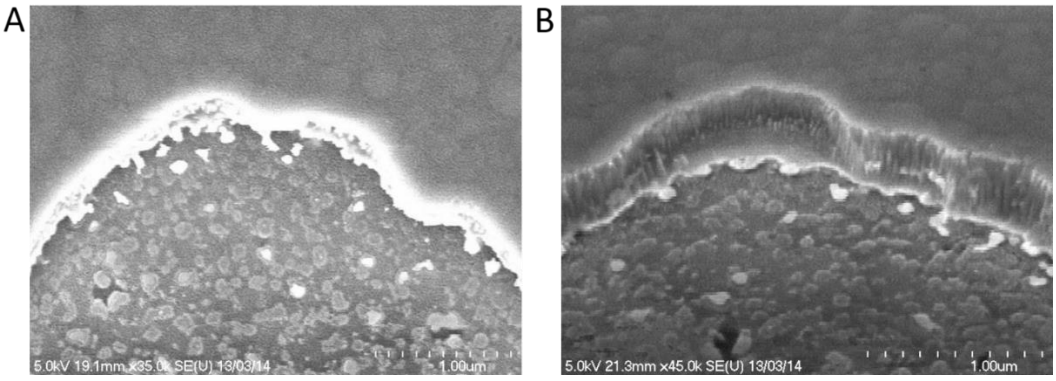

Figure 2.9. SEM's of an MNEE cavity in a device from the completed first batch. (A) and (B) are SEMs of the corners of cavities in the array. Of note are the glowing "blobs" of platinum that are also notable in (B); these have droplet like shapes suggestive of the platinum having been chemically dissolved and then redeposited upon the drying of the solvent.

A wafer plan was devised that would result in quarter regions of the standard 20 electrode wafer, each with five equivalent devices prepared under different conditions: with and without wet etching, and with and without dicing resist. The wafer had two different regions vertically, with a left-hand side (which had resist coated on it for the final dicing, appendix 3 step 13) and a right-hand side (which did not). The wafer also then had an upper region which was exposed to the wet etching, appendix 3 step 11, whereas the bottom half was shielded from the etchant with photoresist. A schematic of this wafer and its regions is given in figure 2.10.

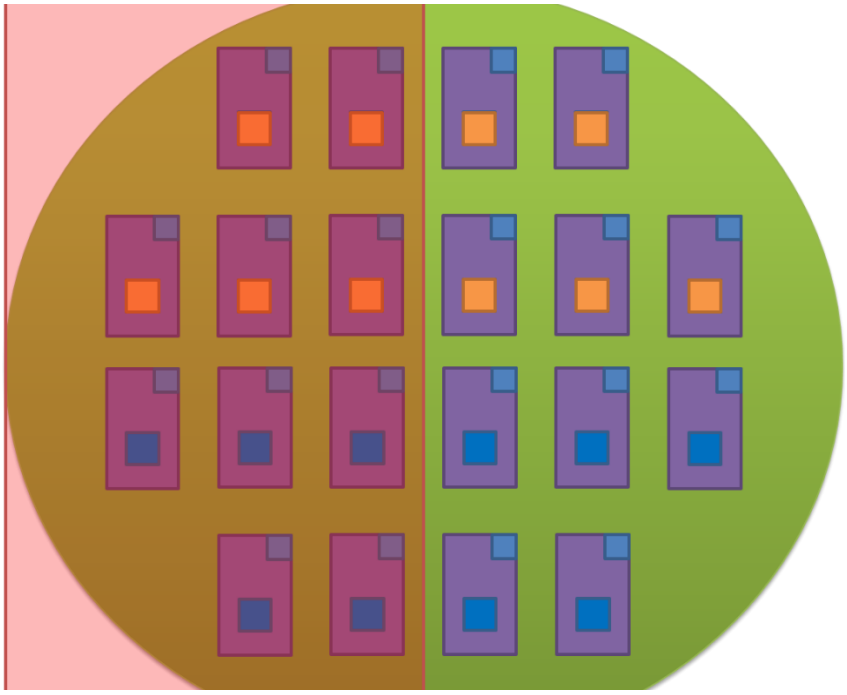

Figure 2.10. A schematic diagram of the second wafer batch preparation showing that the top half of the wafer was wet etched in step 11 (the arrays are shown as orange) while the bottom half was shielded from the wet etch (array area shown as blue) the left-hand side is shaded red to signify that it was coated with photoresist for dicing whereas the right-hand side was not.

The 4 sets of five electrodes were then studied using light microscopy, SEM and electrochemical measurements.

2.4.1. Controls (wet etched and resist for dicing)

It was reassuring that the 5 electrodes that were made in the same manner as the first batch, AP1402, (top left of figure 2.10) had the same issues as this first batch in terms of the resist being impossible to remove, figure 2.11, and with ragged, nonlinear cavity walls, figure 2.12.

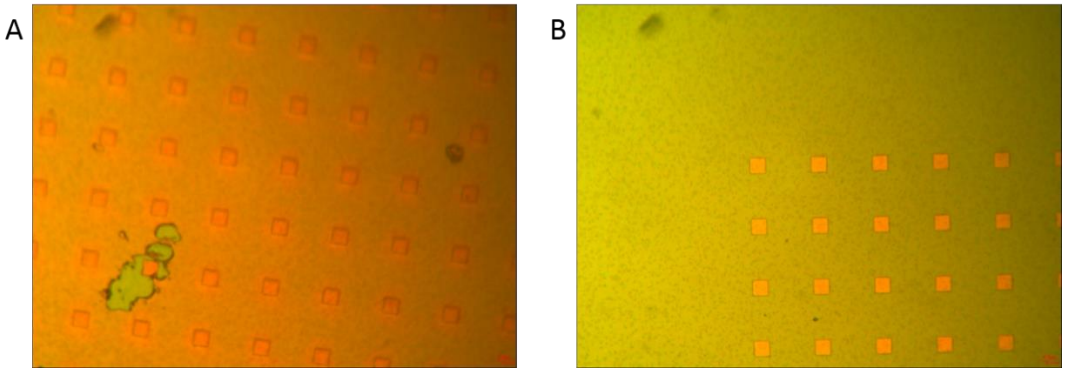

Figure 2.11. Light microscope images at 10x magnification of the second batch control devices that had been wet etched and coated with resist prior to dicing (A) after rinsing with acetone, methanol then water for ten seconds each (B) after 10min sonication in ACT at 50°C.

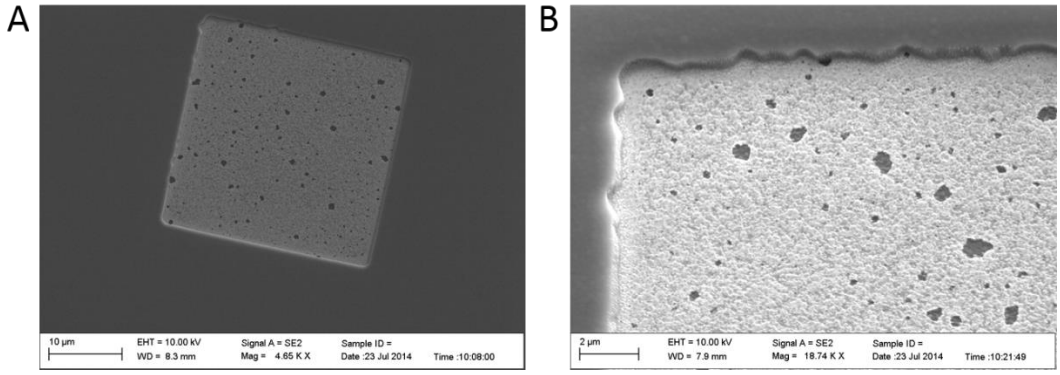

Figure 2.12. SEM images of AP1405 control electrodes that had been wet etched and had SPR350 coated on before dicing. Both (A) and (B) exhibit an under etch of the cavity floor. (B) is a close-up of one of the corners showing the irregularity of the cavity walls.

It is interesting that the SEMs of these electrodes, figure 2.12, also showed a rough and patchy cavity floor; a feature that had not been observed in batch AP1402 or the inherited electrodes; this was attributed to under-etching, in which the combination of argon milling and wet etching steps had not removed the layers sufficiently thoroughly to get to the silicon dioxide insulating layer. Belaidi *et al*[63] argue that argon milling can split the Si-O bond in any exposed silicon dioxide, removing oxygen atoms which will oxidise nearby titanium, which will have a different etch rate to the un-oxidised Ti. This leads to the formation of "chimneys" on the cavity floors and walls, a process which could explain the observed rough and patchy cavity floor.

It is interesting that these features were more apparent in this second batch than in the first batch. This underlines the need for system checks after each stage of the fabrication process to check its effectiveness and completion. The Pt and Ti layers have a yellowish colour under a light microscope whereas the silicon is typically black; in this case checking the cavities under an optical microscope should give a clear indication of robust fabrication control (although using colour to assign materials should be treated with caution, as silicon nitrides and oxides can be different colours depending on their thickness, stoichiometry and roughness). In this case, however it was noted that etching through the metal layers always yielded a black square.

Typical electrochemical responses of the resulting devices are given in figure 2.13.A-D. The CV in figure 2.13.C for one of these control electrodes in sulfuric acid (0.1M), is compared to that (figure 2.13.D) from a later batch of electrodes (AP1508). From the comparison of these two CVs it is clear that the electrode from this batch is not behaving as expected. It is possible that the signal observed is in this case coming from the titanium electrode with its surface titanium dioxide layer.[65, 66] The characteristic electrochemistry of such titanium electrodes is widespread in the literature due to its use as a charge a carrier in solar cells, the CV in figure 2.13.C is in general agreement with the literature, consistent with these AP1405 control electrodes actually being titanium dioxide microsquares as opposed to Pt MNEEs.[65, 66] The Nyquist plots will then be a combination of the response of these active titanium microsquares and the Pt MNEE band, which might account for the extra domes in the EIS, figure 2.13.A and B, as there will now be two charge transfer resistances.

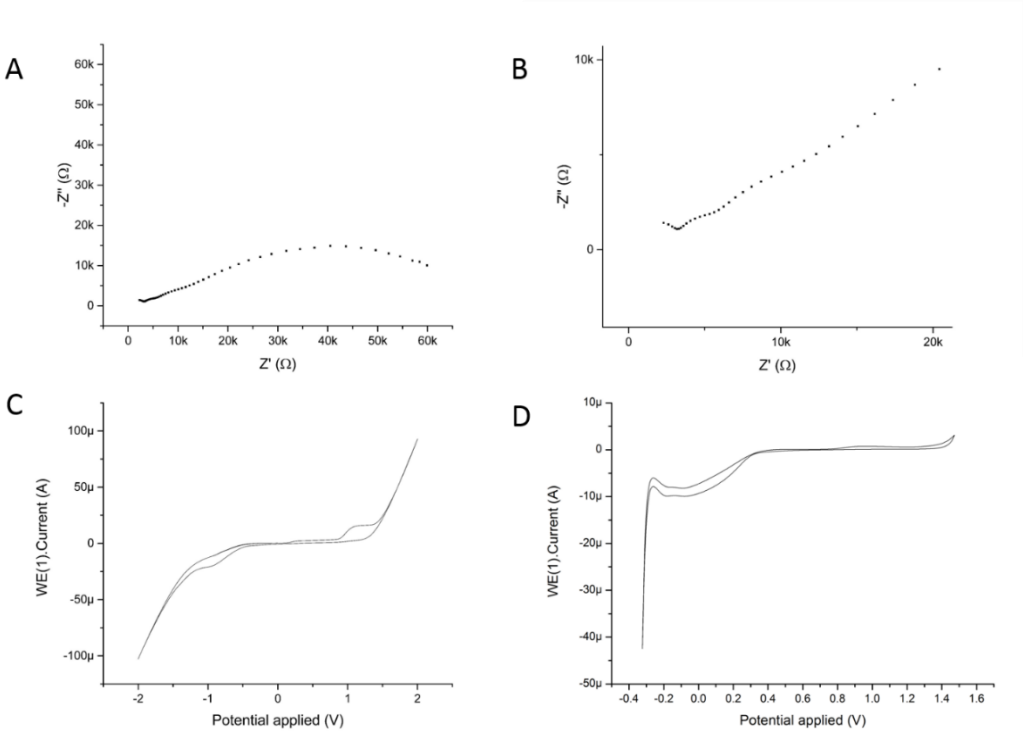

Figure 2.13. Electrochemical data taken from the AP1405 control electrodes that had been wet etched and had dicing resist. The Nyquist plot (A) was recorded in phosphate buffer pH 7.2 containing 1mM potassium ferricyanide and 1mM potassium ferrocyanide. (B) is a close up of the high frequency region of (A) and together they show that >3 observable hemispheres. (C) Is a CV recorded of the AP1405 control electrode in 0.1 M sulfuric acid and (D) is the same experiment repeated with an electrode from a later batch (AP1508) for comparative purposes. All experiments were carried out using a Pt gauze counter electrode and saturated calomel reference electrode.

It can be concluded that these AP1405 control MNEE arrays are not clean Pt nanobands. One intriguing possibility, given the under etch, is that they are titanium microsquares with Pt bands above them, it is interesting to note that the wet etch step that had seemed too harsh in AP1402 had under-etched the titanium in this case.

Another image of interest appeared when analysing the SEM images of these electrodes. Figure 2.14 shows an SEM where the contrast has been increased by + 40% and “watermarks” can be seen on the cavity bed. These markings are only seen on electrodes that have been wet etched and have had resist coated on them for dicing, so these are most probably features due to an uneven and incomplete etching of the cavity floor. This may be as a result of undeveloped resist over the cavities causing an uneven etch.

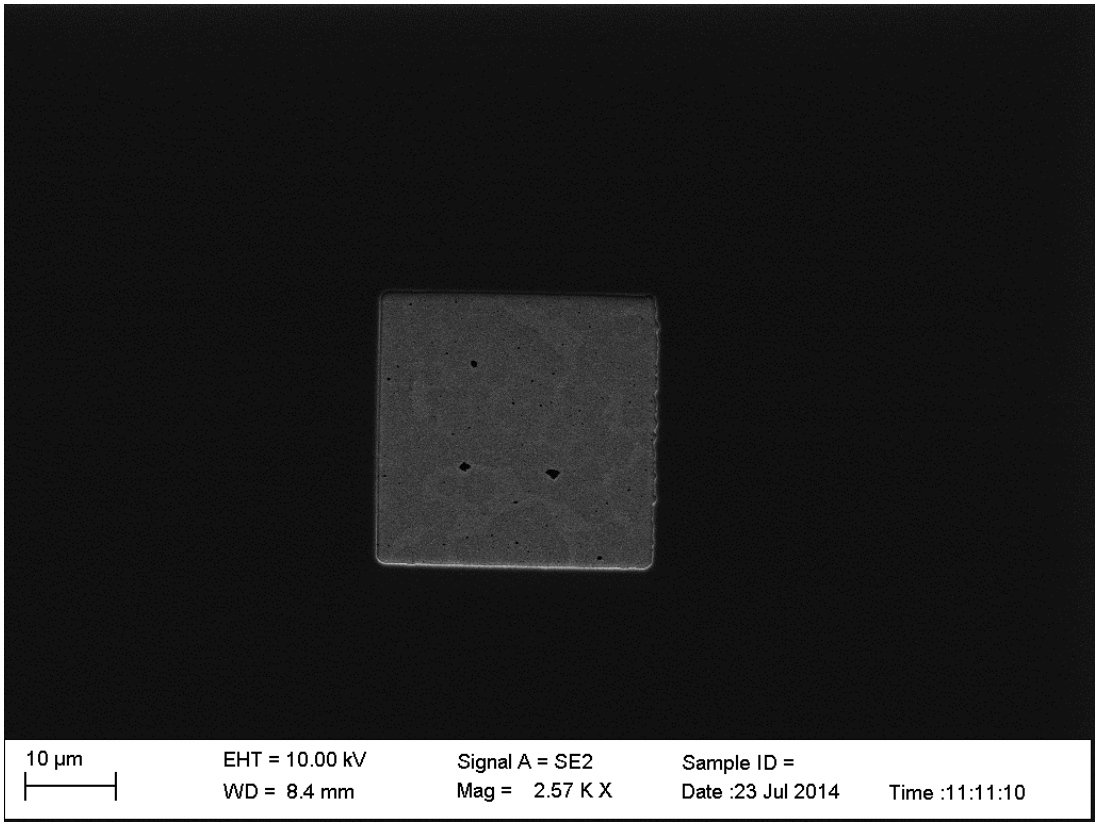

Figure 2.14. SEM with contrast enhanced by + 40% showing patchy watermarks in the coarse titanium at the bottom of the cavity. These were only observable in the AP1405 electrodes that had been wet etched and coated with resist before dicing.

2.4.2. Devices wet etched with no dicing resist

Light microscopy images of the devices that were wet etched and had no dicing resist are given in figure 2.15.

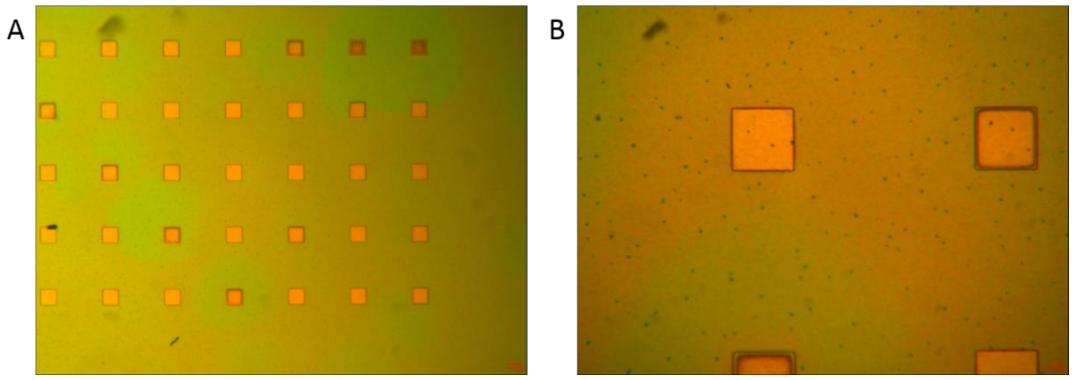

Figure 2.15. Light microscopy images of AP1405 electrodes that have been wet etched but had no resist on them for dicing at (A) 10x magnification and (B) 40x magnification.

Worryingly the images have patches over the entire surface, the greener patches also seem to have darker cavities. It may be that residual photoresist from the cavity etching step was filling some cavities; or that said photoresist was unevenly coated over the wafer and the different coloured cavities have been etched to different heights. The colours of the silicon

nitride should be analysed with caution, as whilst they are indicative of different silicon nitride and/or silicon oxide heights, the colour alone cannot be used to determine the material thickness as the colour is dependent on thickness, roughness and stoichiometry. The only conclusions that can be safely drawn from the images in figure 2.15 is that there is a non-uniformity in the silicon nitride across the image.

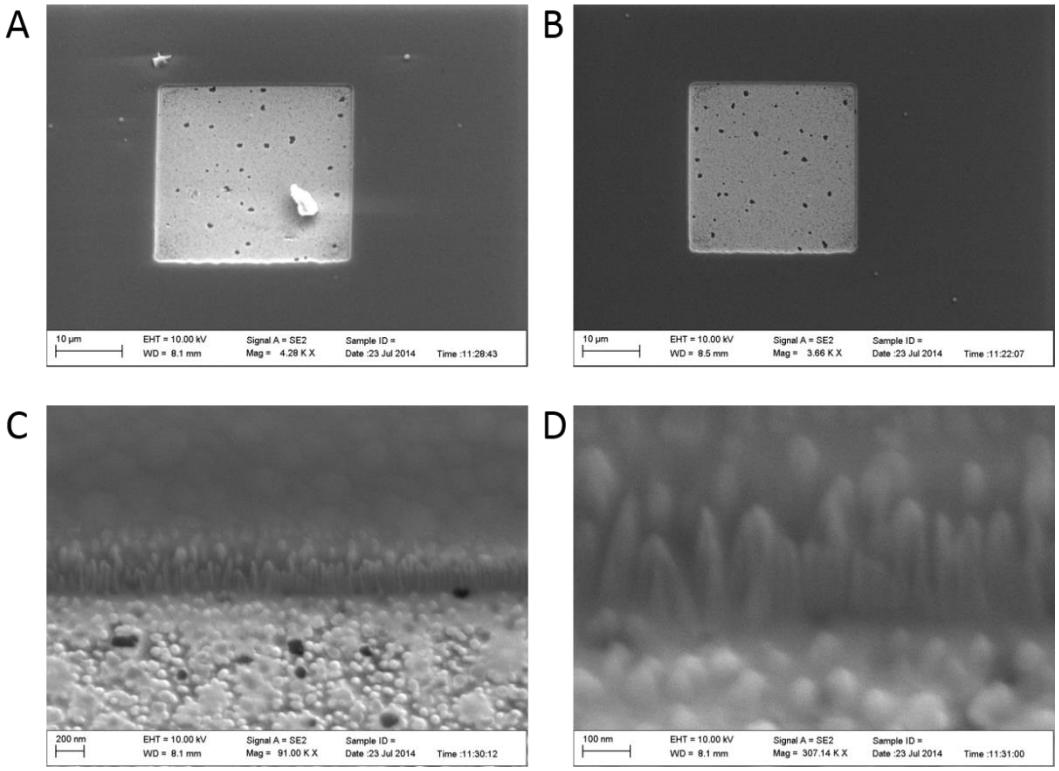

Figure 2.16. SEM images of AP1405 electrodes that have been wet etched but had no dicing resist. (A) Debris resulting from the magnifications of the cavity walls and "chimneys" of Ti; the patchy nature of the nitride layer can be seen in figure (C).

The SEM images of these electrodes are again consistent with the fact that the etch had only gone down to the titanium adhesion layer, which was why the electrochemistry of these electrodes, figure 2.16, mirrored that of the control electrodes from AP1405. The SEM in figure 2.16.A showed that debris created during the dicing had landed in the electrode cavity. The purpose of coating the wafers with SPR350 was to prevent such debris from blocking the electrode, however, in figure 2.16.B one of these electrodes that had been cleaned with a jet of deionised water for 30s was imaged with no visible debris on the electrode. Given this, it would seem preferable to have a short wash step with water rather than coating a wafer with resist that must be removed by harsh treatments that can damage the devices. Figure 2.16.C and D are magnifications of the cavity walls; showing the chimneys of silicon oxide and nitride as described by Belaidi *et al*[63].

The electrochemistry of these electrodes is shown in figure 2.17. They have the same properties as the control electrode data, which would indicate that they are also behaving essentially like titanium micro-square arrays due to process under etch. Notwithstanding the apparent slight discontinuity in the data in the Nyquist plot, due to a small difference in resistor calibration on an automated resistor switch (automated range change) in the

computer controlled potentiostat, the measured impedances are of the same order of magnitude as the control electrodes.

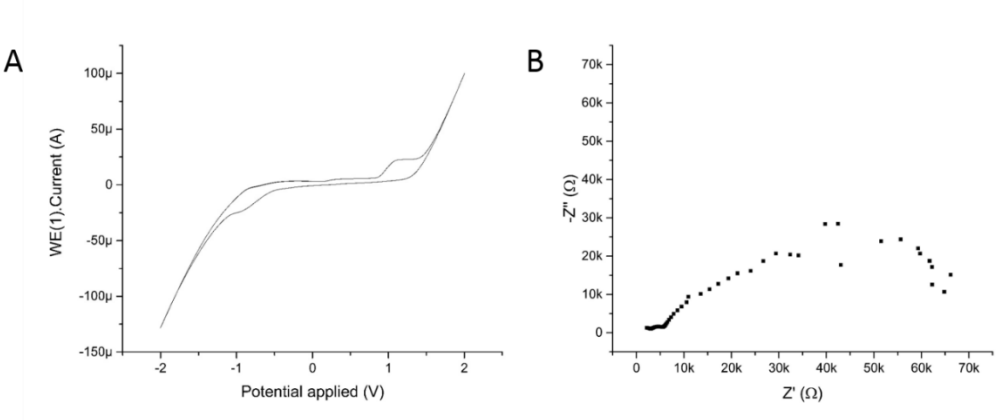

Figure 2.17 (A) CV in 0.1M H_2SO_4 of a 30µm 3D MNEE from batch AP1405 that have been wet etched but had no resist on for dicing. (B) EIS of the same electrode in 0.1M KCl containing 1mM potassium ferricyanide and 1mM potassium ferrocyanide, Both experiments were conducted using a Pt gauze counter electrode and a saturated calomel reference electrode, EIS was recorded at OCP.

Based on these data it was concluded that there is no obvious advantage to using a dicing resist, this process step would therefore be removed from future batches as it is a possible source of error. Its purpose was to protect the electrodes from debris, however, this debris could be easily washed off with water which is preferable as it posed no risk of damaging the arrays. Whilst the removal of the dicing resist from the process did not resolve any of the issues previously experienced, it's exclusion did not appear to be the cause of any electrode issues so its inclusion was deemed unnecessary.

2.4.3. No wet etch, with dicing resist

The light microscopy images in figure 2.18 show the array area before (A) and after cleaning in ACT for 10 minutes at 50°C with sonication (B). From these images, it can be seen that the cavities are all orange, indicative of an under-etch.

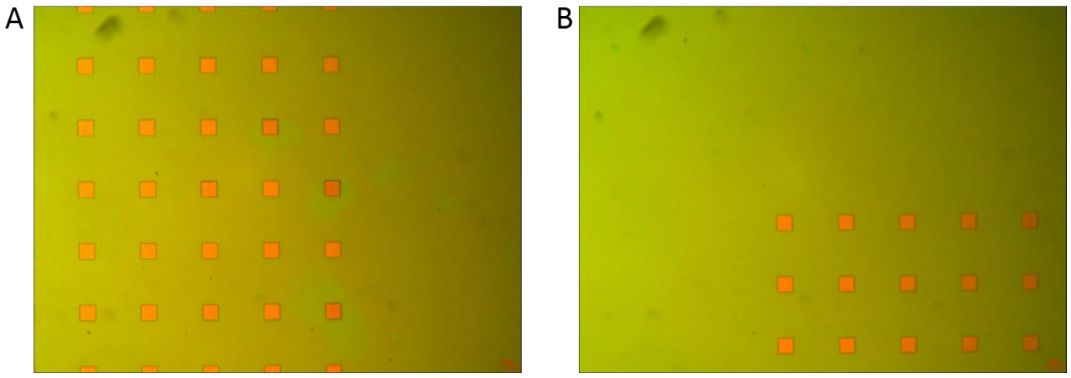

Figure 2.18. Batch AP1405 electrodes that had no wet etch but did have dicing resist (A) after washing with acetone, methanol and water to remove the dicing resist. (B) after further washing for 10min in ACT with sonication at 50°C. Light microscopy images were recorded at 10x optical zoom.

Whilst in theory the removal of the wet etch step should cause a greater under etching than the control electrodes, the optical microscopy images in figure 2.18 and SEM's in figure 2.20

would suggest that they are identical to the controls and that the wet etch step is not producing significant etching of the titanium at the bottom of the cavity. There is also no evidence of a significant change in the unevenness of the silicon nitride, the titanium layer on the cavity floor, or the straightness of the cavity walls, figure 2.19. Whilst this suggests that these imperfections were not a product of the wet etch but most probably arise from the photolithography, the data also show that the wet etch has no significant remedial effect.

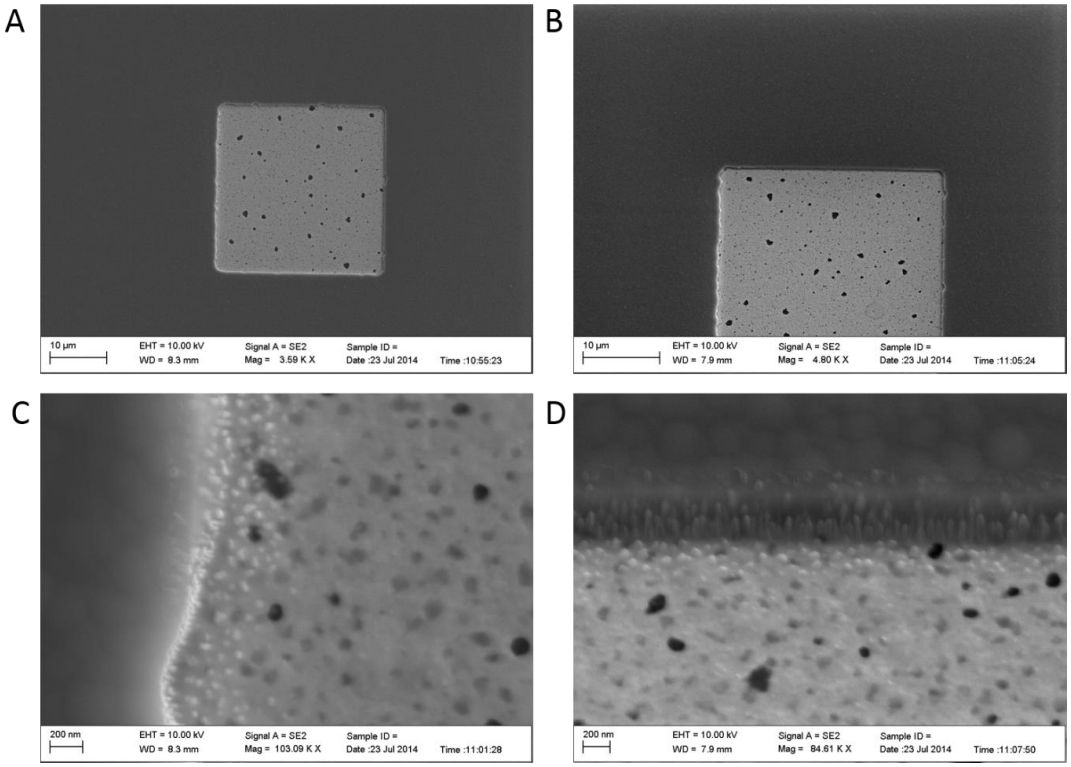

Figure 2.19. SEMs of AP1405 electrodes that had not been wet etched but did have dicing resist.

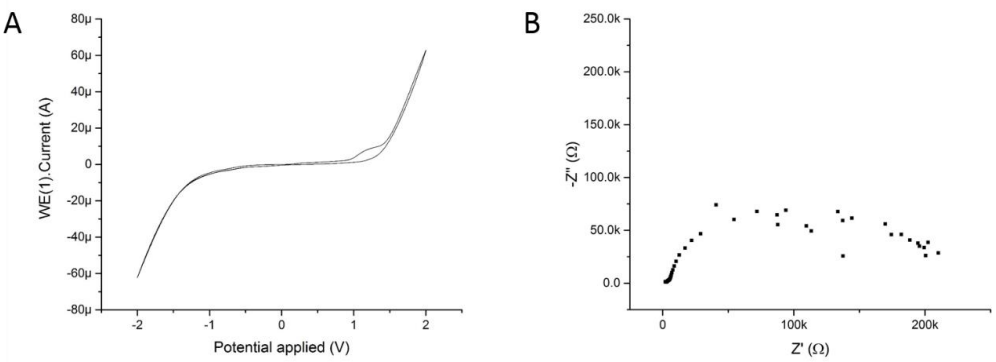

Figure 2.20. (A) CV in 0.1M H_2SO_4 of AP1405 MNEE that have not been wet etched but had dicing resist. (B) EIS of the same electrode in 0.1M KCl containing 1mM potassium ferricyanide and 1mM potassium ferrocyanide. Both experiments were conducted using a Pt gauze counter electrode and a saturated calomel reference electrode.

The electrochemistry suggested that the Ti/TiO_2 at the bottom of the cavities was still producing a signal as the response was similar to figure 2.17, and none of the characteristic

features of a Pt CV in sulfuric acid could be observed in figure 2.20.A. As a result of these tests, the wet etch was removed from the fabrication process.

2.4.4. No wet etch, no dicing resist

The final set of electrodes from batch AP1405 had no wet etch and were not coated with SPR350 prior to dicing. As had previously been established by comparing the control with the other electrodes in this batch, the wet etch and protective resist coating step were not necessary. These electrodes should therefore resemble what a future batch would look like were the wet etch and dicing resist to be removed. The light microscopy images of these electrodes, figure 2.21, show a patchy silicon nitride film as well as uneven cavity etching.

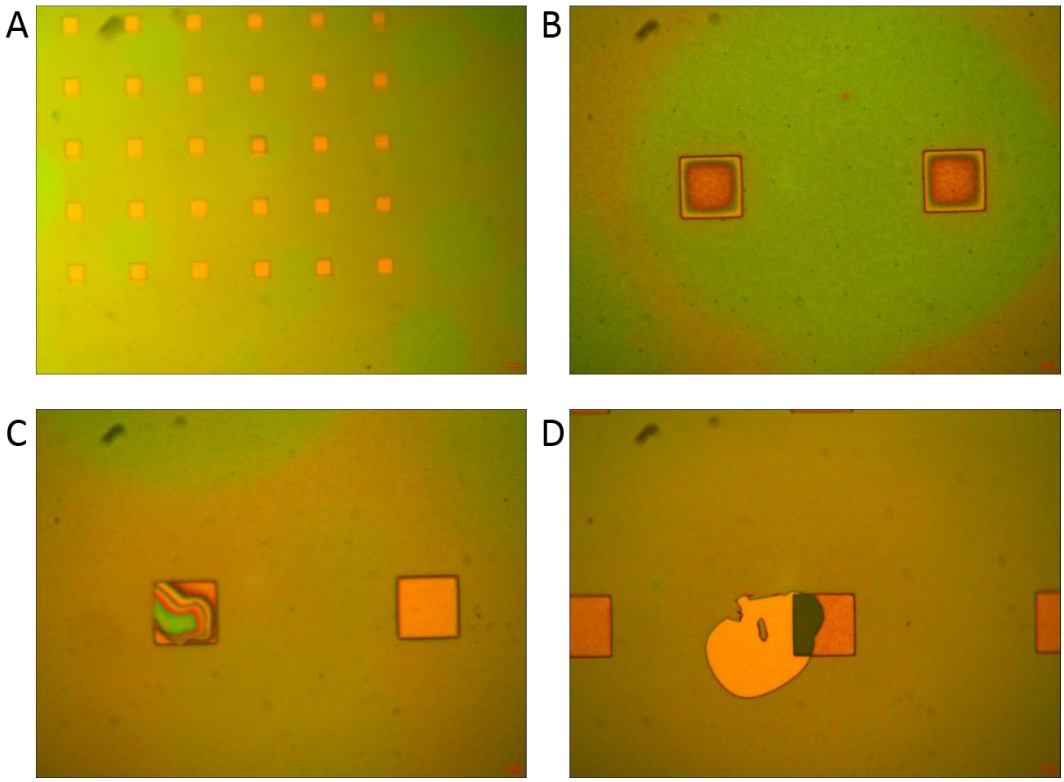

Figure 2.21. Light microscopy images of batch AP1405 electrodes at (A) 10x magnification and (B-D) 40x magnification.

At the time the issues with the nitride layer was initially attributed to a fault with the plasma etcher (JLS). The collaborating engineers suggested that the etching tool might not have been operated correctly, and that the process should be repeated. However, this was not the solution with these problems eventually being attributed to the photolithography parameter being non-optimal, although this was not identified until batch AP1508.

Figure 2.21.D is particularly interesting as a chip removed the silicon nitride layer and metal from the cavity, exposing what is thought to be grey-black silicon oxide underneath based on its colour (this should be confirmed by XPS). This one image provides the best evidence of all the light microscope images that an under-etch has been prevalent across all the electrodes in this batch as none of them have grey-black cavity floors.

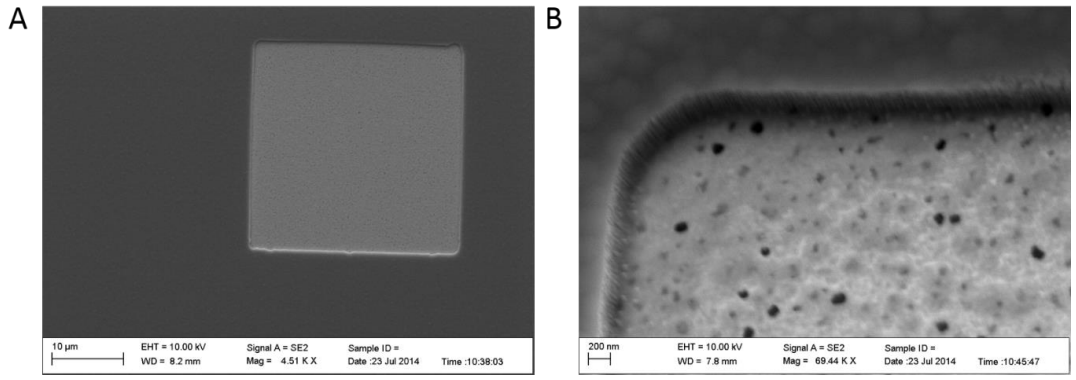

Figure 2.22. SEM images of AP1405 electrodes that had no wet etch and no dicing resist.

The SEM images of the AP1405 electrodes with no wet etch and no resist displayed an under-etch to the titanium adhesion layer which displayed the same electrochemistry as the other electrodes from this batch, figure 2.22.

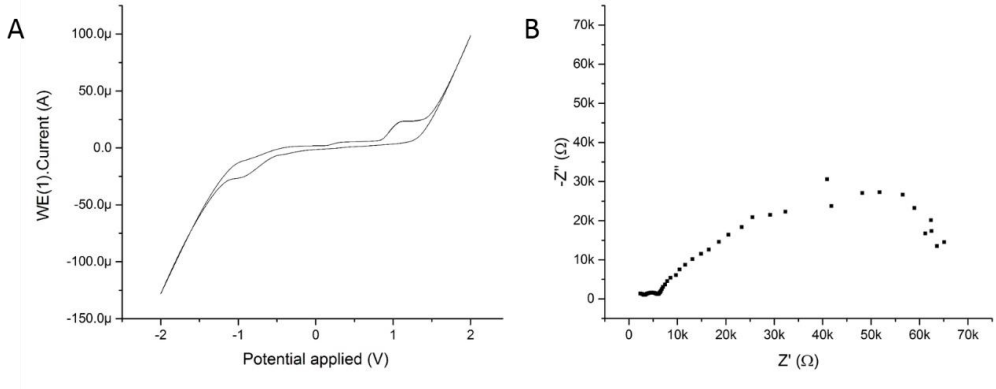

Figure 2.23. (A) Cyclic voltammogram in 0.1M H_2SO_4 of AP1405 30µm 3D MNEE arrays vs a saturated calomel reference electrode and Pt gauze counter electrode recorded at a scan rate of $0.1Vs^{-1}$. (B) Nyquist plot from the same electrode in 1mM potassium ferrocyanide, 1mM potassium ferricyanide and 100 mM KCl recorded at OCP vs a saturated calomel reference electrode and Pt gauze counter electrode.

The electrochemistry of these electrodes has been given in figure 2.23 for completeness and again shows that the majority of the signal is coming from titanium on the cavity floor and the devices are not behaving as they should.

2.4.5. Conclusions from batch AP1405

After analysing all the electrodes in batch AP1405, it can be concluded that the systematic study of the necessity of the wet etch and SPR350 coating prior to the dicing steps revealed that the resist coating process to protect the wafer for dicing was an unnecessary step, as any debris that landed on the electrodes during dicing could be easily washed off with water and the dicing resist was at times impossible to remove without sonication in a resist stripper (ACT), which damages the devices. The wet etch in hot aqua regia has no benefit to the devices. As a result of these findings, both the wet etch and resist coating steps were removed from the run sheet.

2.5. Electrode re-design

Batches AP1503 and AP1506 were fabricated using the run sheet given in appendix 4; which built on the previous fabrication experience. In these batches, new masks were used, so as to introduce changes as part of an electrode architecture re-design. These new electrode designs can be seen in figure 2.24. Firstly, the devices were lengthened to reduce the risk of the electrolyte wetting the bond pad as was observed experimentally and as discussed in chapter 3.6. Secondly, the area of metal under the silicon nitride was reduced to decrease parasitic capacitances caused by the double layer formed at the silicon nitride/electrolyte interface due to the charge induced by potentials applied to the underlying platinum.[30] Thirdly, the new masks feature a range of array designs, the properties of which are summarised in appendix 2.

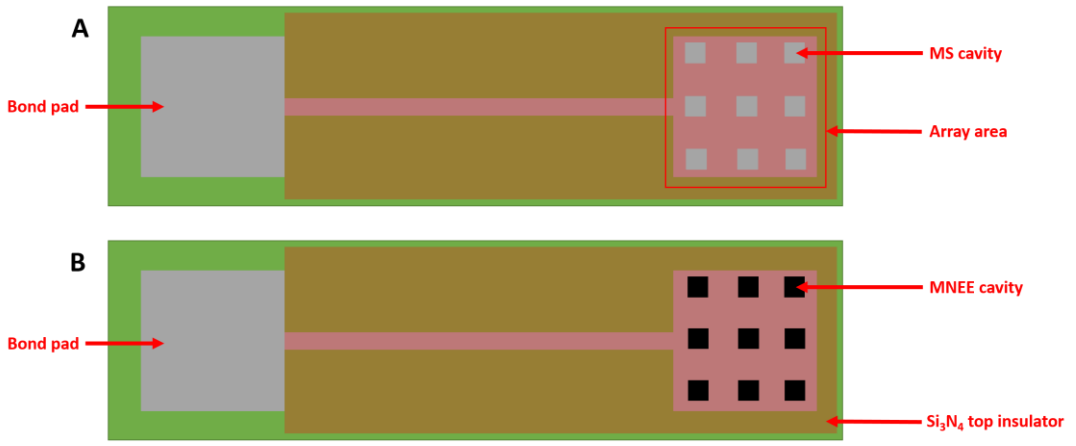

Figure 2.24. Please note that this schematic diagram is NOT shown to scale, and that the number of array elements is therefore not representative. Schematic diagram of the new "long-dip" devices designed for ease of use in (A) MS array and (B) MNEE array formats. The number of squares in each array type are given in appendix 2.

It was noticed that all the fabricated wafers were a different colour in the middle than they were at the edges, an example is given in figure 2.25.A. This suggests the photoresist was being removed and the nitride was being thinned with a bullseye non-uniformity that would be expected from a photoresist layer that was being spun on too thin.

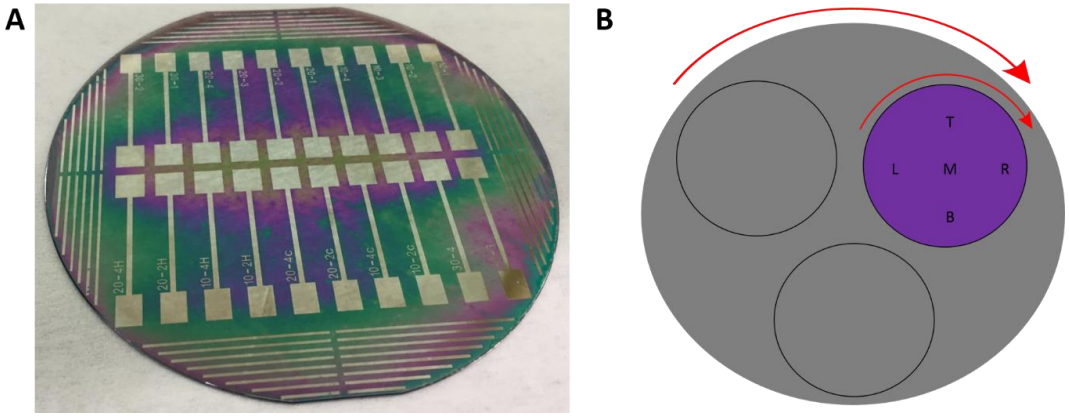

Figure 2.25. (A) photograph of a wafer after part way through fabrication where the electrode metal had been defined. Note the difference in colour between the centre and edges of the wafer. (B) Schematic diagram, not to scale, of the wafer chuck, coloured grey, that could be placed in the plasma etching chamber, with an example wafer shown in purple. Both the wafer and chuck are free to be rotated as indicated by the red arrows.

This suggested that the photoresist was not coated thick enough, so that the argon milling was etching through the resist layer and etching the edges of the wafer, where the resist would be thinner, more than the centre. The working practice at the time was to put a random sized "blob" of photoresist onto the centre of a wafer by hand and spin at 2400 rpm for 60s to get an even coating of photoresist on the wafer. The theory was that the spin speed determined the thickness of the resist and that the volume of resist added was inconsequential. Given the observed inhomogeneity, this theory was tested in the next batch (AP1508).

As well as overspinning there is also the potential for photoresist to "dry out" if left for sustained periods of time. Typically resist would be spun on and left overnight if the etching equipment were not immediately available for use. During this time, organic solvents in the photoresist would evaporate, a process known as outgassing, thereby decreasing the resist thickness. It was therefore decided that in future batches the photoresist would not be left on the wafers for time periods exceeding 2h.

2.6. Optimisation of the photolithography

The theory that spin speed alone determined the thickness of the resist, and that the volume of resist added was inconsequential, was tested in the next batch (AP1508). A set volume of 10 ml of photoresist was poured onto the centre of a clean silicon wafer. This was then spun at different speeds and baked as before, the resulting resist thickness was measured using reflectometry on the "Nanospec".

It was found that, as expected, spinning at faster speeds produced thinner films. The photoresist used was SPR 220 3.0; the 3.0 represents the optimum resist thickness in microns. The spin speed of 2500 rpm with 10 ml of photoresist gave a resist layer thickness of 1.8 μm. In order to get a resist thickness of 3.0 μm, 10 ml of photoresist needed to be spun at a speed of 1400 rpm.

The UV exposure time was also optimised at 25s, this increase was rationalised as an increase from the time in the run sheet due to the thicker resist layer. Once this had been done it was reassuring that the etching times were much shorter and the electrodes fabricated in this batch had one uniform colour across the wafer and straighter cavity edges than any of the previous batches, as shown by the optical images in figure 2.26.

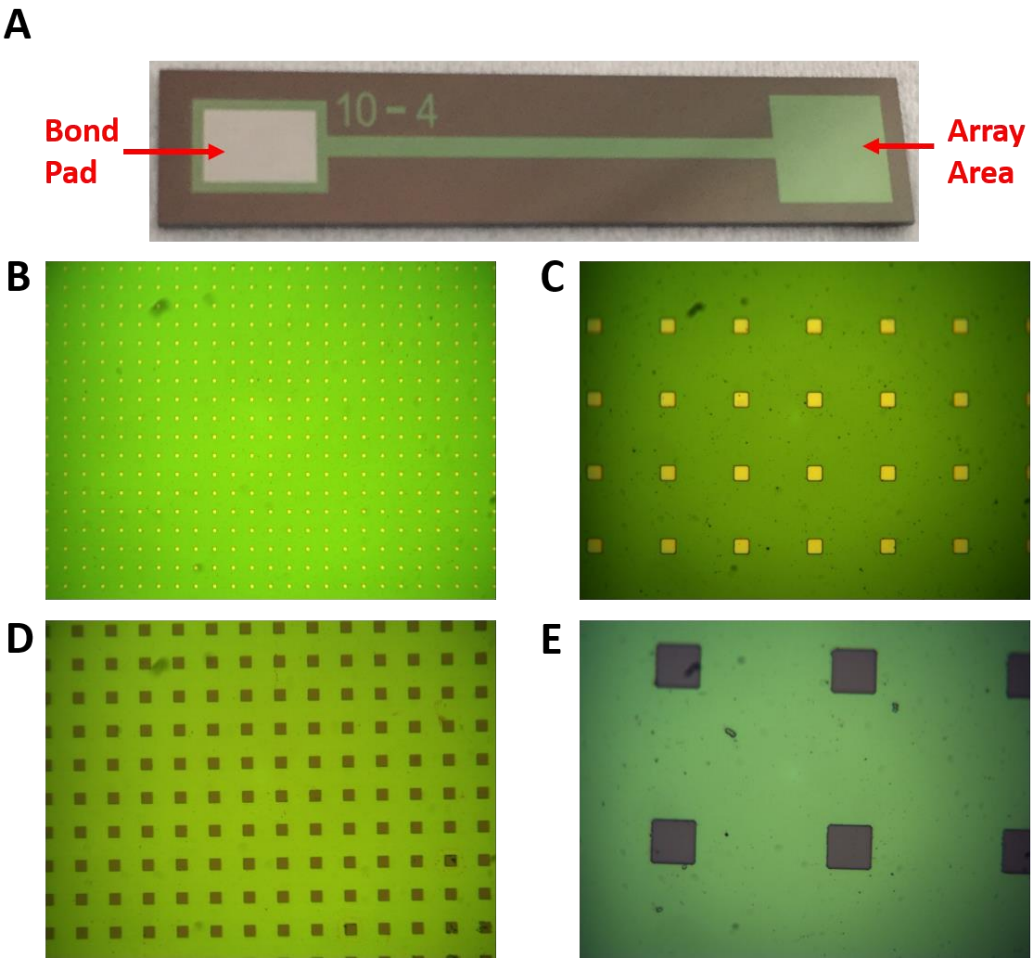

Figure 2.26. Optical Images of AP1508 electrodes. (B) and (C) are optical microscope images of a 10µm 4D MS array at 5x and 10x optical zoom respectively. (D) and (E) are 30 µm 3D MNEE arrays at 5x and 40x optical zoom respectively.

The electrochemical performance of these electrodes is discussed in section 2.7 below. These benchmark measurements show that the devices fabricated by this process, the run sheet for which is given in appendix 5, behave in accordance with the theory.

2.7. The electrochemistry of macro, micro and nanoelectrodes

This section displays the voltammetry and EIS of clean macro electrode disks, along with Micro Square (MS) arrays and Microsquare Nanoband Edge Electrode (MNEE) arrays from batch AP1508 which demonstrate the success of their fabrication. First the electrochemistry of macro electrodes is outlined, which enables physical parameters to be extracted and compared to the literature. These parameters are then measured experimentally on micro and nano electrodes and compared to the macro electrode data to demonstrate that the devices are working.

2.7.1. Macro electrodes

The electrochemical techniques used have previously been discussed in chapter 1.4 and explained in terms of macro electrode systems.

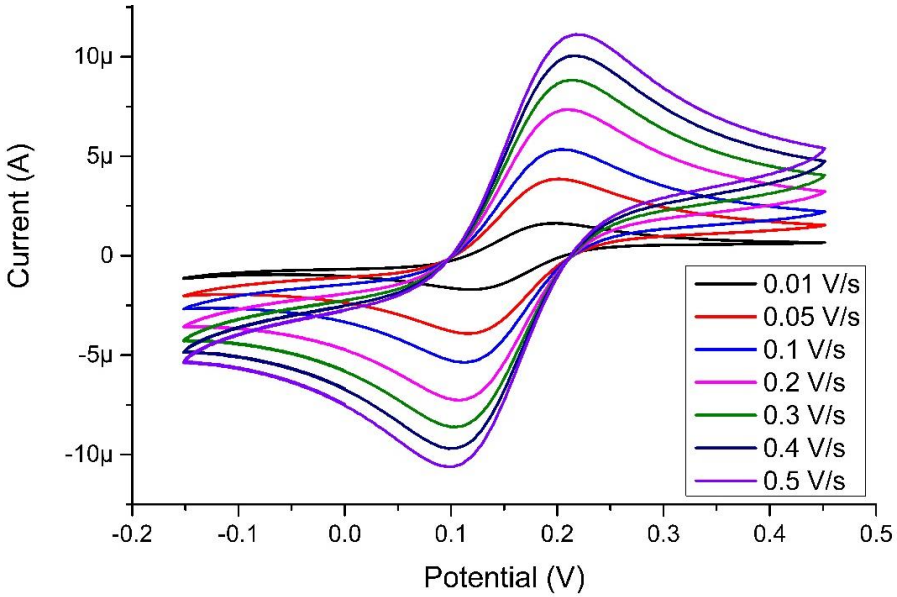

Figure 2.27. Typical cyclic voltammograms of a commercial macro disk electrode with a diameter of 1.6mm a variety of scan rates shown. Plotted are the third scans run between -0.15 V and + 0.45 V, with each scan starting and ending at 0 V. Performed at 25 °C in a degassed buffer of 1 mM potassium ferricyanide, 1 mM potassium ferrocyanide and 100 mM KCl vs a saturated calomel reference electrode and Pt gauze counter electrode.

The typical voltammograms of a Pt macro disk is at a variety of different scan rates are given in figure 2.27, for which the OCP for a Pt electrode in this system is + 170 mV. Peak like responses are seen at all scan rates as expected; there should be a constant 59 mV separation between peaks for a reversible one electron transfer in an ideal system, independent of sweep rate.[31, 53] The deviation of the data to the measured peak separation of 108 mV, and slight increase in peak separation with sweep rate, is most probably due to the iR drop in the solution.[31]

Using the Randles-Sevcik equation, equation 2.1,

$$i_l = 0.4463nFAc\left(\frac{nFvD}{RT}\right)^{0.5} \qquad \text{(Eqn 2.1)}$$

where i_l is the limiting current (in A), n is the number of electrons being transferred, F is Faraday's constant (in C mol^{-1}), A is the Area of the electrode (in cm^2), c is the concentration of redox agent in the bulk electrolyte (in mol cm^{-3}), v is the scan rate (in V s^{-1}), D is the diffusion coefficient (in cm^2 s^{-1}), R is the universal gas constant (in J K^{-1} mol^{-1}) and T is the temperature (in K)), it was possible to calculate the diffusion coefficients for both ferricyanide and ferrocyanide and compare these to literature values. The error was calculated by taking the standard deviation calculated from the diffusion coefficients obtained at each scan rate. It was found using this method that the diffusion coefficient for ferrocyanide was 9.1 (± 1.0) ×

10^{-6} cm^2s^{-1} was within experimental error (three standard deviations) of the literature value of $(6.67 \pm 0.11) \times 10^{-6}$ cm^2s^{-1}.[67]

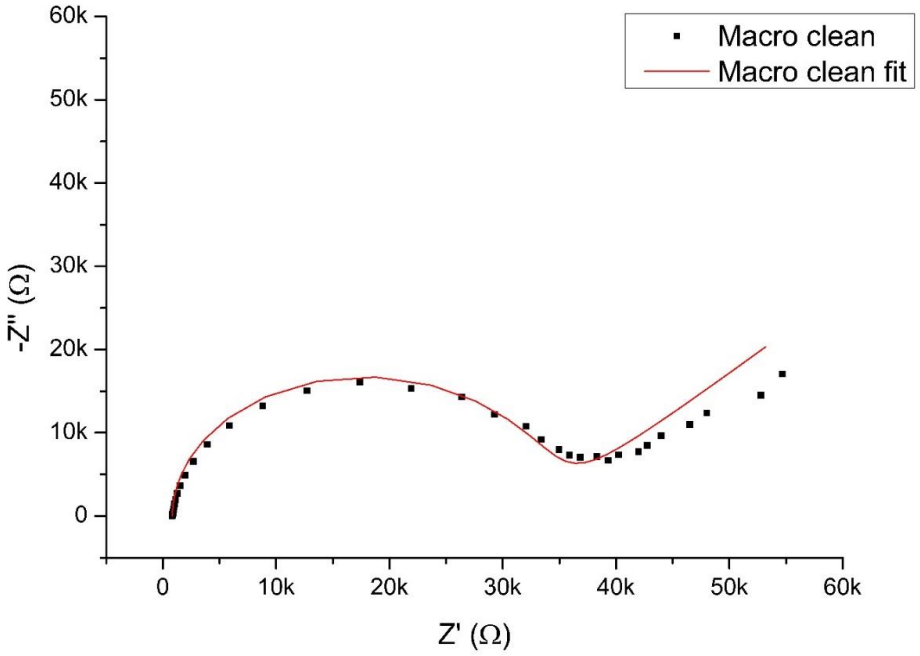

Figure 2.28. Typical Nyquist plot (black squares) with corresponding fit of the regression model (Randles circuit, APP 1.2) to the data (red line), for the 1.6 mm^2 diameter Pt macro disk electrode measured at OCP (+170 mV). Performed at 25 °C in a degassed buffer of 1 mM potassium ferricyanide, 1 mM potassium ferrocyanide and 100 mM KCl vs a saturated calomel reference electrode and Pt gauze counter electrode.

A typical Nyquist plot of the electrode is shown in figure 2.28, where it can be seen that a single semi-circle followed by a near 45° line is obtained. This is the classic response of a macro electrode and fits well to the established Randles' equivalent circuit, APP 1.2, as shown by the fit in figure 2.28 and the fitted values in table 2.1. The χ^2 value is relatively low, at 0.1855, indicating the goodness of the fit; with the majority of the fitting error coming from the Warburg element modelling linear diffusion to the electrode at the low frequency end of the spectrum; this is most probably due to the contribution of electrode surface roughness, which would lead to a constant phase element rather than a capacitance for the electrode, which would slightly flatten the semicircle and reduce the Warburg element angle below 45°.[15, 16] The goodness of fit could be improved by fitting to a constant phase element as opposed to a capacitor. However, this has not been done as this would involve adding a further fitting parameter.

Table 2.1. Equivalent circuit fits and errors in the fits to one standard deviation for each element in the Randles' circuit, equivalent circuit APP 1.2, for the data provided in figure 2.28.

Element	Value
R_s (Ω)	846 ± 13
R_{ct} (Ω)	32 400 ± 700
C_{dl} (µF)	1.15 ± 0.02
Y_0 (µS)	1.40 ± 0.10
χ^2	0.1855

2.7.2. Square Microelectrode (MS) Arrays

In this project, recessed microsquare electrode arrays were used. The response of these arrays has been established, showing close correlation between simulation and experimental measurement[61].

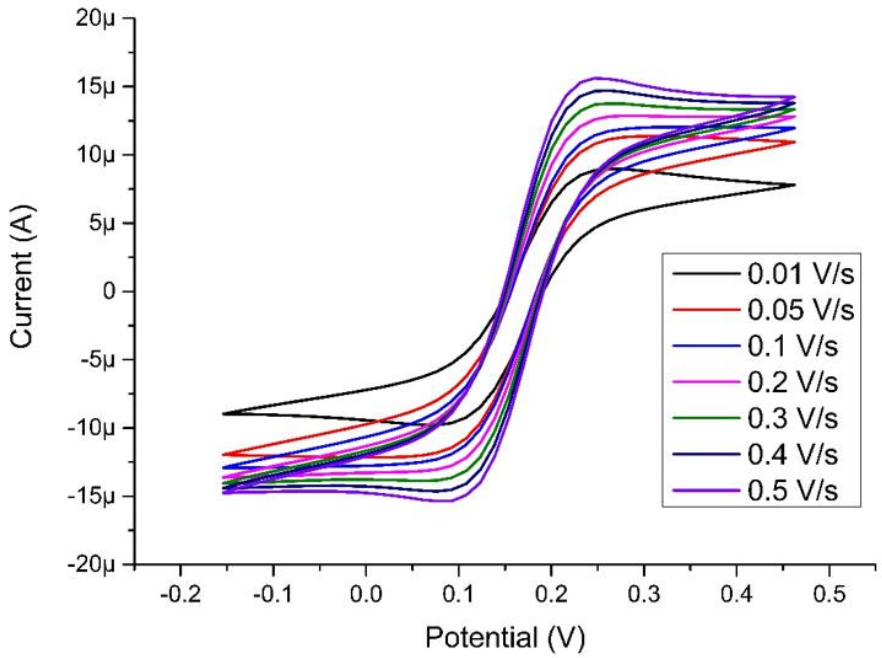

Figure 2.29. Typical cyclic voltammograms of a 30 µm 3D MS array (see APP 2 for more information) at the variety of scan rates shown. The scans shown are overlays of the 3rd, 4th and 5th scans, performed at 25 °C in a degassed buffer of 1 mM potassium ferricyanide, 1 mM potassium ferrocyanide and 100 mM KCl vs a saturated calomel reference electrode and Pt gauze counter electrode.

Cyclic voltammograms of a 30 µm 3D MS array at different scan rates are overlayed in figure 2.29. It can be seen that, as expected, a more wavelike response is observed than for the

macro electrode under the same conditions. The macroelectrode peaks are caused by the time dependence of the linear mass transport of FFC to the electrode, whereas the waves are due to hemispherical mass transport to the MSs in the array. At faster scan rates, there is little or no overlapping of the diffusion fields of neighbouring electrodes in the array. As the scan rate decreases the diffusion fields begin to overlap, causing the current to decrease and mass transport to become more linear and hence more peak like. As a result, the diffusion coefficient should be calculated from the theoretical MS limiting current at the fastest scan rate.

The established limiting current equation for recessed microelectrode square arrays when the scan rate is sufficiently fast that the electrodes in the array are acting independently is given by equation 2.2:[30]

$$i_l = 2.34nNFDcL \qquad \text{(Eqn 2.2)}$$

where i_l is the limiting current, n is the number of electrons transferred, F is Faraday's constant, D is the diffusion coefficient, c is the concentration of redox agent in the bulk electrolyte, L is the edge length on one of the squares in the array and N is the number of individual squares in the array.

Using equation 2.2 it was possible to calculate the diffusion coefficients for the MS array and compare them to that of the macro electrode above and in the literature. It was found that the diffusion coefficient for the ferrocyanide reduction peak for the 0.5 Vs^{-1} scan in figure 2.34 was 7.78 × 10^{-6} cm^2s^{-1}, which is in good agreement with the macro electrode and literature.[68] Given the dependence of the response on scan rate, and equivalent standard deviation could not be determined by the same method as the macro electrode.

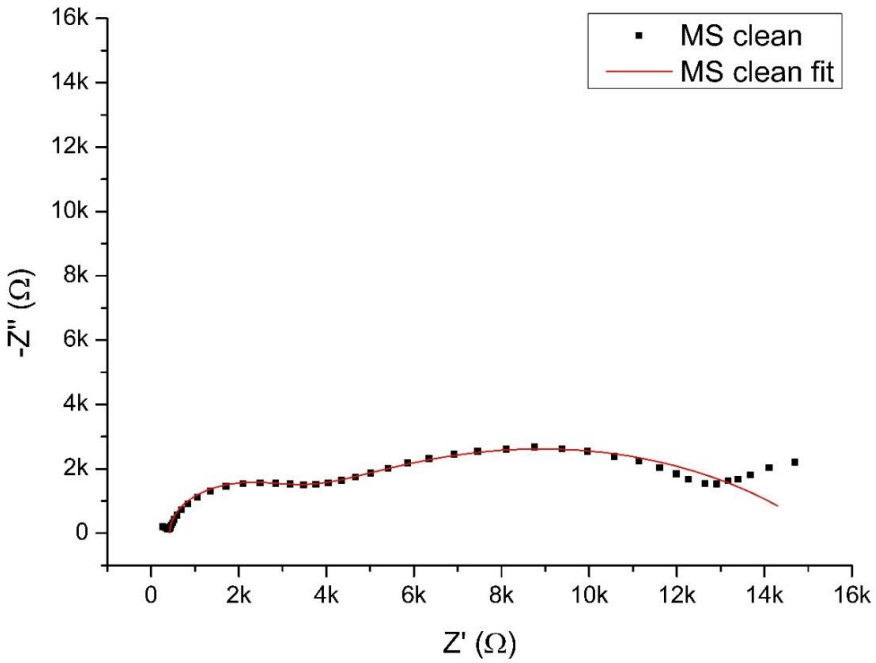

Figure 2.30. Typical Nyquist plot of a 30µm 3D MS array. EIS recorded at OCP at 25 °C in a degassed buffer of 1 mM potassium ferricyanide, 1 mM potassium ferrocyanide and 100 mM KCl vs a saturated calomel reference electrode and Pt gauze counter electrode. The raw data are black squares and the fit to the established modified Randles' circuit for a microelectrode, APP 1.3, is given by the red line. The fitted values and error in said fit are provided in table 4.2.EIS was recorded using the same protocol as the macro electrode data in figure 2.28, however, the fitting was restricted to frequencies greater than 1Hz as opposed to 0.1Hz to exclude the 45° line caused by array overlap, as this region cannot be fitted by the established equivalent circuit.

The Nyquist plot of the 30µm 3D MS array and its corresponding fit to the modified Randles' circuit for a recessed microsquare, APP 1.3, are given in figure 2.35, with a summary of the fits given in table 2.2. It can be clearly seen that there are two apparent semi-circles in the Nyquist plot, a smaller semicircle at the high frequency end of the plot and a larger near semicircular feature at the lower frequency end of the plot. Previous analysis of the two semi-circles showed that the first can be attributed to charging of the double layer capacitance and a resistance due to the electron transfer kinetics.[61] Analysis of the second apparent semi-circle reveals that it most closely resembles a Warburg element in parallel with a resistor. The Warburg element has been attributed to the linear diffusional flow of FFC towards and away from the electrode.[61] The resistor, which becomes increasingly important as the frequency is reduced can be attributed to the evolution of hemispherical, steady-state non-linear diffusion at the electrode surface and so this has been dubbed the non-linear resistance, The Warburg feature at the lowest frequencies is attributable to array overlap. As the equivalent circuit only applies to single microelectrodes (or the response on N independent microelectrodes in an array with no overlap) these data were excluded from the fit in figure 2.35.

At the highest frequencies there is the tail of another very small hemisphere, most probably caused by induction in the wiring in the potentiostat, which occurs even before R_s can be measured. This data would introduce an error in the fit to APP 1.3, which was avoided by excluding these points from this and other fits. Data were therefore recorded over a wider

range than it was necessary to model, with the fitting restricted to the frequency range of interest.

Table 2.2. fitted values and errors in the fits of all the elements in the modified Randles' circuit for recessed 30 µm 3D MS arrays, data and fit shown in figure 2.30. All errors given to one standard deviation.

Element	**Value**
R_s (Ω)	423 ± 85
C_{dl} (µF)	197 ± 24
R_{ct} (Ω)	2 530 ± 180
Y_0 (µS)	37 ± 2
R_{nl} (Ω)	12 300 ± 200
χ^2	0.16917

It is satisfying that the χ^2 value is similar to that of the macro electrode in table 2.1, which is again indicative of a good fit to theory and diagnostic of the expected MS response.

2.7.3. MNEE arrays

The cyclic voltammograms in figure 2.31 show the typical response of a 30 µm 3D MNEE array. As has been established there is again a wavelike response as mass transport to each nanoelectrode is again under hemispherical diffusion, as with the MS array.[30]

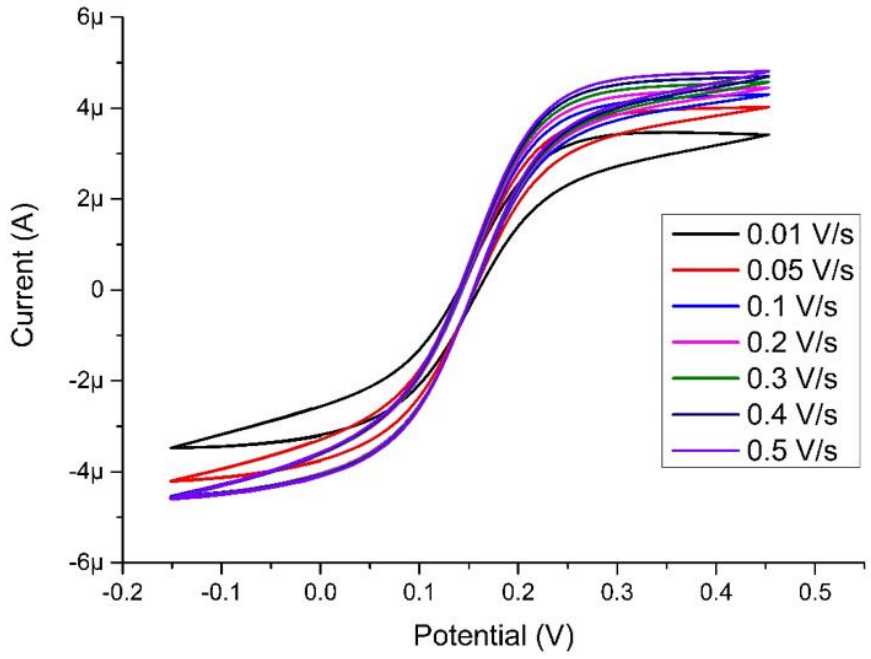

Figure 2.31. Typical Cyclic voltammograms of a 30µm 3D MNEE array at 25 °C in a degassed buffer of 1 mM potassium ferricyanide, 1 mM potassium ferrocyanide and 100 mM KCl vs a saturated calomel reference electrode and Pt gauze counter electrode.

The limiting current for this array of recessed nanoelectrodes, at fast scan rates where each electrode is acting independently and neighbouring diffusion profiles have not begun to overlap, has again been established through simulation and experiment, see equation 2.3:[30]

$$i_l = 0.956nNFDcL \qquad \text{(Eqn 2.3)}$$

where i_l is the limiting current, n is the number of electrons being transferred, F is Faraday's constant, D is the diffusion coefficient, c is the concentration of redox agent in the bulk solution, L is the length of one of the squares and N is the number of squares in the array.

At slower scan rates there is overlap of the diffusion layers of neighbouring electrodes, and the observed current are seen to reduce. At the fastest scan rates, the values of D for the MNEE array was calculated as 7.9×10^{-6} cm^2s^{-1}; this is again the same within experimental error as is observed on the macro and micro electrodes and consistent with the value in the literature.[68]

The Nyquist plot of a clean MNEE array is given in figure 2.32 with the fit to the modified Randles circuit for MNEE arrays, APP 1.3, overlaid and the values for each fitted element given in table 2.3.

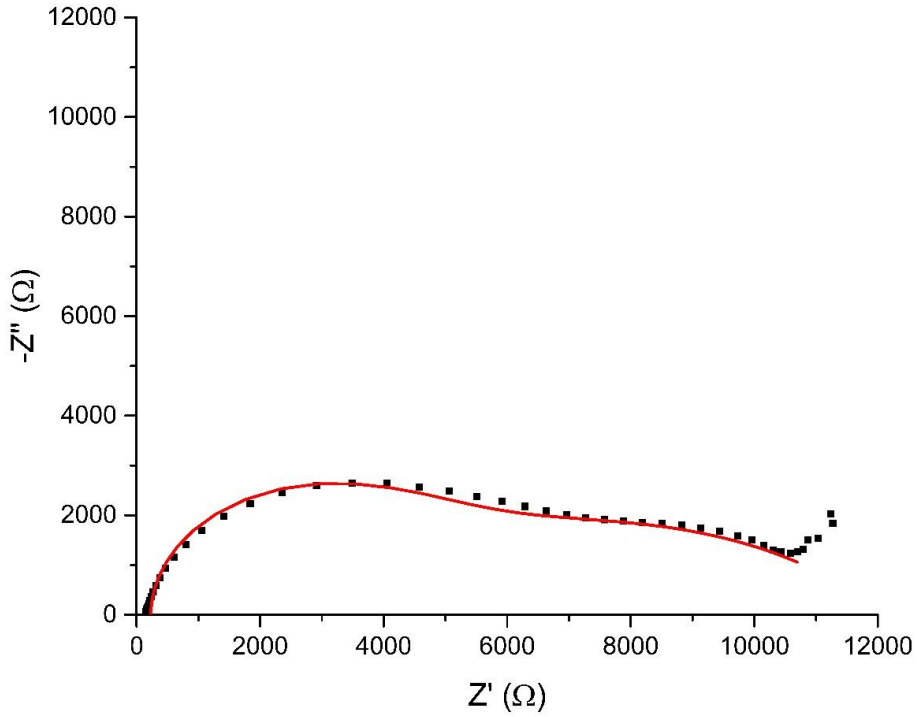

Figure 2.32. Typical data from a 30µm 3D MNEE array recorded at OCP at 25 °C in a degassed buffer of 1 mM potassium ferricyanide, 1 mM potassium ferrocyanide and 100 mM KCl vs a saturated calomel reference electrode and Pt gauze counter electrode. Fit of the modified Randles circuit for MNEE arrays, equivalent circuit 3, where the second hemisphere is fit to a Warburg element as opposed to a capacitor. The low frequency tail due to array overlap was excluded from fitting.

The Nyquist plots for the MNEE have two overlapping apparent semi-circles like the MS arrays. This time the high frequency semi-circle is the larger of the two; the resistance involved can again be attributed to electron transfer. The second, smaller, apparent semi-circle can again be attributed to an equivalent circuit element which is the parallel combination of an element (due to diffusional transport) and a resistance due to non-linear diffusion (R_{nl}), which both signifies and enables quantification of the establishment of steady-state hemispherical diffusion profile. Previous work indicated that a capacitor gave the best fit for diffusional transport, which was interpreted as being due to a rapid depletion of the redox species near the electrode when establishing hemispherical diffusion, due to the enhance diffusion seen at nanoelectrodes.[30] This was supported by the calculation that the amount of charged passed in charging the capacitor was consistent with that required to create a hemispherical depletion zone of redox species above each cavity.[30]

Table 2.3. fitted values for each element in equivalent circuit 3, to which the data in figure 2.32 has been fit.

Element	Value
R_s (Ω)	233 ± 33
C_{dl} (nF)	71 ± 2
R_{ct} (Ω)	4 350 ± 130
R_{nl} (Ω)	7 560 ± 120
Y_0 (µS)	17.7 ± 1.0
χ^2	0.036884

However, fitting of this data to the equivalent circuit APP 1.4 was found to give a worse fit for this data than equivalent circuit APP 1.3, which applies to the MS electrodes and has a Warburg element. These data, are given in table 2.3. The fitted values for the capacitor and Warburg fitted in figure 2.33.A and 2.33.B were C = 2.37 ± 0.33 µF (χ^2 = 4.212) and Y_0 = 17.7 ± 1.0 µMho (χ^2 = 1.270) respectively. The physical reality of the system is most probably linear diffusion to the nanoband within the cavity that then leads to a capacitance at lower frequencies caused by redox depletion of a hemisphere above the cavity. In this instance, the Warburg feature dominates, which shows that the linear diffusion is dominating. This is not unexpected when considering that the previous work[30] used a 10 µm edge length cavity MNEE array whilst this work was conducted using a 30 µm edge length cavity; meaning that linear diffusion will persist over a wider frequency range and the capacitance due to the exhaustive depletion of electrolyte within the cavity is less likely to be observed in this larger cavity.

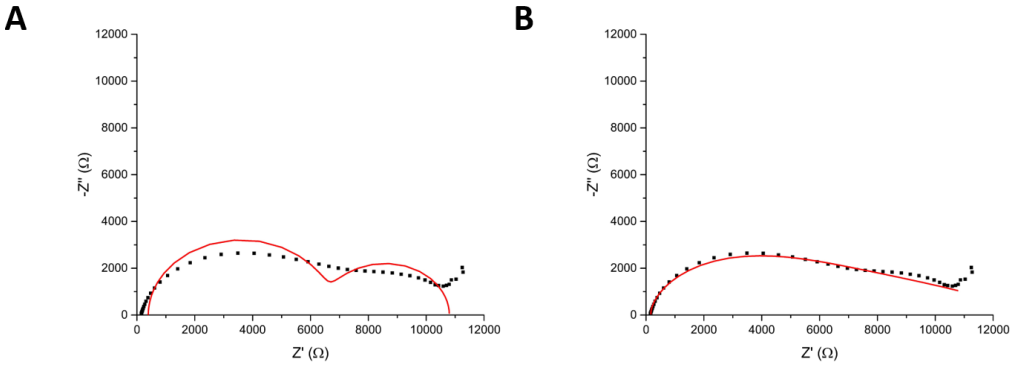

Figure 2.33. The same dataset as in figure 2.32 but fit to equivalent circuit APP 1.4 in (A) where the second hemisphere is fitted used a capacitor corresponding to redox depletion of a hemisphere above each cavity; and (B) where the same apparent semi-circle is fit to a constant phase element, circuit APP 1.5.

2.8. Conclusions and future work

Although a successful process had previously been established for MS and MNEE array fabrication, problems were identified with using this inherited process. After systematic optimisation, it was found that the photolithography process required modification. Three enhancements and/or simplifications to the run sheet were developed as a result; the wet etch of Pt in aqua regia and the dicing resist were found to be at best unnecessary and were therefore removed. It was also found that there were issues with control of the initial cavity etch process; this was due to the photoresist coating being too thin, which resulted in a photoresist layer that was not suitable for the etch required. The optimum spin speed for a set volume of photoresist has been identified and this resulted in wafers with devices that had uniformly flat surfaces and showed reproducible electrochemistry. The fabrication process has also been updated to include process checks to ensure continued device production fidelity. For example; checking of the thickness of the photoresist by depositing a set volume on a dummy wafer at a set spin speed should be performed before each use. Such enhancements led to a significantly more robust MS and MNEE array production. On the initial wafers it was noted that the chips at the centre of the wafer were more likely to, but did not always, perform better than those on the outer edges of the wafer. Once the photolithography had been optimised ever chip on every wafer made by this process worked perfectly.

The proper function of the fabricated electrodes was confirmed by measuring the electrochemical responses of a macro electrode in the experimental system and extracting the physical parameters of the system, and then showing that MS and MNEE arrays performed in accordance with the established responses in the literature. This has produced the benchmark response for subsequent SAM biosensor studies on MS and MNEE arrays.

3. Development of the experimental set up

3.1. Introduction

Given the enhanced sensitivity and reactivity of nanodimensional systems over micro or macrodimensional systems, the purpose of this chapter is to consider the experimental factors that need to be optimised or controlled when working with and comparing nanoelectrode biosensors. These factors include, but are not limited to, electrode cleanliness, system temperature, redox agent choice and the ionic strength of the buffer. Consideration of the optimisation of these parameters, will also require an appreciation of the experimental set up. Confidence that the experimental conditions are optimised can only be obtained by first considering the fundamental electrochemical and expected biosensing behaviour of the MNEE arrays and then discussing the behaviour of the developed system in this context. In order to identify enhancements in the electrochemical behaviour of the nanoelectrodes, they are also compared to macro and microelectrodes where necessary in this chapter. This forms a benchmark for the responses seen in subsequent chapters.

3.2. Cleaning electrodes

Given the fact that MNEE arrays are costly in time and money to fabricate, once used as biosensors it would be ideal if they could "cleaned" i.e. regenerated and reused. For this, it is important either that the thiol SAM used in the biosensing protocol can either be completely removed and the SAM reformed, or that the target can be removed from the probe without damaging the SAM, thereby regenerating the SAM layer for further biosensing study. In this section the removal of thiols from Pt MNEE arrays is therefore investigated. The literature on the topic of thiol removal from (macro)electrodes is extensive and varied.[28, 47, 69, 70] Techniques such as UV lithography[71], plasma cleaning[70, 72, 73], chemical cleaning[70], electrochemical oxidation[69, 70, 74] and electrochemical reduction[69, 70, 75, 76] of thiols on metal surfaces have all been reported and extensively studied. What is clear from the literature is that there is no general consensus established on a procedure to remove thiols from an electrode surface. There are chemically destructive methods of SAM and/or metal surface removal that are agreed to regenerate the electrode surface for re-use whatever the surface layer (e.g. using piranha and/or dilute aqua-regia), but not surprisingly these also have been reported to damage electrodes.[70] The loss of electrode metal from a macroelectrode, whilst undesirable, does at least yield a fresh macroelectrode surface of similar area to that previously; the loss of electrode material from a nanoelectrode, however, will have a greater effect on its active surface area, its profile and therefore its performance. Macro electrode cleaning protocols also tend to involve a mechanical polishing step,[14, 77-79] a process which is not possible on the MNEE or MS arrays due to their fragile, cavity architecture, and the potential for materials transfer onto the nanoelectrode.

Due to the variety of cleaning protocols advocated in the literature it was deemed necessary to test several cleaning techniques in a systematic fashion to determine which worked best.

3.2.1. Quantifying Cleanliness

Electrode cleanliness is a relative concept and as such there need to be ways of quantifying whether an electrode is completely, or at least sufficiently, clean. On macroelectrodes protocols which quantify cleanliness through analysing the position, shape and size of the oxygen and hydrogen evolution peaks observed in sulphuric acid have previously been reported.[80-82] The practice typically involves integrating the Pt oxide reduction peak of a macro electrode in sulfuric acid, figure 3.1 peak F, to calculate the charge passed, and using the knowledge that Pt and Au electrodes pass 200 µC and 100 µC of charge respectively to form a monolayer of adsorbate on every cm^2 of electrode.[31] In theory this can also be done by integrating the hydrogen desorption peaks A, B and C, figure 3.1., but is less commonly done because of the difficulty in resolving these peaks.[83] Both methods determine the active electrode surface area which can be compared to the geometrical dimensions of the electrode to quantify its cleanliness and/or its surface roughness.

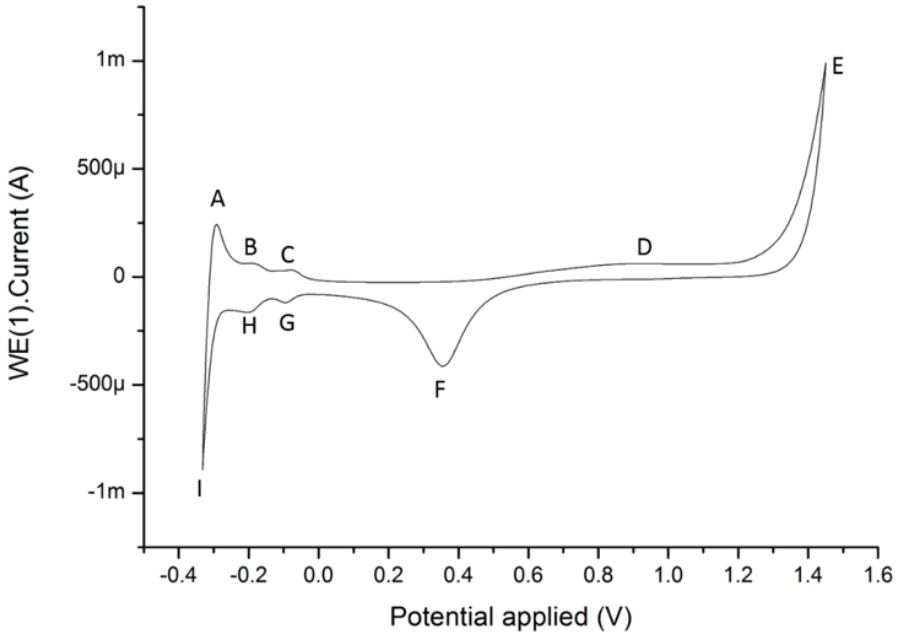

Figure 3.1. CV of Pt macro rotating disc electrode in oxygenated 0.1M H_2SO_4 vs. a saturated calomel reference electrode and Pt gauze counter electrode at a scan rate of 0.1V s^{-1}. The CV shown was the third scan between -0.32 V and +1.5 V starting and ending at 0 V. The peaks A, B and C correspond to hydrogen desorption from the three crystal faces of Pt; D is the formation of a Pt oxide/OH monolayer; E and I are the solvent limits. F is the platinum oxide reduction peak; G and H are the corresponding proton reduction and hydrogen adsorption peaks to B and C.

Figure 3.1. shows the CV of a Pt macro electrode in H_2SO_4 (0.1M), there are nine distinct peaks on this graph. Peaks A, B and C are caused by the oxidation and desorption of hydrogen from the different crystal faces of Pt with H and G being the corresponding proton reduction and hydrogen adsorption peaks. pH studies have shown the process can be achieved by the two mechanisms shown in equations 3.1 and 3.2. below:[80]

$$Pt + H_3O^+ + e^- \rightleftharpoons Pt(H_{ads}) + H_2O \qquad \text{(Eqn 3.1)}$$

$$Pt + H_2O \quad + e^- \rightleftharpoons Pt(H_{ads}) + OH^- \qquad \text{(Eqn 3.2)}$$

There are in fact three hydrogen adsorption peaks that can be better resolved at lower pHs,[84] in the case of figure 3.1 the solvent limit may be obscuring the third hydrogen adsorption peak.

Peak D is attributed to the formation of a Pt oxide/hydroxide monolayer.[53] The reverse process at peak F is the reduction of this oxide/hydroxide layer on Pt, described by equations 3.3-3.6 respectively.[31, 53]

$$Pt + H_2O \rightleftharpoons Pt(OH_{ads}) + H^+ + e^- \qquad \text{(Eqn 3.3)}$$

$$Pt + H_2O \rightleftharpoons Pt(O_{ads}) + 2H^+ + 2e^- \qquad \text{(Eqn 3.4)}$$

$$Pt + OH^- \rightleftharpoons Pt(OH_{ads}) + e^- \qquad \text{(Eqn 3.5)}$$

$$Pt + OH^- \rightleftharpoons Pt(O_{ads}) + H^+ + 2e^- \qquad \text{(Eqn 3.6)}$$

The feature E is the current due to oxidation of the solvent water molecules, known as the solvent limit, which results in oxygen gas evolution at the Pt electrode. Feature I is the solvent limit at the reductive end of the cycle, resulting in hydrogen gas evolution. It is worth noting that the same processes can be seen on gold macroelectrodes but the potentials at which they occur are slightly shifted. One potential advantage of using CV analysis is that gaseous oxygen and hydrogen evolution as a result of features E and I can also be used to clean electrodes through chemical and/or mechanical surface action. Thus, CV cycling can be used to both enhance and monitor surface cleanliness.

Understanding the processes by which hydrogen and oxygen/OH monolayers form on an electrode allows the determination of active electrode surface area. This can be done by integrating to find the area under a peak in which a monolayer is formed or removed and diving by the literature value for charge per unit area for monolayer formation. In the case of Pt this is 200-210 μC cm^{-2} depending on the literature source.[31, 83, 85] Once the experimentally derived active electrode surface area has been calculated it can be compared to the geometric electrode surface area, based on the dimensions of the electrode, to quantify the cleanliness of said electrode. It should also be noted that any roughening of the electrode surface will increase the active electrode surface area and affect these cleanliness calculations.

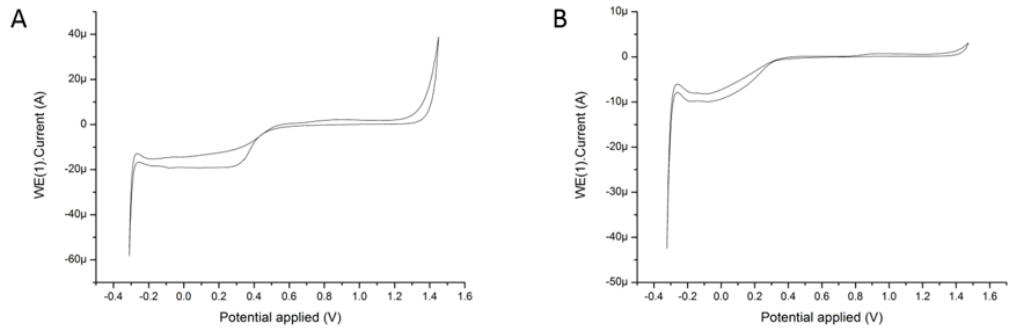

Figure 3.2. Cyclic Voltammograms of (A) a 30 µm edge length 3D spacing microsquare array and (B) 30 µm edge length 3D spacing MNEE array, see chapter 2.2 for details about naming convention, in 0.1M H_2SO_4 vs a saturated calomel reference and Pt gauze counter electrode at a scan rate of 0.1Vs^{-1}. The CVs were run from -0.3 V to +1.5 V with the scans starting and ending at 0 V, the third scan has been plotted in both (A) and (B).

Similar measurements on micro and nano electrodes were found to be not practical. This is due to the relative enhancement of features governed by mass transport in these systems (which scale with length) over those governed by electrode adsorption (which scale with area). Therefore, the reduction of dissolved oxygen dominates the voltammetry (figures 3.2.A and 3.2.B). Such mass transport limited features also become wave like not peak like, as when diffusion limited there is significant and steady state mass transport to each of these systems. It should be noted that the solvent limits are electrode material not area dependant and as such the potential at which features occur should be constant and qualitatively indicative of cleanliness. There are small, hard to resolve peaks on both the micro and nanoelectrode CVs (below -0.1V in figure 3.2.A and 3.2.B) consistent with peaks A to C and G, H but their relative size makes them unfit for quantitative analysis. The Pt oxidation peak, which begins at roughly + 0.8 V is very broad and flat making it difficult to discern the potential window appropriate to integrate across. Also in the case of the MNEE, figure 3.2.B, this peak appears to merge with the oxidative solvent limit. Thus, a different approach was developed for assessing the cleanliness on micro and nanoelectrodes.

3.2.1.1 Measuring electrode active area using voltammetry

A well-established electrochemically reversible redox couple in solution can be used to determine the active area of a macrodisc electrode by relating the measured peak current in voltammetry to the area through the Randles-Sevcik equation, equation 3.7:[31]

$$i_p = 0.4463nFAc\left(\frac{nFvD}{RT}\right)^{\frac{1}{2}} \qquad \text{(Eqn 3.7)}$$

where i_p is the peak current, n is the stoichiometric number of electrons transferred in the redox reaction, F is Faradays constant, A is the active electrode surface area, D is diffusion coefficient of the redox agent, c is concentration of the redox agent, v is the scan rate, R is the universal gas constant and T is the temperature

Practically, a literature value for D can be obtained and the expected limiting current calculated, thus if the electrodes are cleaned by cycling into the solvent limits using cyclic voltammetry, if there is a known concentration of a specific redox agent also in the solution and provided the cleaning and redox reaction processes are independent, cleaning will be

seen to be completed when the expected redox response (in terms of the position of the redox reaction and its calculated limited current) is seen.

Similar equations for determining the theoretical maximum limiting current for MS arrays and MNEE arrays are equations 2.2 and 2.3 respectively. Cyclic voltammograms of macro micro and nano electrodes in FFC buffer of known concentration have been given in chapter 2.7, along with their experimentally measured diffusion coefficients which correlate very well too literature values under the same conditions, thereby establishing this method for assessing the cleanliness of the electrodes.

3.2.2. Oxide layer removal

Another important consideration when making measurements is that metals readily form oxide layers such as Pt oxide and Au oxide, particularly under some of the harsh conditions employed in microfabrication, and that nanoelectrodes, with their enhanced reactivity, are likely to be more prone to such reactions. These are less conductive than the pure metal and therefore can affect the electrode response.[53] However, these oxide layers can also be electrochemically removed, by scanning to negative potentials in aqueous KCl. Figure 3.3 shows CVs of a Pt MNEE electrode fresh from the clean room where consecutive voltammetry scans are taken in -0.1 V increments as the lower potential limit in an aqueous solution of 1mM potassium ferricyanide, 1mM potassium ferrocyanide and 100mM KCl. The ferri/ferrocyanide wave is seen to be almost non-existent when the first CV is taken but grows in as consecutive reductive scans are performed.

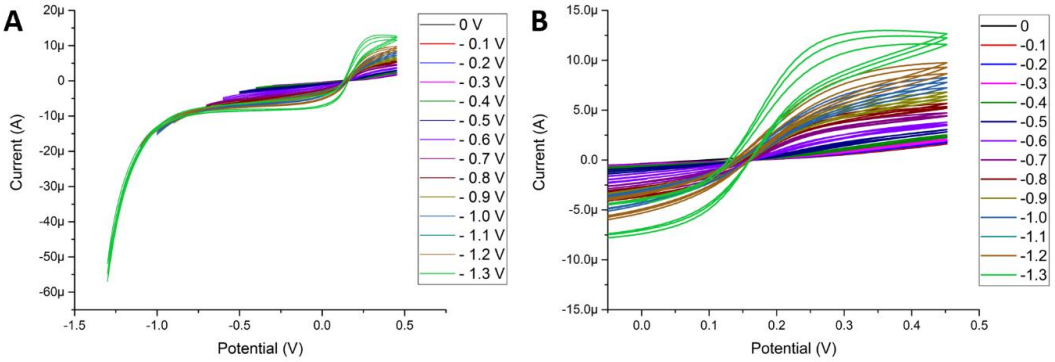

Figure 3.3. Cyclic voltammograms of a 30 µm 3D MNEE array in an aqueous solution of 1mM potassium ferricyanide, 1mM potassium ferrocyanide and 100mM KCl at a set temperature of 25°C at a scan rate of 0.1 Vs^{-1} vs a saturated calomel reference electrode and Pt gauze counter electrode. (B) is simply a magnification of the area of interest in (A). Each potential window was scanned 3 times with all three scans shown in the plots. The lower potential limit is indicated in the legend and the upper vertex potential was set to +0.45V, all scans were set to start and finish at 0 V.

As oxide layers form in the air or in oxygen rich buffers such as water,[53] the electrode used in figure 3.3 was left sitting open to the air overnight in ambient conditions before reductive sweeps between -1.1 V and + 0.45 V in the ferri-/ferro- buffer were run again. The resulting CV scans are given in figure 3.4; the first scan shows a resistive response attributable to an oxide layer which can be almost entirely removed by a single scan down to -1.1 V. On subsequent scans the characteristic ferri/ferrocyanide redox waves are seen, which are of the order of the expected limiting currents (the literature diffusion coefficient of

ferrocyanide, D = 7.7 × 10^{-6} cm^2 s^{-1},[68] gives a limiting oxidation current of 17 µA and of ferricyanide, D = 6.2 × 10^{-6} cm^2 s^{-1},[68] gives a limiting reduction current of -9.7 µA, from equation 2.3).

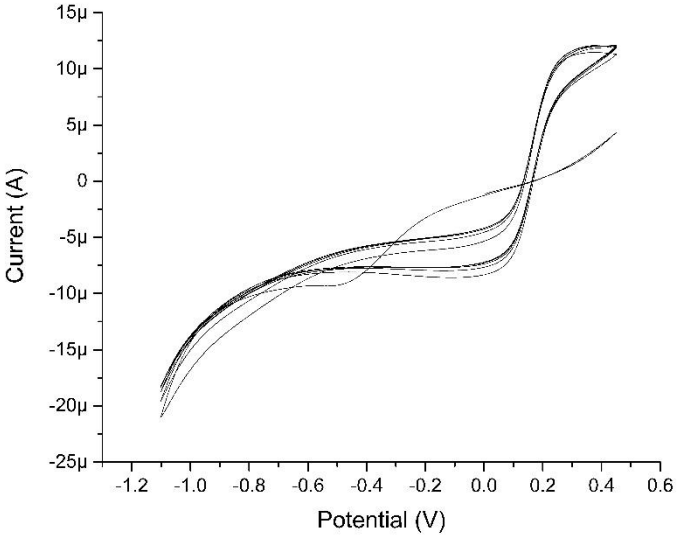

Figure 3.4. Cyclic voltammograms of the electrode in figure 3.3 after being left exposed to the laboratory atmosphere overnight. CVs were performed in 1 mM potassium ferricyanide, 1 mM potassium ferrocyanide and 100 mM KCl vs a saturated calomel reference electrode and Pt gauze counter electrode. CVs were recorded under the same conditions as those in figure 3.3. The first scan was started at 0V and was initially scanned positive, reaching a maximum current of 5 µA at + 0.45 V. The first scan starts at 0V and reaches 5 µA at 0.4 V.

Newly fabricated electrodes can therefore be treated as clean once their oxide layers have been removed and their active surface area has been established to be the same as their geometric surface area.

3.2.3. Electrochemical removal of SAM layers

As with other surface layers, thiols can be oxidised[69, 70, 74, 86, 87] or reduced[69, 70, 75, 76, 87] from an electrode surface electrochemically. The mechanism of each is discussed in more detail below, but it is important at this stage to mention some of the pros and cons involved with both electrochemical removal methods. The major benefit is that since the (particularly nano) electrodes are very small, recessed and surrounded by other materials, it is an advantage that the removal method only applies to the electrode, which reduces the potential for reaction on, and contamination by products from, the surrounding materials. The necessary equipment for cleaning is also cheap and readily available, whereas UV light cleaners or plasma cleaners would require the purchase of further instrumentation. The ability to quantify the cleanliness of the electrode during the removal process is another advantage of using an electrochemical method. Recent work published by Erbe et al[76] in which ellipsometry was used to monitor alkyl SAMs during a reductive clean was consistent with bubbles of H_2 forming under the desorbed SAM. This work showed that even after the M-S bond has been broken the van der Waals forces between neighbouring molecules in the SAM cause the film to retain much of its structure after de-binding, see figure 3.5. These thiols are then capable of resorbing to the metal surface. When hydrogen bubbles are

formed the alkyl chains of the desorbed molecules are thought to aggregate at the surface of the H_2 bubble, reducing the interfacial energy between hydrogen gas and the electrolyte. It is possible that something similar could be true for oxygen and oxygen bubbles formed in oxidative removal protocols.

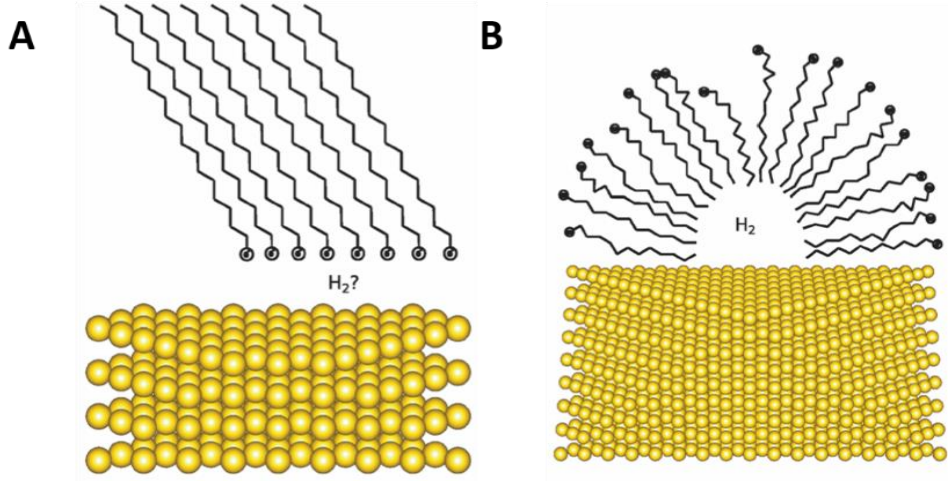

Figure 3.5. (A) Desorbed thiols after a reductive cleaning process are thought to be still in close proximity to one another and are able to re-adsorb to the metal surface. It is not known whether or not there is hydrogen in the interfacial region between thiol and electrode. (B) when bubbles of hydrogen are formed the SAM is thought to restructure to have the alkyl chains at the bubble interface further away from the electrolyte, which makes re-adsorption less likely as the SAM molecules are in the wrong orientation. Image taken from Erbe et al.[76]

Once the thiols have been removed from the electrode surface they are free to diffuse into the bulk solution where the concentration is tiny due to dilution. However, even after the removal process has been completed the thiols are capable of re-adsorbing. Therefore, notwithstanding the large dilution effect, to ensure complete thiol removal it was thought prudent to remove the device to a fresh buffer solution and repeat the method until the correct limiting current was obtained, as stipulated above. This is consistent with similar studies, where longer chain thiols were shown to be harder to remove due to their decreased solubility.[75] The theory below focusses exclusively on breaking Au-S bonds, but oxidative and reductive thiol removal can also be applied to the other gold sulfur bond types discussed in section 1.3.

3.2.3.1. Oxidative thiol removal

The principal concept behind this method is to oxidise the platinum surface, forming platinum oxide, breaking the metal thiol bond and oxidising the thiol species bound to the electrode surface. The literature suggests that the oxidation of thiols bound to noble metals is a complex process and depends heavily on the reaction conditions. In alkaline medium, IR spectroscopic studies have shown that the thiol can be oxidised to sulphate in an 11 electron process that also breaks the S-C bond, fragmenting the thiol species, equation 3.8:[87]

$$M - SCH_2R + 14OH^- \rightarrow M(0) + SO_4^{2-} + RCO_2^- + 8H_2O + 11e^- \qquad \text{(Eqn 3.8)}$$

In acidic media the 5 electron process below has been observed:[88]

$$M - SR + 3H_2O \rightarrow M(0) + 5e^- + RSO_3^- + 6H^+ \qquad \text{(Eqn 3.9)}$$

whilst other studies using IR and ellipsometry suggest a 3 electron transfer in acidic media leading to the formation of sulfonic acid:[89]

$$M - SR + 2H_2O \rightarrow M(0) + RSO_2H + 3e^- + 3H^+ \quad \text{(Eqn 3.10)}$$

It can therefore be concluded that the oxidative desorption of thiols is a complex process with a variety of possible mechanisms, all of which are postulated in resulting in the loss of chemically modified thiol and the production of an oxide surface. If an electrode were cleaned oxidatively it will therefore have an oxide layer present which must be removed as discussed in section 3.2.2. There are also a variety of fragmentation products which can be generated, the adsorption of which could complicate the process.

3.2.3.2. Reductive thiol removal

The literature on the reductive desorption mechanism indicates it to be much less complex than that for oxidative desorption. Reductive desorption is typically studied in high pH media (>8.5) so as to see the reduction peak clearly without interference from the hydrogen adsorption and evolution peaks.[75] The accepted reduction mechanism is a simple 1 electron reduction given in equation 3.11:[47, 75, 87, 89]

$$M - SR + e^- \rightarrow M + RS^- \quad \text{(Eqn 3.11)}$$

3.2.3.3 Testing electrochemical thiol removal on MNEE

To establish a suitable nanoelectrode thiol removal protocol, a 20 µm 4D MNEE array was first coated in a mercaptohexanol film as described in section 3.7. The electrode array was assessed for reductive thiol removal in a solution of 1mM FFC in 100mM KCl by cycling between -1.1 V and +0.45 V vs. a saturated calomel reference electrode for 2 minutes at a scan rate of 0.1 Vs^{-1}. The same electrode was then cleaned oxidatively in the same buffer by cycling between -0.1 V and +0.8 V vs a saturated calomel electrode. The oxide layer was removed by 4 consecutive scans as in section 3.2.2. CVs of the FFC wave from the SAM coated electrode at each stage are overlaid in figure 3.6.

Even after two minutes of cleaning by either method the current were enhanced, showing that both are viable methods for SAM removal. It was determined that the reductive cleaning would be used in future as it did not necessitate a further oxide removal step. The final cleaning protocol was to reductively clean by cycling between -1.1 V to + 0.45 V in 1mM FFC and 100 mM KCl , replacing the buffer periodically, in practice this was done every 10min, to dilute the thiol concentration in the bulk solution. Cleaning was only stopped when the limiting current of the FFC waves reach the expected limiting currents, i.e. the electrode active area is the same as its geometric area. This method allowed the real-time assessment of electrode cleanliness during the process.

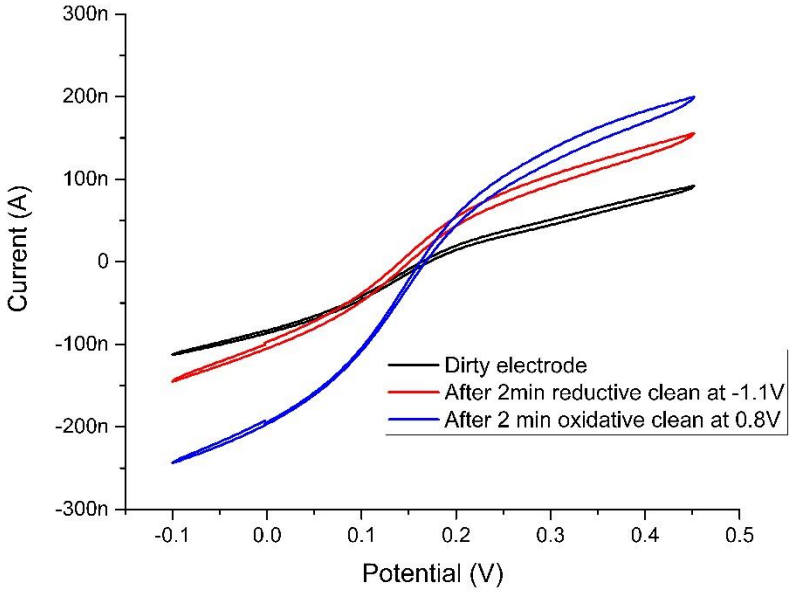

Figure 3.6. CVs of a 20µm 4D MNEE array coated with mercaptohexanol (black) then after 2 minutes cycling between -1.1V and +0.45V (red) and then finally after 2 minutes cycling between -0.1V and +0.8V (blue); in both cases the cycling started and ended at 0V. All CVs were recorded in a solution of 1 mM FFC and 100 mM KCl vs a saturated calomel reference electrode and Pt gauze counter electrode.

3.3. The measurement buffer

The choice of buffer used is an important consideration when designing an experiment. There are a multitude of redox couples that have been extensively characterised and published in the literature, [12] based on the cleaning method outlined in section 3.2 where the cleanliness of the electrode can be calculated using a redox couple, it was vital to use a very well characterised redox couple that has been extensively characterised in the literature.

3.3.1. The (potassium) ferricyanide/ferrocyanide (FFC) redox couple

The FFC redox couple is the most widely used of all the redox couples, being extensively cited in the literature. [23, 58, 77, 79, 90-92] Some of the major benefits are its high solubility in aqueous media (46.4g/100ml at room temperature)[93] and its large overall negative charges of 3- and 4-, which can cause a large impedance effect through electrostatic repulsion when negatively charged DNA is bound to the electrode surface (this electrostatic repulsion is known as the Donnan effect). This couple had an experimentally derived open circuit potential of +170 mV vs. a saturated calomel reference electrode on a Pt working electrode in 100 mM KCl when both species were present at mM concentrations, which is also a useful region within the solvent window where few competing processes are taking place.

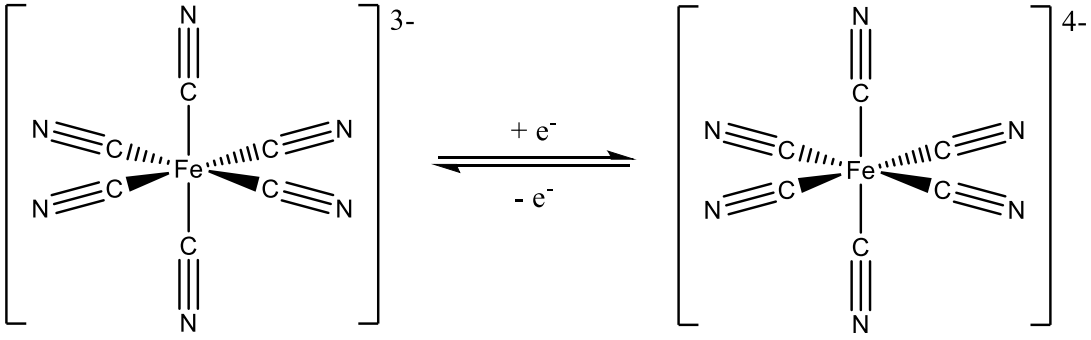

Figure 3.7. The molecular structures of ferricyanide (LEFT) and ferrocyanide (RIGHT).

The use of the FFC redox couple is somewhat contentious in the literature, with one recent paper suggesting that it forms an insoluble prussian blue precipitate during use which fouls the electrode.[94] Prussian blue is a polynuclear mixed valence iron cyanide complex of potassium ferro/ferricyanide hexacyano hexahydrate $Fe_4^{III}[Fe^{II}(CN)_6]_3.6H_2O$.[27, 94] During the course of this project a blue residue (consistent with prussian blue formation, although it should be noted it could also be a related polynuclear mixed valence iron complex) was formed from buffers containing FFC on multiple occasions, however, it was noted that it would only form on devices previously cleaned in H_2SO_4 solutions. To test the theory that the acid is responsible for causing the formation of the Prussian blue, 0.1M H_2SO_4 was added to a 1mM FFC buffer. Within a matter of minutes, the solution had gone from yellow to colourless with a blue precipitate lined at the base of the beaker. It should be noted that no electrochemical measurements were necessary to form Prussian blue, this was a spontaneous chemical and/or photochemical reaction. This was a major motivation behind devising a protocol to enable cleaning of electrodes in non-acidic media.

WARNING: Great care should be taken when adding any acids to ferric cyanide solutions, as this can trigger the release of highly toxic cyanide gas. This experiment was only ever performed with dilute acid (0.1M H_2SO_4) in controlled conditions.

3.3.2. Background electrolyte

There are multiple background electrolytes used in the literature, such as tris-HCl, phosphate buffered saline (PBS), 4-(2-hydroxyethyl)-1-piperazineethanesulfonic acid (HEPES), tris-saline and KCl to name a few. Some redox agents will undergo different electrochemistry at different pHs, so it is important in some instances to select a supporting electrolyte to buffer the pH at a selected value.

After testing different background electrolytes it was determined to use KCl for this project. All the afore mentioned supporting electrolytes worked perfectly well but KCl was chosen because of its low cost and purity.

3.3.3. Ionic strength

The ionic strength of a solution (*I*) can be calculated using the concentration (*c*) and formal charge (*z*) of each ionic species (n) in solution, using equation 3.12. Calculating in its

dimensionless form also requires (c^{θ})which is equal to 1 mol kg^{-1}. For 1:1 electrolytes such as KCl, the ionic strength is equal to the solution concentration, equation 3.12:

$$I = \frac{1}{2}\sum_n \frac{c_n}{c^{\theta}} . z_n^2 \qquad \text{(Eqn 3.12)}$$

In chapter 5, the electrode responses in different ionic strength buffers is tested to study the of charge on and in the films. Having higher concentrations of background electrolyte in the SAM allows the neighbouring charges in SAM films to be more efficiently shielded from one another. The four background electrolyte concentrations used were 1 mM, 10 mM, 100 mM and 500 mM KCl, each also containing 1 mM potassium ferrocyanide and 1 mM potassium ferricyanide (FFC, which has a calculated ionic strength of 16 mM). Using equation 3.12. these solutions have calculated ionic strengths of 0.017, 0.026, 0.116 and 0.516 mM respectively. It is important for these calculations to remember to include the counter ions in the potassium ferricyanide and potassium ferrocyanide salts and it is clear that the FFC is progressively less of a contributing factor to the total ionic strength of the solution at higher supporting electrolyte concentrations.

3.4. Temperature dependence of the electrode response

The electrochemical response of the electrodes was found to be extremely dependant on the temperature of the system. The graph in figure 3.8 is an example overlay of the impedance response of a Pt MNEE array (which is resistive as it from an early batch, but the exposed Pt band still shows the trend being discussed) and the room temperature measured over the course of 48 h. The two are clearly inversely correlated as expected, but it is clear even small temperature fluctuations (e.g. at the 20 hour point) cause relatively large changes in the measured impedance.

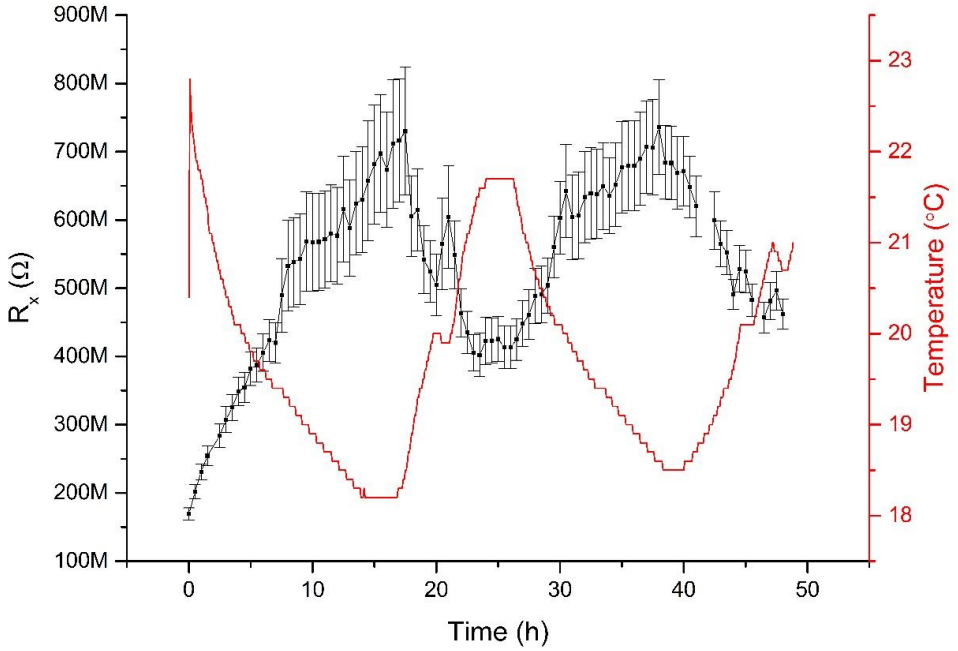

Figure 3.8. Plot showing the fitted R_x values from equivalent circuit APP 1.1 fit to a resistive 30µm 3D MNEE array from batch AP1402; where the clean electrode was left sitting in 1 mM FFC and 100 mM KCl, see chapter 4.4.6. Both EIS measurements and temperature were recorded at 1h intervals. All EIS was recorded at OCP vs a saturated calomel reference electrode and Pt gauze counter electrode.

As a result of these findings it was determined that fine control over the temperature of the experiments was an absolute necessity, especially for the kinetic experiments in Chapter 4 where k_{off} of a 6-mercapohexan-1-ol film would be measured over the course of several days.

Two water baths were built in house using parts donated by other groups within the school (the author would like to extend his thanks to the Hulme group for the parts). The units were from old water baths and had controlled heating units and pumps. A water jacket was then made in house and connected by tubing to the heating/pumping unit that was placed in a bucket of water. After calibration, this was shown to be able to hold the buffer in the unit at a stable temperature to within ± 0.1 °C. Photographs of the baths built in house are given in figure 3.9.

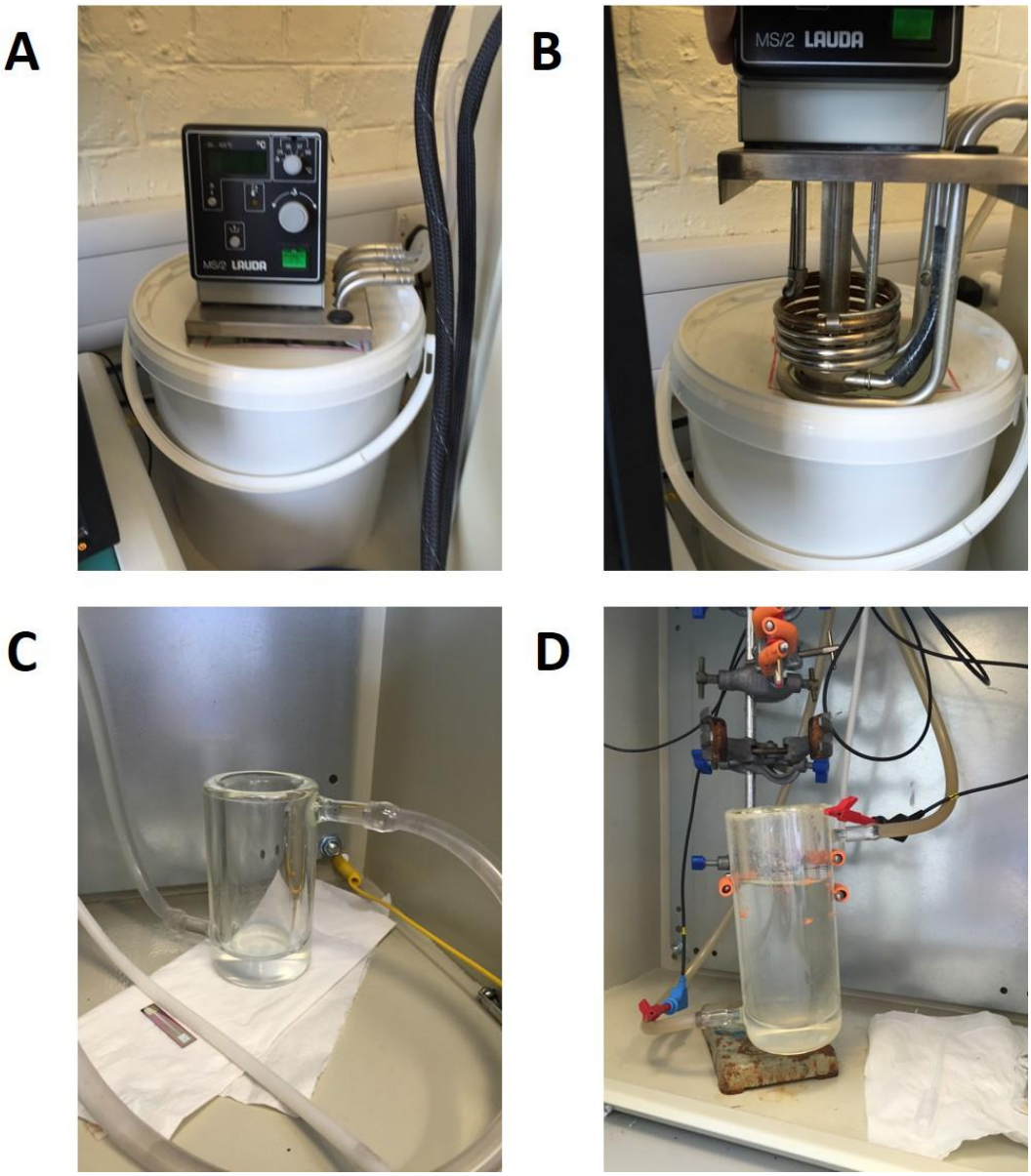

Figure 3.9. Photographs of a water bath built in house. Figures (A) and (B) show the control unit with heating element and pump, as well as the bucket of water in which it sat. (C) and (D) show the custom-built glass heated jacket where the water was pumped through the bottom inlet and then exited back to the bucket from the top outlet. Thus, heated water passed around the inner jacket which was filled with measurement buffer. A thermocouple was placed in the measurement buffer and the control settings enabled control of temperature to 25 ± 0.1 °C.

3.5. Degassing

Degassing (more accurately sparging) the buffers through bubbling inert gas is common practice to remove O_2 from solution because it is redox active.[31] It has already been shown in the cleaning section of this chapter how oxide formation on Pt affects the electrochemistry of the working electrode. In order to counter this, it was necessary to not just sparge the buffers with argon prior to use but keep them sparged over the course of the experiments, which in the case of the k_{off} experiments in chapter 4 meant keeping solutions sparged for several days. Typically, this was done by creating an argon blanket over the cell by flowing gas over the sparged solution. This was unfortunately found to expedite the loss of the

solvent, which could increase the effective concentration of redox agent in the solution. Constantly bubbling the solution had a similar effect with the added disadvantage of disturbing the buffer and occasionally the electrode surface if the gas flow moved the stream of bubbles over the electrode. Over the course of the experiments the gas flow therefore needed to be kept constant as the depleting pressure in the gas line over the course of the experiments added variability to the experiments. Parafilm was used to create a lid over the experiment, closing the system in an argon atmosphere to prevent oxygen entering the system. However, the parafilm seal was never airtight and some oxygen could still enter the cell.

In the end it was found that having a very low flow of argon, controlled by a gas flow regulator, into an already degassed buffer with a parafilm lid offered an acceptable method to prevent oxygen entering the buffer. Over longer periods of time however, the solvent would condense on the parafilm and drop down back into the solution, these drops would occasionally land on the electrode bond pad and cause shorting. For the purposes of the kinetic experiments done in chapter 4, any experiments in which this occurred had to be excluded and repeated. The characteristic electrochemical response was a sudden decrease in impedance as the device shorted and current flowed directly through the bond pad. This was the motivation for changing the electrode design to the long dip electrodes, chapter 2.5.

3.6. Reproducible device connection

The connection between electrode and potentiostat was vitally important. A more resistive connection was unreliable, gave decreased currents and irreproducible and slower responses due to longer charging times.

The main issue with the connections on an MNEE array is that the bond bad is a square of Pt 50 nm thick and most connections require a good grip and no loss of Pt from the bond pad to get the best possible connection. A risk is therefore that the abrasion on connection will lead to an increase or variability of connection resistance. One solution could be to make the bond pads thicker and more robust e.g. by depositing a thick layer of metal over the bond pads to prevent the effects of abrasion. It was deemed too costly and time consuming to incorporate this additional processing step during microfabrication.

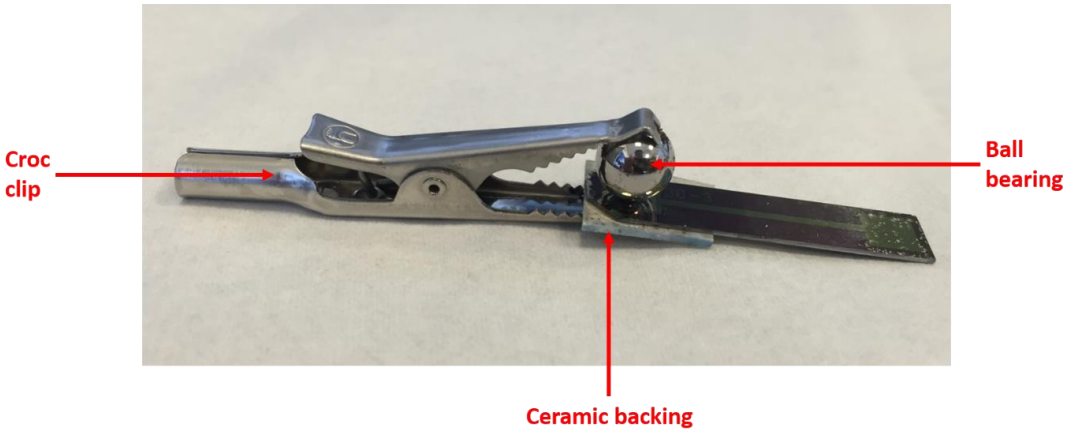

Figure 3.10. Photograph of electrode connection using a croc clip with a ball bearing to prevent abrasion of the bond pad.

It was decided that the best approach would be to soften the teeth of a croc clip but still use the force of its spring action to get a good connection. This was first done by folding aluminium foil and clamping it between the croc clip and bond pad. Although this did prevent the abrasion of the bond pad there was an appreciable loss of connection reproducibility, as the force of the clip was now too well distributed across the bond pad area. Instead a somewhat fiddly connection was developed where a steel ball bearing was sandwiched between croc clip and bond pad which concentrated the downward pressure of the croc clip onto a single rounded point on the bond pad. Because the ball bearing was spherical any knocking or minor movements of the connection did not abrade the bond pad surface. Whenever using a croc clip on these devices a ceramic plate was used on the back of the electrodes to protect them from the bottom teeth of the croc clips which also could break the electrode. A picture of this connection set up is provided in figure 3.10.

3.7. SAM formation protocol development

Unfortunately, unlike DNA thiols, PNA thiol molecules are markedly less soluble and prone to aggregation in aqueous solution, and require the addition of an organic cosolvent to enable the production of a viable PNA solution from which to form SAMs. The established cosolvent for this protocol was DMSO.[18] However, electrode devices (particularly nanoelectrodes) have been shown in this and other previous work to be sensitive to adsorption, particularly of low level impurities. To optimise the cosolvent buffer for SAM-PNA formation, studies were therefore undertaken using clean Pt macro electrodes. These were incubated with 1.5 µM PNA probe, 30 µM MCH and 150 µM TCEP in one of either 50:50 v/v DMSO (≥99.7%) and H_2O;[18] neat ethanol (≥99.8%) or neat deionised water for 16h.[51] Each was then exposed to 30mer DNA target in deionised water overnight at 5°C to saturate. The resulting data are plotted in figure 3.11 and show that DMSO does indeed form SAM probe films with markedly lower impedances than water (despite the low solubility of PNA), which itself shows a lower impedance than those deposited from ethanol. Furthermore, the increase in impedance observed on target binding is also greater for ethanol deposited SAMs, which is consistent with the SAMs formed in ethanol being of the highest integrity. As a result of these studies the published procedure[18] was adapted to use EtOH as the solvent in PNA SAM deposition.

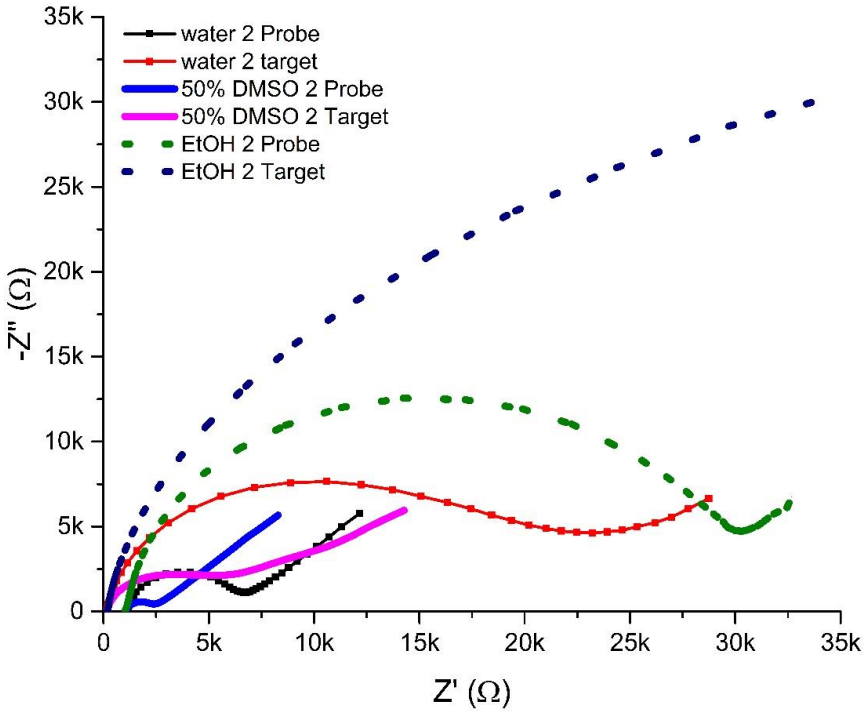

Figure 3.11. Overlayed Nyquist plots of films put down in 50% DMSO, pure water and pure ethanol solutions to show that the most densely packed PNA probe SAM films were formed in solutions of pure ethanol. All experiments were carried out on a 20µm 4D MNEE array in 1 mM FFC and 100 mM KCl, all EIS was recorded at OCP in degassed measurement buffers at 25°C.

3.8. Conclusions

In order to set up an experiment and get the best possible nanodevice data many factors need to be optimised. It was the purpose of this chapter to detail the optimisation undertaken in this project, partly to act as a practical guide to anyone intending to either repeat these experiments or to develop their own set up for their own investigations. The crucial experimental optimisations included the choice of the solution redox couple, the optimisation and analysis of the nanodevice cleanliness and the enhancement of device connectivity through changing from a resistive edge connector. This chapter also displayed the sensitivity of nanoelectrode devices to fluctuations in temperature, and how this was avoided through temperature control.

Through a discussion of the literature on electrode cleaning and experimental data it was shown that electrochemical cleaning of MNEE arrays in KCl to desorb thiols is possible, and capable of returning the electrode surface to what it was prior to experimentation. This discussion also led to an appreciation of oxide formation on Pt and the need to keep the solution stringently sparged during use, especially during the long kinetics experiments undertaken during this project, see chapter 4. This paves the way for the study of the nanoelectrode device response to SAM film and hydrogel formation presented in the following chapters.

4. The study of the formation of self-assembling monolayers (SAMs) on nanoelectrodes

4.1. Introduction

An introduction to self-assembling monolayers is given in chapter 1.3. The purpose of this chapter is to compare the kinetics of SAM formation on macro and nano electrodes. The description of SAMs in chapter 1.3 details that the structure of SAMs is dependent on the electrode bulk to edge ratio, which is smaller on nanoelectrodes than macro electrodes. It is therefore of interest to determine if the kinetics of SAM formation are different on macro and nano electrodes, as this would inform as to whether the rate of SAM formation is dependent on the structure of the SAM formed.

4.2. Experimental challenges

A variety of techniques can be used to image and analyse thiolate SAMs, however, due to the structure of the MNEE most of these techniques are not suitable. The major limitation being that the electrodes are on the inside of a cavity wall, making them inaccessible to AFM and STM tips. It was also deemed impossible to obtain ellipsometry, XPS or IR measurements on the electrodes due to their architecture preventing an incoming beam of radiation from being reflected in a measurable plane. Only electrochemical measurements were possible in this system for analysing SAMs on the MNEE. Electrochemically measuring the kinetics of SAM formation and desorption on macro and nanoelectrodes would divulge information as to the SAM structure. Measuring the film stability over time after it had formed would inform as to the dynamic nature and stability of the monolayer. EIS was utilised as it yields more information and is more sensitive than other electrochemical techniques, the responses of different fitted elements in the equivalent circuit might yield a better understanding of the nature of film.

It was deemed most appropriate to study the film kinetics using an incubation buffer for making the film and a measurement buffer for the electrochemical measurements; rather than adding the alkanethiol to the measurement buffer and monitoring film formation in real time. There were many reasons for doing this, not least that it is the system most applicable to the final intended use of the devices. Commercially available sensing films are obviously manufactured and distributed to the point of use before the sample to be tested (blood, saliva, mucus, etc.) is put on the electrode for analysis. Thus, understanding the change of a film structure as it is switched between different buffers is of great practical importance. A typical EIS takes 3 min to record, scanning 50 frequencies logarithmically from 100 kHz to 0.1Hz, which makes it difficult to record a signal quickly enough to measure the MNEE MCH film formation kinetics. Whilst this could be fixed by further diluting the alkanethiol, using multi-sine or single frequency EIS; it was decided to go down the route of separate incubation and measurement buffers.

The literature is inconsistent as to the time it takes for a monolayer to form. There are thought to be two stages in SAM formation, a rapid diffusion controlled adsorption followed by a slow re-crystallisation process taking days.[51] However, other sources state that densely packed well-ordered films form within a two hour period[50], albeit at a temperature of 36°; or in as little as 150s at an increased potential.[41] In general left under ambient conditions SAMs are left for at least 24 hours to saturate a clean macroelectrode surface.[48] For the purposes of this study it was determined to leave the MCH monolayer in the incubation buffer overnight to ensure that the film had reached a thermodynamic steady state. This was confirmed by taking repeated measurements after subsequent time periods in the incubation buffer to determine that the impedance signals measured did not change.

Since thiol film formation on macro electrodes has been extensively studied using a variety of techniques, the experiment could be tested and optimised on a macro electrode to test its suitability and validity. It was decided that for the purposes of these experiments, the simplest possible model should be tested. Using DNA or PNA probe thiols that can non-specifically bind to each other through their respective base pairs, or in the case of DNA repel each other through their negatively charged phosphate backbones, adding a level of complexity and variability to the system. It was decided that using a 6-mercaptohexan-1-ol (MCH) only film would still yield the necessary information about SAM formation. MCH is used extensively in the literature as a backfilling agent so it's SAM formation properties have a broad impact within the field.[18, 23, 58, 79, 95, 96]

4.3. Experimental conditions

4.3.1. Electrochemical measurements

All electrochemical measurements were performed in a Faraday cage using a Metrohm Autolab PGSTAT128N with a FRA32 module (Metrohm Ltd.). The measured voltages reported were with respect to a saturated calomel reference electrode (SCE, Accumet® 13-620-61, Fischer Scientific) unless otherwise stated, and the gauze counter electrode was made in house using Pt gauze and wire (Sigma-Aldrich). The "measurement buffer" was the same as the cleaning buffer described previously and consisted of 1 mM potassium ferricyanide, 1 mM potassium ferrocyanide (FFC) and either 10 mM or 100mM KCl as stated throughout (all from Sigma-Aldrich, Cumbria, UK) in ultrapure water (18.2 $M\Omega.cm^{-1}$, Millipore MilliQ). This was used to characterise the clean electrodes in that their voltammetric and EIS responses could be analysed to check that they were behaving according to the established theory for their size and shape, see chapter 2.7. The solution was degassed prior to use by bubbling with Argon for 10-15 minutes, during the experiments the solution was kept degassed by bubbling through a syringe at a constant flow rate of 0.1 litres per minute using a gas flow regulator (Key Instruments, USA). This prevented oxygen dissolving into the measurement buffer and oxidising the electrode during the course of the experiment, see chapter 3.5. The temperature was held at 25°C using a water bath built in house, see chapter 3.4.

All EIS spectra were recorded from 100 kHz → 0.1Hz scanning 50 frequencies logarithmically spaced with the amplitude of the potential sinusoid set to 10 mV rms. All EIS were performed at the open circuit potential for a clean electrode in the measurement buffer (+170 mV).

4.3.2. Electrode cleaning

Macrodisk Pt electrodes with a diameter of 1.6 mm (geometric area 2.01 mm^2) were obtained from IJ Cambria. These were cleaned in piranha solution (WARNING, explosive, use with extreme caution) for 30s to regenerate the electrode surface. The electrode was then polished in slurries of 1.0 µm, 0.3 µm and 0.05 µm alumina micropolish (Buehler, IL, USA) consecutively on a polishing microcloth (Buehler, IL, USA). Electrochemical cleaning involved cycling between -1.1 V and +0.45 V in 1 mM potassium ferricyanide, 1 mM potassium ferrocyanide and 10 mM KCl (all from Sigma-Aldrich, Cumbria, UK) in ultrapure water (18.2 $M\Omega.cm^{-1}$, Millipore MilliQ). Cleaning was stopped when the peak current for the solution made using FFC waves reached the calculated currents for an electrode of this geometry, using the Randles-Sevcik equation and literature diffusion coefficients of 7.26×10^{-6} cm^2s^{-1} for ferrocyanide[68] and 6.67×10^{-6} cm^2s^{-1} for ferricyanide[68]; the oxidation and reduction peak currents should be 4.8 µA and 4.5 µA respectively at a scan rate of 0.1 Vs^{-1}, temperature of 25°C (controlled using a water bath built in house). For more information on the electrode cleaning protocol see chapter 3.2.

4.3.3. 6-mercaptohexan-1-ol SAM formation

The "incubation buffer" consisted of 30 µM 6-mercaptohexan-1-ol (MCH; Sigma-Aldrich, Cumbria, UK), 150 µM tris-(2-carbocyethyl)phosphine (TCEP, Sigma-Aldrich, Cumbria, UK) in a 50:50 mixture of dimethylsulfoxide[1] (DMSO, Fisher Scientific) and ultrapure water (18.2 $M\Omega.cm^{-1}$, Millipore MilliQ). For the MNEE experiments this solution was diluted by a factor of 1 000 to give 30 nM MCH and 150 nM TCEP in 50:50 DMSO:water by volume.

4.3.4. Kinetic measurements

The electrode was dipped in the incubation buffer for a set time before rinsing with a jet of ultrapure water and transferring to the measurement buffer. Electrochemical measurements were started as soon as possible after moving to the measurement buffer. After each measurement, residual measurement buffer would be washed off the electrode with ultrapure water and the electrode placed back in the incubation buffer, this process was repeated until the film had reached a steady state. The electrode would be left in the incubation buffer overnight in an evaporation proof chamber prior to measuring again to obtain the steady state film response. Once the film had formed the electrode was left in the measurement buffer with electrochemical measurements automated to run at set time intervals using Autolab's NOVA 1.10 software package. All experiments were conducted at a controlled temperature of 25 °C water baths built in house (see chapter 3.4); and with constant sparging optimised to not disrupt the system (see chapter 3.5).

[1] DMSO was used according to the previously established protocol but it was later found that using ultrapure water alone gave the SAM with the highest impedance, see chapter 3.7. These experiments had been completed at the time of this discovery and there was insufficient time to repeat them using a different incubation buffer.

4.4. Results and discussion

4.4.1. Macro electrode SAM formation kinetics

Examples of Nyquist plots obtained during these experiments are given in figure 4.1, with the fitted values and errors in the fits given in table 4.1. All macro electrode data were fitted to the Randles' circuit (APP 1.2) and the changes in each of the fitted parameters is discussed in more detail below.

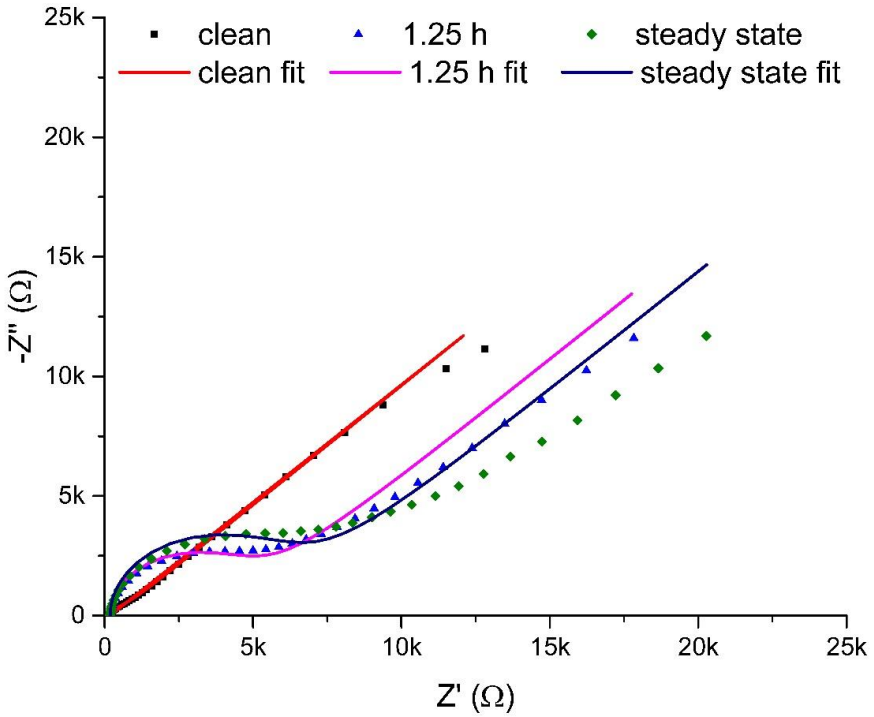

Figure 4.1. Nyquist plots of a clean electrode (black squares), an electrode partially covered with MCH after a combined total of 1.25 h in the incubation buffer (blue triangles) and once a steady state had been reached (green offset squares). Plots of the fits to the Randles' equivalent circuit, APP 1.2, are given by the line plots for a clean electrode (red), partially covered electrode (pink) and steady state film (navy blue). The values from these fits are given in table 4.1. All measurements were made at OCP, at 25°C in a degassed solution of 1mM potassium ferricyanide, 1mM potassium ferrocyanide and 100 mM KCl vs a saturated calomel reference electrode and Pt gauze counter electrode.

Table 4.1. The fitted values and errors in the fits to one standard deviation for each of the Randles' circuit elements fitted in figure 4.1.

	Clean	1.25 hours MCH	Steady state
R_s (Ω)	184 ± 1	184 ± 3	185 ± 4
C_{dl} (nF)	1022 ± 19	764 ± 15	689 ± 16
R_{ct} (Ω)	381 ± 12	4418 ± 125	5770 ± 200
Y_0 (μS)	76.3 ± 0.5	66.7 ± 1.8	61.2 ± 2.3
χ^2	0.0247	0.1643	0.2682

It is evident that the χ^2 values in table 4.1 increase as the film forms, with the majority of the error coming from the low frequency domain of the EIS spectra. This is hardly surprising as the film is known to be dynamic and the dynamic motion of the film will cause more variability within the film at the lower frequencies, and when more film is present on the electrode. The act of measuring the EIS may also be affecting the film. As ions are brought to the electrode surface during the measurement, they will change the local solvation state which will affect the film structure.

4.4.1.1. Macro electrode film formation kinetics, R_s

On examining figure 4.2, it can be observed that there is no change in R_s caused by MCH binding to the electrode. As discussed in Chapter 1.4.6.1., R_s is a measure of the conductivity of the electrolyte.

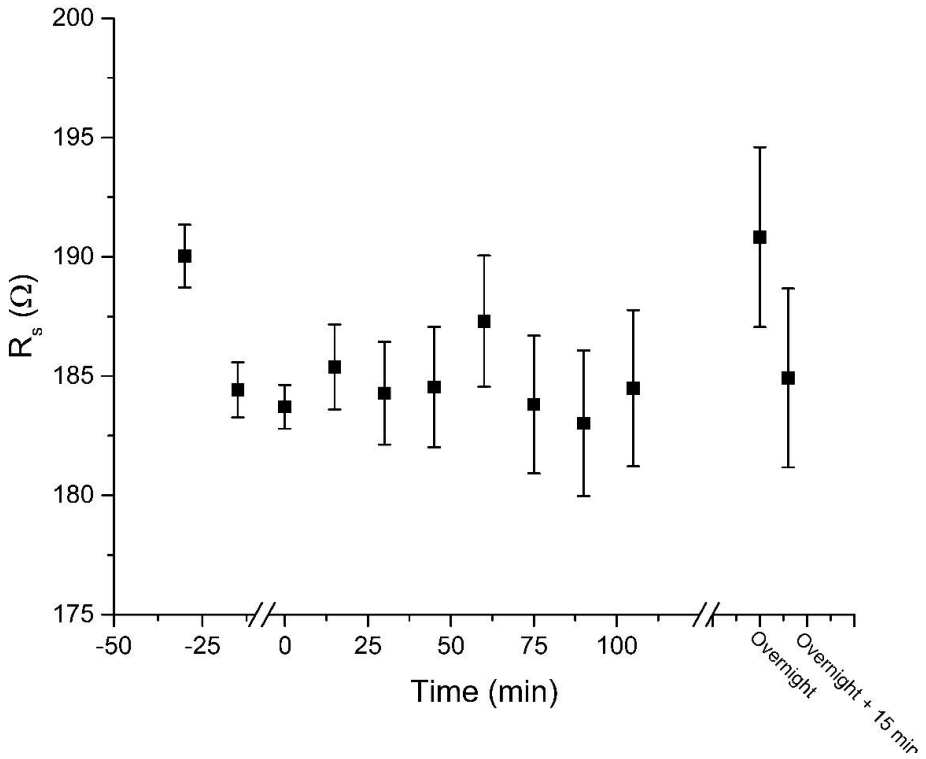

Figure 4.2. Plot of R_s vs. time. All data recorded on a Pt macro electrode in measurement buffer. All time points below 0s were repeat measurements of a clean electrode in the measurement buffer to ascertain the baseline signal.

Since in these experiments the electrode is being taken out of the buffer to have thiol added, the conductivity of the measurement buffer should undergo no significant change. This is confirmed by figure 4.2. (note: where $t < 0$ a clean electrode was measured repeatedly in the measurement buffer to obtain a baseline signal for the system). The values of R_s remain constant throughout the experiment never deviating significantly from 180-195 Ω (3.6-3.9 $\Omega.cm^2$), to one standard deviation. R_s offers no information as to the SAM film but the consistency across these values can at least provide an indication as to the stability of the experimental setup.

4.4.1.2. Macro electrode film formation kinetics, R_{ct}

Typical fitted values of R_{ct} from these experiments are given in figure 4.3.

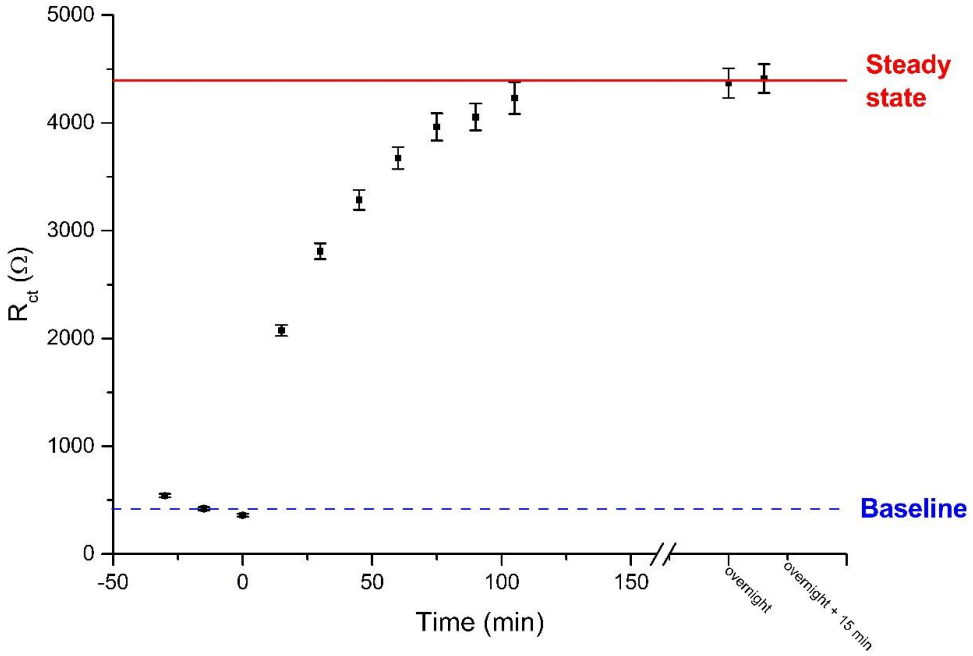

Figure 4.3. R_{ct} vs time from the Pt macro k_{on} experiments. The film was left to saturate overnight in the incubation buffer as shown by the red line two measurements were then taken 15 minutes apart to confirm that the film had reached a steady state. The error bars are from the error in the fit to one standard deviation.

The formation of the MCH film on the surface increases R_{ct} as the uncoated electrode surface decreases. In figure 4.3 the fitted values of R_{ct} increase and asymptotically approach the steady state which is reached after about two hours, during which the values of R_{ct} increased from 500 Ω (10 Ω.cm^2) to 4500 Ω (90 Ω.cm^2) from baseline to equilibrium. This nine-fold increase in R_{ct} is the biggest change in any of the fitted parameters, making R_{ct} the most sensitive candidate for studying film formation and potentially biosensing.

4.4.1.3. Macro electrode film formation kinetics, C_{dl}

Typical fitted values of C_{dl} from these experiments are given in figure 4.4.

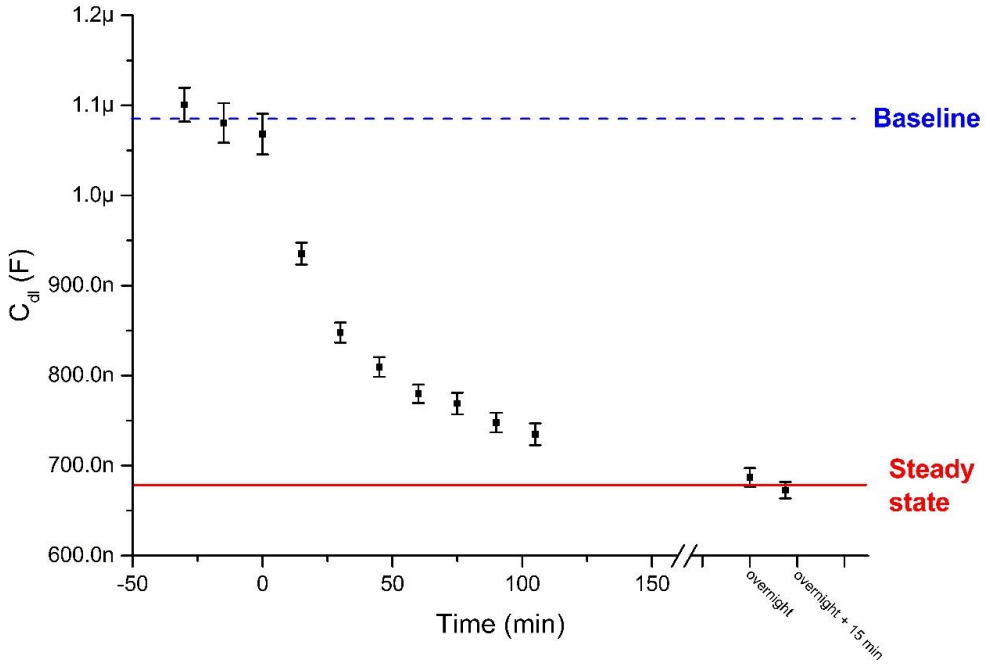

Figure 4.4. Plot of C_{dl} vs time from the K_{on} experiments on a Pt macro electrode. The electrode was left to saturate in the incubation buffer overnight at the saturation point shown by the red line. After this saturation, there were two measurements taken 15 minutes apart.

Figure 4.4 shows the film takes just under two hours to reach a steady state, with the values dropping by 36% from the baseline, 1.1 µF (0.55 F/m^2) to 0.7 µF (0.35 F/m^2). C_{dl} decreases from the baseline asymptotically approaching the steady state over the two-hour period. There appears to be a smooth change in all the fitted parameters, on the same timescale as was observed for R_{ct}. This decrease in C_{dl} can be explained by the decrease in uncoated electrode surface area as a film forms as well as a reduction in the dielectric permittivity at the electrode surface as the water is replaced by MCH.

4.4.1.4. Macro electrode film formation kinetics, W

The characteristic Warburg admittance, Y_0, of the electrodes decreases as a film forms, as would be expected for an electrode as the uncoated surface area decreases, reaching a constant value as the steady state is reached, figure 4.5.

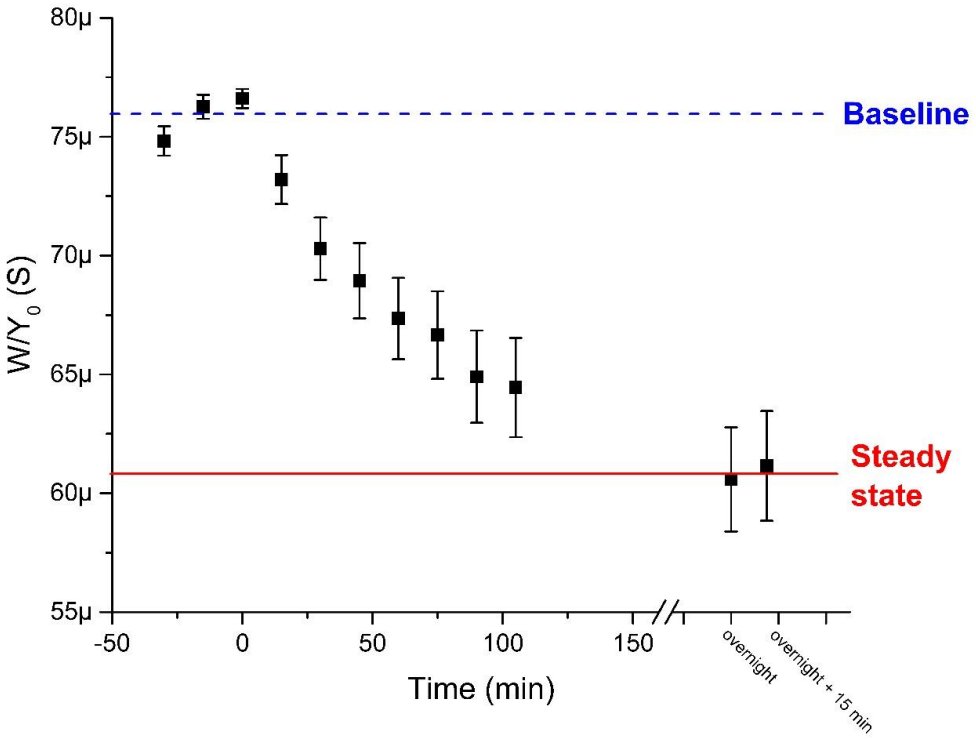

Figure 4.5. Y_0 vs time from the Pt macro k_{on} experiments. The error bars are from the error in the fit to one standard deviation. The electrode was left overnight to saturate in the incubation buffer as indicated by the red line, repeat measurements were taken 15 minutes apart to check the signal consistency of the saturated film.

The fitted value of Y_0 decrease from 76 µS to 61 µS when going from a baseline to a thermodynamic equilibrium. This equates to a 20% decrease from the baseline to the steady state value. The admittance follows the same trend as R_{ct} and C_{dl} of asymptotically approaching the steady state over a period of around 2 hours. There are two competing processes that could be decreasing Y_0; either as the film forms the electrode area is decreasing and pinholes in the film still allow diffusion to a smaller active electrode surface area, or the film inhibits the flow of redox agent to the electrode, thereby decreasing the diffusion coefficient and lowering Y_o. It is not known which of these processes is dominating but this warrants further investigation.

4.4.1.5. Summary of macro electrode MCH film formation kinetics

The data shows that all fitted elements except for R_s asymptotically approach a steady state from the baseline signal over a period of about two hours. The model of SAM formation put forward in this thesis is based on conlcusions drawn from this and the MNEE array data in 4.4.2. It is thought that there is rapid stochastic binding of SAM that then re-arranges to a steady state conformation (postulated to be the ϕ-phase over the bulk of the electrode and ε-phase at the edges) over time, which from the data in this section takes approximately 2

hours. Since there are multiple phases that the SAM could theoretically be in before re-arranging to the steady state it is not known what kinetic function should be fit to the data in this section.

4.4.2. MNEE array SAM formation kinetics

Initially experiments were conducted under the same experimental conditions as employed with the macro electrode. However, it was found that to measure the kinetics of film formation on MNEEs the concentration of MCH in the incubation buffer needed to be diluted 1 000 fold from 30 µM to 30 nM as the rate of film formation was too rapid to be measured on a practical timescale at the higher concentration. This already demonstrates a nanoelectrode kinetic enhancement.

These experiments were not all conducted on nanoelectrodes from the final fabricated batch, AP1508, and before the development of a proper electrode cleaning protocol. Earlier batches typically gave different electrochemical performances as discussed in chapter 2.3. Despite these discrepancies the data can still be qualitatively analysed as what is being analysed here is a relative change in fitted elements as a film forms. The data is still consistent with the response of nanoelectrodes but the fitted values are not quantitatively comparable with other chapters in this thesis. Repeats with batch AP1508 were not possible due to time constraints but should form the basis of future work. The goodness of the fits of the equivalent circuits to the data obtained on these electrodes is evidenced by the error bars in the figures throughout this chapter.

The experiments were conducted with two different ionic strengths of measurement buffer; both 10 mM KCl and 100 mM KCl measurement buffers were used. The lower ionic strength buffer was used first as it was the same as used in the macro electrode experiments. Typical data are shown in figure 4.6.

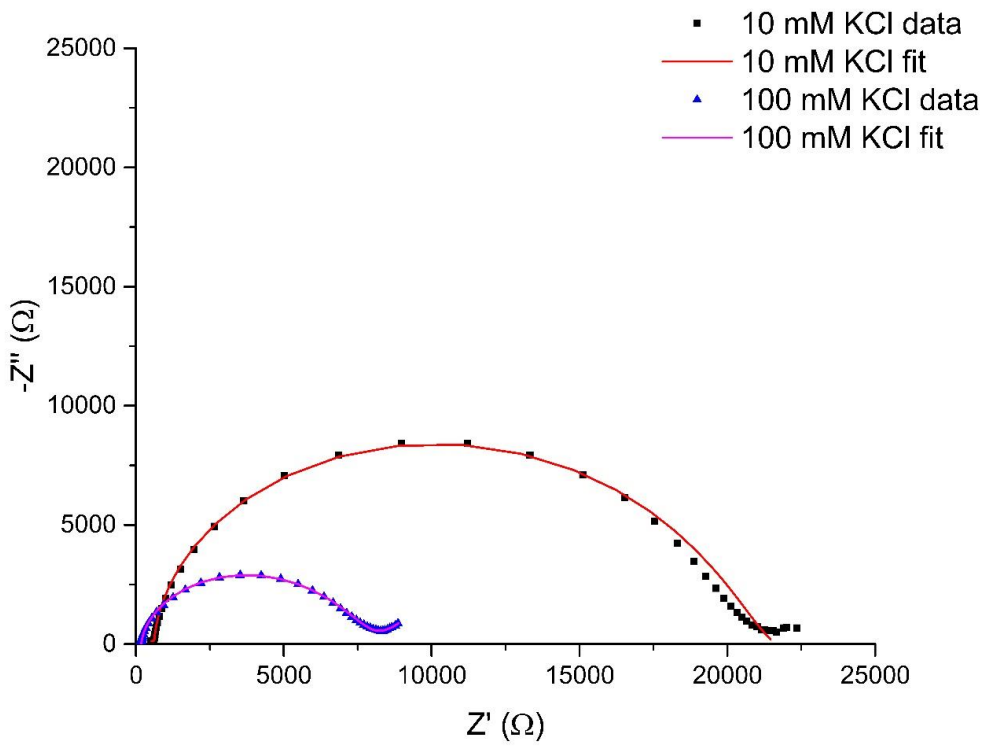

Figure 4.6. Nyquist plot showing a clean 30 µm 3D MNEE array in measurement buffer with 100 mM background KCl, blue triangles, which can be fit to the modified Randles' circuit for MNEE arrays (equivalent circuit APP 1.3, fit given as pink line). The same electrode was then analysed in diluted measurement buffer (10 mM KCl) the response (black squares) becomes apparently close to and dominated by a single near semi-circular feature (equivalent circuit APP 1.1, fit shown as red line).

At these ionic strengths, the characteristic MNEE response was not retained and fits to the modified Randles' circuit for a MNEE array, equivalent circuit APP 1.3, produced large errors. An in depth discussion of the responses of micro and nano electrodes in different ionic strength buffers is given in chapter 5.3.1., where they were investigated in more detail experimentally. It is suffice to say that the second apparent semi-circle could not be resolved and studied in 10 mM KCl, however, changing the salinity of the measurement buffer to 100 mM did allow the investigation of the lower frequency fitted elements. Although this change to the buffer may have also affected the SAM film through changing the dielectric permittivity of the solution and solvation of the MCH film.

The 10 mM KCl data were fit to a single semi-circle, equivalent circuit APP 1.1. This circuit consists of a resistor to model R_s, a constant phase element to model the combination of C_{dl} and Y_0; and R_x to model the combination of R_{ct} and R_{nl}. In chapter 5, where experiments are performed using probe SAMs on MNEE arrays from batch AP1508, it is shown that the majority of change in the EIS comes from a change in R_{ct}; therefore, it is assumed that the majority of R_x changing during these experiments comes from a change in R_{ct} rather than R_{nl}. Analysis of the MCH film formation in both sets of measurement buffers is important to allow direct comparison with the macro electrode kinetics (in 10 mM KCl) as well as analysing film through the changes to different equivalent circuit elements (in 100 mM KCl).

4.4.2.1. MNEE array film formation kinetics, R_x

Figure 4.7 shows the variation of the extracted values of R_x vs. time.

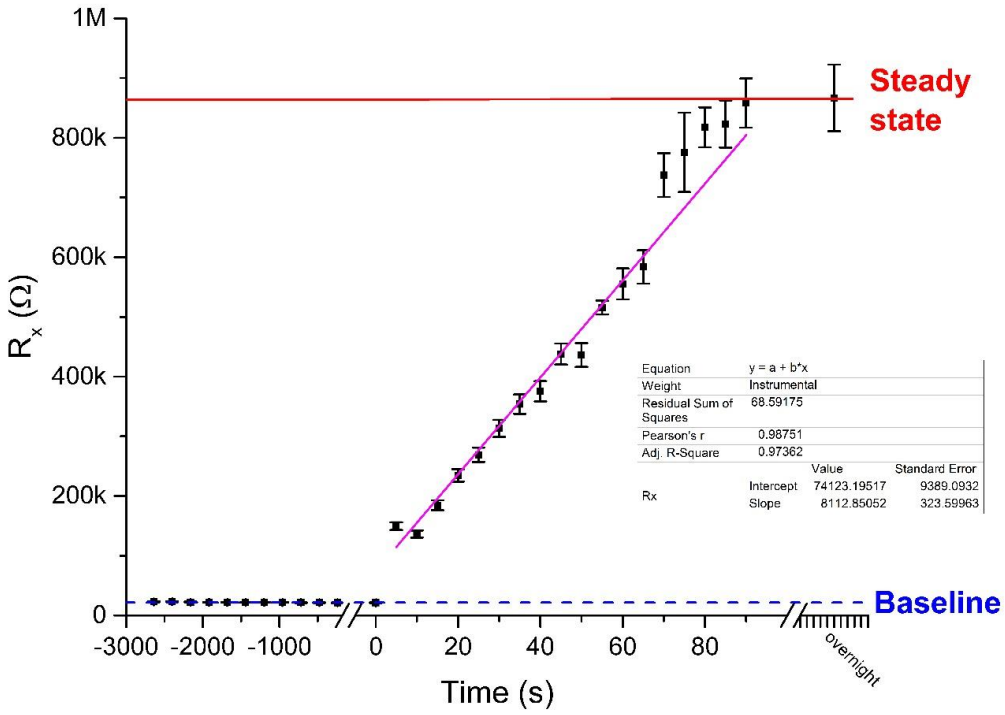

Figure 4.7. Plot of R_x vs. time including a baseline obtained by taking repeat measurements of a 30 µm 3D MNEE array in 10 mM measurement buffer as shown in all the time points below 0s. The kinetic experiments were performed as described in the experimental section until a steady state was reached as indicated by the red line. All errors given are the errors in the fits given to one standard deviation. The magenta line is a linear fit through all the non-zero time-points measured, excluding the overnight steady state R_x value.

The value of R_x was seen to increase linearly with time. The linear rate of change indicates a zero order rate dependency, the rate of formation is independent of the amount of film formed. This could be the result of reduced steric stress in the film by the reduced bulk to edge electrode ratio meaning that a much greater proportion of the film is in the ε-phase on nano electrode films than macro electrode films, therefore allowing a rapid SAM rearrangement on the nanoelectrodes.

An immediate rush of MCH to the electrode surface that then re-arranges to a more resistive film conformation over time would theoretically produce zero order film formation kinetics. This re-arrangement occurs at a constant rate over 100 s and would require the electrode to be completely covered with MCH in a time less than the first measured increment (5s). This theory is supported by the fact that the linear fit shown in figure 4.7 does not cross through the origin.

The steady state is reached in a matter of minutes, as opposed to hours on the macro electrode, despite diluting the concentration of MCH in the incubation buffer by a factor of 1 000, which may be important in filling any pinholes created during SAM rearrangement. However, the theory could still be applicable to both systems, the film re-arrangement to a

more resistive conformation would theoretically take longer on a macro electrode than a nano electrode due to the larger bulk to edge ratio and an increased surface roughness due to cleaning macro electrodes by polishing in alumina slurry. As mentioned above the steric strain will theoretically be greater in macro electrode SAMs as a result of them having a higher bulk to edge ratio, this could conceptually increase the rate of thiol desorption on macro electrodes meaning that they would follow first order rate kinetics, as observed in section 4.4.1.

4.4.2.2. MNEE array film formation kinetics, W/Y_0

The fitted values of Y_0, given in figure 4.8, show that there is an instantaneous decrease from the baseline to the steady state.

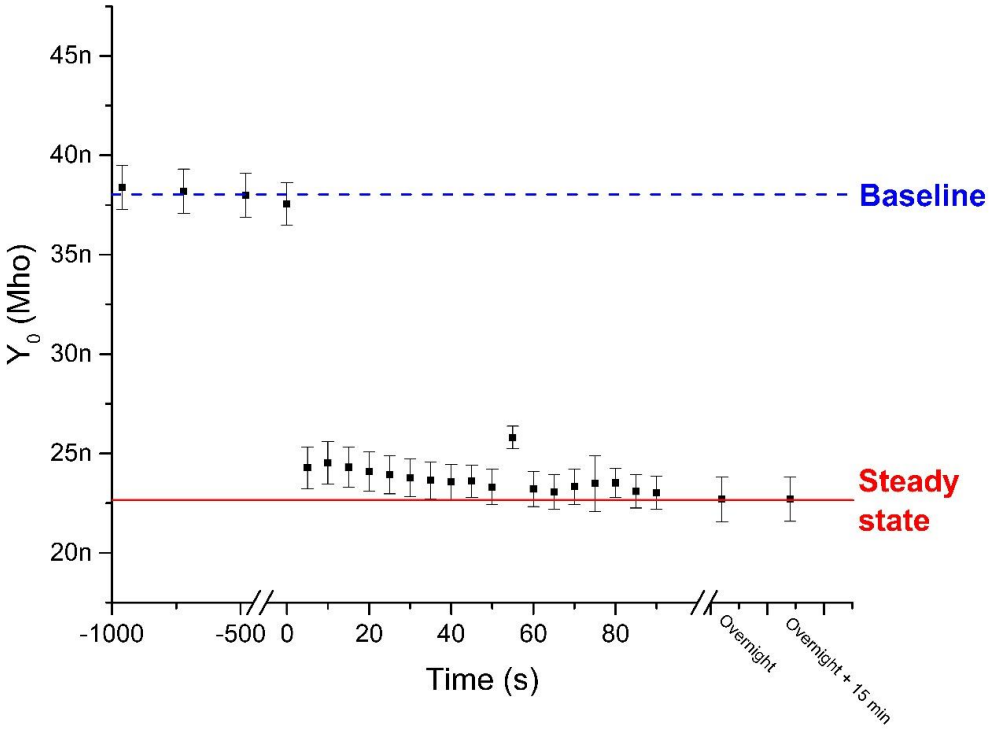

Figure 4.8. Relationship between Y_0 and time including a baseline obtained by taking repeat measurements of a 30 µm 3D MNEE array in 10 mM measurement buffer as shown in all the time points below 0s. The kinetic experiments were performed as described in the experimental section until a steady state was reached as indicated by the red line. All errors given are the errors in the fits given to one standard deviation.

This is in agreement with the model of rapid stochastic film formation that re-arranges to a more resistive conformation. The film re-arrangement is not as noticeable in Y_0 as it was in R_x. The presence of all phases over the entire electrode will still change the dielectric permittivity (ε_r), subsequent re-arrangement must have a minimal effect on the magnitude of ε_r.

4.4.2.3. MNEE array film formation kinetics, R_s

The fitted values of R_s are constant over the course of the experiment, figure 4.9, as would be expected, as it was observed in the macro electrode experiment, section 4.4.1.1.

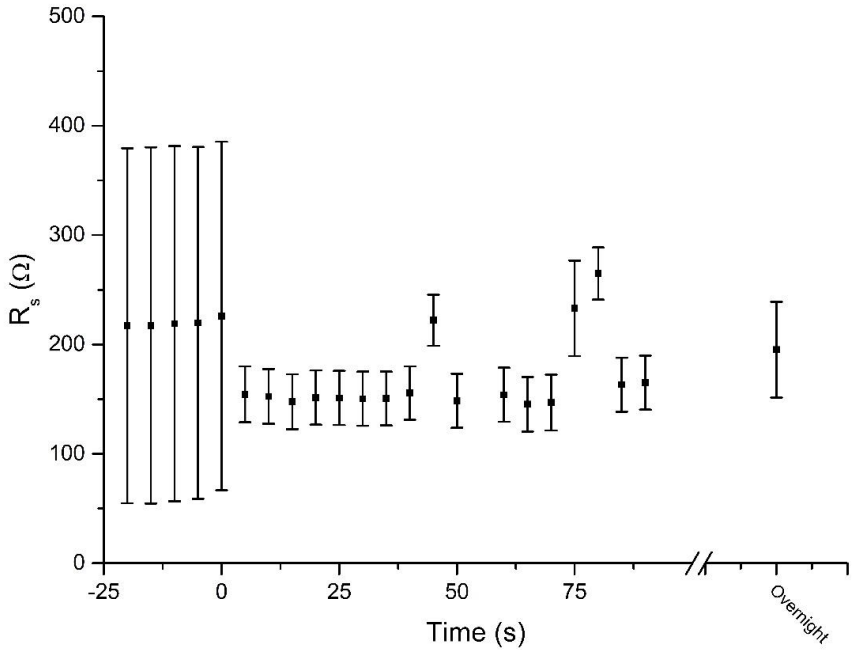

Figure 4.9. Plot of R_s vs. time including a baseline obtained by taking repeat measurements of a 30 µm 3D MNEE array in 10 mM measurement buffer as shown in all the time points below 0s. The kinetic experiments were performed as described in the experimental section. All errors in the fits are given to one standard deviation.

It is interesting to note that the error in the fit markedly decreases when a film has formed. This may be as a result of changing values of R_x and Y_0 meaning that a better fit of R_s is obtained. As there was no significant change in fitted error this was not investigated in more detail.

4.4.3. MNEE in 100 mM KCl

4.4.3.1. MNEE array SAM formation kinetics, R_s

Figure 4.10 shows the value of R_s stays constant during the film formation experiments on the MNEE arrays in 100 mM KCl, just as it did in 10 mM KCl, figure 4.9, and for the macro electrode, figure 4.2.

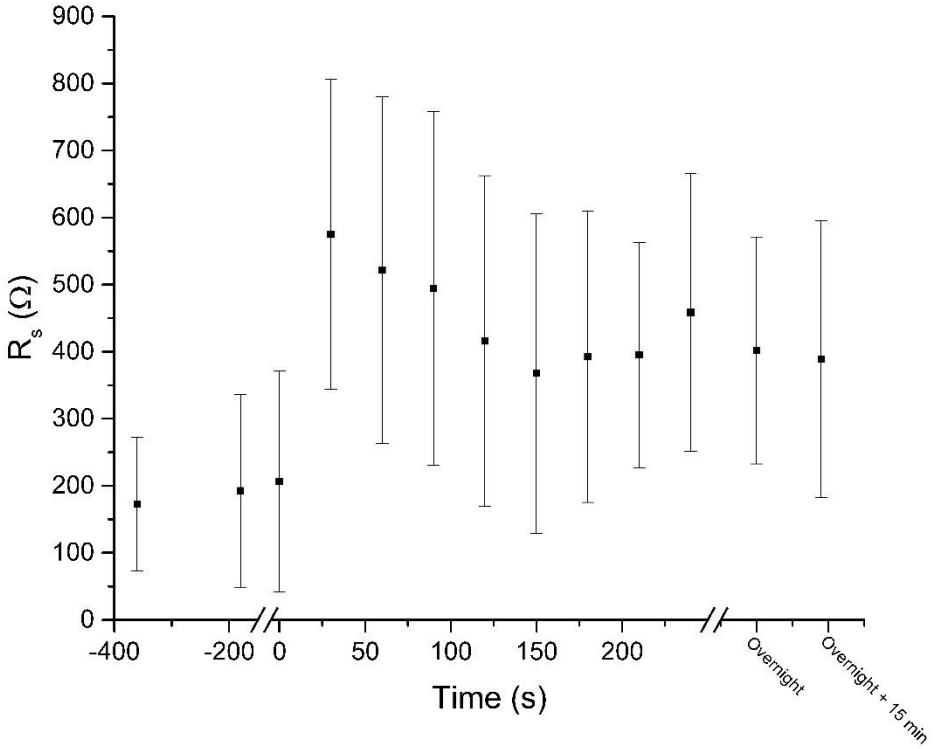

Figure 4.10. The values of R_s during the MNEE SAM formation experiments. All time points below and including 0s are from a clean 30 µm 3D MNEE array in 100 mM KCl buffer to establish a baseline. The error bars are from the error in the fit to one standard deviation.

It is satisfying that the fitted values of R_s are the same for the macro and nano electrodes as the solution resistance does not scale with electrode area. R_s offers no information as to the film structure or stability and has only been included to give confidence in the fits. It is interesting that at in these higher ionic strength buffers there are larger errors in the fits, since this is also observed in the baseline readings it is probably a function of the improper electrode fabrication discussed in chapter 2.

4.4.3.2. MNEE array SAM formation kinetics, R_{ct}

The fitted values of R_{ct} for MCH SAM formation on an MNEE array measured in 100 mM KCl are given in figure 4.11.

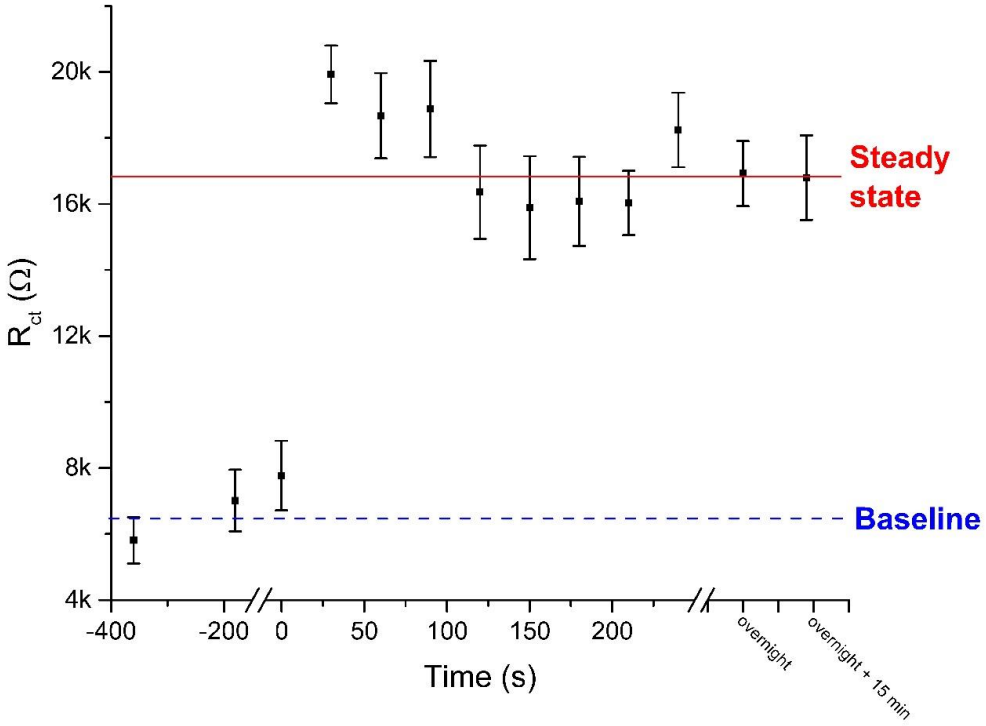

Figure 4.11. R_{ct} as a function time showing the baseline signal for a clean MNEE 30µm 3D MNEE array in measurement buffer at time-points below 0s. The electrode was left in the incubation buffer for 30 s intervals with EIS recorded in the measurement buffer after each incubation. The electrode was left in the incubation buffer overnight to reach a steady state as indicated by the solid red line. All errors given are the errors in the fits of the data to one standard deviation.

Figure 4.11 shows that the film forms in a steady state conformation rapidly on the MNEE with the R_{ct} values rising from baseline to steady state after the first incubation. Even with further incubations the resistance remains constant within three standard deviations, implying that the steady state was reached almost immediately. This is different to the data obtained in the 10 mM KCl buffer, meaning that the subsequent re-arrangement is not observed in 100 mM KCl. Since the SAMs were formed in the same incubation buffer and only the measurement buffers were changed, there can only be two explanations for this finding. Either the SAM that formed in the incubation buffer does not need to re-arrange in the 100 mM KCl buffer as it is already in the most stable state, which would mean that the thermodynamic steady state conformation of a SAM layer is dependent on the buffer in which it is placed. Or the more likely situation which is that the rate of SAM re-arrangement is increased in higher ionic strength buffers, to the extent where it is too rapid to be detected over the timescales investigated in these experiments.

One possible explanation for this trend that has not been examined up till now is the trapping of solvent in the SAM layer. As stated in section 4.3.3, the MCH is put down in 50% DMSO in water. It is highly likely that there will be DMSO trapped within the SAM layer, the release of

which will be dependent on the partition coefficient of DMSO from the MCH film into the measurement buffer. This partition coefficient will naturally change with changing ion concentration in the measurement buffer, which could drive the rate of re-arrangement. Given the hydrophobic nature of the SAM layer it is unlikely that much hydration of the layer will occur, but the rate of this process could also be driving the re-arrangement rate.

4.4.3.3. MNEE array film formation kinetics, R_{nl}

The values of R_{nl} mirror the sharp increase in resistance after the first exposure to MCH seen in R_{ct}, figure 12.

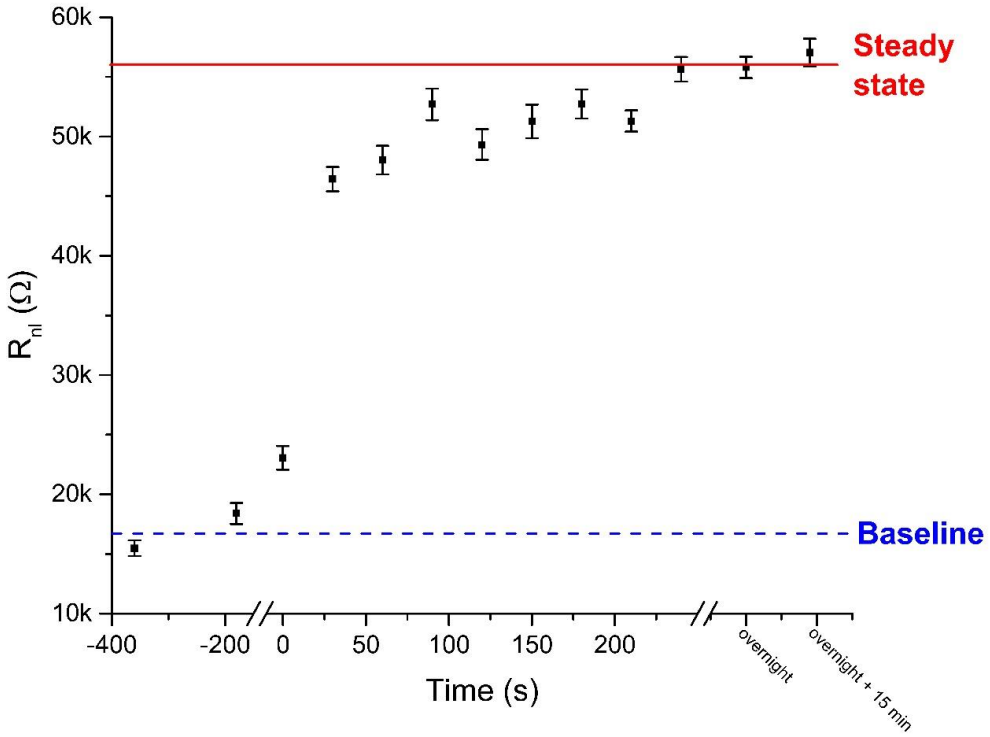

Figure 4.12. Plot od R_{nl} vs. time showing the baseline signal for a clean MNEE 30µm 3D MNEE array in measurement buffer at time-points below 0s. The electrode was left in the incubation buffer for 30 s intervals with EIS recorded in the measurement buffer after each incubation. The electrode was left in the incubation buffer overnight to reach a steady state as indicated by the solid red line. All errors given are the errors in the fits of the data to one standard deviation.

In both R_{ct} and R_{nl} there is a nearly three-fold increase from the baseline to the steady state resistance. This rapid increase in impedance would suggest the rapid formation of a film. No linear fit has been plotted on this data as the trend in Rnl over the course of these incubations does not appear to deviate significantly from the baseline trend. Since it is fit to the low frequency end of the EIS spectrum R_{nl} is naturally more prone to noise caused by random fluctuations in the system that could not be controlled (e.g. convection currents in the measurement buffer); as such steady baseline signals could not be accurately obtained.

4.4.3.4. MNEE array SAM formation kinetics, C_{dl}

The fitted values of C_{dl} increase instantly when the MCH film forms, figure 4.13. They then decrease linearly before levelling out at the steady state which is the same within error as the baseline signal.

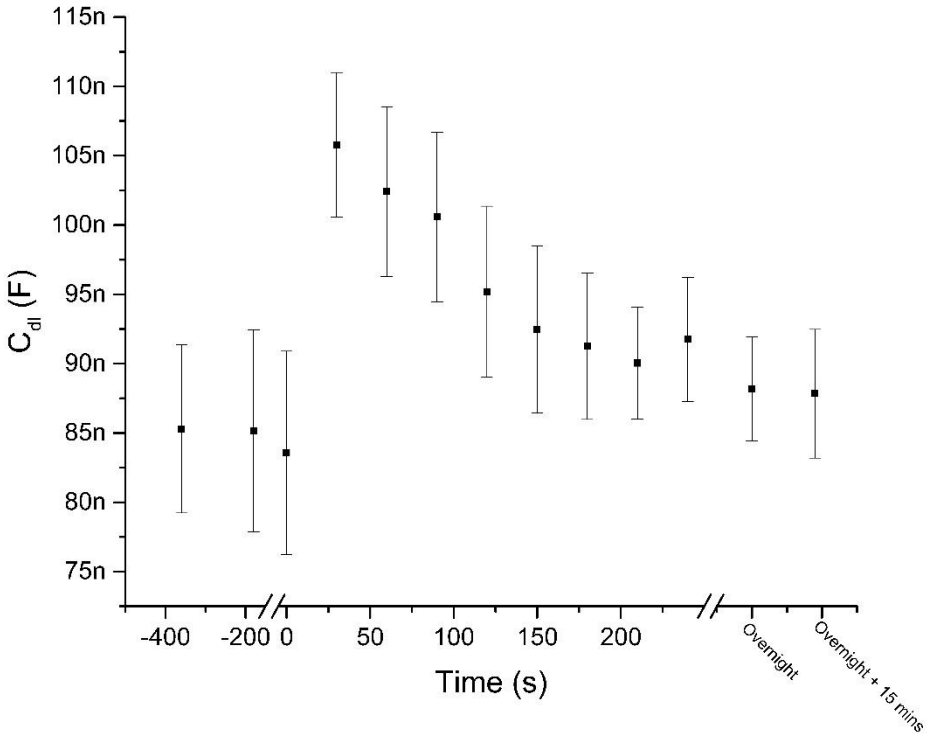

Figure 4.13. Plot of C_{dl} vs. time during the k_{on} experiment for a 30 µm 3D Pt MNEE array. The negative time points are where the clean electrode had measurements taken repeatedly in the measurement buffer to obtain a baseline. The error bars are representative of the errors in the fit of C_{dl} to one standard deviation.

In the macro electrode and MNEE array in 10 mM KCl experiments, the capacitance was seen to decrease significantly, by 38% and 36% respectively when taken from baseline to steady state. Over the course of this experiment, using an MNEE array in 100 mM KCl, there is no significant change from baseline to steady state to more than one standard deviation of the error in the fit. Although to one standard deviation the data hints that some re-arrangement might be taking place. These variations may be due to stray capacitances within the system.

4.4.3.5. MNEE array SAM formation kinetics, W

A plot of the change in admittance, Y_0, during the experiment is given in figure 4.14.

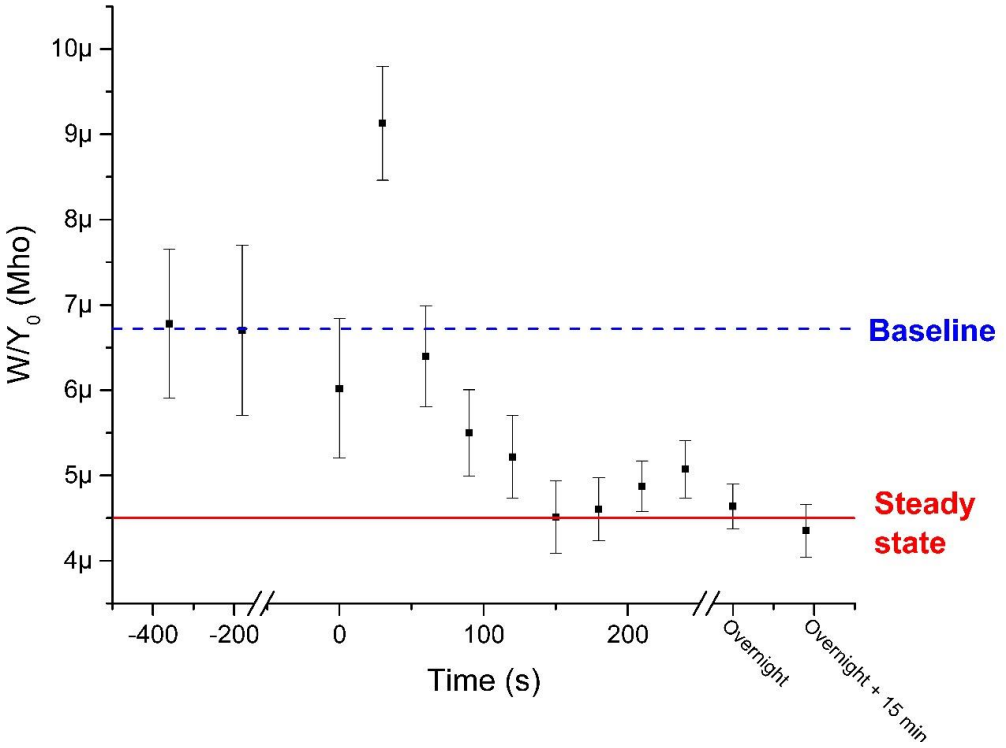

Figure 4.14. Plot of Y_0 vs. time during the k_{on} experiment for a 30 µm 3D Pt MNEE array. The negative time points are where the clean electrode had measurements taken repeatedly in the measurement buffer to obtain a baseline. At the 0s time point the electrode was placed in the incubation buffer for 5 second intervals and the impedance of the film formed measured in the measurement buffer. After a total of 250 seconds of film formation the electrode was left in the incubation buffer for overnight to saturate. The error bars are representative of the errors in the fit to one standard deviation.

The fits for the Warburg element were constant to within two standard deviations of the error in the fit. Mirroring the response seen in C_{dl}; again, hinting that there is some re-arrangement but not proving so comprehensively.

4.4.4. Discussion of SAM formation kinetics on macro and nano electrodes

The percentage change in each fitted element on macro and nanoelectrodes is given in table 4.3.

Table 4.2. The percentage change in each of the fitted elements from baseline to steady state from the k_{on} experiments on both macro electrodes and 30 µM 3D MNEE arrays.

	Baseline → Steady state (Δ%)	
	Macro (10 mM KCl)	Nano (100 mM KCl)
R_s	0	0
C_{dl}	-36	-38
R_{ct}	+800	+150
W	-22	-33
R_{nl}	-	+205
R_x (MNEE in 10 mM KCl)	-	+2900

Comparing the data for the macro and nano electrodes; it is encouraging that the relative change in C_{dl} is roughly the same on both electrode types. The decrease of about a third of the signal is expected as the literature dictates that for a ϕ-phase SAM, one third of all the available binding sites on the electrode surface will be occupied.[40, 44] Depending on the experimental conditions the capacitance double layer may extend beyond and above the monolayer, but will definitely be able to form on the unoccupied sites between neighbouring alkanethiols, as shown in figure 4.15. Thus, the decrease of a third of the signal implies that a ϕ-phase film was obtained in the steady state. There may be patches of alkanethiol in other phases, which will have a capacitance double layer formed above them as all other phases have the alkane chains in a "lying down" conformation, this and the ε-phase MCH on the edge of the electrode accounts for the signal decrease being slightly more than 33%.

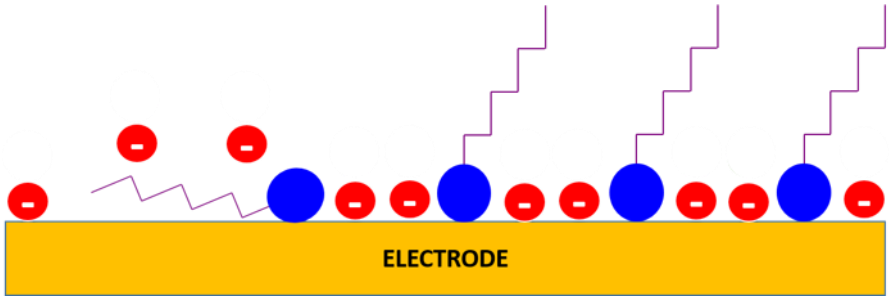

Figure 4.15. Schematic cartoon (not to scale) showing the capacitance double layer forming between neighbouring alkanethiols in the MCH film and a relatively smaller double layer forming above a molecule in a "lying down" orientation. The red circles represent the anions and the blue circle is the sulfur head group of the MCH in one of its bound states.

The value of R_{nl} doubles, consistent with the diffusion coefficient, D, halving when a layer is formed; caused by the increased impedance of having to diffuse through the film, see equation 1.22. This change in D is further evidenced by the decrease in Y_0 of roughly 30%, which would be expected by halving D in equation 6.4.

Again, the working theory is that the film rushes onto the electrode in a variety of phases, the film must then rearrange to the thermodynamic steady state. This process is faster on nanoelectrodes because they are better able to cope with stress within the film. As the different phases re-arrange to the most thermodynamically stable ϕ-phase the sulfur head groups migrate closer to each other, in the ϕ-phase the sulfur head groups are more closely packed than any of the preceding phases. This densification of the film causes the impedance to increase. In order for more thiol to bind to the surface it must approach pinholes in the monolayer or alkanethiols in the ε-phase where binding sites are available. The increased ratio of ε-phase MCH on the MNEE, because of the increased edge to bulk ratio, means that theoretically this densification process would be faster on the MNEE. An incoming thiol can bind at the edge of the electrode and the bulk bound molecules can "re-shuffle" to a more stable conformation by translocating on the electrode surface. On a macro electrode this "re-shuffling" process will take longer as there is more bulk. A cartoon depicting this process is given in figure 4.16. The MCH would theoretically bind preferentially to the ε-phase because it provides less steric hindrance to an incoming molecule. Pinholes are perhaps better described as unoccupied binding sites as they can encompass those sites blocked by "lying down" alkanethiols.

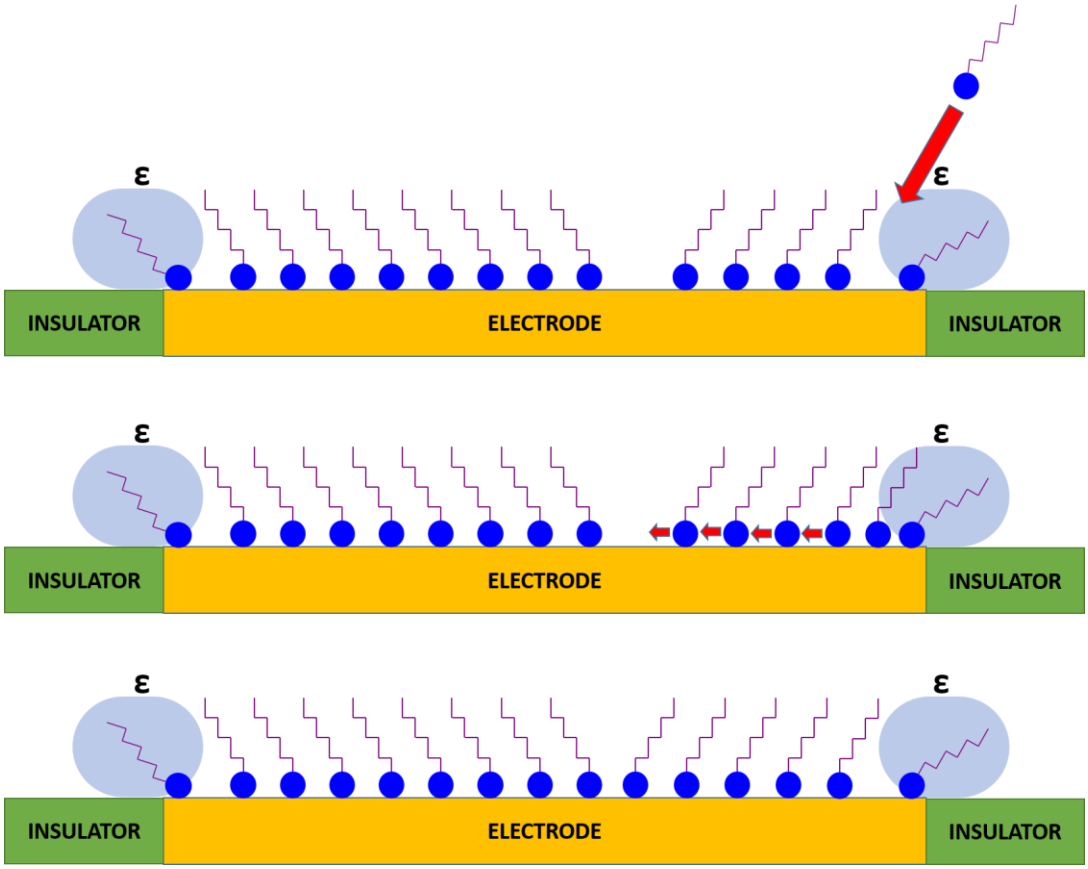

Figure 4.16. Proposed mechanism of film densification where an incoming MCH molecule can bind at the ε-phase SAM on the edge of the electrode causing the electrode bound thiols to translocate and fill pinholes in the bulk of the film.

It is interesting to note that the ionic strength of the measurement buffer appears to be altering the SAM rearrangement kinetics. The incubation buffer was kept constant, it was only the ionic strength of the measurement buffer that was changed. Clearly the act of transferring the film to a measurement buffer is affecting the film, and that the different ionic strength buffers affect the film to different extents. The proposed explanation for this is that the increased concentration of ions in solution are competing for solvation by the water molecules which increases the amount of aggregation within the SAM film, as there are fewer free water molecules to solvate the hydrophobic SAM film, thereby affecting the rate of re-arrangement.

If there is an increased risk of aggregate formation in higher ionic strength buffers there is also the increased risk of MCH multilayer formation. MCH is a surfactant capable of forming micelles on the electrode surface as shown in figure 4.17. The critical micelle concentration (CMC) is a measure of the concentration of a surfactant at which it begins to form micelles in solution, knowing the CMC for MCH in 10 mM and 100 mM KCl would determine whether or not aggregates are capable of existing in these conditions. Unfortunately, these values could not be found in the literature and due to time constraints could not be determined experimentally.

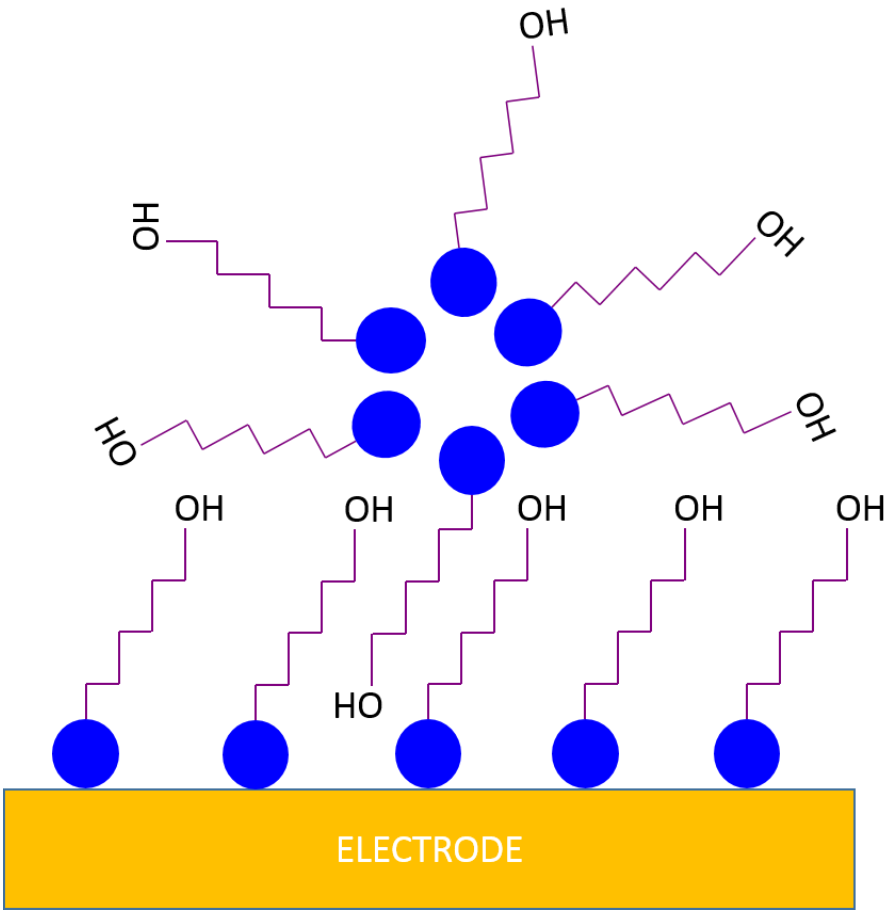

Figure 4.17. Schematic showing the possible structure of a micelle on an electrode. With a hydrophilic alkane chain intercalating with an ϕ-phase SAM. Other aggregate structures are possible; this is merely given as one example. The blue circles represent the polar sulfur head group in one of its three possible stable states.

4.4.5. SAM desorption kinetics

After the SAM had formed it was left in the measurement buffer so as to determine the stability of the SAM for extended periods of time. As described in section 4.3.4, these data were collected by leaving the electrode with a formed SAM layer in measurement buffer and taking repeated EIS measurements over a 3 day period.

4.4.5.1. Macro electrode MCH desorption kinetics, R_s

When measuring the rate of thiol desorption, the values of R_s were similar to the first hald of this chapter, in that the value drops gradually, figure 4.18, from 184 Ω (3.7 Ω.cm^2) to 171 Ω (3.4 Ω.cm^2).

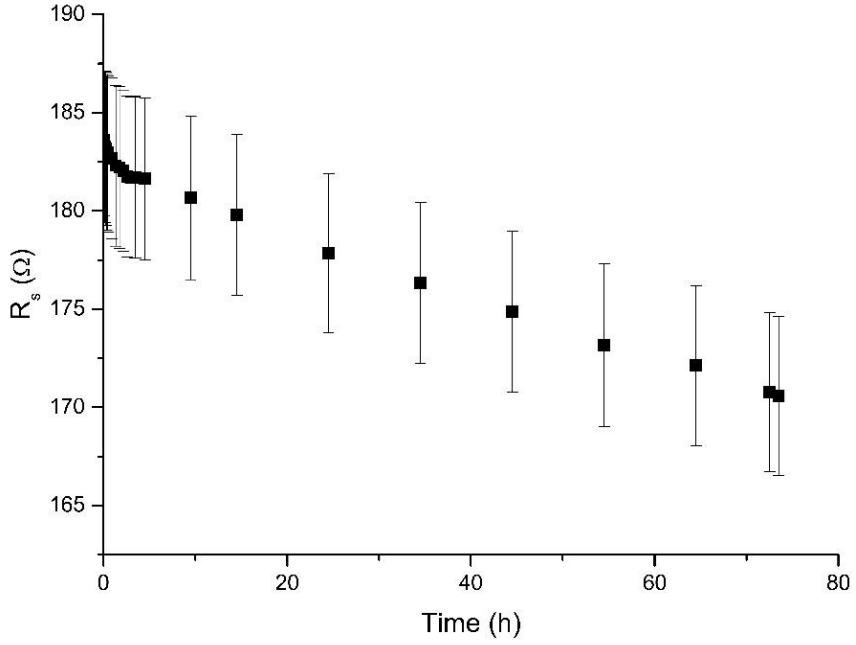

Figure 4.18. Plot of R_s vs. time in measurement buffer once a saturated MCH film has been made on a Pt macro disk electrode.

This decrease is small enough to be attributed to the changes in the buffer over long periods of time, such as evaporation of the water increasing the effective concentration of FFC. As stated before R_s offers no information on the film and has only been included for completeness and to inspire confidence in the experimental set up.

4.4.5.2. Macro electrode MCH desorption kinetics, R_{ct}

The measured R_{ct} values are highly variable.

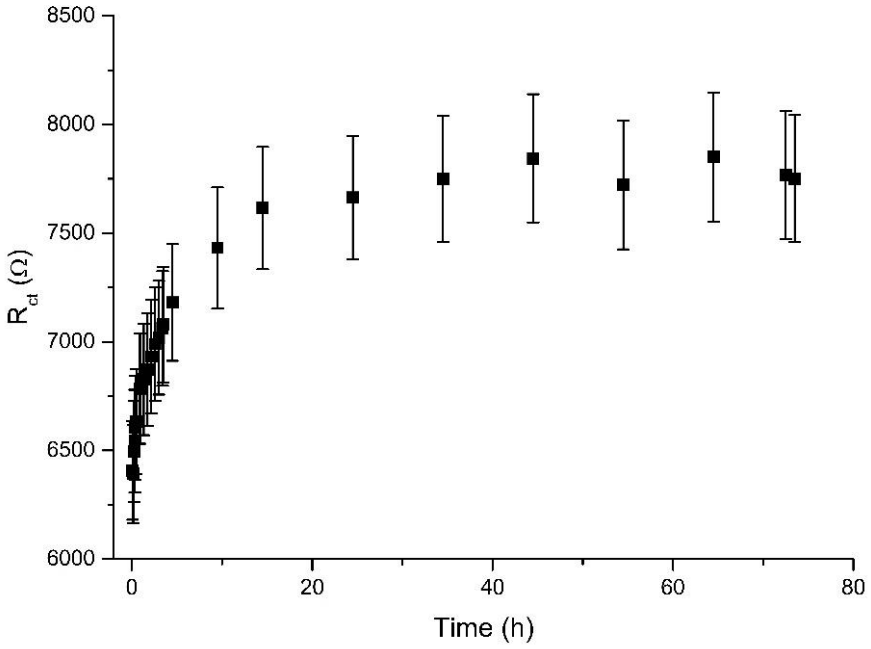

Figure 4.19. R_{ct} vs time from the Pt macro k_{off} experiments. The error bars are from the error in the fit to one standard deviation.

Since the trend is not observed in the fitted values of R_s, figure 4.18, the change cannot be due to experimental flaws, including but not limited to a loss of temperature control or oxygenation of the buffer, so must be a real phenomenon.

The data is indicative that there is some, as yet, unexplained transformation within the SAM films in measurement buffer over time. It is interesting to note that the values of R_{ct} never drop below the value of the steady state response. Thus, the SAM does not appear to be coming off the gold surface, as would be expected due to the strength of the Au-S bond.

The practical relevance of these findings is small, as most sensors aim to make readings as quickly as possible thus minimising the change in signal due to the effect observed here.

4.4.5.3. Macro electrode MCH film desorption kinetics, C_{dl}

The fitted values of C_{dl} from the k_{off} experiments have been plotted in figure 4.20.

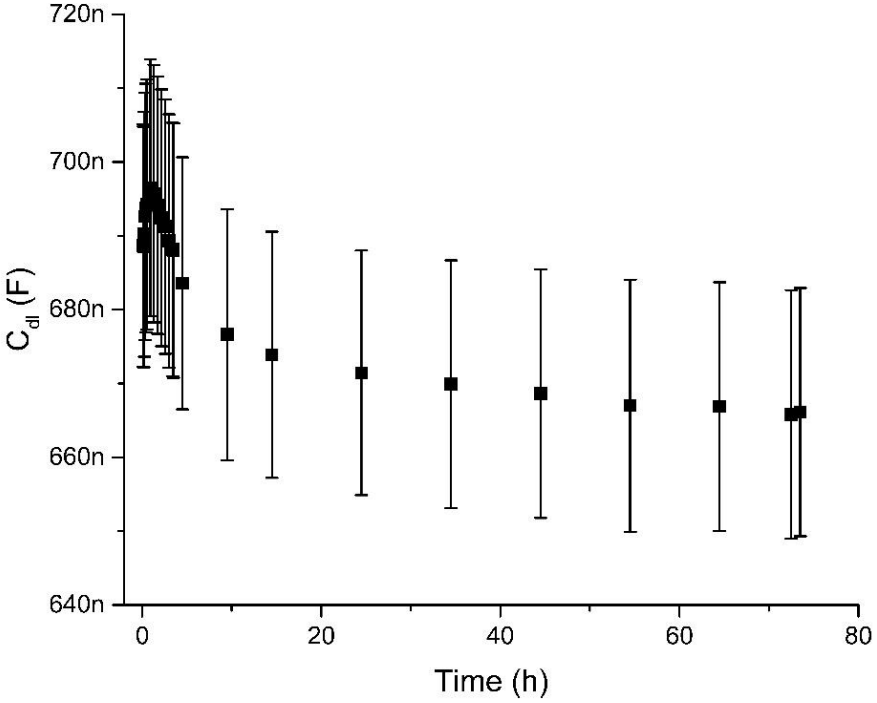

Figure 4.20. Plot of C_{dl} vs time from the k_{off} experiments on a Pt macro electrode. The error bars are from the error in the fit to one standard deviation.

The fitted values of C_{dl} are constant within error over the course of the experiment, consistent with the findings of section 4.4.5.2 which show that there is no SAM desorption over the time course measured.

4.4.5.4. Macro electrode MCH film desorption kinetics, W

Figure 4.21 shows that the admittance of the electrode remains constant within error during the K_{off} experiment.

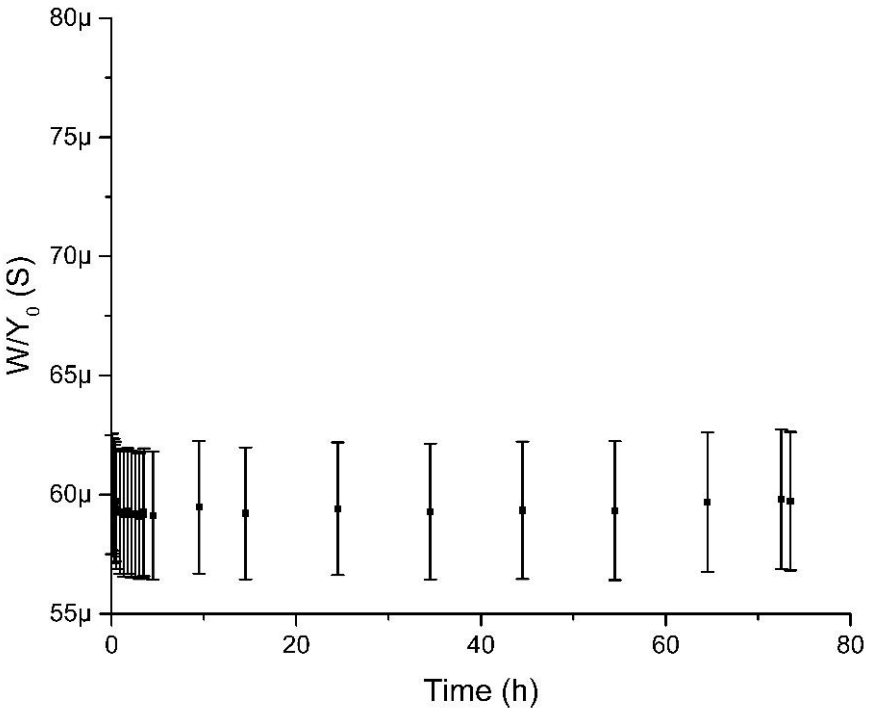

Figure 4.21. Plot of fitted values of W vs time from the Pt macro k_{off} experiments. The error bars are from the error in the fit to one standard deviation. The scale has been chosen to match that given in the k_{on} experiments.

This data is again consistent with the finding that there is no thiol desorption over the course of the experiment.

4.4.6. MNEE MCH film desorption kinetics

As stated in section 4.3.5, the desorption kinetics of an MCH film on the MNEE arrays was done for completeness sake

4.3.6.1. MNEE MCH film desorption kinetics: R_x, R_{ct} and R_{nl}

The fitted values of R_x, R_{ct} and R_{nl} for a MNEE array from 3 separate experiments, to determine MCH film desorption kinetics are given in figure 4.22.

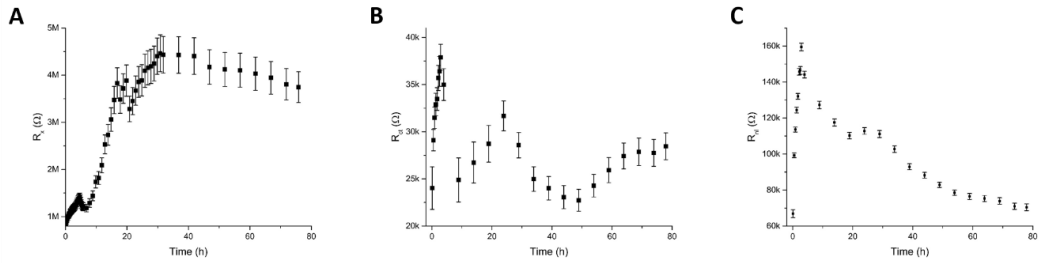

Figure 4.22. Plot of the changing values of (A) R_x (B) R_{ct} and (C) R_{nl} when a saturated MCH film on a Pt 30 µm 3D MNEE array is left in measurement buffer for 72 hours. The error bars are the error in the fits to one standard deviation.

As with the macro electrode data there is an inexplicable change in impedance over the time course investigated. It is again encouraging that the final impedance value does not drop below that measured for a steady state SAM, ruling out any thiol desorption.

4.3.6.2. MNEE MCH film desorption kinetics: R_s, C_{dl} and Y_0

The fitted values of R_s, C_{dl} and Y_0 for a MNEE array from 3 separate experiments, to determine MCH film desorption kinetics are given in figure 4.23.

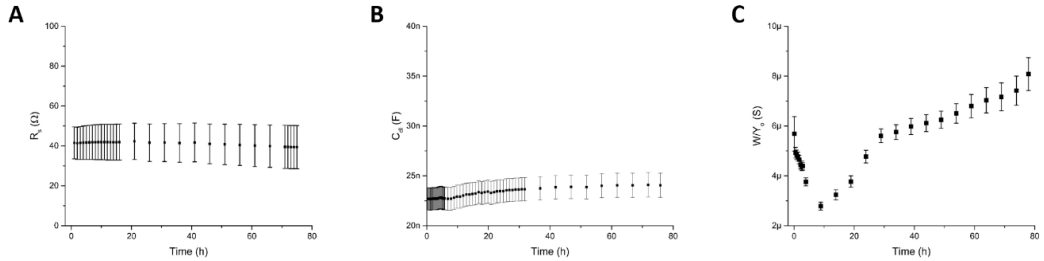

Figure 4.23. Plot of the values of (A) R_s (B) C_{dl} and (C) Y_0 when a saturated MCH film on a Pt 30 µm 3D MNEE array is left in measurement buffer for 72 hours. The error bars are the error in the fits to one standard deviation.

The fitted values of R_s, C_{dl} and Y_0 for a MNEE array are roughly constant just as they were for the macro electrode. This is again indicative of there being no thiol desorption over the time course measured.

4.5. Conclusions and future work

For the first time the differences in SAM formation on macro and nano electrodes has been reported. In both instances there is rapid binding of SAM to the electrodes which then rearranges to a stable conformation. This rearrangement process is much more rapid on nanoelectrodes, occurring over hundreds of seconds, than on macro electrodes where it can take hours.

It was found that the nanoelectrodes reach a thermodynamic equilibrium in a matter of seconds to minutes using 1000 times more dilute MCH than the macro electrode. This is a clear advantage for the use of nanoelectrode sensors as the probe molecules put down in a SAM layer can be prohibitively expensive. EIS has been used to investigate the mechanism of film formation and suggests that the enhanced rate of film formation on the MNEE may be down to the ability of the film to respond to increases in stress. This ability of the film to cope with the rearrangement process is a result of the increased edge to bulk ratio of MNEE compared to macro electrodes.

Analysis of the stability of an MCH monolayer once it has been moved to a measurement buffer showed that there is a period over which the film becomes more resistive. This process occurs on a timescale of hours and is sensitive to changes in the ionic strength of the measurement buffer. There is also a difference in the time of this rearrangement between macro and nano electrodes. Electrochemical analysis of these data may be indicative that aggregates formed in one of either the incubation buffer or measurement buffer is causing the increase in impedance.

Whilst EIS is a very powerful technique, it cannot be used to differentiate between what different SAM phases are present within a film. The differences in the kinetics of different phase formation and stability could not be ascertained using EIS. Having another mechanism to check what phases the film is in and whether or not aggregates have formed should be the subject of future work. This should involve using spectroscopic techniques such as SPR, XPS, ellipsometry, etc. on MNEE fabricated on glass as opposed to silicon wafers, used as shown in figure 4.24. MNEE have already been fabricated on glass wafers by Belaïdi et al[63] so the fabrication has already been optimised and spectroscopic analysis of the electrode is possible through the glass.

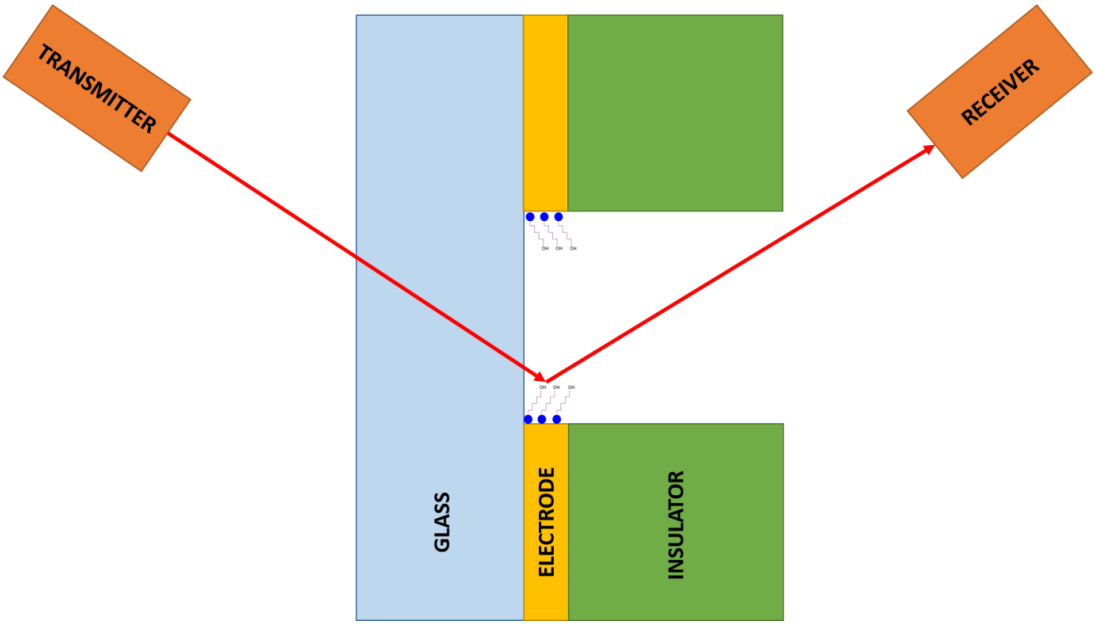

Figure 4.24 Schematic of MNEE fabricated on a glass wafer showing its ability to allow spectroscopic measurements of the electrode surface through the glass. Such electrodes have been fabricated and used for spectroscopy by Belaïdi et al.[63]

5. Specific DNA detection on macro, micro and nano electrodes

5.1. Introduction

In this chapter the biosensing ability of the MNEE arrays will be studied by comparing their probe film and target binding responses to those of macro and micro electrodes. The previously published sensing protocol for the *mecA* cassette of Methicillin Resistant *Staphylococcus aureus* (MRSA)[18] is used as it utilises a protocol established within the group of relevance to MRSA sensing and detection. A 15 base peptide nucleic acid (PNA) probe homologous to the DNA target sequence of interest is immobilised on a Pt macro electrode by using and AEEEA thiolate linker.[18, 92] This is then exposed to a 30 base ssDNA target sequence and an increase in impedance reported.[18, 92] It has previously been reported that an overhang of 15 base pairs from the target DNA gives the optimum increase in impedance upon hybridisation.[92] Shorter overhangs give a lesser increase in the impedance attributed to a smaller barrier to charge transfer at the interface and longer sequences also give a lesser impedance attributed to a decrease in the degree of target binding to the increase in the repulsive interactions and/or re-organisational energy that must be overcome for target hybridisation.[92] The SAM detection protocol had been fully optimised for macro electrodes prior to this study, but its optimisation and characterisation for micro and nano electrodes would be novel.

Furthermore, these findings could inform the optimisation of similar sensing systems for smaller electrodes. As the field of electrochemical biosensors moves towards smaller scale electrodes[11, 33, 97, 98] it would be advantageous to take pre-established sensing protocols, established on macro electrodes, and transfer them to nanoelectrodes to exploit the enhanced sensing capabilities that nanoscale electrodes possess. Thus a fundamental study of the biosensing protocol on macro, micro and nanoelectrodes will inform the field as to what considerations must be made when optimising a macro electrode sensing protocol for smaller scale electrodes. To enable this, a comparison was made between DNA and PNA probe films along with the differences in the electrochemical response of the different probe films formed on macro, micro and nanoelectrodes. It is a purpose of this chapter to investigate the biosensing properties of these different electrodes; this will include differences in the electrochemical signal observed for a probe SAM on an electrode using voltammetry and EIS, and the study of PNA and DNA probe film layers to determine how the presence of probe backbone charge affects the film response. Also the effect of DNA target binding to each of the probe films will be investigated on micro and nano electrodes to determine their limits of detection and probe the physicochemical processes taking place within each film as the target binds.

The literature is full of different observations as to the direction and magnitude of the changes in impedance (and the processes) which occur when target binds to a probe film.[12, 21] First, the impedance has been observed to increase, as the target binds to the probe, explained by hindered access of the negatively charged redox agent to the underlying electrode, due to the film becoming denser and having an increasingly repulsive negative charge density.[33, 77, 79, 90, 91, 99] Conversely, probe films have been shown to be less resistive

with target hybridisation.[100] This phenomenon of a reduction in surface impedance is attributed to densely packed films, with the opening up of channels within a densely packed film on target binding. Charge is also reported to be an important property in determining SAM behaviour, as it is widely accepted that the negatively charged DNA phosphate backbone will repel a negative redox agent such as ferri-/ferro-cyanide (FFC), causing a greater increase in impedance,[79, 90] whilst a film with an opposite charge to the redox agent is used, the target can bring said redox agent to the electrode surface, thereby causing a decrease in impedance.[33, 101] The effects of charge can be studied by performing the experiments in buffers of different ionic strengths.[79] High ionic strength buffers can shield charges,[79] so more DNA could theoretically bind at higher ionic strengths. In reality there will be a combination of both steric and electrostatic effects that change the signal upon target binding.[12] There are therefore a multitude of competing steric and electrostatic processes at each stage of the biosensing process, which can be used to justify both current increases and decreases upon target binding. This chapter will investigate these processes in more detail with the specific aim of characterising which of these processes are dominating in the electrode systems. If the electrode dimension causes a different film structure to form, how do the films in each orientation respond to the steric and electrostatic changes of target binding?

5.2. Experimental

5.2.1. Electrochemical set up

A 1.6 mm diameter Pt macro disk electrode (IJ Cambria, UK) was cleaned by polishing using alumina MicroPolish™ slurries of first 1.0 µm then 0.3 µm and finally 0.05 µm alumina on a polishing microcloth (all supplied by Buehler). All electrochemistry was performed using an Autolab PGSTAT128N controlled using NOVA 1.10 software (Metrohm Autolab, Utrecht, Netherlands). All experiments were conducted in a Faraday cage that was built in house from a metal fuse box (RS components, UK). All voltages are quoted vs a saturated calomel reference electrode and all studies were carried out at a temperature of 25 ± 0.05 °C (controlled with a water bath built in house) and in solutions sparged with argon (Boch, UK) for 10 minutes prior to use. During measurements the solution was constantly sparged at a flow rate of 0.01 Litres per minute of argon to keep it deoxygenated; this flow was controlled using an analogue gas flow regulator (Ki systems). All EIS measurements were performed at the open circuit dc potential (OCP) of the system, fixed by the ferri/ferrocyanide couple, superimposing a potential sinusoid with a 10 mV rms amplitude over a frequency range of 100 kHz to 0.1 Hz. In total 50 frequencies were scanned, logarithmically spaced, which resulted in 5 frequencies per decade. The MS arrays and MNEE arrays were cleaned electrochemically by the process discussed in chapter 3.2. Once clean the electrodes were transferred to the measurement buffer of 1 mM potassium ferricyanide, 1mM potassium ferrocyanide and KCl of the appropriate concentration (one of either 1 mM, 10 mM, 100 mM or 500 mM). EIS and cyclic voltammetry were run to ensure typical clean electrode responses, these are shown in the data sets for all experiments included in this chapter.

5.2.2. Probe film formation

Fifteen base probe films (sequence 5'-TTCCAGGAATGCAGA-3') were formed in solutions containing 30 µM MCH, 150 µM TCEP (both Sigma-Aldrich, UK) and one of either 1.5 µM DNA Probe (Sigma-Aldrich, UK) or 1.5 µM PNA Probe (Panagene, Daejeon, South Korea) as appropriate in a solution of 50:50 by volume ethanol (Sigma-Aldrich): deionised water (resistivity 18.2 $M\Omega cm^{-1}$, from Millipore MilliQ). Note that this solution was diluted by a volume factor of 1000 for the nano electrodes before film formation. SAM film formation was done for 16 hours overnight in an evaporation chamber to ensure sufficient time for the film to reach a steady state. Once the film had been formed the electrodes were rinsed with Ultrapure water and placed in the appropriate measurement buffer before EIS and CVs were recorded as described above.

5.2.3. Target hybridisation

Thirty base target ssDNA (sequence 5'-GTATGCTTTGGTCTTTCTGCATTCCTGGAA-3') was obtained from Sigma-Aldrich and made to 1 µM in deionised water, no salt was added to this target buffer so as to not screen the charges between probe and target during hybridisation. Hypothetically target binding efficiency could be improved by introducing electrolyte into the target hybridisation buffer to screen charge repulsion and increase film density and therefore impedance. The SAM probe films were then incubated in this target solution overnight to allow hybridisation to equilibrate before being washed in a stream of deionised water and placed back into the measurement buffer for electrochemical characterisation. In the limit of detection studies the film was first incubated in 1 aM target solution for 1h, before the electrochemical response was recorded in measurement buffer. This process was repeated with the different target solutions in ascending concentration from 1 fM target until 1 µM target. A final measurement was made after an overnight incubation in 1 µM target solution to obtain the response from high concentration, equilibrated probe-target binding. These different concentrations of target were obtained by performing serial dilutions of the stock 1 µM target solution.

SAM films undergo a change in impedance when transferred to a new buffer. For the purposes of these experiments the electrode had EIS measured as quickly as possible after transferring from the probe/target incubation buffers to the measurement buffer to minimise this effect; i.e. the film was in the steady state reached in the incubation buffer.

5.3 Results and discussion

5.3.1 Response of clean microelectrode and nanoelectrode arrays to the ferri/ferrocyanide couple in different ionic strength measurement buffers

It is vital for the purpose of this study to be able to resolve the two apparent semi-circles when a SAM film was put on the micro and nano electrodes. Since R_{ct} and R_{nl} change to different extents when going from clean → probe → target, the optimum ionic strength buffer for resolving these two features may be different at each stage of the process. A balance must be struck between using low ionic strengths to maximise the absolute values of R_{ct} and R_{nl} (and therefore increase the absolute change in impedance upon probe target

hybridisation) and increasing supporting electrolyte concentrations to resolve the two semi-circles. Changing the ionic strength of the buffer will change the electrochemical response observed, so for comparing the change in each circuit element as the electrode goes through the biosensing procedure from clean → probe → target, the ionic strength of the buffer used must be kept constant throughout. The responses of clean MS arrays and MNEE arrays in buffers across a range of different ionic strengths (1 mM FFC with 1 mM, 10 mM, 100 mM and 500 mM background KCl) were tested to ascertain which gave the best response for studying the fundamentals of biosensing, figure 5.1.

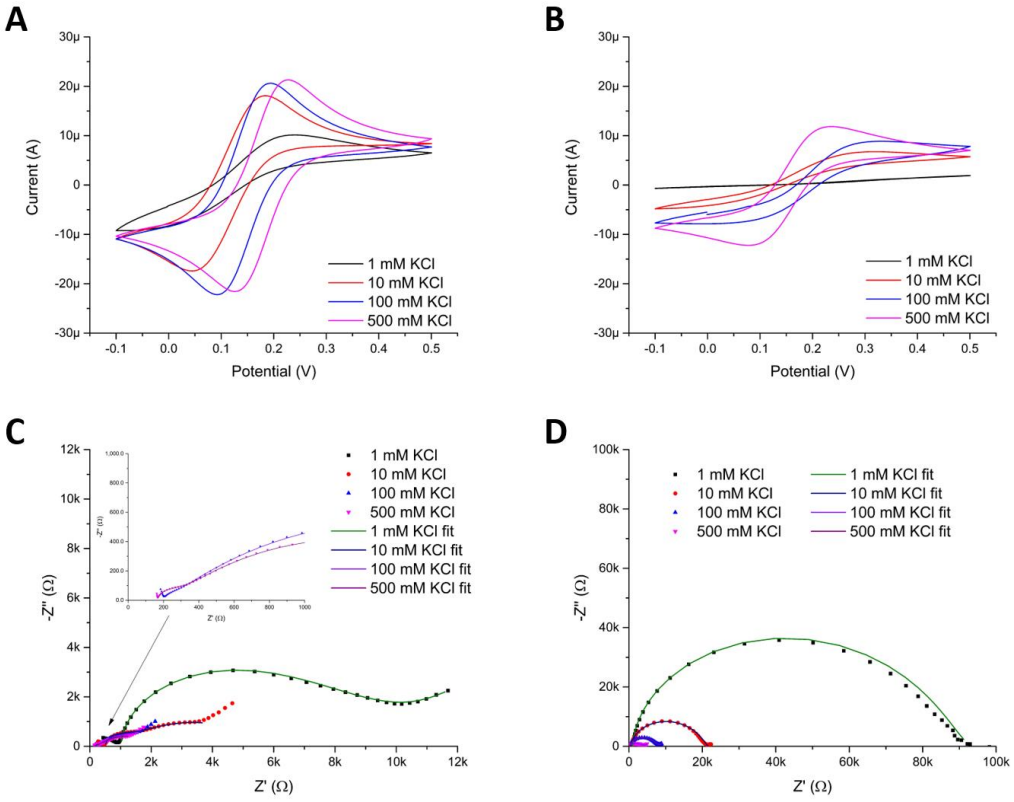

Figure 5.1. The electrochemical responses in 1 mM potassium ferricyanide, 1 mM potassium ferrocyanide and background KCl concentrations as indicated in the figure legends of clean electrodes vs a saturated calomel reference electrode and Pt gauze counter electrode. All CVs were performed at a scan rate of 0.1 Vs^{-1} and EIS performed at the OCP in each buffer. (A) the CV of a 30 µm 1D MS array (B) The CV of a 30 µm 1D MNEE array (C) Nyquist plot of a 30 µm 1D MS array with inset close-up of the high frequency region and (D) Nyquist plot of a 30 µm 1D MNEE array. Both (C) and (D) include fits to the equivalent circuit APP 1.3.

From the voltammograms in figure 5.1.A and 5.1.B, it can be seen that the lower ionic strength buffers are under a different rate limiting process, where the diffusion of FFC to the electrode is prevented by the build-up of negative charge at the electrode surface. Insufficient counter ions, in this case K^+, are present to balance the negative charge of the FFC accumulating at the electrode. This build-up of charge is preventing more FFC from approaching the electrode by electrostatically repelling it. In order for fresh FFC to reach the electrode more cations need to permeate the negatively charged field. At lower ionic strengths the reduced quantity of cations in solution means that this flux of K^+ is the rate limiting step on the reductive scans.

On the MNEE array, figure 5.1.B, the voltammogram in 1 mM KCl buffer is extremely resistive and gives a much worse response than the micro electrode in the same buffer. This data shows that that the MNEE array will make worse voltammetric sensors than micro electrodes in low ionic strength media. The voltammetry also becomes more capacitive at higher ionic strengths on electrodes of all dimensions.

On the micro electrode the OCP increases with ionic strength, this is not the case for the nano electrode. This discrepancy may be an experimental error from incorrectly weighing out the correct mass of potassium ferricyanide, potassium ferrocyanide and KCl. Whilst the limits of precision of the balance are quoted as ± 0.000005 g; in practice the balance is nearly 6 years old and well used, so is less precise than quoted. It may also be that at higher ionic strengths the potential across the reference electrode junction will be varied. A saturated calomel reference electrode is used so the flow of ions from the saturated KCl in the RE through the frit to the solution will be greater in lower concentration KCl buffers. This may cause the potential across the frit to be different in different ionic strength buffers. This change in the reference electrode would account for the systematic increase in OCP with increasing ionic strength, whilst the deviation from this trend by the 500 mM KCl buffer with an MNEE array may be due to human experimental errors.

The impedance data is best evaluated by looking at the fitted values for each element in the equivalent circuit, table 5.1. It should be stressed that the EIS were run at the open circuit potential for the electrodes in each buffer.

Table 5.1. Fitted values each element in the equivalent circuit (equivalent circuit APP 1.3) for clean 30 µm 1D MS and MNEE arrays in 1 mM potassium ferricyanide, 1 mM potassium ferrocyanide and KCl as indicated. The errors in the fits are provided to one standard deviation. All EIS recorded at the OCP vs a saturated calomel reference electrode and Pt gauze counter electrode at 25 °C in a solution that had been degassed and any oxide electrochemically removed.

MS array	1 mM KCl	10 mM KCl	100 mM KCl	500 mM KCl
R_s (Ω)	995 ± 18	499 ± 5	200 ± 1	167 ± 1
C_{dl} (nF)	1 094 ± 20	1 020 ± 22	793 ± 45	1032 ± 26
C_{dl}/A (µF/cm^2)	17.6 ± 0.3	16.5 ± 0.4	12.8 ± 0.7	16.6 ± 0.4
R_{ct} (Ω)	4039 ± 173	745 ± 20	58 ± 2	106 ± 2
R_{ct} × A (Ω.cm^2)	250.4 ± 10.7	46.2 ± 1.2	3.5 ± 0.1	6.6 ± 0.1
Y_0 (µS)	34 ± 3	103 ± 3	200 ± 2	246 ± 3
R_{nl} (Ω)	5 424 ± 138	4 474 ± 123	2 560 ± 35	1 985 ± 34
χ^2	0.0029	0.0072	0.0029	0.0042
MNEE array	**1 mM KCl**	**10 mM KCl**	**100 mM KCl**	**500 mM KCl**
R_s (Ω)	1 034 ± 23	613 ± 9	209 ± 10	169 ± 4
C_{dl} (nF)	104 ± 2	92 ± 1	135 ± 2	87± 1
C_{dl}/A (µF/cm^2)	252 ± 5	223 ± 2	327± 4	210 ± 2
R_{ct} (Ω)	35 552 ± 1 298	8 372 ± 153	6 667 ± 377	774 ± 38
R_{ct} × A (Ω.cm^2)	14.70 ± 0.53	3.46 ± 0.06	2.76 ± 0.14	0.32 ± 0.02
Y_0 (µS)	18 ± 3	22 ± 2	39 ± 4	130 ± 5
R_{nl} (Ω)	56 842 ± 2275	12 338 ± 332	8 956 ± 294	3 185 ± 37
χ^2	0.2003	0.0636	0.0814	0.0092

The EIS shows that at higher ionic strengths R_s decreases as would be expected. It is satisfying that the values of R_s are the same for micro and nanoelectrodes, except for the anomalous case of the 10 mM KCl buffer.

The capacitance double layer is constant at all ionic strengths for micro and nano electrodes. The literature dictates that a clean macro electrode will have a C_{dl} of about 20-60 µF/m^2,[16] it is known that smaller electrodes will have relatively smaller capacitance double layers which is why the fitted micro electrode values are slightly below these values.[102] The values of C_{dl} are the same as those reported on MNEE arrays by Mount *et al*[30], the C_{dl} from figure 11 of said paper can be calculated as 195 ± 6 µFcm^{-2}.

The double layer effects on R_{ct} are commonly described by the Frumkin effect.[31] The potential decreases exponentially from the outer Helmholtz plane out into solution. Therefore if the double layer is large, then electron transfer has to take place from farther away from the electrode surface which will reduce electron transfer kinetics and increase R_{ct}. From the data in table 5.6 the fitted values of C_{dl} are larger per unit area on a nano electrode than on a micro electrode. This correlates to a decreased mean electrode-ion distance and therefore enhanced electron transfer kinetics. It is therefore encouraging that the normalised R_{ct} values are also lower on the nano electrode than the micro electrode. The values of C_{dl} do not vary with ionic strength of the supporting electrolyte which would be expected, they should only vary with the applied potential; and since all of these systems were run at OCP, which is fixed by the ferri-ferrocyanide couple which was constant throughout, it is encouraging that there is no significant change in the fited values of C_{dl}.

The admittance, Y_0, can be used to calculate the diffusion coefficient of the redox agent in solution with equation 5.1.[61] In which, The diffusion coefficient (*D*) can be determined using the universal gas constant (R), temperature (*T*), admittance (Y_0), the number of electrons transferred (*n*), Faraday's constant (F) the area of the electrode (*A*) and the concentration of redox agent in solution in the bulk solution (c_0).

$$D = \left(\frac{2RTY_0}{n^2F^2Ac_0}\right)^2 \qquad \text{(Eqn 5.1)}$$

The fitted values of Y_0 increase as ionic strength increases which shows that the flux of FFC to the electrode is increasing with increased ionic strength. This supports the theory that the flux is limiting the electron transfer kinetics observed as the values of Y_0 are well below those needed to get the literature values of D. For the reaction considered, a 1 electron transfer between the electrode and 1 mM ferri/ferro cyanide at 25°C the diffusion coefficient should be 7.26 ×10^{-6} cm^{2}s^{-1}.[68] Therefore the expected values of Y_0 for a 30 µm 1D MS array and 30 µm 1D MNEE array are 845 µMho and 209 µMho respectively.

R_{nl} decreases with increasing ionic strength. This is probably due to the increased shielding between ferricyanide ions in solution which will increase the diffusion coefficients of the FFC ions, by reducing electrostatic drag, thereby decreasing R_{nl}.

In summary, it can be deduced that the process of electron transfer of FFC is affected by a multitude of factors. The micro electrodes display electron transfer kinetics in agreement with literature values in solutions with 100 mM and 500 mM supporting electrolyte whereas the MNEE arrays perform better in higher ionic strength buffers. This is an important consideration when selecting a sensor for a real-world system. Because of these findings it

was determined that the limits of detection experiments should be performed in 500 mM KCl, however, in order to compare the performances of electrodes of different dimensions, their responses in 10 mM KCl would be analysed. The justification for this is to make them directly comparable to the responses published on a macro electrode.[18] It should also be noted that using higher ionic strength buffers may be better for studying the fundamental processes of electron transfer, it may not be the best buffer for sensing, so a systematic study of the electrodes biosensing in different ionic strength media may show that the different electrodes with different probes have different sensitivities in various buffers.

The motivation behind doing these experiments was partially, as outlined above, to determine the best buffers for sensing on different sized electrodes; but was also to determine the effect of charge within the film on both the film structure and target binding. This was achieved by using PNA and DNA probes to bind DNA target on different sized electrodes in different buffers. The data in table 5.1 shows that whilst the electron transfer kinetics are not in line with the literature at the highest ionic strength used, the differences in response between probe and target in different ionic strength buffers will still elucidate information as to the effects of charge within the film.

5.3.2. Macro, micro and nano electrodes with a PNA probe

5.3.2.1. Macro electrodes with PNA probe

The procedure was first repeated on a macro disk electrode using the protocol found in the literature, see section 5.2,[18] to check the experimental set up and outline the expected responses.

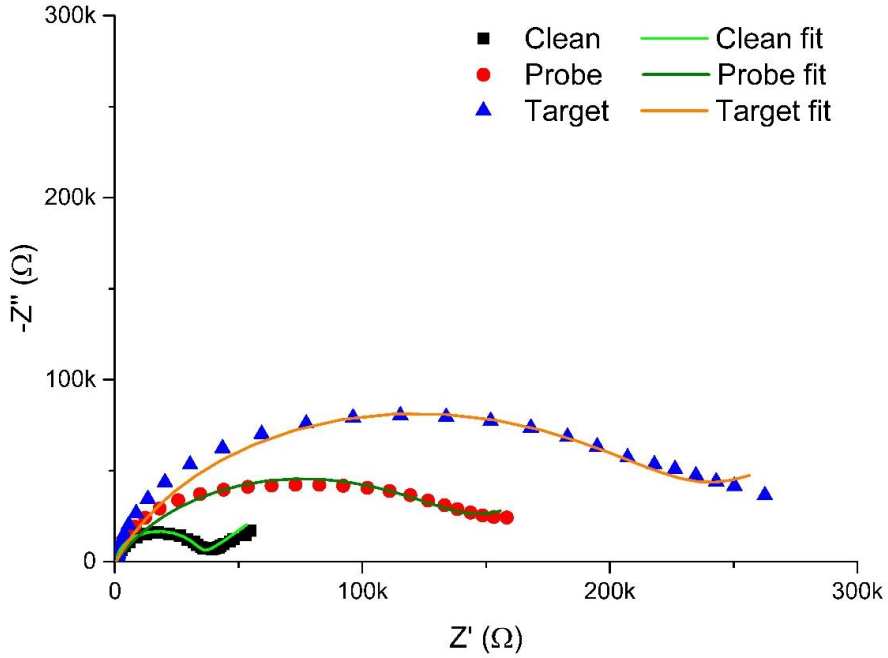

Figure 5.2. Nyquist plots overlayed from a Pt macro electrode when clean (black squares), with a PNA probe film (red dots) and after having been exposed to 1 µM target DNA (blue triangles). The corresponding fits are plotted in fluorescent green, olive green and orange for the clean, probe and 1 µM target respectively. All data were recorded at OCP vs a saturated calomel reference electrode and Pt gauze counter electrode in 1 mM potassium ferricyanide, 1 mM potassium ferrocyanide in 10 mM KCl.

The Pt macro electrode can be fit to the Randles' circuit and, as seen in figure 5.2, the impedance increases with going from clean → probe → target. The fitted values of interest are given in table 5.2.

Table 5.2. Fitted values for selected elements from the Randles' circuit to which the macroelectrode data shown in figure 5.2 was fit. The values of C_{dl} and R_{ct} have also been normalised per unit area. All values in red were fixed from the clean electrode values to obtain a better fit, as the value was sufficiently small that it could be fixed without introducing significant error.

MACRO	Clean	PNA Probe	Target
R_s (Ω)	846 ± 13	846	846
C_{dl} (nF)	1 150 ± 23	-	-
C_{dl}/A (μF/cm^2)	57 ± 1	-	-
CPE Y_0 (nS)	-	2 986 ± 101	1 795 ± 53
CPE Y_0/A (μS/cm^2)	-	148 ± 5	89 ± 3
CPE N	-	0.71 ± 0.01	0.77 ± 0.01
R_{ct} (Ω)	32 366 ± 695	142 760 ± 2 484	229 490 ± 3 435
$R_{ct} \times A$ (Ω.cm^2)	651 ± 14	2 869 ± 50	4 613 ± 69
Y_0 (μS)	140 ± 10	142 ± 14	78 ± 6
χ^2	0.1855	0.1289	0.1136

The fitted circuit for a clean electrode uses a capacitor, when a film is formed on the electrode a constant phase element (CPE) must be used. The use of constant phase elements is a source of controversy within the field as their physical basis in reality has never been established.[103-105] One theory is that when a heterogeneous film is formed a constant phase element can account for the non-uniform coverage of the SAM.[16, 29, 56, 105] Perhaps when a perfectly formed, single phase monolayer is formed a capacitor can be used in the equivalent circuit; however, the data in chapter 4 showed that the system is much more complicated with multiple phases and possibly aggregates within the film, so a constant phase element is required to get a good fit. Switching between elements as we go from a clean electrode to one with a SAM film may account for the changes to the measured value of C_{dl}, as such the capacitance values have not been analysed in detail. The CPE has units of $F/s^{(1-\alpha)}cm^2$ so is not directly comparable to the capacitor values when $\alpha \neq 1$.[104]

The fitted value of C_{dl} for the clean electrode is within the expected range which suggests that the electrode is working properly.[16] R_{ct} on the clean electrode is 32 kΩ, which equates to a k^θ of 8×10^{-5} cms^{-1}. This would imply that the electron transfer is in some way inhibited. As discussed before the flow of redox agent to the electrode surface is limiting the electron transfer at this concentration of supporting electrolyte. It should again be noted that this protocol was taken straight from the literature[18] and was not optimised in any way during this project.

From table 5.2 it can be seen that the major change observed is in R_{ct} which increases 4.4 fold from clean → PNA probe then 1.6 fold from PNA probe → target. This increase is expected as the binding of target not only further sterically blocks the surface, but the introduction of negative charge at the electrode surface will repel the highly negatively charged FFC redox agent.

The published limits of detection for this system were femtomolar.[18]

5.3.2.2. Pt Microsquare array (30 µm 1D) with PNA Probe

The MS array was tested in 4 measurement buffers of different ionic strength. The CV and EIS of the electrode in 1 mM, 10 mM, 100 mM and 500 mM background KCl are given in figures 5.3.A-D, for a clean electrode, after PNA probe film formation and after DNA target binding.

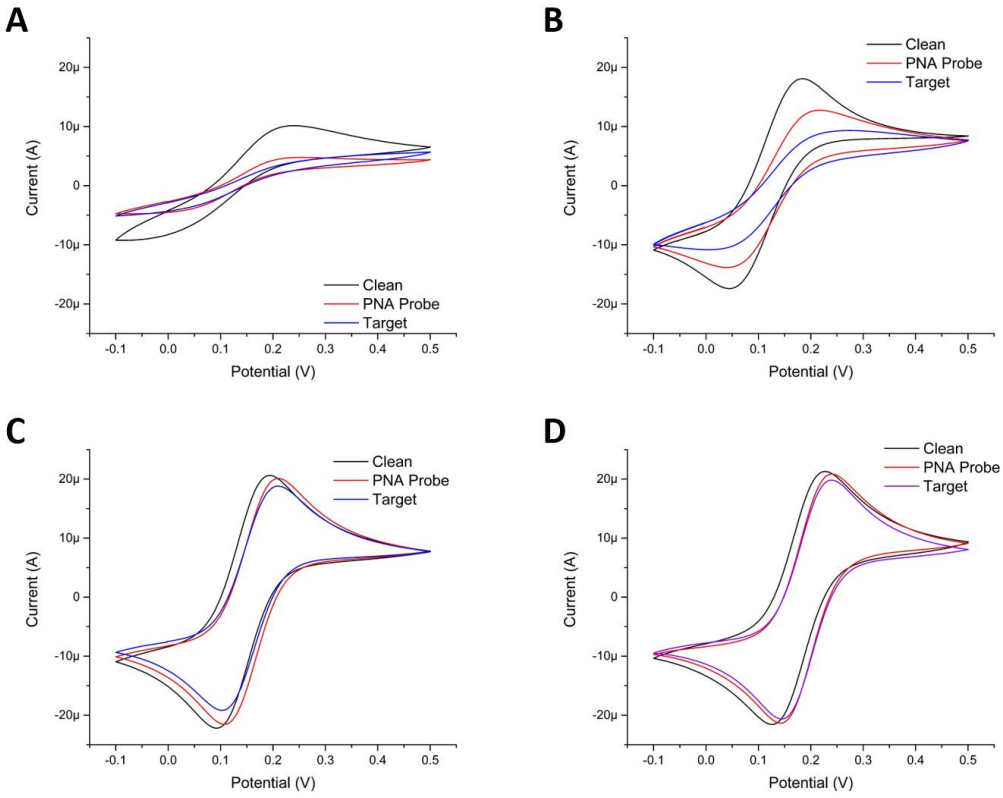

Figure 5.3. Cyclic voltammograms of a 30µm 1D microsquare array when clean (black line), with a PNA probe SAM (red line) and after incubating overnight with 30 mer Target DNA (blue line). All CV's recorded at 10 mVs^{-1} vs a saturated calomel reference electrode and Pt gauze counter electrode in a solution of 1 mM potassium ferricyanide, 1 mM potassium ferrocyanide and (A) 1 mM KCl (B) 10 mM KCl (C) 100 mM KCl and (D) 500 mM KCl.

The cyclic voltammograms given in figure 5.3 show that there is an appreciable change in peak current for the oxidation of ferrocyanide → ferricyanide when going from clean → probe → target; with the peak current decreasing at each stage in every buffer. The same is true for the reduction peak current where ferricyanide is converted to ferrocyanide but in the lowest ionic strength buffer the change in reduction peak current is not as pronounced as for the oxidation. In all the CVs the peak shifts to the right (more positive) when the probe film is formed on the clean electrode, these changes are better analysed by DPV, figure 5.4. These studies suggest that the optimum buffer for these experiments is that containing 10 mM KCl background electrolyte, because it has the greatest change in peak current at each stage of the process. This is in agreement with the macro electrode protocol as published by Corrigan et al.[18]

When DNA target binds to the PNA probe a negative charge is introduced to the film and again the flow of cation into the negative field to balance the charge is the rate limiting step, that is why there is no change in the reduction peak current when target binds in buffers

with a low concentration of supporting electrolyte, the peak is limited by the natural convection driven flux of K^+ into the field. At higher ionic strengths there is most probably a breakdown of Donnan exclusion effects.

When the probe film is formed on the electrode it maintains the mass transport controlled peak shaped limiting current associated with diffusion overlap on a microelectrode array, but begins to look a bit more wavelike than it did on a clean electrode in low ionic strength buffers. After target is hybridised the peaks become waves in the 1 mM and 10 mM KCl buffer but not at the higher ionic strengths. This is because the negative charge associated with the DNA target needs to be counterbalanced with the cations in solution. This decreases the amount of K^+ available to shield the DNA from the FFC further impedes the flow of FFC to the electrode.

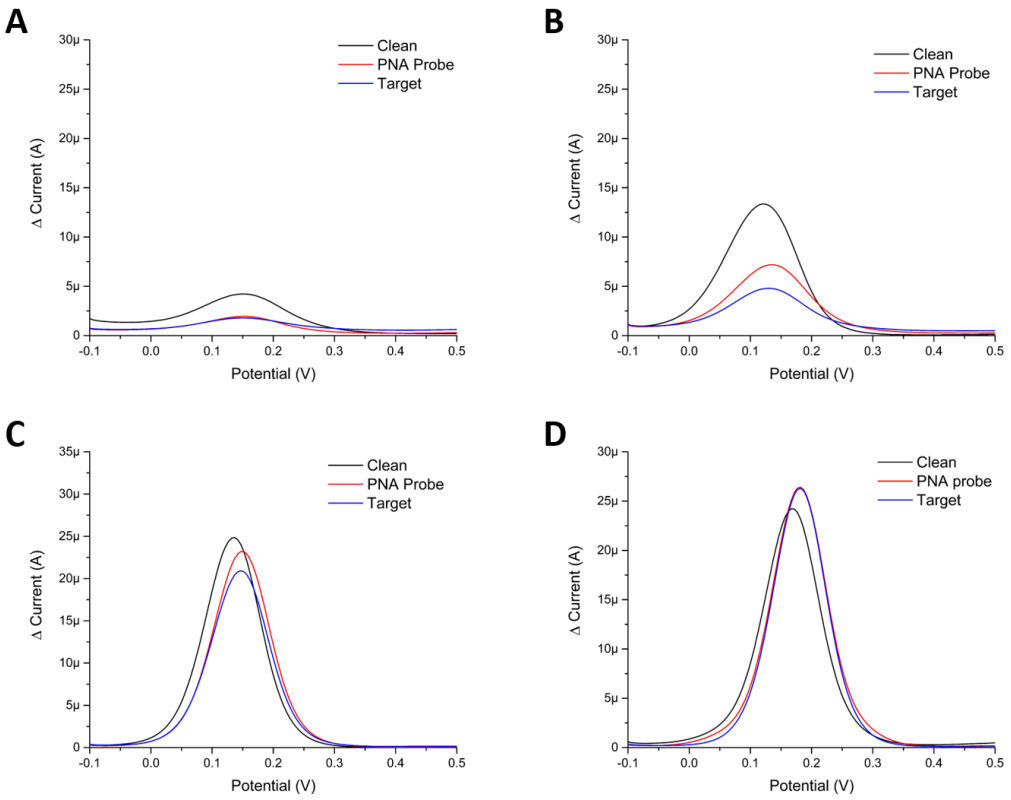

Figure 5.4. DPV of a 30 µm 1D microsquare array when clean (black), after the formation of a PNA probe film SAM (red) and after exposure to 1 µM 30 mer DNA target overnight (blue). The DPV were recorded in at a scan rate of 10 mVs^{-1} vs a saturated calomel reference electrode and Pt gauze counter electrode in a solution of 1 mM potassium ferricyanide, potassium ferrocyanide and (A) 1 mM KCl (B) 10 mM KCl (C) 100 mM KCl (D) 500 mM KCl.

Differential pulse voltammetry was utilised to better investigate the half wave potential shift to a more positive value. In the 10 mM KCl buffer the peak voltages as the electrode goes from clean → PNA probe → target are 0.122 V → 0.137 V → 0.132 V respectively. The peak voltage shifts first positively by +25 mV when the PNA probe film forms on a clean electrode then negatively by -5 mV when the target binds. This shifting of the half wave potential would imply that the electron transfer is impeded when a PNA film forms as would be expected since the surface is covered and the surface area of the electrode decreases.[79] Target binding causes a minimal decrease in the resistivity to the electron transfer but the mass transport of the film is impeded, as the peak position does not change as drastically as the change in

current. In 500 mM KCl, the higher supporting electrolyte concentration shields neighbouring probe-target helices, reducing their repulsion towards each other and therefore decreasing the shift to a less positive voltage. In figure 5.4.D where there is no measurable change in the peak voltage when going from probe → target. Encouragingly the change in peak current is minor which adds weight to the theory that this is a shielding effect at the FFC is also being shielded from the phosphate backbone of the target DNA by the KCl in the buffer.

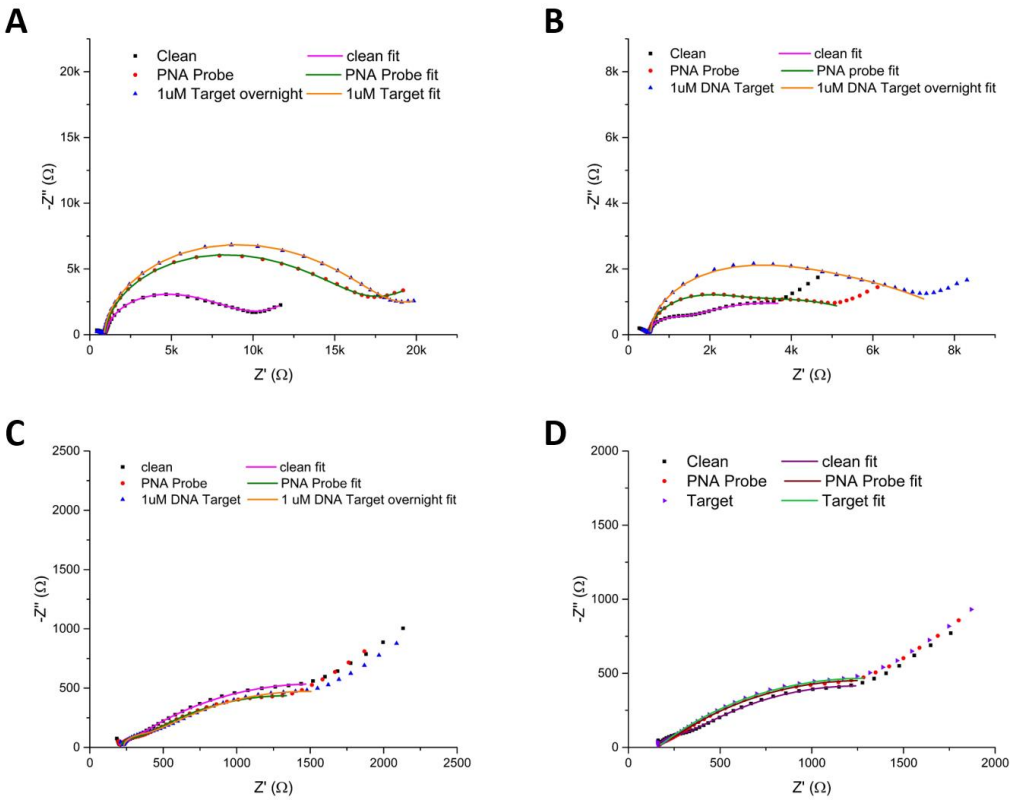

Figure 5.5. Nyquist plots of a 30µm 1D microsquare array when clean (black dots), with a PNA probe SAM (red dots) and after incubating overnight with 30 mer Target DNA (blue dots) and corresponding fits. All EIS recorded at OCP vs a saturated calomel reference electrode and Pt gauze counter electrode in a solution of 1 mM potassium ferricyanide, 1 mM potassium ferrocyanide and (A) 1 mM KCl (B) 10 mM KCl (C) 100 mM KCl and (D) 500 mM KCl.

Figure 5.5 shows that for the microelectrodes the best EIS results were obtained in 10 mM background electrolyte. Both in terms of the % change in signal going from clean → probe → target and the ability to resolve each of the two semi-circles in the Nyquist plot. The data from the 10 mM KCl experiments are discussed in more detail below by analysing the fitted data given in table 5.3. The other fitted data have been omitted for ease of reading.

Table 5.3. Fitted values and errors for each element from the fits in figure 5.5.B. above; for a 30 µm 1D MS array in a 10 mM KCl buffer with 1 mM potassium ferricyanide and 1 mM potassium ferrocyanide when clean, saturated with PNA probe and after target has hybridised to the probe overnight. All errors are given to one standard deviation.

MICRO	Clean	PNA Probe	Target
R_s (Ω)	499 ± 5	516 ± 4	547 ± 6
C_{dl} (nF)	1 020 ± 22	980 ± 12	1 110 ± 17
C_{dl}/A (µF/cm^2)	16.5 ± 0.4	15.8 ± 0.2	17.9 ± 0.3
R_{ct} (Ω)	745 ± 20	1 807 ± 45	2 811 ± 150
$R_{ct} \times A$ (Ω.cm^2)	46 ± 2	112 ± 3	174 ± 9
Y_0 (µS)	103 ± 3	73 ± 4	43 ± 5
R_{nl} (Ω)	4 473 ± 123	4 275 ± 108	5 423 ± 173
χ^2	0.0072	0.0067	0.0136

For the analysis of this data set the fitting was windowed to exclude the inclining tail of the signal at low frequencies, this could have been fit with a Warburg element in series with the modified Randles' circuit for microelectrodes but for the sake of not changing the circuit the data was simply excluded from the fit. This Warburg element is a product of array overlap and is not important for sensing. Each circuit element should be discussed in isolation to gain a fuller understanding of the processes involved during the biosensing protocol.

The values of R_s are constant within three standard deviations of the fit. There will also be a small experimental error from the balance when weighing out the FFC.

The capacitance double layer remains constant when the errors are taken to three standard deviations, in agreement with the findings of chapter 4. The slight deviation in the size of the double layer when target binds is probably due to random experimental errors.

The values of R_{ct} are seen to increase at every stage of the process. The formation of a film on the electrode will reduce the available electrode surface area thereby decreasing the R_{ct}, as discussed in Chapter 4. The hybridisation of a DNA target to a PNA probe film will have multiple effects on the structure and charge of the film but in this instance the values of R_{ct} are seen to increase. Therefore, the dominating effect is the electrostatic repulsion between the DNA and FFC (the Donnan effect). There is a 2.4-fold increase from clean → PNA probe and a 1.6-fold increase from PNA probe → target.

The values of Y_0 decrease at each step therefore the flow of FFC to the electrode is being reduced at each stage. The formation of a probe film causes a 29% reduction in the fitted value of Y_0, subsequent target binding to said probe film causes a 41% decrease in the fitted values. Again, these cannot be directly correlated to the clean macro electrode data as it was fit with a different circuit. But when the target binds to the probe on the macro electrode there was a similar decrease of 45% of the fitted Y_0 value which is encouraging, and would suggest that the micro and macro electrode responses are very similar.

The resistance to non-linear diffusion does not change when going from clean → probe. This is in stark contrast with the findings in chapter 4 where they are seen to rise when a film forms on the electrode. The reasons for this difference are not known but should be the subject of future investigation by repeating the experiments in chapter 4 using a probe film solution as opposed to MCH. When target binds to the probe there is a small but significant

increase in R_{nl}. This may be due to the repulsion of FFC by the DNA target. This increase is minor with the target R_{nl} being 1.26 times the magnitude of the probe R_{nl}.

Intuitively it makes sense that as a neutral film forms there will be minimal to no effect on R_{nl}. The diffusion profile of the electrode should undergo minimal changes during this process. The inclusion of charge when target binds will conceptually make a difference to the diffusion field. This build-up of charge will repel incoming FFC molecules, explaining the increase in resistance observed. If this is true then the formation of a negatively charged DNA probe film, discussed in section 5.3.3.2. below should also cause an increase in R_{nl}, which it does.

5.3.2.3. MNEE array (30 µm 1D) with PNA Probe

On the 30 µm 1D MNEE array there is again a decrease in peak current when going from clean → probe → target. Although the changes occur over such a large range they cannot be observed on the normalised axes in figure 5.6.

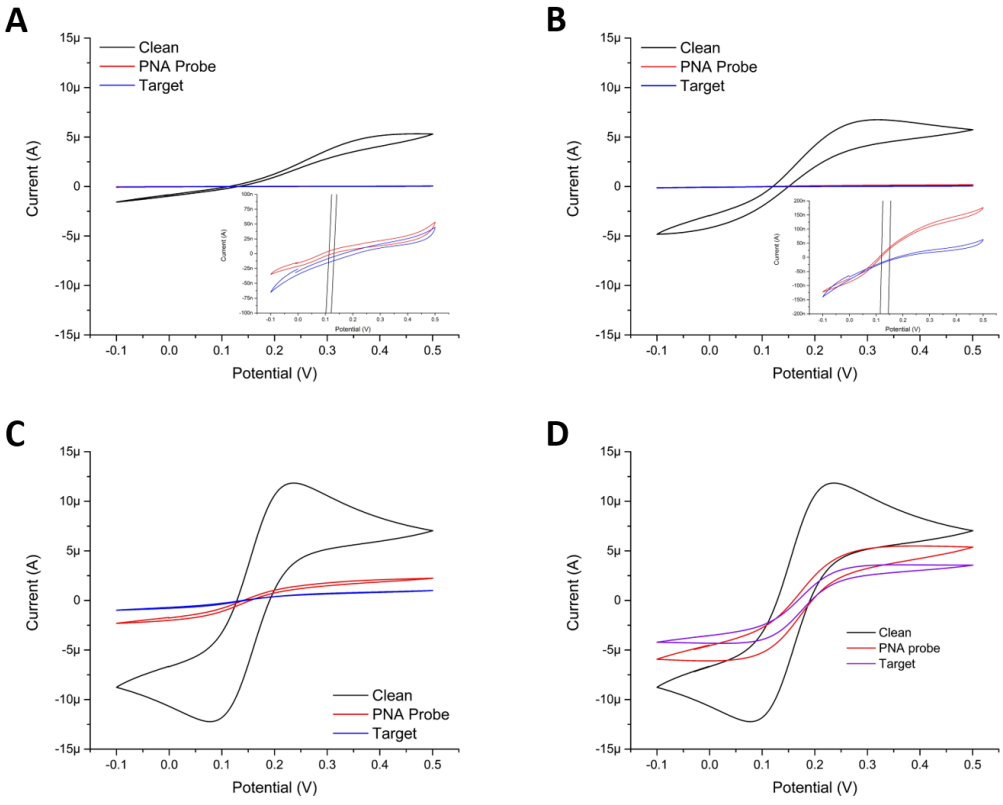

Figure 5.6. Cyclic voltammograms of a 30 µm 1D MNEE array when clean (black), coated with PNA probe SAM (red) and after incubation with 1 µM 30 mer DNA target overnight (blue/purple). All CV's recorded at 10 mVs^{-1} vs a saturated calomel reference electrode and Pt gauze counter electrode in a solution of 1 mM potassium ferricyanide, 1 mM potassium ferrocyanide and (A) 1 mM KCl (B) 10 mM KCl (C) 100 mM KCl and (D) 500 mM KCl. In (A) the PNA probe signal is obscured by the target voltammogram.

Changes in the voltammetry are more pronounced in buffers containing ≥ 100 mM KCl. As with the 30 µm 1D MS array the reduction peak of the clean electrode experiences field effects caused by a lack of cations in solution to balance the negative charge of the FFC which

builds up at the electrode during the positive scan. As the electrode dimensions get smaller they perform better in higher ionic strength buffers. This is only the case when using the PNA probe. For a DNA probe the best data was obtained using a 100 mM KCl buffer, this phenomenon is discussed in more detail in section 5.4.2. after both PNA and DNA probes have been analysed.

The changes in peak currents are greater on the MNEE array than the MS array. It was determined to analyse the CV in 500 mM KCl buffer as this gave the greatest overall change in maximum current between the probe and target measurements.

There is a pronounced shift from a peak shaped voltammogram to a wavelike response whenever a film is formed on the electrode. The theory dictates that wavelike responses are seen for micro and nanoelectrodes where the diffusion is enhanced.[31, 106] The only reason that peak like responses are seen for the clean electrode is the overlapping of the diffusion fields of neighbouring electrodes in the array and the response is effectively that of a macro electrode with dimensions of the array area. This can be negated by increasing the separation between neighbouring electrodes in the array or increasing the scan rate. The literature states that the separation required to remove array overlap under most normal conditions is 8-12 times the diameter of neighbouring electrodes.[31, 53] In future the MNEE arrays should be fabricated with larger spacing's to remove array overlap. The reason for the change to a more wavelike voltammogram when a probe film forms is that the current is now coming from defects in the SAM layer which behave like nano electrodes.[79]

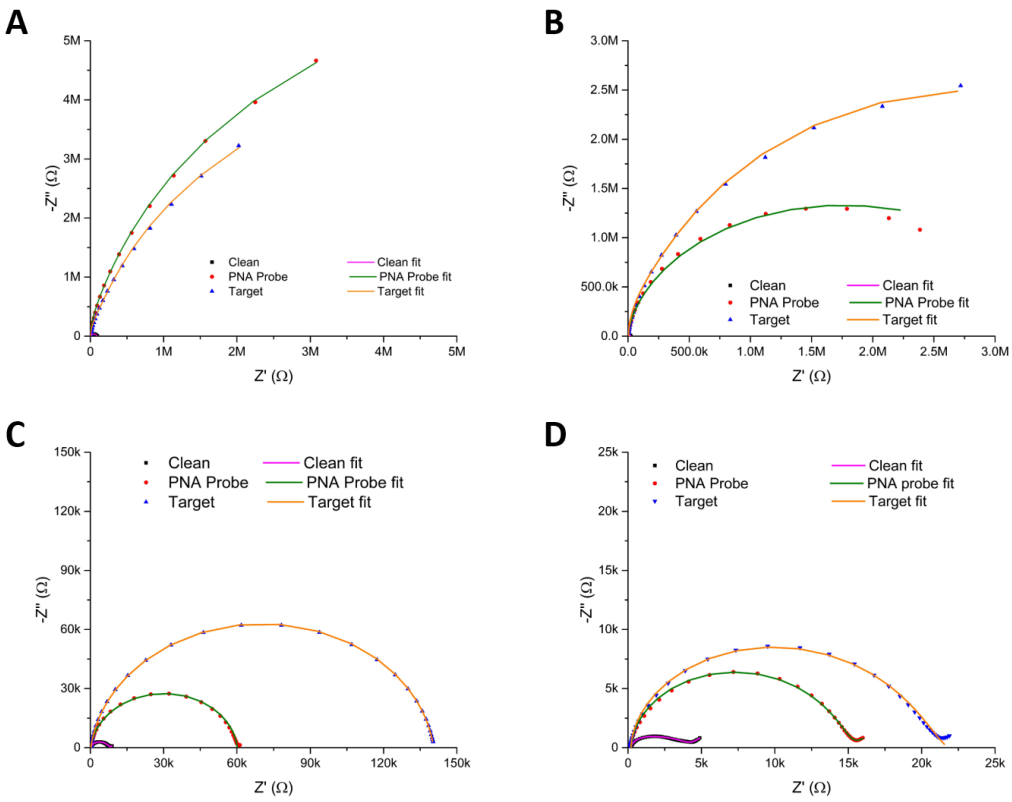

Figure 5.7. Nyquist plots of a 30µm 1D MNEE array when clean (black dots), with a PNA probe SAM (red dots) and after incubating overnight with 30 mer Target DNA (blue dots) and corresponding fits. All EIS recorded at OCP vs a saturated calomel reference electrode and Pt gauze counter electrode in a solution of 1 mM potassium ferricyanide, 1 mM potassium ferrocyanide and (A) 1 mM KCl (B) 10 mM KCl (C) 100 mM KCl and (D) 500 mM KCl.

Table 5.4. Fitted values for the equivalent circuit elements for the 30 µM 1D MNEE array in the 10 mM KCl solution. The values in red were fixed from the clean electrode fit.

NANO	Clean	PNA Probe	Target
R_s (Ω)	613 ± 9	613	613
C_{dl} (nF)	92 ± 1	265 ± 4	278 ± 4
C_{dl}/A (µF/cm²)	223 ± 2	641 ± 11	673 ± 178
R_{ct} (Ω)	8 372 ± 153	2 280 000 ± 41 600	4 720 000 ± 93 500
R_{ct} × A (Ω.cm²)	3.46 ± 0.06	942 ± 17	1951 ± 39
Y_0 (µS)	22 ± 2	22	22
R_{nl} (Ω)	12 338 ± 332	12 338	12 338
χ^2	0.0636	0.0863	0.56536

When fitting the data for the MNEE arrays with probe and probe-target hybridised films, the values of R_s, Y_0 and R_{nl} were fixed to those obtained in the clean electrode fit. This was done to get a good fit; whilst the values of Y_0 and R_{nl} are liable to vary slightly, especially when target binds, the micro electrode data shows that the major change in signal comes from the change in R_{ct}. Analysis of figure 5.7.C and 5.7.D by eye can inform the reader as to the difficulties of fitting the second much smaller semi-circle in this data. The plots for a clean electrode in figure 5.7.A and B have been included but cannot be distinguished due to the scale needing to encompass the probe and target plots. It was the authors opinion that the change in signal between probe film and target film was more important for the purposes of biosensing than that of clean → probe, the scales were therefore chosen to reflect the change in impedance when going from probe → target.

The greatest absolute increase in impedance from probe → target was observed in 10 mM KCl buffer, although the greatest relative change in impedance was in the 100 mM KCl buffer. The best buffer for analysing and fitting both semi-circles, so the best for studying the fundamentals of the system was the 500 mM KCl buffer. So as to be compared with the other data in this chapter the fitted values from the 10 mM KCl buffer has been summarised in table 5.4, the limits of detection studies, section 5.4.3, were performed in 500 mM KCl buffer to investigate better investigate the fundamental changes in the system as different concentrations of target were bound to the probe.

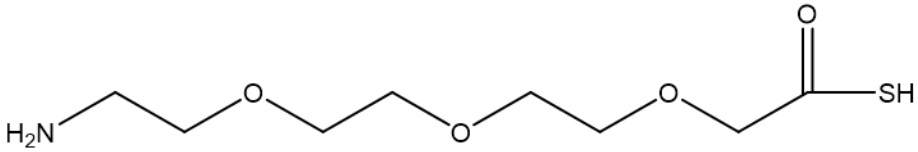

Figure 5.8. The AEEEA thiol linker used to attach the probe sequence to the electrode. The linker has a maximum length of 1.8 nm.

The probe oligomer is attached to the electrode by an AEEEA linker, figure 5.8, and 15 bases of either PNA or DNA were used; the probe-target double helices will have persistence lengths on the scale of tens of nano meters, assuming an axial base separation of 0.34nm.[107] Notwithstanding the fact that the probe-target helices could be in the A-form, B-form or Z-form and the 15 base overhang will be, like the single stranded probe, in constant dynamic motion,[108] the probe and/or probe-target film height will be on the same order of magnitude as the MNEE width. As a result of this the film structure on a MNEE could theoretically be very different to that on macro and micro electrodes, adopting a more "splayed out"

formation as shown by the schematic in figure 5.9. This probe conformation has been reported on nanoelectrodes before,[8, 10, 109] but always on electrodes with spherical structures, so it is not known if the film structure is a property of the probe-electrode size ratio or that of curved electrodes.

Figure 5.9. Schematic diagram showing the orientation of probe molecules in (Left) the ϕ-phase that theory dictates will form on the bulk of a macro and micro electrode (Right) a "splayed out" conformation that would theoretically form on a MNEE.

If the above theory about the fanning out of probe molecules on nanoelectrodes is true, then it may be the case that the films formed on MNEE are better able to cope with the stress induced by DNA target binding to a PNA probe as it can orientate the like charges further away from each other than the bulk ϕ-phase probe on a macro and micro electrode. Furthermore, such a packing style could allow for a denser DNA probe film to form on the MNEE than MS for the same reasons of charge separation. Analysis of the impedances of each of the probe films per unit area should inform as to the packing density on electrodes of different dimensions. It should be stressed that whilst EIS is a powerful information rich technique it can only give an indication as to the probe structure. It can be used to investigate the relative densities of different films on different electrodes but cannot be used to ascertain the true structure of the film. The proposed fanning out of the film would be better studied by another technique such as AFM or STM,[40, 49, 110] this was not possible due to the architecture of the MNEE arrays preventing easy access to the electrode.

It has previously been reported that PNA forms more densely packed films than DNA, as the charge of DNA probes makes them repel neighbouring molecules in the film.[111] At higher concentrations of supporting electrolyte, the shielding might mean the DNA probe film will be denser, but the shielding will also reduce the Donnan exclusion of FFC. It is conceivable that there is an optimum film ionic strength at which the DNA film will cause the greatest change in impedance upon target hybridisation. If the film does have a different structure on MNEE arrays, then perhaps the DNA probe can become more tightly packed as the charges are better separated then they would be on a macro electrode. PNA films are reportedly very dense due to their neutrality and should therefore always form tighter packed films than DNA probe films,[108, 111] it is not known if the proposed splayed out nature of the film on MNEE arrays will make these even denser than reported on macro electrodes.

Other than being able to cope with the stress introduced within the film; the fanned out probe can increase the rate of target hybridisation as there is less steric hindrance to incoming target molecules.[8] The kinetics of target binding were not studied in this project due to time constraints but should form the basis of future investigation. The association constant of the probe in solution and on the different electrodes could also be indicative of a splayed out film structure. In solution the thermodynamics of PNA-DNA target

hybridisation have been studied using UV-Vis spectroscopy and isothermal titration calorimetry.[52, 112] The temperature at which half the probe-target double helix has de-hybridised, T_m, can be used to calculate the association constant of the probe and target in solution,[52] the association constant would theoretically be lower when the probe is fixed to an electrode as it has fewer degrees of freedom and steric hindrance from neighbouring probes within the film. A splayed out film on an MNEE would hypothetically have an association constant between those of the probe free in solution and on a macro electrode. Again, due to time constraints these experiments could not be conducted but should form the basis of future work to determine the film structure on MNEE arrays.

5.3.3. Micro and nano electrodes with a DNA probe

5.3.3.1. Microsquare array (30 µm 1D) with DNA Probe

When the tests were repeated using a DNA as opposed to PNA Probe the first trend that catches the reader's attention is that the addition of target makes the current increase, figure 5.9. This is the opposite trend to that observed using a PNA probe.

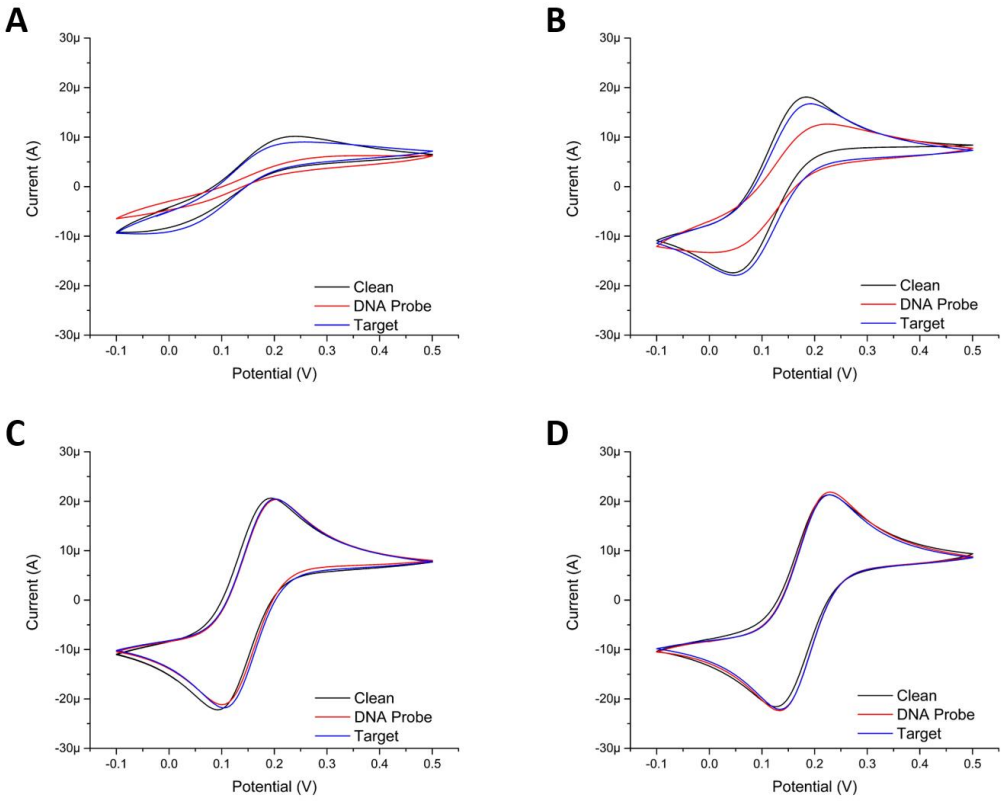

Figure 5.10. Cyclic voltammogramms of a 30 µm 1D MS array when clean (black), coated with DNA probe SAM (red) and after incubation with 1 µM 30 mer DNA target overnight (blue). All CV's recorded at 10 mVs^{-1} vs a saturated calomel reference electrode and Pt gauze counter electrode in a solution of 1 mM potassium ferricyanide, 1 mM potassium ferrocyanide and (A) 1 mM KCl (B) 10 mM KCl (C) 100 mM KCl and (D) 500 mM KCl.

This is a perfect example of the inconsistencies within the literature where target hybridisation can cause both the increase[18, 77-79, 90, 91, 99] and decrease[33, 100, 101] of current/impedance. The addition of target introduces negative charge into an already negatively charged film. Perhaps this increase in stress leads to degradation of the SAM. At

higher ionic strengths, the Donnan exclusion of FFC from the film has reduced the signal change to such a degree that the voltammograms barely differ throughout the protocol. This is a good example of the influence of charge within the SAM layer on the signal response.

At higher ionic strengths, figure 5.10.C and D, the change in peak current is too small to be discerned on this scale. The voltammogram of in the 10 Mm KCl buffer has a diffusion limited peak, as opposed to a wave, when the electrode is clean. Once a DNA probe film has been formed on the electrode the CV has a more wavelike response and there is a drop in peak current. Target binding then returns the signal to a more peak-like response. Continuing with the theory that the signal comes from defects within the film,[79] the hybridisation of target is introducing more disorder and opening up channels to the electrode surface and reducing the impedance of the film. This is most probably as a result of the stress introduced into the film with negatively charged target binding into a negatively charged probe SAM.

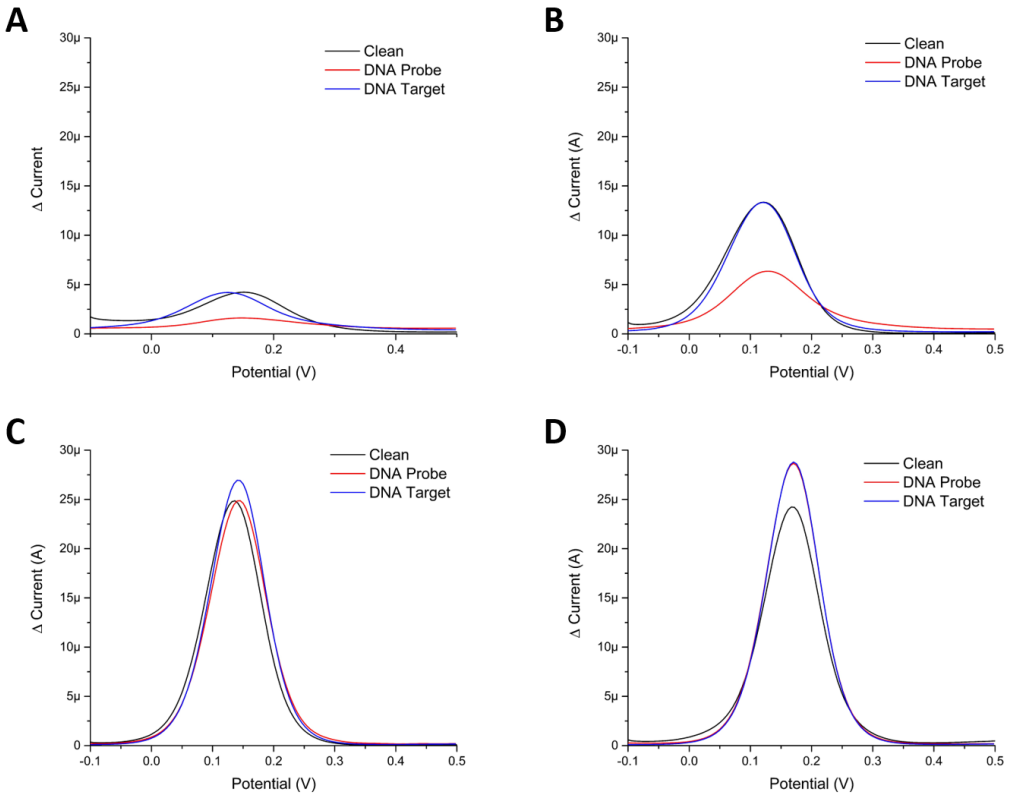

Figure 5.11. DPV of a 30 µm 1D microsquare array after the formation of a DNA probe film SAM (red) and after exposure to 1 µM 30 mer DNA target overnight (blue). The DPV were recorded in at a scan rate of 10 mVs^{-1} vs a saturated calomel reference electrode and Pt gauze counter electrode in a solution of 1 mM potassium ferricyanide, potassium ferrocyanide and 10 mM KCl.

Analysis of the DPV in this buffer shows that the peaks first shift to a more positive potential when a DNA probe film is formed before returning to the same voltage as the clean electrode, figure 5.11. The absolute values of these peak voltages going from clean → DNA probe → target are 122 mV → 130 mV → 120 mV. Increased supporting electrolyte concentration again reduces the change in the current differential, and reduces the peak voltage changes due to enhanced shielding protecting the FFC from the film and neighbouring probe and probe-target molecules from interacting with each other respectively.

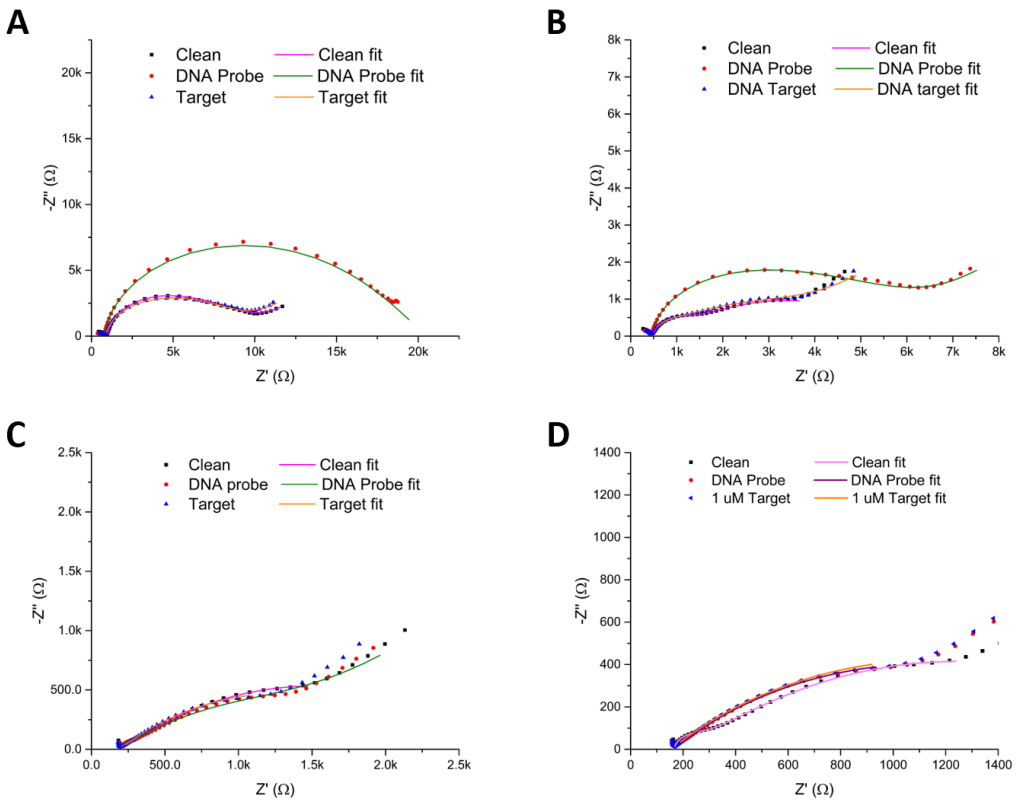

Figure 5.12. Nyquist plots of a 30µm 1D MS array when clean (black squares), with a DNA probe SAM (red dots) and after incubating overnight with 30 mer Target DNA (blue triangles) and corresponding fits. All EIS recorded at OCP vs a saturated calomel reference electrode and Pt gauze counter electrode in a solution of 1 mM potassium ferricyanide, 1 mM potassium ferrocyanide and (A) 1 mM KCl (B) 10 mM KCl (C) 100 mM KCl and (D) 500 mM KCl.

The best EIS of the 30 µm 1D MS array during the biosensing protocol was found to be the 10 mM KCl solution, both in terms of the change in fitted impedance values and the ability to fit to resolve the two semi-circles. The fitted values for each element for this experiment are given in table 5.5.

Table 5.5. Fitted values and errors for each element from the fits in figure 5.12.B above; for a 30 µm 1D MS array when clean, saturated with DNA probe and when different concentrations of target have hybridised to the probe. All errors are given to one standard deviation.

MS array	Clean	DNA Probe	Target
R_s (Ω)	454 ± 14	434 ± 13	443 ± 12
C_{dl} (nF)	912 ± 81	1270 ± 52	971 ± 98
C_{dl}/A (µF/cm^2)	14.7 ± 1.3	20.5 ± 0.8	15.7 ± 1.6
R_{ct} (Ω)	561 ± 56	1560 ± 209	393 ± 55
$R_{ct} \times A$ (Ω.cm^2)	35 ± 3	97 ± 13	24 ± 3
Y_0 (µS)	84 ± 7	33 ± 4	71 ± 4
R_{nl} (Ω)	2554 ± 66	4403 ± 180	2987 ± 59
χ^2	0.0401	0.0157	0.0250

Within error the values of R_s and C_{dl} are, as before, constant throughout the experiment. The value of R_{ct} increases 2.8-fold upon the formation of a DNA probe film then decreases back to the same value of the clean electrode within error. Y_0 decreases upon probe film formation before increasing when target binds. The reverse, an increase on probe SAM formation and

decrease on target binding, can be observed in R_{nl}. These changes are discussed in more detail in section 5.4.2 below but are believed to be representative of a resistive, charged probe film forming that is then degraded by target binding introducing more stress into the film which causes its degradation. This stress can be mitigated by increased shielding at higher ionic strengths of supporting electrolyte.

5.3.3.2. MNEE array (30 µm 1D) with DNA Probe

The CV data shows that binding DNA target to a DNA probe film increases the peak currents on the MNEE arrays just as it did for the MS arrays, figure 5.13.

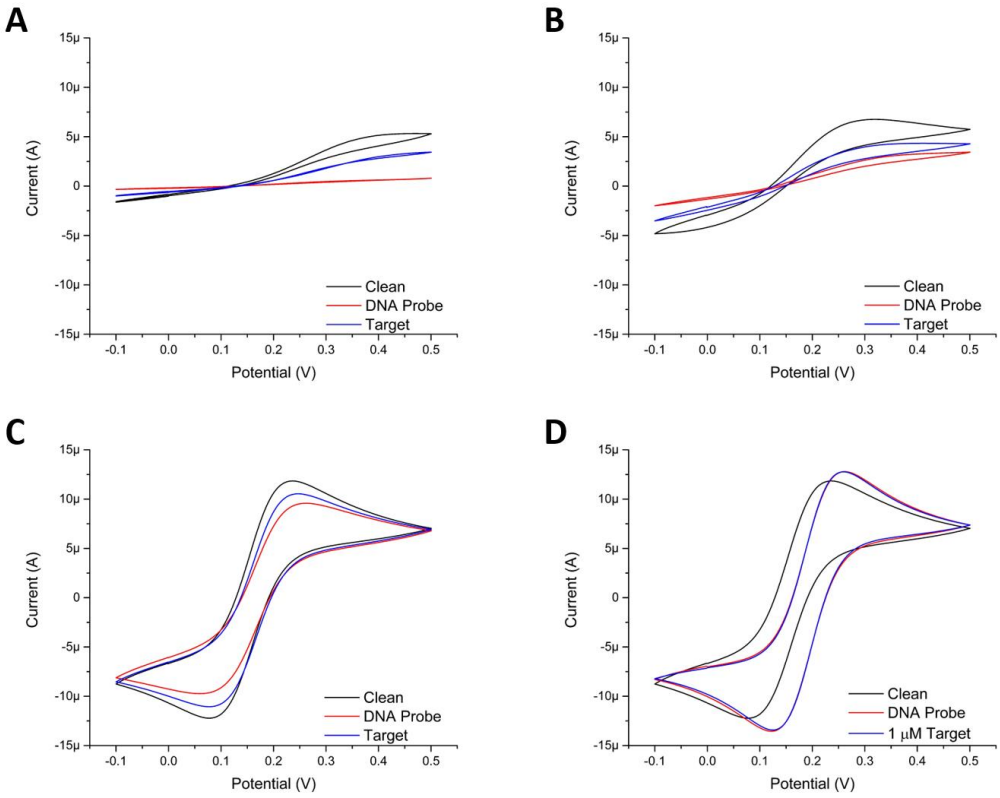

Figure 5.13. Cyclic voltammograms of a 30 µm 1D MNEE array when clean (black), coated with DNA probe SAM (red) and after incubation with 1 µM 30 mer DNA target overnight (blue). All CV's recorded at 10 mVs^{-1} vs a saturated calomel reference electrode and Pt gauze counter electrode in a solution of 1 mM potassium ferricyanide, 1 mM potassium ferrocyanide and (A) 1 mM KCl (B) 10 mM KCl (C) 100 mM KCl and (D) 500 mM KCl.

The readers eye is first drawn to the fact that the peak currents are larger for the electrode with a probe film and probe-target hybridised film than of a clean electrode in the 500 mM KCl buffer, figure 5.13.D. The reasons for this is most probably down to experimental error. During the course of these experiments, fresh buffer needed to be made, there would be a human error in the concentration of FFC in the buffers made on different days. The EIS data in figure 5.14 below is consistent with the voltammograms above in showing this trend. Secondly the observer might note that in the 500 mM KCl buffer, figure 5.13.D, the peaks have shift to a more positive potential than in the other buffers when a probe film forms, this should again be attributed to changing of the buffer.

As in section 5.3.3.1, there is a difference between the oxidation and reduction peaks at the lower ionic strengths. The same justification of a rate limited by the diffusion of cation to

counter the field effects of the FFC is given. It is encouraging that when limited by natural convection, the voltammograms all tend towards the same current in figures 5.13.A and 5.13.B, implying that they are limited by the same process, the flow of cation into the double layer to neutralise the FFC. The same is also true of figures 5.13.C and 5.13.D, in this case the current is limited the diffusion of FFC to the electrode.

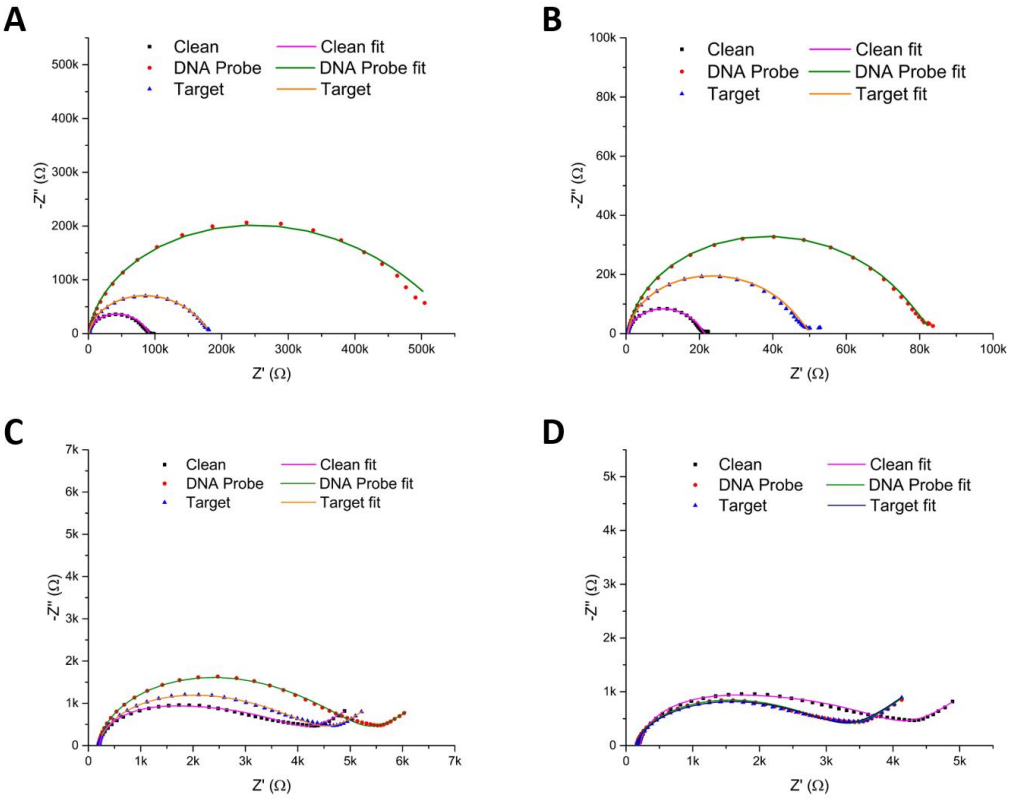

Figure 5.14. Nyquist plots of a 30µm 1D MNEE array when clean (black squares), with a DNA probe SAM (red dots) and after incubating overnight with 30 mer Target DNA (blue triangles) and corresponding fits. All EIS recorded at OCP vs a saturated calomel reference electrode and Pt gauze counter electrode in a solution of 1 mM potassium ferricyanide, 1 mM potassium ferrocyanide and (A) 1 mM KCl (B) 10 mM KCl (C) 100 mM KCl and (D) 500 mM KCl.

The EIS of the MNEE going through the biosensing protocol with a DNA probe in each of the four buffers is presented in figure 5.14. The fitted values for each element have been provided in table 5.6, for the 10 mM KCl buffer.

Table 5.6. Fitted values and errors for each element from the fits in figure 5.14.B above; for a 30 µm 1D MNEE array when clean, saturated with DNA probe and when target has hybridised to the probe. All errors are given to one standard deviation. All values coloured red were fixed.

MNEE array	Clean	DNA Probe	Target
R_s (Ω)	757 ± 66	757	757
C_{dl} (nF)	104 ± 2	217 ± 6	189 ± 6
C_{dl}/A (µF/cm^2)	253 ± 5	529 ± 15	461 ± 15
R_{ct} (Ω)	16 082 ± 451	72 795 ± 734	42 290 ± 452
R_{ct} × A (Ω.cm^2)	6.6 ± 0.2	29.9 ± 0.3	17.3 ± 0.2
Y_0 (µS)	22 ± 6	22	22
R_{nl} (Ω)	5236 ± 415	5236	5236
χ^2	0.0261	0.2992	0.3139

The values of R_s, Y_0 and R_{nl} have been fixed as for the MNEE with the PNA probe so will not be analysed in detail.

As with all the other data in this chapter there is an increase in R_{ct} when a film forms on the electrode, in this case a 4.5-fold increase. As with the MS array data there is then a 42% reduction in the fitted value of R_{ct} when target binds. This is discussed in relation to the other electrode responses in section 5.4.1 below.

5.4. Discussion

5.4.1. Macro, micro and nano electrodes with PNA in 10 mM KCl

The purpose of this section is to compare the responses of the different electrodes with using the PNA probe. Tables 5.7-5.9 are reproductions of tables 5.4, 5.5 and 5.6; shown next to each other for ease of comparison.

Table 5.7. Reproduction of table 5.4, showing the fitted values and associated errors in the fits to one standard deviation of a Pt macro electrode when clean, after a PNA SAM has been formed and after target hybridisation.

MACRO	Clean	PNA Probe	Target
R_s (Ω)	846 ± 13	846	846
C_{dl} (nF)	1 150 ± 23	-	-
C_{dl}/A (µF/cm^2)	57 ± 1	-	-
CPE Y_0 (nS)	-	2 986 ± 101	1 795 ± 53
CPE Y_0/A (µS/cm^2)	-	148 ± 5	89 ± 3
CPE N	-	0.71 ± 0.01	0.77 ± 0.01
R_{ct} (Ω)	32 366 ± 695	142 760 ± 2 484	229 490 ± 3 435
R_{ct} × A (Ω.cm^2)	651 ± 14	2 869 ± 50	4 613 ± 69
Y_0 (µS)	140 ± 10	142 ± 14	78 ± 6
χ^2	0.1855	0.1289	0.1136

Table 5.8. Reproduction of table 5.5, showing the fitted values and associated errors in the fits to one standard deviation of a Pt 30 µm 3D MS array when clean, after a PNA SAM has been formed and after target hybridisation.

MICRO	Clean	PNA Probe	Target
R_s (Ω)	499 ± 5	516 ± 4	547 ± 6
C_{dl} (nF)	1 020 ± 22	980 ± 12	1 110 ± 17
C_{dl}/A (µF/cm²)	16.5 ± 0.4	15.8 ± 0.2	17.9 ± 0.3
R_{ct} (Ω)	745 ± 20	1 807 ± 45	2 811 ± 150
R_{ct} × A (Ω.cm²)	46 ± 2	112 ± 3	174 ± 9
Y_0 (µS)	103 ± 3	73 ± 4	43 ± 5
R_{nl} (Ω)	4 473 ± 123	4 275 ± 108	5 423 ± 173
χ^2	0.0072	0.0067	0.0136

Table 5.9. Reproduction of table 5.6, showing the fitted values and associated errors in the fits to one standard deviation of a Pt 30 µm 3D MNEE array when clean, after a PNA SAM has been formed and after target hybridisation.

NANO	Clean	PNA Probe	Target
R_s (Ω)	613 ± 9	613	613
C_{dl} (nF)	92 ± 1	265 ± 4	278 ± 4
C_{dl}/A (µF/cm²)	223 ± 2	641 ± 11	673 ± 178
R_{ct} (Ω)	8 372 ± 153	2 280 000 ± 41 600	4 720 000 ± 93 500
R_{ct} × A (Ω.cm²)	3.46 ± 0.06	942 ± 17	1951 ± 39
Y_0 (µS)	22 ± 2	22	22
R_{nl} (Ω)	12 338 ± 332	12 338	12 338
χ^2	0.0636	0.0863	0.56536

The resistance of the solution does not vary significantly when going from clean → PNA probe → target, this allowed the values to be fixed for the macro and nano electrodes, in order to obtain better fits. There is a difference in the values of R_s between the different sized electrodes, this may be down to the human error in weighing out the KCl and FFC, or the error introduced by fitting to a different equivalent circuit in the case of the macro electrode.

On the macro electrode the capacitor in the equivalent circuit has been changed to a constant phase element which makes direct comparison of the values difficult.[104] A capacitor is fit with equation 5.2, whilst a CPE is fit with equation 5.3,[16, 104, 105] where the impedance (Z) is related to the capacitance (C), admittance (Y_0),the frequency in radians, ω, and the correction factor, N .

$$Z = \frac{1}{i\omega C} \qquad \text{(Eqn 5.2)}$$

$$Z = \frac{1}{Y_0(i\omega)^N} \qquad \text{(Eqn 5.3)}$$

The fitted value of 57 µFcm^{-2} for a clean macro electrode is in agreement with the literature.[16] The micro electrode response is of the same order of magnitude but overall slightly lower, this is again in agreement with the literature.[30] The Nanoelectrodes however have a much larger capacitance in agreement with the literature.[30, 113, 114]

The values of the capacitance double layer do not change significantly when going from clean → PNA probe → DNA target on the micro electrode, but increase significantly at each stage

on the nanoelectrode. Measuring the double layer as a sensing technique has become fashionable recently,[12, 14, 96] this data suggests that nanoelectrodes have less error in the fits than macro and micro electrodes so could potentially make superior capacitive sensors. However, the errors reported here are errors in the fitting, not experimental errors. As stated above, it is the authors belief that the increase in capacitance when a probe film on the MNEE arrays is formed is due to an experimental error as it is counter intuitive and not in-keeping with the literature.[79] The formation of a neutral SAM film on the electrode should reduce the solvent accessible electrode surface area and cause a decrease in capacitance.[78, 79]

By far the largest change in any of the fitted elements is in R_{ct}; with each electrode showing an appreciable change in R_{ct} as the probe film forms and target binds. One of the aims of these experiments was to determine if different probe film phases would form on the nanoelectrodes as their dimensions are of the same order of magnitude as the persistence length of the PNA probe. It can be seen that the impedance increase 4.4-fold on a macro electrode when a PNA probe film is formed on the clean electrode. A 2.4-fold increase is observed for the same experiment on the MS array, however, the charge transfer resistance increases 272-fold when a PNA probe film is formed on an MNEE array. This change in resistance is indicative that a much more resistive film is formed on the nano electrodes than the macro and micro electrodes. Whilst the theory of a splayed-out film forming might explain this increase in impedance it should be made clear that it is still just hypothesised as a result of this data. Only direct imaging of the PNA probe SAM layer on a nanoelectrode with AFM/STM or other such techniques can prove beyond a doubt the phase of the film. Again, these techniques are not possible on these MNEE arrays due to their architecture preventing an AFM tip from reaching the electrode surface. Until such concordant experiments have been run on nanowires or other planar nano electrode systems all this data can say for certain is that more resistive PNA films are formed on nanoelectrodes.

When DNA target binds to the probe there is a 1.6-fold increase in R_{ct} on the macro electrode, a 1.6-fold increase on the MS array and a 2-fold increase on the MNEE array. These relative increases are all very similar which would indicate that the more resistive film formed on nano electrodes is not that much better able to bind target than the films formed on macro and micro electrodes. However, the absolute values measured on the MNEE arrays would mean that they will make much more sensitive sensors. In these experiments the target was incubated on the probe film overnight so as to obtain a film at thermodynamic equilibrium of bound and unbound target. Bearing this in mind it may be that the proximity of neighbouring probe-target hybrids is limiting the target surface coverage. The phosphate backbones of bound target sequences can repel incoming target strands, limiting the surface target density. This spacing is a result of the effect that neighbouring bound target sequences have on each other so will not be in any way affected by the electrode area. The target sequence used here is a 30 base sequence designed to have a 15 base overhang, testing with different length targets would inform as to whether or not this theory is correct, with shorter less charged films in theory resulting in more densely packed films. However, the reduced number of negative charges in the film would lessen the repulsion of the FFC. In short the experiments put forward here only show that target binding reaches a steady state that causes the approximately same relative increase on macro, micro and nano electrodes. Further analysis using other techniques warrants future investigation to visualise the film structure when DNA target has bound to the PNA probe.

Due to the nature of the fit, it may be that the values of Y_0 fitted for a macro electrode are thrown off by the switching to a constant phase element from a capacitor, as there is a region of overlap between the two semi-circles. As a result, the changes in admittance on the macro electrode will not be analysed in depth, all that can be ascertained from this dataset with any confidence is that Y_0 decreases upon target hybridisation. This is to be expected as the inclusion of a negative charge within the film will repel the FFC redox couple, thereby reducing the admittance and slowing the flux of redox agent. The diffusion coefficient of the redox agent can be calculated from Y_0 using equation 5.4, where the diffusion coefficient, *D*, is determined from the admittance, Y_0, where R is the universal gas constant, *T* is the temperature, *n* is the number of electrons being transferred, F is Faraday's constant, *A* is the area of the electrode and c_0 is the concentration of the redox species being investigated in the bulk of the solution.

$$D = \left(\frac{2RTY_0}{n^2F^2Ac_0}\right)^2 \qquad \text{(Eqn 5.4)}$$

From equation 5.4 it can be seen that *D* and Y_0 are directly proportional, if Y_0 decreases as target binds to the probe then the diffusion coefficient is also decreasing and flow of FFC to the electrode is being impeded. On the macro electrode Y_0 decreased to 0.54 times the value with just probe present, on a micro electrode the same process reduces Y_0 0.59 times, which would indicate that the flow of FFC is being impeded to the same extent in both systems. On the MNEE arrays these values have been fixed so cannot be analysed. It was very difficult given the shapes of the responses to ascertain good fits for the second hemisphere as it is so small relative to the first semi-circle. In other words, the signal is swamped by the change in R_{ct} and although Y_0 will theoretically decrease, it cannot be observed. A more accurate fit of the parameters of the first semi-circle is obtained by fixing the elements of the second semi-circle. Although this is not an ideal solution to the problem; the macro and micro electrode data in tables 5.7 and 5.8 show that these parameters in the second hemisphere are all of the same order of magnitude and the χ^2 values reflect the difficulties in fitting to the MNEE with target bound to the same equivalent circuit as the previous data.

The values of R_{nl} can clearly not be compared between all the electrodes as the it is not part of the Randles' circuit used to fit the macro electrode and needed to be fixed to get reasonable fits for the nano electrode. Going off of the micro electrode data there is no appreciable change in R_{nl} when a PNA probe film is formed and a relatively minor but significant increase when target binds. At the risk of repetition this also indicates that the negative charge introduced by target binding is repelling the FFC in solution. The decision to fix R_{nl} for fitting to the MNEE array was based on the assumption that the changes in R_{nl} were less significant than the changes in R_{ct}.

5.4.2. Comparison of DNA and PNA probes in 10 mM KCl

The purpose of this section is to compare the responses of the different PNA and DNA probes. Tables 5.10 and 5.11 are reproductions of tables 5.5 and 5.6; shown next to each other for ease of comparison.

Table 5.10. Reproduction of table 5.5, showing the fitted values and associated errors in the fits to one standard deviation of a 30 µm 3D MS array when clean, after a DNA SAM has been formed and after target hybridisation.

MS array	Clean	DNA Probe	Target
R_s (Ω)	454 ± 14	434 ± 13	443 ± 12
C_{dl} (nF)	912 ± 81	1270 ± 52	971 ± 98
C_{dl}/A (µF/cm^2)	14.7 ± 1.3	20.5 ± 0.8	15.7 ± 1.6
R_{ct} (Ω)	561 ± 56	1560 ± 209	393 ± 55
$R_{ct} \times A$ (Ω.cm^2)	35 ± 3	97 ± 13	24 ± 3
Y_0 (µS)	84 ± 7	33 ± 4	71 ± 4
R_{nl} (Ω)	2554 ± 66	4403 ± 180	2987 ± 59
χ^2	0.0401	0.0157	0.0250

Table 5.11. Reproduction of table 5.6, showing the fitted values and associated errors in the fits to one standard deviation of a Pt 30 µm 3D MNEE array when clean, after a DNA SAM has been formed and after target hybridisation.

MNEE array	Clean	DNA Probe	Target
R_s (Ω)	757 ± 66	757	757
C_{dl} (nF)	104 ± 2	217 ± 6	189 ± 6
C_{dl}/A (µF/cm^2)	253 ± 5	529 ± 15	461 ± 15
R_{ct} (Ω)	16 082 ± 451	72 795 ± 734	42 290 ± 452
$R_{ct} \times A$ (Ω.cm^2)	6.6 ± 0.2	29.9 ± 0.3	17.3 ± 0.2
Y_0 (µS)	22 ± 6	22	22
R_{nl} (Ω)	5236 ± 415	5236	5236
χ^2	0.0261	0.2992	0.3139

The exact same electrodes were used as for the PNA probe tests to avoid any irreproducibility between electrodes, the SAMs were cleaned off using the process outlined in chapter 3.2.3. It is therefore satisfying that the clean electrode fits are the same within error as those in the PNA probe experiment, tables 5.10 and 5.11. The only exceptions to this agreement are the fitted values of R_{nl} on the MS array and R_{ct} and R_{nl} on the MNEE arrays. These deviations do not change the order of magnitude of the fitted values so are most probably due to random errors in the experimental set up such as fluctuations in temperature or incomplete oxide removal.

The fitted values of R_s are the same within error as the PNA experiments and like in those experiments do not change as the electrode goes from clean → DNA probe → DNA Target.

The fitted values of the capacitance double layer on the MS array are again constant within error at each stage of the biosensing process as well as being the same within error as in the PNA experiments. On the MNEE arrays there is again a change outwith the errors in the fit. As before such changes in C_{dl} could be caused by random errors in the experimental set up and cannot be treated as significant as there is no corresponding change in the micro electrode response. Even though in this case there is some literature to support an increase in the size of the double layer on DNA film formation as the charge of the phosphate backbone increases the cation concentration at the electrode surface.[79]

As before the changes in the charge transfer resistance are much greater than those for any other fitted element. Forming a DNA probe film layer on the MS array causes a 2.8-fold

increase in R_{ct}, comparable to the 2.4-fold increase when a PNA probe film was formed on the same electrode. This would imply that the different probes form very similar films on the micro electrode. On the MNEE array the PNA probe caused a 272-fold increase in R_{ct}, the DNA probe on the same electrode caused a 4.5-fold increase in R_{ct}. It is clear that a much more resistive PNA probe film is formed on the MNEE array than the DNA probe film. The charge on the DNA must therefore be affecting the packing density of the probe film. It is interesting to note that the two different probes make equally resistive films on the micro electrodes. The charge of the DNA probe means that it should repel the FFC more than the PNA probe. It may therefore be the case that the DNA probes in the film are spaced further apart, reducing the film coverage but their charge is repelling the FFC and the combination of these effects has coincidentally formed a probe film equally resistive to charge transfer as the PNA probe. On the MNEE arrays the charge of the DNA probe has prevented it from adopting the resistive film conformation that the PNA probe adopted. This may be as a result of packing constraints.

PNA is known to be more "sticky" than DNA because of its neutrality so can stick to itself and its neighbours,[108, 112] it may be that the probe is forming aggregates with nearby probe molecules bound to the electrode and in solution to create a denser film. This would be less likely to happen with a DNA probe as it is less prone to non-specific hybridisation. If the probe is in the ϕ-phase on the micro electrodes there is steric blocking of probe in solution from binding into the film, thus a splayed out film on a nanoelectrode might conceptually be more likely to form aggregates, figure 5.15.

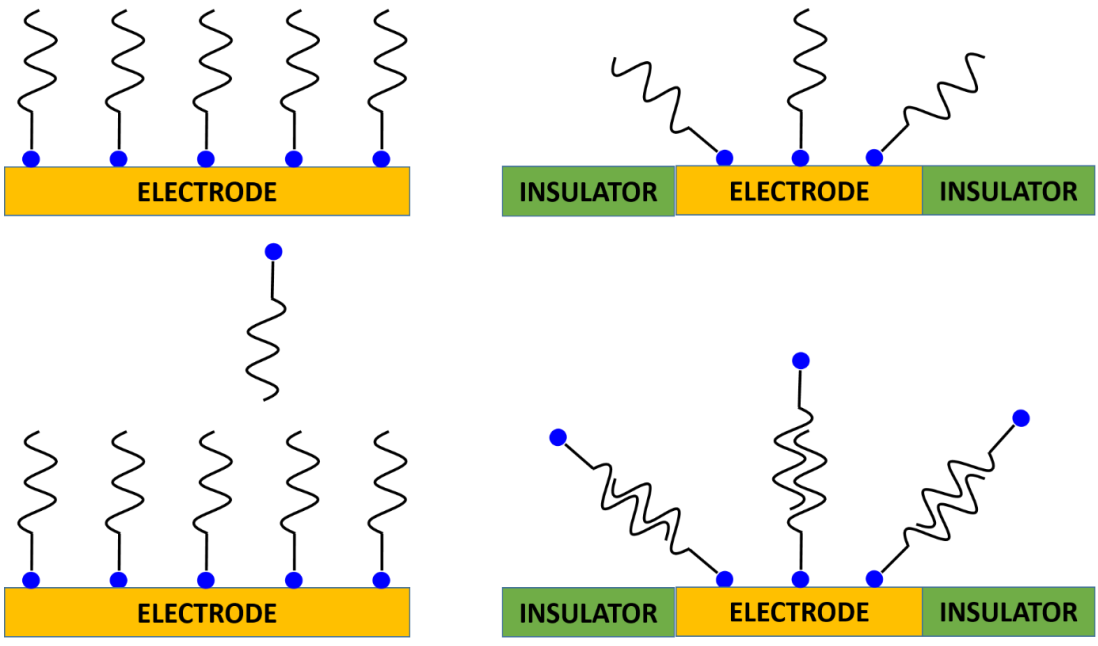

Figure 5.15. Schematic representation (NOT TO SCALE) of the proposed probe structure on a macro electrode (TOP LEFT) and on a planar nanoelectrode (TOP RIGHT). The steric blocking of aggregate formation of the macro electrode film structure has been given (BOTTOM LEFT) next to the likely aggregate structure on the nanoelectrode (BOTTOM RIGHT) made possible by a hypothetical splayed out film orientation.

When the DNA probe film forms on the MNEE array its relative change in impedance is greater than that formed on the MS array. This is again indicative of a more resistive film structure being formed on the nanoelectrodes. However, the increase in impedance of the film when going from micro to nano electrodes is far smaller using the DNA probe than the PNA probe. It can therefore be concluded that the film structure on nano electrodes is much more sensitive to charge than the structure on the micro electrodes. This may be because the charge on the probe makes aggregate formation less likely, or the structure of the film brings like charges into closer proximity to one another, although the splayed out structure proposed has a greater spacing between the probe tails than the classical ϕ-phase film structure, it may be the case that the nucleotide closest to the thiol linker is closer to its counterpart on a neighbouring probe, figure 5.16. Again, this is all speculative and only direct imaging of the different probes will yield the true structure of the film.

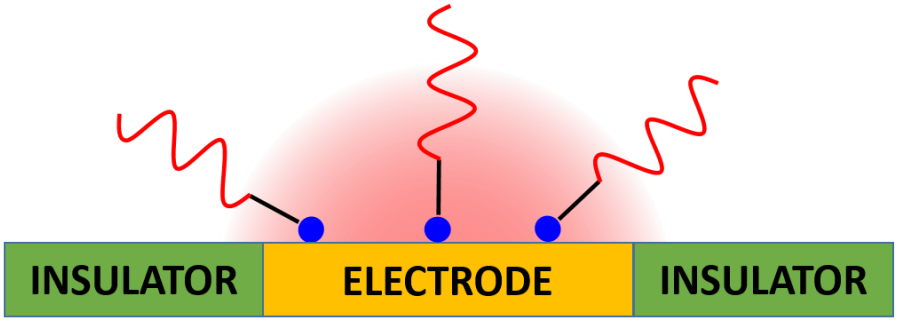

Figure 5.16. Schematic representation of the postulated DNA probe film on a MNEE (NOT TO SCALE). The DNA has been coloured red to denote negative charge and the stress within the film has been shown by the red shading.

Target binding to a DNA probe causes a decrease in impedance whereas binding to a PNA probe causes an increase in impedance. Target binding to PNA probe has been discussed above and showed a 1.6-fold increase in R_{ct} on macro and micro electrodes and a 2-fold increase in R_{ct} on nano electrodes. Target binding to a DNA probe decreased in R_{ct} of 75% on the MS array, back to within error the same value as the clean electrode. On the MNEE array, R_{ct} decreased by 42% from the fitted DNA probe resistance. There are various explanations in the literature of phenomenon that can decrease the impedance on target binding.[100, 101, 115] One such explanation is the binding of target causes the globular single stranded probe to become more rigid when target binds, this opens up channels within the film for the redox agent to pass through and lowers the impedance of the film.[100] It is possible that this effect is taking place here as the decrease is greater on the micro electrode system than the nano electrode may be as a result of the film structure on the nanoelectrodes being different. The change in structure to a more rigid probe which blocks a smaller relative area of the electrode will logically have a larger effect on more tightly packed probe film layers.

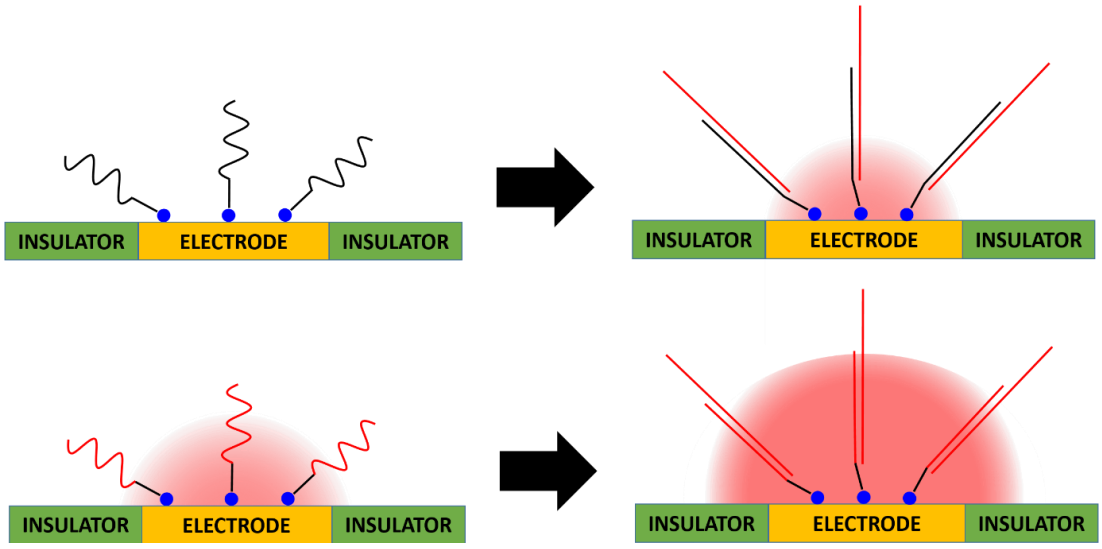

Figure 5.17. Schematic representation (NOT TO SCALE) of PNA (TOP) and DNA (BOTTOM) probe film on MNEE as target binds. The DNA has been coloured red to indicate negative charge and the red shading is intended to convey the stress in the film as a result of increased charge density at the electrode surface.

Another possible explanation is that target binding is causing a degradation of the probe film. When DNA target binds to a DNA Probe film there is a lot of like charge localised in a small volume; this increased stress within the film may cause the probe to dissociate and create pinholes in the SAM, reducing the impedance. A schematic representation of this process is given in figure 5.17. This is again more likely to occur on the DNA probe than the PNA probe as the charge density, and therefore stress, will be greater. This effect could theoretically be lessened by performing the experiments at higher ionic strengths, where the charges will experience more shielding from each other. It is therefore encouraging that in figures 5.10-5.14, the data consistently shows a relatively smaller decrease in impedance upon target binding as the concentration of supporting electrolyte increases.

Thermodynamically if the DNA-DNA hybridisation energy is lower than the Pt-S bond enthalpy then rather than thiol dissociation to create pinholes the target would simply de-bind from the probe to reduce stress. The strength of a hydrogen bond in water is 20 $kJmol^{-1}$.[60] Since the bases in complimentary stands of DNA are held together by either 2 or 3 hydrogen bonds depending on the bases, and the sequence is 15 bases long the minimum hybridisation enthalpy (for 15 A=T bonds) would be 600 $kJmol^{-1}$; much larger than the Pt-S bond enthalpy which is thought to be similar to the Au-S bond enthalpy of 254 kJ mol^{-1}.[43] Therefore the thermodynamics would indicate that Pt-S bond dissociation is a more favourable method of reducing the stress in the film than target de-hybridisation.

If the increased impedances are caused by aggregate formation, then it is possible that the observed changes upon target binding are the result of disrupting the aggregate layers formed. Again it must be stressed that the true nature of the films cannot be discerned by EIS alone, all that can be properly concluded from these data are that the DNA probe film becomes less resistive upon target binding, with a larger relative change occurring on micro electrodes than nano electrodes. There is however a more resistive DNA probe film formed on nanoelectrodes than micro electrodes which would indicate that a film of a different structure has been formed and this film is better able to cope with the stress induced by charged target binding. Although the change in impedance is lower for the nanoelectrodes

using the DNA probe the absolute values of the resistances measured are much higher so they will make more sensitive sensors.

As the concentration of supporting electrolyte increases the change in impedance upon target binding can be seen to decrease. This adds weight to the charge induces stress theory as there is more shielding in the film at higher ionic strengths and therefore the changes in impedances are visibly reduced. However, this may also be due to increased shielding of the FFC from the film.

The fitted values of Y_0 decrease when a DNA probe layer is formed on a micro electrode. The values for the MNEE array needed to be fixed so cannot be discussed. When a PNA probe film is formed on a clean electrode there is a decrease of 30 μS or put another way the value decreases by 29% the clean value. When a DNA probe film is formed on the same electrode using the same protocol the fitted value of Y_0 decreases by 51 μS, 61% lower than the fitted clean value. Thus, the DNA probe causes double the decrease in admittance on a micro electrode than the PNA probe. This is undoubtedly as a result of the charge of the DNA probe repelling the FFC.

When target DNA binds to the PNA probe there is a further decrease in admittance, again by 30 μS, 42% lower than the fitted PNA probe value. When target binds to the DNA probe there is an increase in admittance with a 2.15-fold increase when going from DNA probe to DNA probe-target hybrid. The only explanation for this is a loss of charge from the film. This is concordant with the theory of film degradation as discussed for R_{ct}, as it is the only model that accounts for the removal of charge from the film upon target binding.

For the PNA probe there was no appreciable change in R_{nl} when a probe film formed, but a 1.27-fold increase when charged target is bound into the film on a micro electrode. As with the admittance, the values are fixed for nanoelectrodes so cannot be analysed. When a DNA probe film is formed on the MS array there is a 1.72-fold increase, again since there was no increase in R_{nl} at this stage using a PNA probe this must be an effect of the charge, it is also satisfying that at higher ionic strengths the change in R_{nl} upon DNA probe film hybridisation is lessened due to shielding of the FFC from the probes. The fitted target value then drops by 33% from the fitted probe value; this is again a feature of the stress introduced into the film upon target hybridisation causing the degradation of the SAM and making it easier for the FFC to flow to the electrode.

5.4.3. Limits of detection studies on MNEE arrays

Due to time constraints the limits of detection studies were only performed on the MNEE arrays in 500 mM KCl supporting electrolyte. They were performed using both PNA and DNA probes.

5.4.3.1. Limit of detection on an MNEE array with a PNA probe

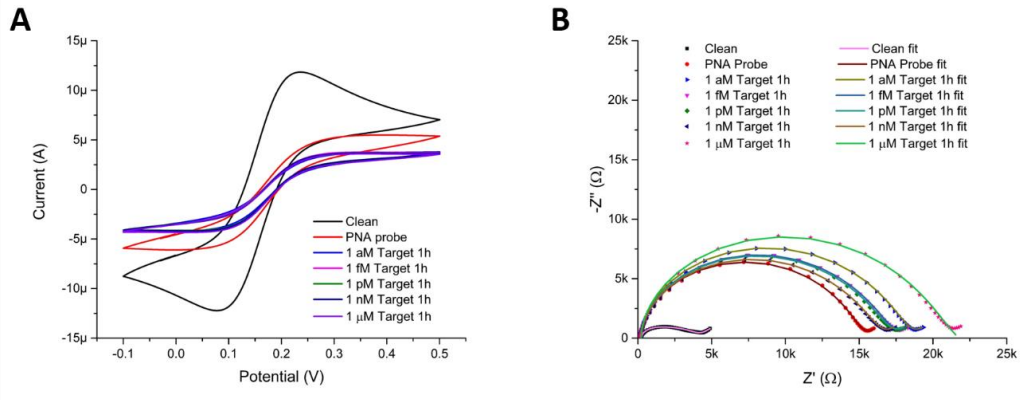

Figure 5.18. (A) Cyclic voltammograms (B) Nyquist plots of a 30 µm 1D MNEE array when clean (black) with PNA probe (red) and after successive incubations with increasing concentrations of 30 mer Target DNA (as indicated in the legend). All CVs were recorded at 10 mVs^{-1} and all EIS at OCP vs a saturated calomel reference electrode and Pt gauze counter electrode in a solution of 1 mM ferricyanide, 1mM ferrocyanide and 500 mM KCl.

It was decided that limits of detection studies should be carried out for the MNEE in the 500 mM KCl buffer to ascertain what changes in each element would occur when different amounts of target had bound to the probe monolayer, and this buffer gave the best resolution between the two semi-circles. The clean electrode was hybridised as above with a PNA probe before being incubated in target of increasing concentration for 1h intervals with CVs and EIS recorded after each exposure. The CVs show a drop in maximum current from probe → target of 5.5 µA → 3.5 µA on the forward oxidation scan and -6.1 µA → -4.3 µA on the reductive reverse scan after leaving the probe film in 1 aM target for 1h, figure 5.18. If the 100 mM KCl buffer were used it is not unreasonable to assume that limits of detection for the 30 mer DNA target using this PNA probe could be further reduced. Such low limits of detection are naturally met with some scepticism but there is precedent in the literature for measuring such low analyte concentrations by similar mechanisms.[32, 116, 117] This process was published as having femtomolar limits of detection on macro electrodes[18] so it is not unreasonable to assume sub-attomolar LOD's could be achieved when the process is optimised for nanoelectrodes.

There is also concern that there may not be sufficient probe target double helices on the electrode surface to give a measurable signal. The 30 µm 1D MNEE array has a total geometric surface area of 4.13×10^{10} nm^2. Watson and Crick base pairing tells us that the diameter of a double stranded DNA helix is 2nm. So, if each probe-target double helix is treated as occupying a cyclindrical volume perpendicular to the electrode, then the total electrode surface area occupied by each double helix is approximately 3.14 nm^2. Ignoring packing constraints and electrostatic repulsion between neighbouring helices, it is theoretically possible to calculate the maximum possible number of double helices that could fit on the electrode area by dividing 4.13×10^{10} nm^2/3.14 nm^2 = 1.3×10^{10} double helices. Although there will undoubtedly be less than this due to steric and electrostatic packing

constraints as well as the assumption of all double helices occupying a volume parallel to the electrode area being unrealistic on a nanoelectrode where a splayed-out probe structure is likely. When there are aM concentrations of target present, there are 1 $\times 10^4$ target ssDNA molecules in solution. It should be noted that the actual number is likely to be quite variable due to the practical difficulties in making up solutions of such small concentrations and may be lower due to non-specific binding of target molecules to eppindorf tubes, pipette tips, etc. However, if the assumption is made that the probe SAM is exposed to a solution containing 1 $\times 10^4$ target molecules and they all bound to the available probe molecules then there is still only a very small fraction of the probe molecules binding to target, only 1 in every million PNA probe strands will have bound to a DNA target oligomer. It is therefore important that the control experiment with a non-complimentary DNA sequence be performed in future to rule out other changes in the system causing this change in impedance.

The addition of further target has no apparent effect on the voltammetry; as voltammetry is not a sensitive enough technique to analyse any changes on the addition of more signal. The EIS yielded more information as to the effects of adding more target.

Table 5.12. Fitted values and errors for each element from the fits in figure 5.18.B above; for a 30 µm 1D MNEE array when clean, saturated with PNA probe and when different concentrations of target have hybridised to the probe. All errors are given to one standard deviation. The values in red were fixed for fitting and taken from the clean electrode fit.

	Clean	PNA Probe	1 aM Target	1 fM target	1 pM target	1 nM target	1 µM Target
R_s (Ω)	169 ± 4	376 ± 67	431 ± 92	433 ± 91	433 ± 92	420 ± 88	468 ± 107
C_{dl} (nF)	87 ± 1	176 ± 3	160 ± 3	174 ± 4	177 ± 4	178 ± 4	178 ± 4
C_{dl}/A (µF/cm²)	210 ± 2	425 ± 8	387 ± 8	420 ± 10	429 ± 10	431 ± 10	431 ± 10
R_{ct} (Ω)	774 ± 38	13 489 ± 97	16 332 ± 135	15 166 ± 134	14 996 ± 135	14 366 ± 129	18 599 ± 162
R_{ct}*A (Ω.cm²)	0.32 ± 0.02	5.58 ± 0.04	6.75 ± 0.06	6.27 ± 0.06	6.20 ± 0.06	5.94 ± 0.05	7.69 ± 0.07
Y_0 (µMho)	13.0 ± 0.5	13.0 ± 0.5	13.0 ± 0.5	13.0 ± 0.5	13.0 ± 0.5	13.0 ± 0.5	13.0 ± 0.5
R_{nl} (Ω)	2 185 ± 37	2 185 ± 37	2 185 ± 37	2 185 ± 37	2 185 ± 37	2 185 ± 37	2 185 ± 37
χ^2	0.0092	0.0603	0.0812	0.0908	0.0942	0.0934	0.0914

The Nyquist plots over-layed in figure 5.18 and the corresponding fit data in table 5.12 show that when going from clean → PNA probe → Target there is an overall increase in R_{ct} at every stage as expected.

EIS is known to be one of the most sensitive electrochemical techniques and as such a change is seen in the signal when more target binds to the probe that could not be seen in the CVs. EIS is, however, a controversial technique and some may attribute these changes to the enhanced sensitivity of the technique picking to random experimental errors.[17] Small fluctuations in temperature, the act of taking repeat measurements and possible changes to the SAM structure over this timescale (as discussed in chapter 4) could cause the reader to assume that the changes discussed here are random experimental errors rather than trends.[17] With the DNA probe below a control was run with a mismatched DNA target sequence that caused no significant change in R_{ct}, within the fitting error. As such the changes in R_{ct} outwith the error in the fits will be presumed significant. Not running the same control experiment on the PNA probe was an oversight and should be included in future work.

The fitted values of R_s are constant within three standard deviations of the error in the fit. The error in the fit increases as the semi-circles get bigger, this is a product of the fitting software and cannot be helped without fixing the value of R_s.

The capacitance double layer is thought to remain constant as it did in the previous data presented in this chapter. The increase from clean to probe may be, like R_s as a result of fitting to a much larger semi-circle.

The fitted value of R_{ct} increases 17 fold when going from clean → PNA probe. This is lower than the that observed at lower ionic strengths because of the charge transfer is being limited by the flow of FFC to the electrode surface which is dependent on counter ions to balance the charge at the electrode and reduce the field effects of accumulating FFC at the electrode surface. There is then a 1.2-fold increase in R_{ct} upon 1 aM target binding, due to the Donnan effect between the FFC and the target hybridised film. The effects of increased shielding at in 500 mM KCl means this increase is smaller than the 2-fold increase seen in 10 mM KCl buffer. Further target binding causes a gradual decrease in R_{ct}. It is not known whether this is a real effect of further target hybridising into the probe film or just the gradual degradation of the film over the course of the experiment (each incubation step lasted 1h). Incubation with 1 µM target overnight then causes an increase in impedance to 1.3 times the impedance measured after the 1 nM incubation. This is could be due to the formation of platinum oxide on bare patches of the electrode. Oxide removal was not attempted during the course of these experiments for fear of disrupting the SAM layer.

5.4.3.2. Limits of detection on an MNEE array with a DNA probe

The limits of detection for the MNEE with a DNA probe were calculated using the same experiment as for the PNA Probe. These were therefore performed in the 500 mM KCl buffer which, although the most appropriate so as to compare to the PNA probe, gave the smallest change in impedance for the DNA probe experiments.

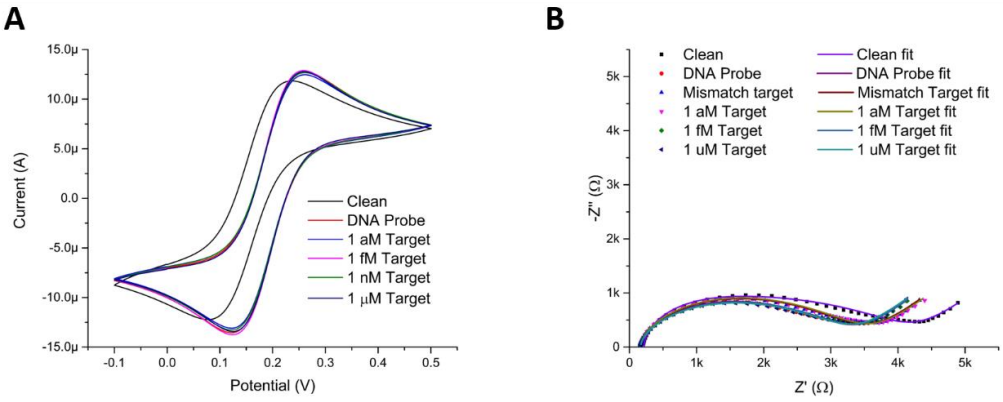

Figure 5.19. (A) Cyclic voltammograms (B) Nyquist plots of a 30 µm 1D MNEE array when clean (black) with DNA probe (red) and after successive incubations with increasing concentrations of 30 mer Target DNA (as indicated in the legend). All CVs were recorded at 10 mVs^{-1} and all EIS at OCP vs a saturated calomel reference electrode and Pt gauze counter electrode in a solution of 1 mM ferricyanide, 1mM ferrocyanide and 500 mM KCl.

The cyclic voltammograms show an increase in peak current when the film is formed on the MNEE arrays, this may be the result of experimental errors as discussed in section 5.3.3.2. There is a minor change in peak current when target binds to probe but the changes are not as great as those observed when using a PNA probe. As before the changes EIS data is more

informative than the voltammetry. The equivalent circuit fits for the Nyquist plots in figure 5.19 are given in table 5.13.

Table 5.13. Fitted values and errors for each element from the fits in figure 5.19 above; for a 30 µm 1D MNEE array when clean, saturated with DNA probe and when different concentrations of target have hybridised to the probe. All errors are given to one standard deviation.

Element	Clean	DNA probe	1 nM DNA mismatch	1 aM Target	1 fM Target	1 µM Target
R_s (Ω)	217 ± 9	160 ± 1	158 ± 1	162 ± 1	157 ± 1	166 ± 1
C_{dl} (nF)	97 ± 3	130 ± 2	127 ± 2	127 ± 2	122 ± 2	123 ± 2
C_{dl} (nF/m^2)	2.35 ± 0.07	3.15 ± 0.05	3.07 ± 0.05	3.07 ± 0.05	2.95 ± 0.05	2.97 ± 0.05
R_{ct} (Ω)	1059 ± 49	350 ± 34	352 ± 36	383 ± 37	279 ± 34	327 ± 31
$R_{ct} \times A$ (µΩ.m^2)	44 ± 2	14 ± 1	15 ± 1	16 ± 2	12 ± 1	14 ± 1
W or Y_0 (µS)	17.3 ± 0.8	12.6 ± 0.4	12.0 ± 0.4	11.9 ± 0.4	12.6 ± 0.4	13.1 ± 0.4
R_{nl} (Ω)	2970 ± 46	2856 ± 31	3054 ± 34	3054 ± 35	2954 ± 33	2857 ± 29
χ^2	0.0091	0.0047	0.0050	0.0052	0.0052	0.0049

As with the PNA experiments the values of R_s and C_{dl} do not vary significantly, as a result they will not be analysed in any great detail.

There is no significant deviation of R_{ct} in these experiments, it is interesting to note that at the higher ionic strength there is more shielding between neighbouring probe strands. Albeit the fitted value of R_{ct} with a DNA probe film layer is still much lower than that of a PNA probe SAM. In the 500 mM KCl buffer the DNA probe fitted value is 37 times lower than the PNA probe value, whereas in the 10 mM KCl buffer the value it is 4 310 times lower. This proves beyond doubt that the probe packing is being controlled to some extent by the charge within the film.

There is a decrease in R_{ct} when going from clean to probe, this is most likely an experimental error and repeat measurements should be taken to analyse if this effect is real before being discussed in greater detail. Unfortunately, due to time constraints repeat experiments could not be undertaken through the course of this project. What is clear is that the changes in R_{ct} on the addition of more target are not significant. R_{ct} was seen to decrease significantly when target bound in 10 mM KCl buffer, this was justified as being because the stress introduced into the film by target binding causing degradation of the SAM structure. At higher ionic strengths, this effect is clearly lessened by increased shielding of neighbouring DNA backbones in the film.

5.5. Conclusions and future work

The main highlight of this work is that there are potentially sub-attomolar limits of detection on MNEE arrays, although the control for this experiment should be done as the main priority of any future work. This is an improvement on the published fM limit of detection observed for the same probe on macro electrodes.[18] What can be concluded from these experiments is that there is an optimum ionic strength for each probe. The electrochemistry of the probe film formed on nanoelectrodes is seen to be different to that on macro and micro electrodes, this is rationalised as being caused by the probe having a different structure within the film or possibly by aggregate formation. Analysis of probe film SAMs by direct imaging techniques is necessary to determine the true nature of the films formed. These imaging techniques could not be used on MNEE arrays due to their architecture preventing AFM or STM tips from reaching the electrode surface. As discussed in chapter 4.5, the electrodes should be fabricated on glass wafers so as to allow optical imaging of the electrode surface to rule out aggregate formation. Also the experiments should be repeated on nanowires to allow AFM and/or STM imaging of the probe film structure to determine its true structure.

It was found that the nano electrodes were more sensitive to changes in the film structure than macro and micro electrodes, with the greatest change in any fitted parameter occurring to the charge transfer resistance. An increase in R_{ct} was observed upon target binding to a PNA probe, with the MNEE array displaying sub attomolar limits of detection in a 500 mM KCl buffer. The binding of target is rationalised as increasing the impedance of the film by sterically and electrostatically increasing the films impedance of the FFC redox couple (the Donnan effect).

When a DNA probe is used, a decrease in impedance is observed upon target binding; this was explained by the increase in localised charge at the electrode surface when target binding causing so much stress within the film that the probe film degrades. Further evidence for this hypothesis came from performing the experiments at different ionic strengths and it was seen that there was a greater breaking apart of the film at lower ionic strengths where the charges within the film experience less shielding from the supporting electrolyte.

6. Electrochemically trigger hydrogels to map diffusion fields and prevent biofouling

NOTE: the following chapter has been written into a paper that at the time of writing is under review for publication. Said paper has been attached at the end of this chapter.

6.1. Introduction

Both nanoelectrodes and hydrogels have received much interest from the biosensing community in recent years.[11, 100, 118-120] The benefits of nanoelectrode arrays (enhanced sensitivity, enhanced response rate, insensitivity to convection) have already been extensively covered in the introductory chapter of this thesis so will not be repeated here. Hydrogels are water rich, biocompatible matrices known to be permeable to small molecules.[121] Properties of hydrogels beneficial to biosensing include their ability to encapsulate and support biomolecules on an electrode surface[119, 122-124] (thereby increasing their stability, activity and longevity) and to prevent larger biomolecules from reaching and fouling electrode surfaces.[125] The objective of this chapter is to study the formation of hydrogels at a nanoelectrode array.

This work was done in collaboration with Prof Dave Adams and Dr. Ben Alston from the University of Liverpool, who have previously reported the electrochemically induced gelation of hydrogels at an electrode surface.[126] A pH drop localised at an electrode surface can be induced by reducing hydroquinone to para-benzoquinone as shown in equation 6.1 below:[126]

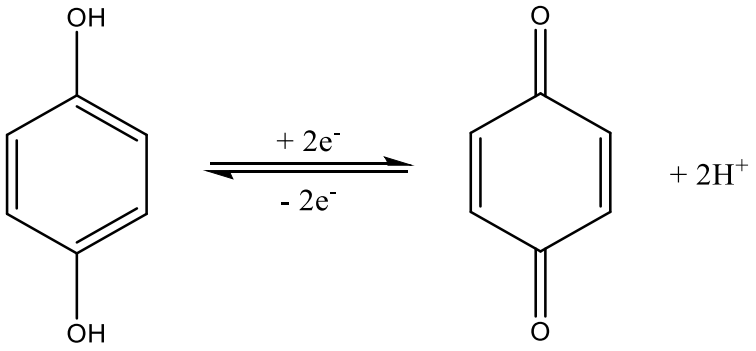

Hydroquinone para-benzoquinone (Eqn 6.1)

By using gelators whose gelation is initiated by an acidic pH swing it is therefore possible to electrochemically induce hydrogel formation at an electrode surface. It was the aim of this collaboration to electrochemically induced hydrogel formation at MNEE arrays, and study the structure and the resulting properties both electrochemically and optically. The anti-biofouling properties of the hydrogel were also then assessed by exposure to bovine serum

albumin (BSA) which is a well understood biofouling molecule used in the literature as a biofouling standard.[127, 128]

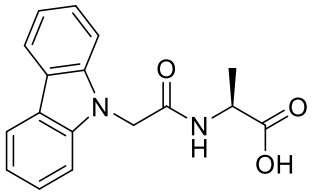

Figure 6.1. The molecular structure of carbazole alanine.

The gelator used in this project was carbazole alanine, figure 6.1, the hydrogel grows as fibres of π-π stacked monomers with the alanine free to hydrogen bond to water molecules and neighbouring fibres.[129] SEM images of these fibres are given in figure 6.11. Assembly is known to only be initiated at low pH's with the removal of charge from the acid portion of the alanine.[130] The theory is that the deprotonated, charged, form of the molecule will not be able to π-stack with other molecules due to electrostatic repulsion between molecules. When the pH decreases the acid region of the molecule becomes protonated, removing its charge allowing stacking to take place and gelation to occur.

6.1.1. Hydrogel imaging

Previous simulations done within the Mount group had shown that the corners of the MNEE cavities have enhanced current densities where the diffusion fields of the bands on neighbouring cavity walls overlap.[30, 61] If hydrogel growth, controlled by the local pH change, were diffusion limited at nanoelectrodes, this should result in enhanced hydrogel growth in the corners of the cavities and hence a resulting hydrogel structure which reflects the inhomogeneous diffusion field. In order to investigate this, the hydrogels were grown for different time periods on the electrodes and imaged using light microscopy, confocal microscopy and scanning electron microscopy. These optical studies were complemented by electrochemical characterisation, to probe their porosity, through their permeability to redox agents.

The hydrogel structure was characterised optically using three techniques: light microscopy, scanning electron microscopy (SEM) and confocal microscopy.

6.1.1.1. Light microscopy

Light microscopy was used to image the native hydrogels; as they are highly hydrated and colourless, their refractive index is very similar to the surrounding aqueous medium the hydrogel needed to be removed from solution to obtain sufficient contrast. However, as the water evaporates at a faster rate from the surrounding MNEE insulator than from the hydrogel the essentially hydrated hydrogel was observed if left to sit and dry for a couple of minutes. This was a quick and easy method for checking the progress of hydrogel growth. Typical images of hydrogels analysed in this method are given in figure 6.2.

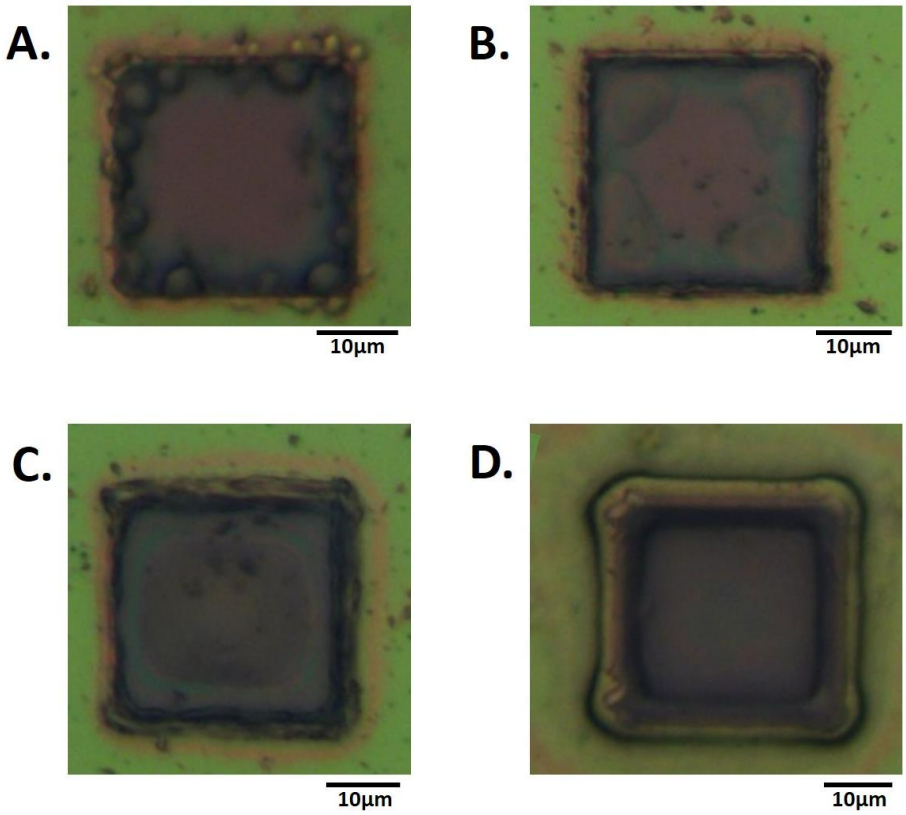

Figure 6.2. Typical images of carbazole alanine hydrogels grown on MNEE arrays and imaged under an optical microscope after being allowed to partially dry in the atmosphere.

6.1.1.2. Scanning electron microscopy (SEM)

A brief introduction to SEM can be found in chapter 1.5.1. Since there is a necessity to perform SEM measurements under a vacuum the technique cannot be used to image the hydrogels in a hydrated state, dehydrated hydrogels are commonly referred to as xerogels. SEM allows for the high resolution characterisation of the xerogel structure (the organic hydrogel framework), which is particularly applicable to the study of the nanostructure of the xerogel when attached to the MNEE. As stated in chapter 1.5.1, the charging of metals in a sample can distort the image. The carbazole alanine xerogel also charges and can be damaged by the intense electron beam. As such the samples needed to be sputtered with gold prior to imaging, see section 6.2.3. The gold nanoparticles on the sample absorb a lot of the charge from the electron beam and reduce this damage.

6.1.1.2. Confocal microscopy

Confocal microscopy is an imaging technique used only in this chapter. It involves growing the hydrogels in the presence of a Nile blue stain, figure 6.3, which intercalates with the carbazole alanine π-π stacked polymer as it forms.

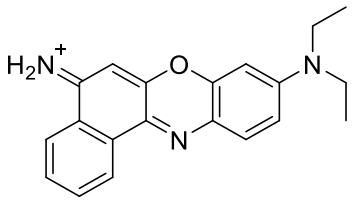

Figure 6.3. The molecular structure of Nile Blue.

Confocal visible light microscopy using a Nile blue stain has previously been reported as a suitable technique for analysing the hydrated hydrogel.[131] The Nile blue is excited by visible light at a wavelength of 633 nm, the Nile blue has been shown to fluoresce, producing emission at wavelengths between 638 nm and 758 nm. Where there is a more intense Nile blue excitation there will therefore be more hydrogel.

The confocal microscope used for this projected were all performed at the University of Liverpool by an operator unknown to the author. Unfortunately, the information as to where in the z-plane the images were obtained was not recorded. The confocal images can therefore only be treated as two dimensional images in this chapter that still allow the proper investigation of gels in their hydrated state grown for different time periods on MNEE arrays. A full copy of all the images received has been included in appendix 6.

In conventional light microscopy, light is reflected by a sample and focused by lenses to the eye-piece. Since the light is being scattered from the sample there is destructive interference from the diffracted light waves emanating from the illuminated sample. Thus, two objects close to each other in the sample can only be resolved from one another if they are far enough apart that the scattered light will not destructively interfere with one another. In practise this means that the minimum distance between two objects that must be resolved must be greater than the wavelength of light used to investigate the sample. The "Airy radius" (r_{Airy}) is a measure of the smallest distance between two objects in a sample that can be clearly resolved, it can be calculated using equation 6.2 in which "λ" is the wavelength of the incident light and "a" is the numerical aperture of the objective lense.

$$r_{Airy} = \frac{0.61\lambda}{a} \qquad \text{(Eqn 6.2)}$$

The numerical aperture of an objective lens (a) is given by equation 6.3, in which the refractive index of the lens material (n_r) is related to half the angle of the cone of light being scanned by the lense (α).

$$a = n_r \sin\alpha \qquad \text{(Eqn 6.3)}$$

In confocal microscopy the numerical aperture is changed so as to achieve a good balance between resolution and brightness. If the numerical aperture is increased beyond 1 Airy unit (AU) the image become brighter but there will be more diffracted light entering the objective which blurs the image by deconstructive interference. By reducing the numerical aperture to below 1 airy unit less light is allowed to enter the objective, which reduces interference

and sharpens the image, but also reduces brightness of the image. It is therefore common practice to quote the Airy units and numerical aperture of the lenses used in confocal image acquisition, section 6.2.3.

6.1.2. Electrochemical characterisation of hydrogels

The working hypothesis going into these tests was that at very early stages of growth the hydrogel would grow evenly across the electrode. Hypothetically this would cause an increase in both R_{ct} and R_{nl} as the electrode surface area would decrease and the diffusion to the electrode will be disturbed by the hydrogel matrix above it. The carbazole alanine hydrogel used forms wire like spindles that intertwine into root like structures after extended periods of growth.[129] It would be of interest to note over which timescales the spindles would begin to intertwine, this could be imaged and related to the electrochemistry to ascertain if there was a change in the EIS when the hydrogel structure changes. Over longer periods of growth, it would be expected that diffusion to the electrode surface would be further impeded, this would theoretically increase R_{nl} and decrease W, both of which can be used to calculate the diffusion coefficient of a redox agent to the electrode using equations 6.4 and 6.5.[30] In both of these equations the diffusion coefficient , *D*, can be calculated using the universal gas constant, R, the temperature, *T*, the admittance, Y_0, the number of electrons transferred, *n*, Faraday's constant, F, the area of the electrode, *A*, the concentration of redox agent in the bulk electrolyte, c_0, the number of squares in the array, *N*, the length of one of the square in the array, *L*, and the resistance to non-linear diffusion R_{nl}.

$$D = \left(\frac{2RTY_0}{n^2F^2Ac_0}\right)^2 \qquad \text{(Eqn 6.4)}$$

$$D = \frac{4NRT}{0.96nF^2c_0LR_{nl}} \qquad \text{(Eqn 6.5)}$$

6.2. Experimental

6.2.1 Electrochemical measurements

All electrochemical measurements were made at a constant temperature of 25 °C, controlled by a water bath built in-house. They were performed in a Faraday cage using an Autolab PGSTAT128N with a FRA32 module (supplied by Metrohm Ltd.) controlled by a PC using NOVA 1.10 software. All potentials are reported with respect to the saturated calomel reference electrode (SCE, Accumet® 13-620-61, Fischer Scientific) unless otherwise stated, and the gauze counter electrode was made in house using Pt gauze and wire (Sigma-Aldrich). All solutions were prepared using deionized water (18.2 MΩcm^{-1}, Millipore MilliQ) with sodium chloride (BioXtra ≥99.5%), potassium ferricyanide (ACS reagent ≥99%), potassium ferrocyanide (ACS reagent ≥99%) and hydroquinone (reagentplus® ≥99.5%) all supplied by Sigma Aldrich and used as received. All pH measurements were performed using a Fisherbrand Hydrus 400 pH meter with a Mettler Toledo InLab®Routine Pro pH probe. Electrochemical impedance spectroscopy (EIS) measurements were carried out in an aqueous solution of potassium ferrocyanide (1 mM, Sigma Aldrich) and potassium ferricyanide (1 mM, Sigma Aldrich) in KCl (0.1 M, Sigma Aldrich) background electrolyte. EIS was performed by applying a sinusoidal potential of 10 mV rms superimposed on the measured open circuit potential (OCP), to ensure no overall Faradaic reaction. 50 logarithmically spaced frequencies were applied in the range between 100 kHz and 0.1 Hz. The OCP was measured before each EIS measurement and, as expected for the

ferricyanide/ferrocyanide couple, was constant at between + 165 and + 170 mV with respect to SCE. This confirms effective hydrogel solvation and redox access to the underlying nanoelectrode for all experiments.

All experiments in this chapter were conducted on 30µm 3D MNEE arrays, fabricated and cleaned as described in chapters 2 and 3 of this thesis respectively.

6.2.2. Carbazole-alanine synthesis and hydrogel formation

The carbazole-alanine hydrogel was prepared as described previously.[126] A solution of the gelator was prepared by stirring carbazole-alanine (2 mg/mL) in aqueous sodium hydroxide (6.75 mM) at room temperature overnight until it had fully dissolved. Aqueous HCl (1 M) and NaOH (6.75 mM) solutions were used as appropriate to adjust the bulk pH to 8.0. Hydroquinone (255 mM, Sigma Aldrich) and NaCl (0.1 M, Sigma Aldrich) were added as the pH swing inducer and the background electrolyte respectively. Gelation was induced using chronopotentiometry, holding the MNEE array working electrode at +100 µA unless otherwise stated in a three-electrode system, using a Pt wire as a pseudoreference electrode. The experiments were performed on a small scale (10ml total solution volume) so as to save the gelator which was sent up by the collaborators in Liverpool, as a result of this conventional reference electrodes would not fit into the smaller beakers which is why a Pt pseudoreference electrode was used.

Hydrogel was grown on separate MNEE arrays for different time periods, separated by 5 s increments, before imaging by light microscopy, confocal microscopy, SEM and analysis by EIS in 1 mM FFC in 100 mM KCl, pH 4.3 adjusted with NaOH and HCl as appropriate.

6.2.3. Imaging (SEM and confocal microscopy with Nile blue stain)

SEM images were obtained using a Hitachi S-4800 FE-SEM at 3 keV. After hydrogels were electrochemically grown on to the MNEE array, it was fixed onto an aluminium SEM stub with carbon tabs and left out to dry overnight. The MNEE arrays were then gold coated for 1.5 minutes at 20 mA using a sputter EMITECH K550X sputter coater prior to imaging.

Confocal microscopy images were obtained on a Zeiss LSM510 using Plan-Apo 100x (1.4 NA oil) and 63x (1.46 NA oil) objectives. The gelator solution was prepared as described in section 6.2.2, with the addition of 0.001 M Nile Blue (Sigma Aldrich) and imaged after successive 5s growth increments. Nile Blue fluorescence was excited at a fixed wavelength of 633 nm using a Helium Neon laser and emission was detected between wavelengths of 638 and 758 nm (collecting all this range using a filter) using a pinhole diameter of 1 Airy unit (approx. 0.8 µm resolution). The hydrogel coated MNEE array was placed in an uncoated borosilicate MatTek dish with a 20 mm diameter glass coverslip. Images were analyzed using the Zeiss AIM software (Zeiss, Jena, Germany) and ImageJ software. All confocal Images were obtained by collaborators at the university of Liverpool and not by the author, due to a lack of access to an inverted confocal microscope at the university of Edinburgh.

6.2.4. PNA SAM formation, DNA target binding and biofouling studies

PNA SAM formation was carried out using 1.5 nM PNA (Panagene, Daejeon, South Korea), 150 nM tris-2-carboxymethylphosphine (TCEP, Sigma-Aldrich) and 30 nM 6-mercaptohexan-1-ol (MCH, Sigma-Aldrich) in a 50:50 mixture by volume of DMSO and deionized water.[18] 50 µl of this mixture was placed on the MNEE array for 1 hour to form the PNA SAM on the electrode array surface, followed by the induced growth of the carbazole-alanine hydrogel

by galvanostatically passing a current of +100 µA for 10 s in the gelator solution described in section 6.2.2). The hydrogel grown over 10s was chosen to study biofouling at random. Future work should include testing the biofouling capabilities of hydrogels grown at different currents for different periods of time. This functionalized MNEE array was then exposed to a 50 µL droplet of 100µM aqueous solution of 30 mer complementary target DNA (Sigma-Aldrich) sequence:

5'-GTATGCTTTGGTCTTTCTGCATTCCTGGAA-3'

for 30 minutes. Measurement of target binding involved performing EIS as above, using redox buffer (1 mM/1 mM $K_3[Fe(CN)_6]/K_4[Fe(CN)_6]$ in aqueous 1x tris-HCl buffer, pH 4.3, as in section 6.2.1) so as to ensure hydrogel stability. For proof of principle biofouling kinetic experiments, this redox buffer was also selected as it has been previously established that bovine serum albumin (BSA) is stable under this pH regime.[128] BSA (Sigma Aldrich, UK) was obtained as a lyophilized powder and made up to a final 100 µM concentration in the redox buffer, followed by pH readjustment as required using HCl and NaOH as described in section 6.2.1.

6.3. Results and discussion

6.3.1. Analysis of hydrogel growth

Carbazole-alanine hydrogel was first grown galvanostatically at + 100 µA (0.94 kA m^{-2}) for 1000s to establish that hydrogel growth could be recreated on an MNEE array. This was important as the enhanced mass transport of buffering species to the nanoelectrodes could mean that the pH drop localised at the electrode surface would not be sufficient to induce gelation. The highest current density possible was selected to offset this buffering, the literature used a maximum of 14.2 A m^{-2} on macro electrodes.[126] Figure 6.4A shows the potential time transient recorded during this experiment along with a photograph of the hydrogel covering the MNEE array after growth.

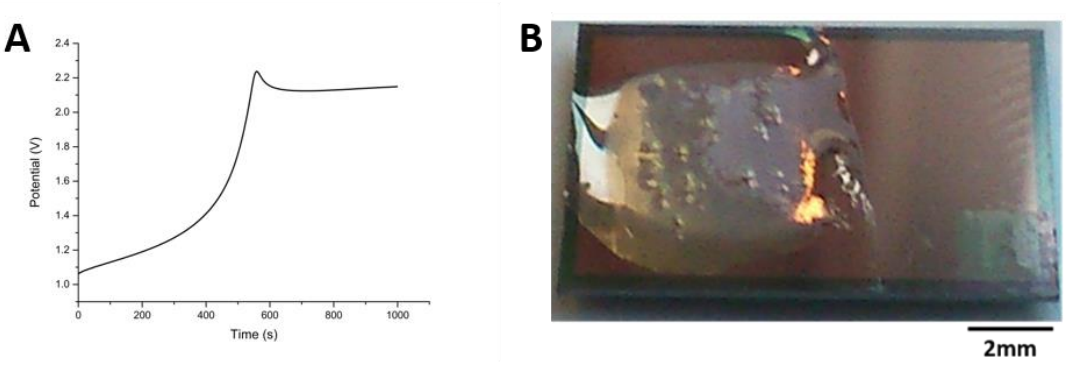

Figure 6.4. (A) The potential time transient observed during hydrogel growth for 1000 s at +100 µA on the MNEE array photographed in (B) after the growth. The potentials recorded were vs the Pt pseudo counter electrode in the gelation buffer.

The potential time transient, figure 6.4.A, shows that the potential increased linearly with time until about 400 seconds, after which it rose sharply to 2.2V where it plateaued. The physical explanation for this rapid change in potential after 400s is that the reaction being driven at this current can no longer continue, due most probably to the hydroquinone being locally depleted.[31] In other words, there is insufficient flux of hydroquinone to the electrode

to maintain the fixed current. In order to maintain the current, the potential then increases rapidly until the next process can begin; in this case at around +2.2 V the solvent limit of water is reached and oxygen bubbles are evolved and can begin to form on the electrode surface; this explains the bubbles seen on the chip in figure 6.4.B.

After establishing that this hydrogel could be grown on MNEE arrays, the growth of the hydrogel was studied by characterising hydrogels grown for different increments of time on different MNEE arrays. For the purposes of the discussion the analysis of these data has been broken up into three distinct time domains. The first will focus on short periods of time where the hydrogel grown is at the electrode surface, the second intermediate time period will focus on the growth of the hydrogel within the cavity before the final period which will investigate the hydrogel growth for longer periods of time, where the hydrogel grows outwith the cavity.

6.3.1.1. Initial hydrogel growth at the electrode surface

Over time periods up to 5 s the hydrogel was seen to grow across the electrode surface, figure 6.5. This is most evident in the confocal microscopy images in figure 6.5.B. The light microscopy images, figure 6.5.A, are somewhat more difficult to analyse and interpret; the "bubbles" are actually water droplets on the dry electrode encapsulated and supported by the hydrogel.

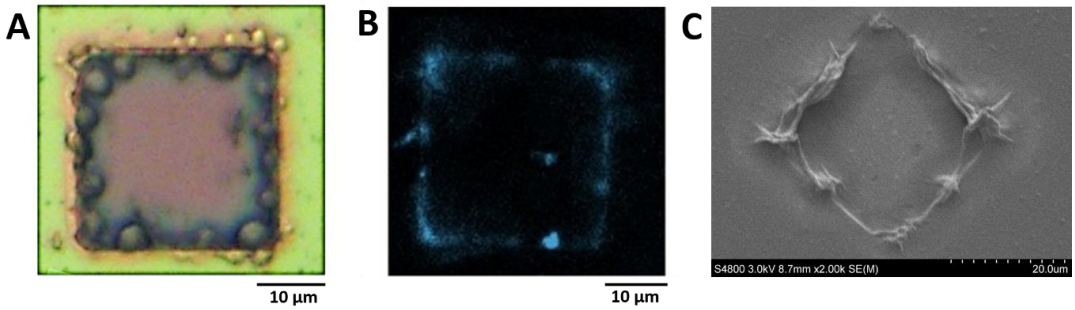

Figure 6.5. (A) light microscopy, (B) confocal microscopy with Nile blue stain and (C) SEM images of the carbazole alanine hydrogel after 5 s growth on a 30 µm 3D MNEE array at +100 µA.

The similarities of the amount of hydrogel grown for 5s in the confocal and light microscopy images, which were obtained by different researchers in separate experiments, speaks to the reproducibility of the experiment. The reproducibility across the array was also good as can be seen in figure 6.7.F. As with all the other SEM images provided in this chapter, figure 6.5.B should be treated with caution as the xerogel structure has collapsed under rapid dehydration due to the UHV conditions. It is possible to determine that hydrogel has grown over the entirety of the electrode area and the resulting structure must therefore be nanodimensional; other observable features are likely the result of xerogel structural collapse upon dehydration. Whilst the nature of the hydrogel-electrode bonding is not known it is clear that the hydrogel has not been lifted from the surface during vacuum desiccation so the bonding must be relatively strong.

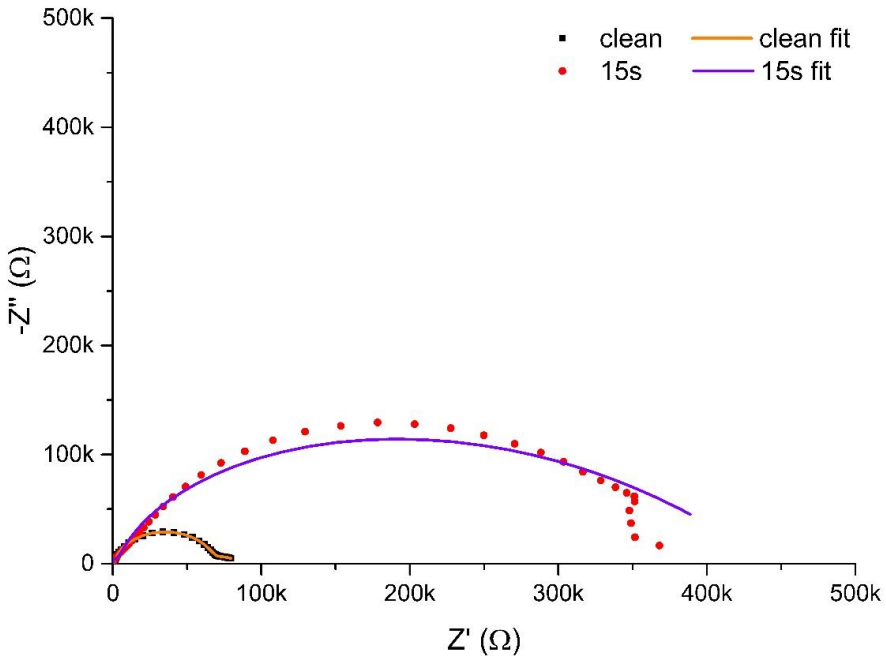

Figure 6.6. Nyquist plots of a MNEE array when clean (black squares) and after 15s (red dots) hydrogel growth at +100 µA. Only the 15s growth plot has been included so as to clearly demonstrate the unchanging nature of the first semi-circle. The solid lines are the fits to the appropriate equivalent circuit (see text below and figure 6.5)

Table 6.1. Table of regression fits for hydrogels grown over the short timescales, t, shown. Data were those in the Nyquist plots shown in figure 6.6, NOTE the 5s and 10s data were not plotted in figure 6.6 for clarity.

Parameter	Time (s)			
	0	5	10	15
R_s (Ω)	173 ± 9	164 ± 3	170 ± 6	179 ± 45
C_{dl} (nF)	21.3 ± 0.5	21.9 ± 0.3	23.0 ± 0.3	19.1 ± 0.3
R_{ct} (kΩ)	15.7 ± 0.3	14.5 ± 1.5	19.9 ± 1.7	14.9 ± 0.7
C_n (nF)	NA	22.5 ± 0.3	15.6 ± 1.8	35.6 ± 1.9
Y_o (nS)	14400 ± 1772	513 ± 18	302 ± 29	428 ± 20
Calculated D using Y_o ($\times 10^{-6} cm^2 s^{-1}$)	7.228 ± 0.89	0.258 ± 0.009	0.152 ± 0.015	0.215 ± 0.010
R_{nl} (kΩ)	9.0 ± 0.3	73 ± 1	101 ± 3	366 ± 4
Calculated D using R_{nl} ($\times 10^{-6} cm^2 s^{-1}$)	7.244 ± 0.241	0.893 ± 0.012	0.646 ± 0.019	0.161 ± 0.016
X^2	0.0651	0.0239	0.0561	0.0238

NB, the reader should note that a different equivalent circuit has been used to fit the data when hydrogel is present on the electrode. The C_N element is not necessary for a clean electrode.

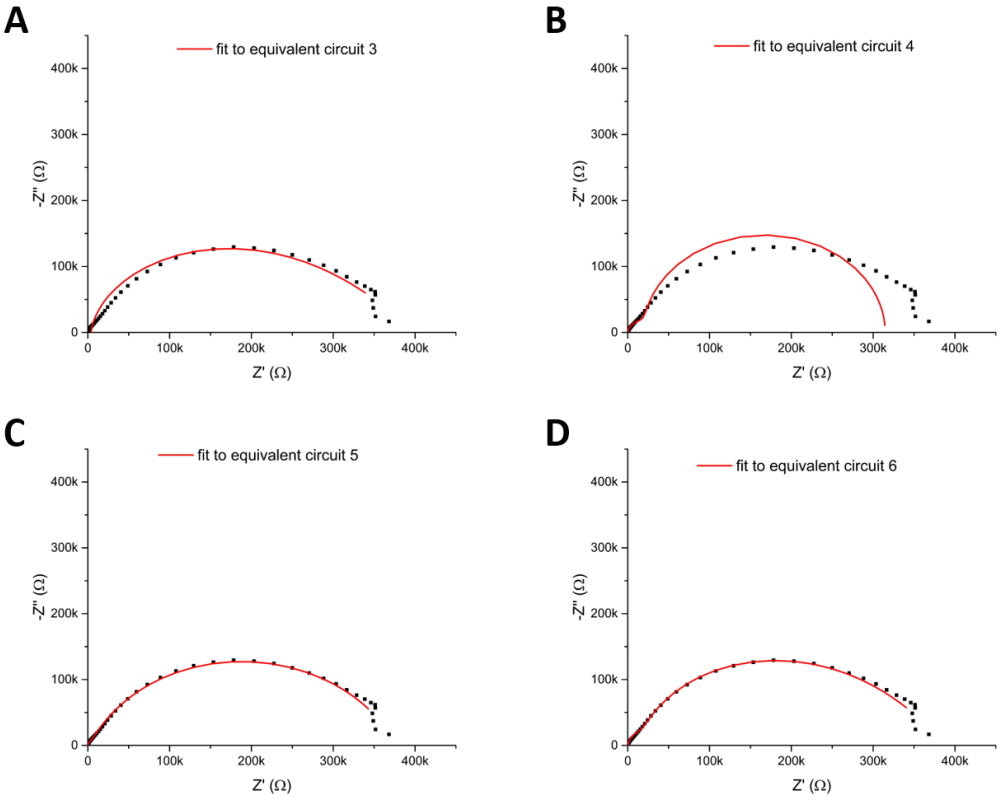

Figure 6.7. The Nyquist plot of 15s hydrogel growth from figure 6.6 fit to (A) equivalent circuit 3 (B) equivalent circuit 4 (C) equivalent circuit 5 and (D) equivalent circuit 6. A summary of the fits is given in table 6.2.

Table 6.2. Table of fits for 15s hydrogel growth fit to equivalent circuits 3-5 to accompany the Nyquist plots shown in figure 6.7.

Parameter	Equivalent circuit 1.3	Equivalent circuit 1.4	Equivalent circuit 1.5	Equivalent circuit 1.6
R_s (Ω)	6611 ± 1361	571 ± 198	1875 ± 2250	179 ± 45
C_{dl} (nF)	56.3 ± 2.4	23.6 ± 1.1	27.0 ± 20.5	19.1 ± 0.3
R_{ct} (kΩ)	15	34 ± 3	14 ± 27	15 ± 1
C_N (nF)	-	78.7 ± 5.4	-	35.6 ± 1.9
Y_o (nS)	384 ± 13	-	-	428 ± 20
Q, Y_o (nS)	-	-	264 ± 29	-
Q, N	-	-	0.69 ± 0.04	-
R_{nl} (kΩ)	391 ± 5	280 ± 12	370 ± 27	366 ± 4
χ^2	0.0818	0.7750	0.0520	0.0238

When hydrogel is grown on the MNEE arrays the equivalent circuit to which the data is fit changes from equivalent circuit 3 to equivalent circuit 6. This is a novel equivalent circuit based on the previously established equivalent circuit for MNEE arrays, equivalent circuit 3. It was found that the inclusion of C_N improved the fit so an explanation as to the physical phenomenon that could be modelled as a capacitance that only arises when hydrogel is formed needed to be found. Looking forward to table 6.3, it can be seen that there is no trend in the fitted value of C_N as different amounts of hydrogel are grown on the MNEE arrays. There is as yet no concrete physical explanation as to the nature of the C_N, but the

inclusion of a capacitor in parallel to W and R_{nl} in the modified Randles' circuit for MNEE arrays clearly improves the fits, table 6.2. Postulations as to the nature of C_N include the formation of a double layer on the hydrogel solution interface or a capacitance arising from the hydrogel acting as an insulator between electrode and electrolyte. From table 6.4 it is clear that the formation of a more porous hydrogel increases the fitted value of C_N.

Despite the gel density being greatest at the electrode surface the stability of R_s, C_{dl} and R_{ct} as more hydrogel is formed, table 6.1, would suggest that the concentration of polymer at the electrode surface must be negligible. The hydrogel is effectively behaving like solvent, which would be expected considering that hydrogels are composed of over 95% water. [132, 133] The fibrils of the hydrogel structure are emanating from a nanoelectrode surface and splaying out into a rapidly expanding volume. So their effective concentration would theoretically decrease if there was no coalescing of the polymer strands. A cartoon of the hydrogel structure is given in figure 6.8.

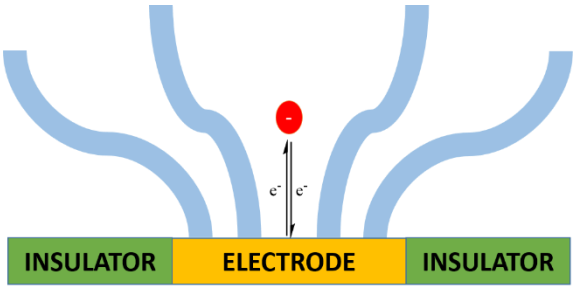

Figure 6.8. Schematic diagram (NOT TO SCALE), showing that the fibril thickness in comparison to the electron tunnelling distance means that hydrogel growth will have a minor if any effect on R_{ct}.

There is a sharp and significant decrease in admittance and corresponding increase in R_{nl} after 5s of hydrogel growth. The fitted value of Y_0 decreases from 14.4 → 0.5 µS and R_{nl} increases from 9 → 73 kΩ. Both indicate that the flow of redox agent to the solution is impeded by the hydrogel. The corresponding changes in the calculated diffusion coefficient both show that the values have dropped to the same order of magnitude. The value of Y_0 measures linear diffusion close to the electrode surface whereas R_{nl} models hemispherical diffusion further into the bulk solution. It is therefore satisfying that the calculated diffusion coefficient for FFC is lower for Y_0 than that calculated for R_{nl} as it shows that the hydrogel is more tightly packed close to the electrode surface, as one would expect for a hydrogel emanating from an electrode surface then expanding out into a larger volume.

6.3.1.2. Hydrogel growth within the MNEE cavity

Over 5-25 s the hydrogel is seen to grow within the cavity, with enhanced growth in the corners. This experimentally confirms the finite element calculations previously published by the Mount group which show enhanced current density in the corners of the cavities.[30, 61]

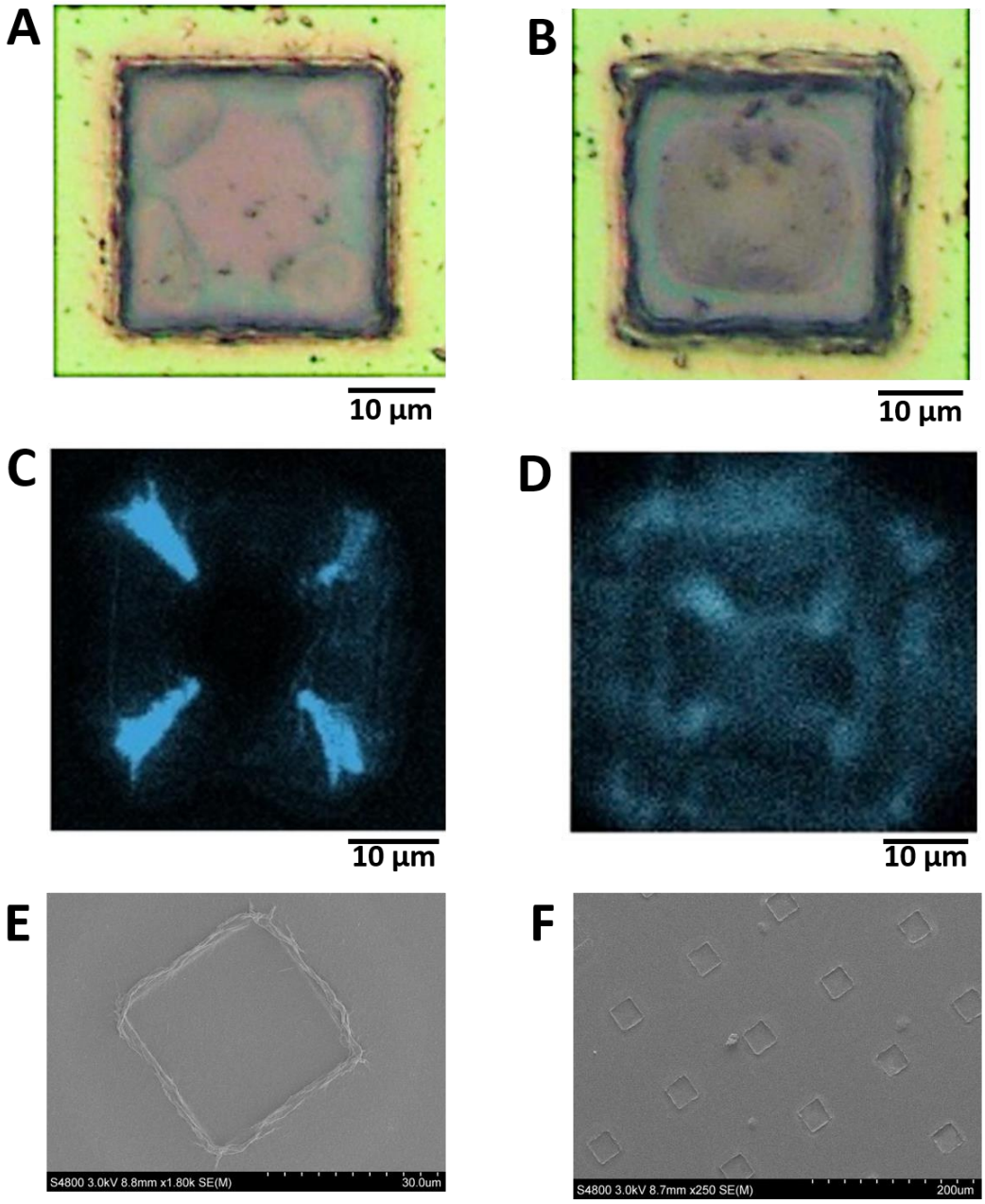

Figure 6.9. Light microscopy image of a hydrogel grown for (A) 5s and (B) 15s, with confocal microscopy images after (C) 5s and (D) 20s of growth in the presence of a Nile blue stain. (E) and (F) are light microscope images after 20s of growth. All hydrogels were grown at +100 µA vs a Pt wire counter electrode and Pt pseudo reference electrode.

The confocal microscopy data, figure 6.9.C and 6.9.D, would indicate that not only is the hydrogel growing extensively in the corners but the intensity of the fluorescing Nile blue stain shows that the hydrogel formed in the corners of the cavity is denser, as denser hydrogels bind more Nile blue and fluoresce more intensely.[131] The increased density on the corners of the cavities creates a heterogeneity in the hydrogel matrix within the array cavities. Up until now electrochemically trigger hydrogels have been assumed to be homogeneous, the heterogeneity was subject to further investigation presented in section 6.4.

It is interesting to note that the growth of the hydrogel emanates from the electrodes and then grows progressively into the centres of the cavities. There is little or no growth outside the cavity walls in this time domain. This would insinuate that the flow of protons takes them towards the centre of the cavity. This diffusion profile had not been previously simulated but can be observed in the light microscopy, confocal microscopy and SEM data. It is probable that the pH drop will be greatest in the cavity as there is less effective transport of buffering solutions to the cavity floor. Thus, a larger pH excursion will form along the cavity floor and direct gel growth into the cavity centre.

The SEM in figure 6.9.F. displays the reproducibility of the hydrogels grown across an array up to this 20 s time point. It speaks not only to the reproducibility of the gelation process on multiple electrodes but the uniformity of the electrodes in the array.

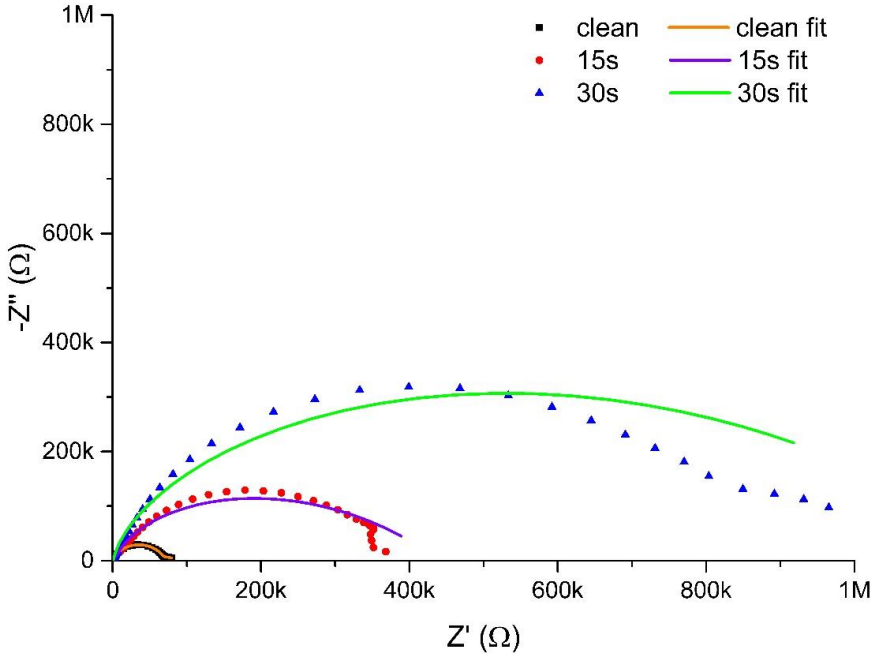

Figure 6.10. Nyquist plots of a 30 µm 3D MNEE array when clean (black squares) and after 15s (red dots) and 30s (blue triangles) of hydrogel growth at +100 µA. EIS was recorded at the OCP of 1mM potassium ferricyanide, 1mM potassium ferrocyanide and 100 mM KCl at pH 4.3 vs a saturated calomel reference electrode and Pt gauze counter electrode at room temperature and pressure.

Table 6.3. Equivalent circuit fits for hydrogels grown over short and intermediate timescales as shown in the Nyquist plots in figure 6.10, NOTE not all data have been plotted in figure 6.10 for clarity.

Parameter	Time (s)					
	0	5	10	15	20	30
R_s (Ω)	173 ± 9	164 ± 3	170 ± 6	179 ± 45	163 ± 21	178 ± 17
C_{dl} (nF)	21.3 ± 0.5	21.9 ± 0.3	23.0 ± 0.3	19.1 ± 0.3	18.4 ± 0.6	59.6 ± 8.9
R_{ct} (kΩ)	15.7 ± 0.3	14.5 ± 1.5	19.9 ± 1.7	14.9 ± 0.7	22.1 ± 1.8	16.0 ± 5.8
C_n (nF)	NA	22.5 ± 0.3	15.6 ± 1.8	35.6 ± 1.9	21.3 ± 0.9	55.4 ± 10.4
Y_o (nS)	14400 ± 1772	513 ± 18	302 ± 29	428 ± 20	140 ± 9	192 ± 26
Calculated D using Y_o ($\times 10^{-6} cm^2 s^{-1}$)	7.228 ± 0.89	0.258 ± 0.009	0.152 ± 0.015	0.215 ± 0.010	0.070 ± 0.005	0.096 ± 0.013
R_{nl} (kΩ)	9.0 ± 0.3	73 ± 1	101 ± 3	366 ± 4	1778 ± 67	737 ± 68
Calculated D using R_{nl} ($\times 10^{-6} cm^2 s^{-1}$)	7.244 ± 0.241	0.893 ± 0.012	0.646 ± 0.019	0.161 ± 0.016	0.037 ± 0.001	0.089 ± 0.008
X^2	0.0651	0.0239	0.0561	0.0238	0.0792	0.0995

The domes in the Nyquist plots gets larger with increased hydrogel growth, which indicates that the technique can be used to monitor growth progression. It is again satisfying that the values of R_s, C_{dl} and R_{ct} do not change within error as more hydrogel is grown; indicating that the structure of the hydrogel at the electrode remains constant throughout the growth period, i.e. the hydrogel is essentially behaving like solvent. Bearing in mind that each hydrogel was grown on a different electrode and that they are in constant dynamic motion in the solution, it can be said that the values of C_N and Y_0 stay relatively constant as hydrogel is grown between 5-20s. With the increase in impedance being attributed to R_{nl}. This is again encouraging as Y_0 measures linear redox agent flow close to the electrode surface while R_{nl} measures hemispherical diffusion towards the electrode further into the solution; so Y_0 should reach a steady state faster and be more stable than R_{nl}. Thus the diffusion field to the electrode has a linear shape within the cavity and becomes hemispherical as it extends out with the cavity. The C_N in the equivalent circuit is thought to be caused by the depleted concentration of redox agent within the hydrogel matrix compared to the bulk solution creating a small capacitance that builds up between the electrode and the bulk electrolyte. This capacitance follows no obvious trend with increasing hydrogel growth and may vary with the amount of polymer intertwining.

6.3.1.3. Hydrogel growth and overlap outside the cavities

As the hydrogel growth extends beyond the cavity the uniformity of the hydrogels across the array appears to be starting to break down in the SEM and light microscopy images, figure 6.11.

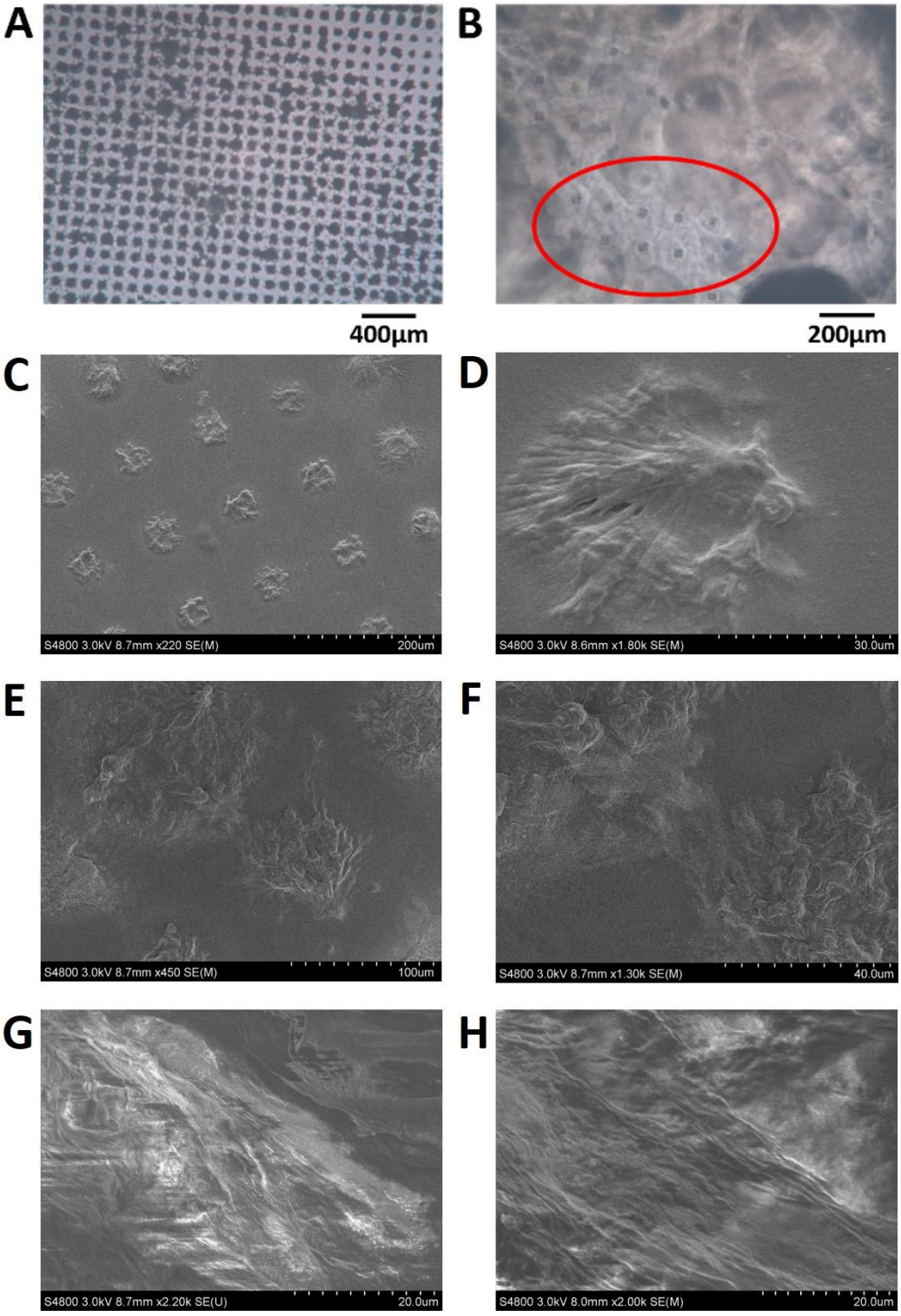

Figure 6.11. Light microscopy images of the hydrogel on a 30 µm 3D MNEE array after (A) 30s growth and dehydrated overnight and (B) 1000 s and still hydrated where the individual cavities in the array are still visible in regions as highlighted. SEMs of the xerogel after (C and D) 20s, (E and F) 30s and (G and H) 1000 s of growth at 50 µA.

However, it should be remembered that for these images the hydrogel had to be either partially or fully dehydrated in order to image. All the data consistently shows the hydrogels growing out in hemispherical shapes centred around the middle of the cavity. Up until

around the 30s mark the hydrogels grow independently of one another but as gelation proceeds they begin to overlap and imbricated with the hydrogels from neighbouring electrodes in the array.

The light microscopy images of the hydrogel grown for 900s, figure 6.11.B, reveals the circular shapes of the diffusion patterns visible in the hydrogel. However, this is not consistent across the image. Even the light microscopy images of hydrogels grown for 30s shows that the uniformity across the array is lost at these time periods. This could be attributed to defects within the array or non-uniformity of growing hydrogel as it becomes exposed to natural currents within the solution. It may have been shielded from the natural convections whilst growth was restricted to the cavity and shorter growth durations.

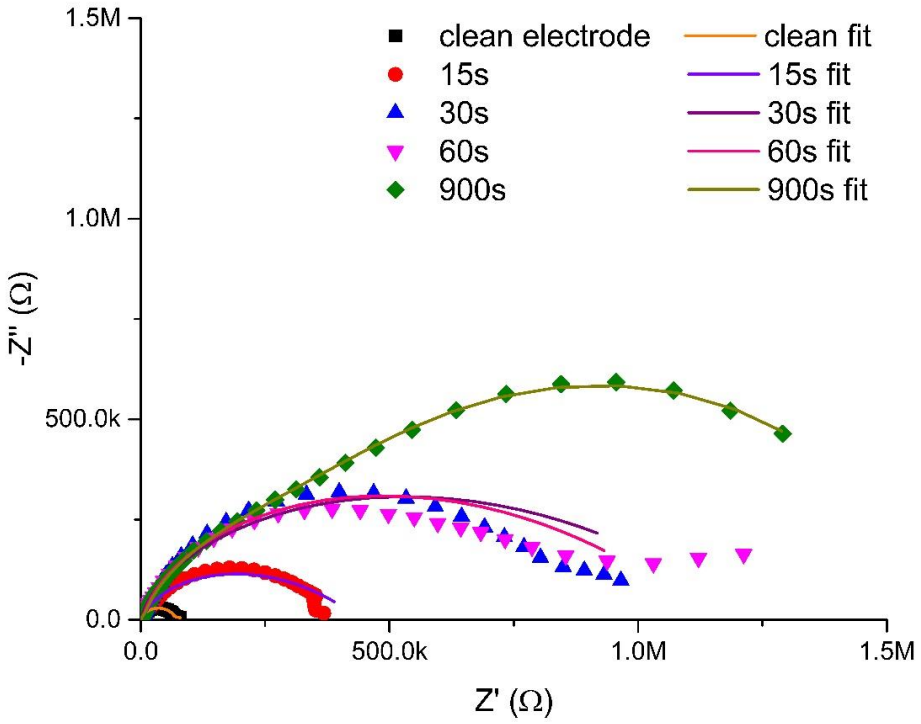

Figure 6.12. Nyquist plots of a 30 µm 3D MNEE array when clean (black squares) and after 15s (red dots), 30s (blue triangles), 60s (pink inverted triangles) and 900s (green offset squares) of hydrogel growth at +100 µA. EIS was recorded at the OCP of 1mM potassium ferricyanide, 1mM potassium ferrocyanide and 100 mM KCl at pH 4.3 vs a saturated calomel reference electrode and Pt gauze counter electrode at room temperature and pressure.

Table 6.4. Equivalent circuit fits for hydrogels grown over short, intermediate and longer timescales as shown in the Nyquist plots in figure 6.12, NOTE not all data have been plotted in figure 6.12 for clarity.

Parameter	Time (s)							
	0	5	10	15	20	30	60	900
R_s (Ω)	173 ± 9	164 ± 3	170 ± 6	179 ± 45	163 ± 21	178 ± 17	173 ± 32	176 ± 17
C_{dl} (nF)	21.3 ± 0.5	21.9 ± 0.3	23.0 ± 0.3	19.1 ± 0.3	18.4 ± 0.6	59.6 ± 8.9	23.4 ± 0.8	40.2 ± 10.2
R_{ct} (kΩ)	15.7 ± 0.3	14.5 ± 1.5	19.9 ± 1.7	14.9 ± 0.7	22.1 ± 1.8	16.0 ± 5.8	18.8 ± 2.0	23.2 ± 8.6
C_n (nF)	NA	22.5 ± 0.3	15.6 ± 1.8	35.6 ± 1.9	21.3 ± 0.9	55.4 ± 10.4	23.1 ± 1.6	49.8 ± 7.9
Y_o (nS)	14400 ± 1772	513 ± 18	302 ± 29	428 ± 20	140 ± 9	192 ± 26	293 ± 16	490 ± 18
Calculated D using Y_o $(\times 10^{-6} cm^2 s^{-1})$	7.228 ± 0.89	0.258 ± 0.009	0.152 ± 0.015	0.215 ± 0.010	0.070 ± 0.005	0.096 ± 0.013	0.147 ± 0.008	0.246 ± 0.009
R_{nl} (kΩ)	9.0 ± 0.3	73 ± 1	101 ± 3	366 ± 4	1778 ± 67	737 ± 68	1030 ± 45	715 ± 40
Calculated D using R_{nl} $(\times 10^{-6} cm^2 s^{-1})$	7.244 ± 0.241	0.893 ± 0.012	0.646 ± 0.019	0.161 ± 0.016	0.037 ± 0.001	0.089 ± 0.008	0.063 ± 0.003	0.091 ± 0.005
$C_{dl,2}$ (nF)	-	-	-	-	-	-	-	938 ± 28
$R_{ct,2}$ (kΩ)	-	-	-	-	-	-	-	874 ± 23
X^2	0.0651	0.0239	0.0561	0.0238	0.0792	0.0995	0.1560	0.0105

The impedance data shows that during extended periods of growth there is no appreciable change in any of the elements from the modified Randles' circuit for MNEE arrays or C_N. Instead a third semi-circle begins to form, this does not fit very well for the 30s or 60s growth fits but is much more pronounced for the 900s growth data. The equivalent circuit must therefore include elements to fit another semi-circle; this is achieved by including a CR parallel circuit in series with the previously used circuit. The final equivalent circuit that is proposed to be able to fit MNEE arrays with any amount of hydrogel on the surface is given in figure 6.13.

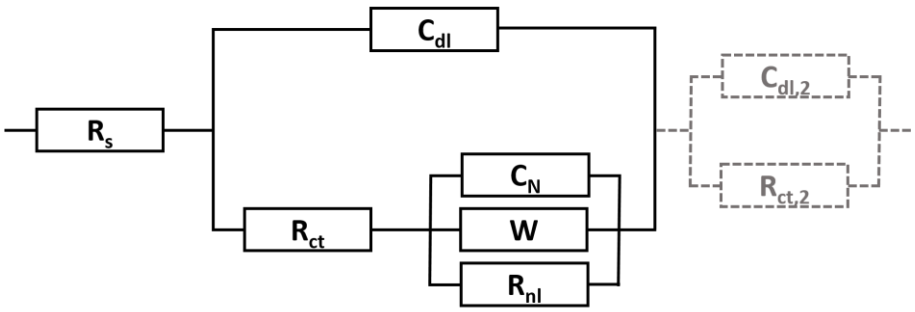

Figure 6.13. Equivalent circuit for MNEE arrays with hydrogel grown on the electrode surface for extended time periods to model: the resistance of the solution (R_s), the capacitance double layer (C_{dl}), the charge transfer resistance (R_{ct}), the capacitance between the electrode and the bulk electrolyte separated by the depletion of electrolyte in the cavity (C_N), linear diffusion of redox agent to the electrode (W), the resistance to non-linear diffusion (R_{nl}), The double layer at the hydrogel solution interface ($C_{dl,2}$) and the resistance to moving charge into the film ($R_{ct,2}$).

The last two elements, $C_{dl,2}$ and $R_{ct,2}$, have been coloured grey and marked in checked boxes as they need only be included for extended periods of hydrogel growth. The physical basis of these two elements is not yet fully understood and should be analysed by bole plot analysis

to determine whether or not the third semi-circle is under thermodynamic or kinetic control. Such experiments were not carried out due to time constraints. The elements have been dubbed $C_{dl,2}$ and $R_{ct,2}$; their physical reality is postulated to be the formation of a double layer on the hydrogel boundary which is modelled by $C_{dl,2}$ and a resistance to moving charge across the membrane, $R_{ct,2}$. Although it must be stressed that these explanations are hypothetical and there is insufficient evidence at this stage to assign the elements to any real physical parameters.

6.4. Controlling the global structure of the hydrogel

As stated in section 6.3.1.2, the heterogeneity of the hydrogel density warranted further investigation. To do this, hydrogels were grown for the same time period at different currents. The currents selected were 50 and 100 µA, and it was determined that the hydrogel would be grown for 15s, picked at random from intermediate time domain as it was more reproducible than extended growth periods. It was determined to fix the time the experiments were run for rather than the charge passed to see the amount of hydrogel formed with the same sized diffusion fields rather than quantity of protons evolved. By keeping the diffusion fields constant it was thought the volume of hydrogel would be the same but the structure within the hydrogel might be different. Comparable experiments where the charge passed is kept constant were not performed due to time constraints but should form the basis of future investigation.

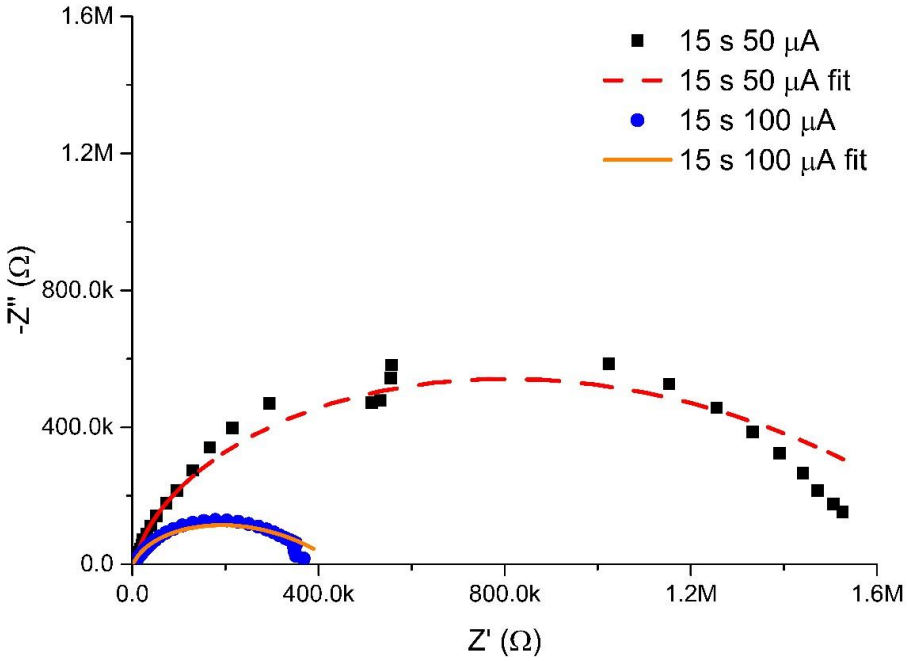

Figure 6.14. Nyquist plots of a 30 µm 3D MNEE array after 15 s of hydrogel growth at +50 µA (black squares) and +100 µA (blue dots). The "noise" in the +50 µA at medium frequencies was due to an uncalibrated resistor.

Table 6.5. Equivalent circuit fits for hydrogels grown for 15 s at +50 µA and +100 µA, as plotted in figure 6.14.

Parameter	15 s hydrogel growth	
	50 µA	100 µA
R_s (Ω)	158 ± 17	179 ± 45
C_{dl} (nF)	12.7 ± 0.4	19.1 ± 0.3
R_{ct} (kΩ)	18.0 ± 1.7	14.9 ± 0.7
C_n (nF)	22.7 ± 1.7	35.6 ± 1.9
Y_o (nS)	150 ± 2	428 ± 20
Calculated D using Y_o $(\times 10^{-6}\mathrm{cm}^2\mathrm{s}^{-1})$	0.075 ± 0.001	0.215 ± 0.010
R_{nl} (kΩ)	1983 ± 128	366 ± 4
Calculated D using R_{nl} $(\times 10^{-6}\mathrm{cm}^2\mathrm{s}^{-1})$	0.033 ± 0.002	0.161 ± 0.016
X^2	0.0463	0.0238

The data does indeed show that the hydrogels grown at different currents for the same length of time have different responses, with the hydrogel grown at a higher current having significantly smaller domes on the Nyquist plots.

There is a minor increase in C_{dl} compared to the hydrogels grown at lower currents which might suggest that the packing density of the hydrogels at the electrode has increased, but R_s and R_{ct} are the same within error. This is again in-keeping with theory, R_s is independent of electrode area, the double layer is smaller as some of the electrode is covered by hydrogel and electron tunnelling is happening from a distance above the hydrogel tethers and is not being affected by the increased density of the hydrogel at the electrode surface. There is an increase in R_{nl} and a corresponding decrease in Y_0 when comparing the gels grown at 100 µA to those grown at 50 µA. Thus a denser, less porous film forms when the hydrogel is grown at higher current. This has potential impact for the anti-biofouling properties of the hydrogels. If the porosity of the hydrogel can be controlled electrochemically then it is not unreasonable to assume that the maximum size of analyte that can diffuse to the electrode surface will also be electrochemically tuneable. Thus, a system in which a size selective semi-permeable membrane should be possible using this technology. Tests to determine the maximum size of analyte that can penetrate film grown at different currents should form the basis of future investigation but were not conducted in this project due to time constraints. Also, confocal imaging of hydrogels grown at different currents would affirm the difference in densities/porosities measured electrochemically.

It is not fully understood why hydrogels grown at lower currents have more resistive structures. At higher currents the pH change is greater and therefore the effective pH at the polymerisation region is lower. The extent of secondary binding between hydrogel spindles may be pH dependant. This is a working hypothesis that has not been tested and is only offered as a possible explanation to the observed data trend.

6.5. Anti-biofouling properties of hydrogels

There are many publications extolling the virtues of using hydrogels as an anti-biofouling agents,[119, 125, 134] the previous section showed the ability to electrochemically tune the structure of these hydrogels which makes them ideal candidates for anti-biofouling agents as they can be made size selective as required. It is therefore important as a final test of these hydrogels to show that they are capable of preventing unwanted biomolecules from fouling the electrode surface whilst at the same time allowing target to penetrate the hydrogels. It is vital that the hydrogel can grow around any probe molecules on the surface without changing its efficacy for target binding.

There is precedent in the literature for encapsulating enzymes within hydrogels and maintaining their activity whilst increasing their shelf lives.[119, 120, 135] However, this study is meant to act as a proof of principle and hydrogels can be formed over the PNA probes used in chapter 5 to test the permittivity of the hydrogel to a DNA target. Bovine serum albumin (BSA) was used to test the ability of the hydrogels to prevent larger biological material from fouling the electrode surface. BSA was selected as it has previously been published as a good platform for biofouling studies,[7, 127, 136] it has also been shown to maintain its wildtype structure at pH's above 4.3.[128] It was because of these findings that all tests were conducted in 1 mM FFC in 100 mM KCl at pH 4.3.

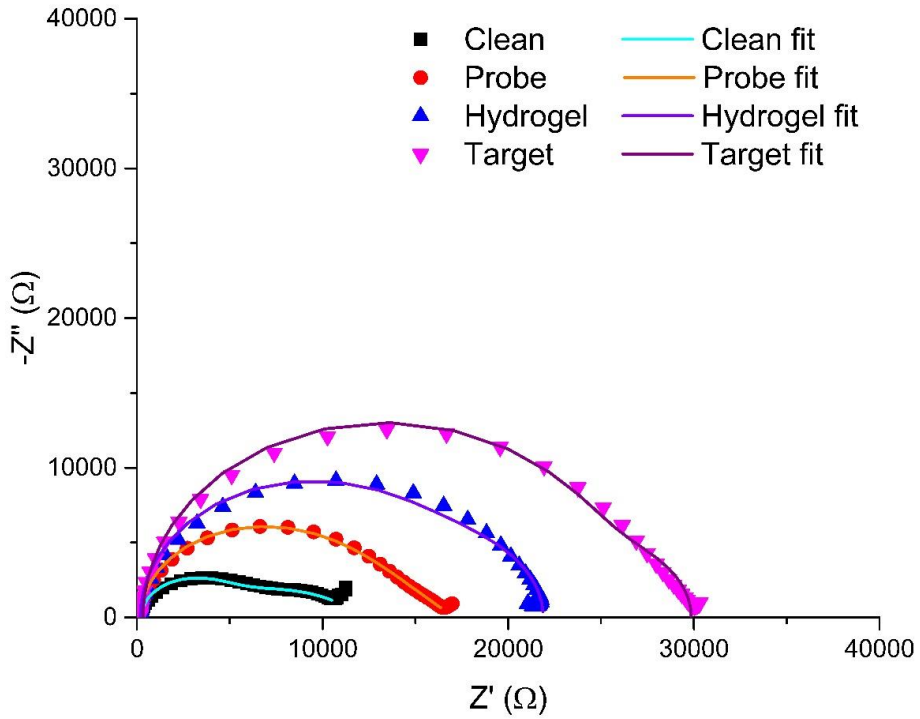

Figure 6.15. Nyquist plots of a 30 µm 3D MNEE array when clean (black squares), after a PNA probe SAM had been formed (red dots), after hydrogel has been grown over and around the SAM (blue triangles) and after exposure to 15 mer DNA target for 30 mins. EIS were recorded at the OCP of 1mM potassium ferricyanide, 1mM potassium ferrocyanide and 100 mM KCl at pH 4.3 vs a saturated calomel reference electrode and Pt gauze counter electrode at room temperature and pressure.

Table 6.6. Equivalent circuit fits for the 30µm 3D MNEE array data shown in figure 6.15.

Parameter	Clean	PNA Probe	Hydrogel	DNA Target
R_s (Ω)	233 ± 33	210 ± 21	233 ± 22	334 ± 103
C_{dl} (nF)	71 ± 2	54 ± 1	54 ± 1	51 ± 1
R_{ct} (kΩ)	4.3 ± 0.1	10.0 ± 0.2	16.7 ± 0.8	26.0 ± 0.2
C_N (nF)	-	-	430 ± 270	400 ± 70
Y_0 (nS)	17700 ± 1000	8400 ± 700	3400 ± 2400	3650 ± 750
R_{nl} (kΩ)	7.6 ± 122	6.8 ± 184	10.3 ± 0.9	10.6 ± 0.6
χ^2	0.0369	0.0049	0.0648	0.0445

Figure 6.15 and table 6.6 show the results of an experiment in which a clean MNEE array was functionalised with a PNA probe SAM film as described in chapter 5.2.2, hydrogel was then grown over the SAM film, as outlined in section 6.2.2. Finally, 15 mer DNA target (30 µM) was incubated on the hydrogel in Ultrapure water to ascertain if it could pass through the hydrogel matrix and bind to the PNA probe. EIS were recorded at each stage of the process and have been plotted, with fits to the appropriate equivalent circuits, in figure 6.15. The fitted values for each circuit element are given in table 6.6.

The changes in fitted circuit elements when going from a clean MNEE array to one with a PNA probe SAM layer have been discussed previously in chapter 5.3.2.C so will not be reproduced here. In these experiments a more porous film PNA film was formed than in chapter 5, this is most probably as a result of these experiments being done in measurement buffer with pH 4.3 (in chapter 5 the pH was not adjusted from that of KCl in water). There is an increase in impedance at each stage of the process which means that the hydrogel can grow on electrodes with PNA SAM coatings, and that these hydrogels are permeable to small ssDNA targets, which bound to the PNA probes and increased R_{ct}.

When the hydrogel grows on the MNEE array with a PNA probe SAM film, the equivalent circuit to which the data is fit changes to equivalent circuit 6. This is the same equivalent circuit used to fit hydrogel grown on a clean MNEE array which is encouraging, as it shows that the presence of the SAM has not introduced any new physical parameters into the hydrogel coated electrode system. When hydrogel is grown over the SAM the fitted values of R_s and C_{dl} stay constant, in keeping with the previous data in this chapter, table 6.3, these values are also of the same order of magnitude as those obtained when hydrogel was grown on clean MNEE arrays which is satisfying as it implies that the hydrogel structure is the same in both experiments.

There is a slight increase in R_{ct} when going from SAM to SAM and hydrogel, table 6.6, this increase of 6 kΩ is similar to the variability in R_{ct} seen in table 6.3, where hydrogels grown for different periods of time were found to have similar range in the fitted values of R_{ct}. It was therefore concluded that the growth of hydrogel over the PNA probe SAM has resulted in a hydrogel with a similar structure at the electrode surface to those grown on clean MNEE

arrays This confirms the theory that the hydrogel coverage directly at the electrode surface is very low, in this system the hydrogel can only grow from pinholes in the SAM structure. The fact that this results in a hydrogel with similar properties to those obtained on clean electrodes implies that the polymer spindles grow from relatively few points on the electrode.

At lower frequencies the fitted values of Y_0 decrease and R_{nl} increases when a hydrogel is grown over the SAM, table 6.6; consistent with previous data, table 6.3, and physically realistic as it shows that the flux of electrolyte to the electrode is being impeded by the hydrogel. However, the decrease in Y_0 and increase in R_{nl} are minor compared to those observed for hydrogel grown on clean MNEE arrays. Therefore, the presence of the PNA probe has resulted in a more porous hydrogel matrix. This is not unsurprising, the secondary binding between polymer spindles is being sterically hindered by the SAM molecules.

The fitted value of C_N is also 10x larger when SAM is present under the hydrogel compared to on a clean electrode; this is inconsistent with the previous theory in that there is a capacitance created by the separation of electrode and electrolyte, as a more porous SAM should decrease this capacitance. This led to the revising of the explanation of C_N, the nature of which is as yet unexplained and should be the purpose of further investigation.

The data also show that there is an increase in R_{ct} when target binds to the probe after permeating through the hydrogel. Consistent with the binding of negative charge into the PNA probe SAM electrostatically repelling the FFC redox couple (the Donnan effect). Indicating that ssDNA target has bound to the PNA probe. The unchanging nature of all the other fitted elements is proof that the hydrogel structure has not been altered by the target binding.

Thus it can be concluded that the carbazole-alanine hydrogel can be grown over SAMs and is permeable to small DNA sequences that can bind to the probe molecules in the SAM without damaging the hydrogel structure. This could, in theory, mean that other pre-established SAM detection techniques can be used in conjunction with this technology; so long as the hydrogel formation process does not adversely affect the probe, for instance such large changes in pH will denature most proteins.

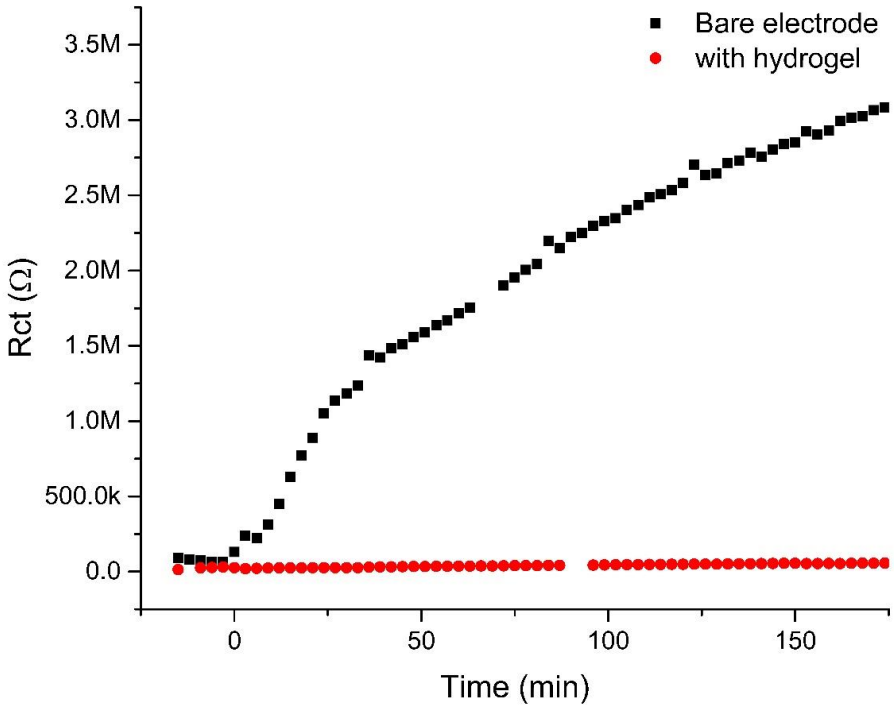

Figure 6.16. Fitted values of R_{ct} vs time for a clean 30 µm 3D MNEE array in a solution of 1 mM potassium ferricyanide, 1 mM potassium ferrocyanide, 100 mM KCl and 100 µM BSA with (red dots) and without (black squares) hydrogel.

After having proven that the hydrogels are permeable to small DNA target oligonucleotides it was determined to prove their anti-biofouling capabilities. Figure 6.16 shows the response of R_{ct} of a bare electrode when left in the measurement buffer and repeated EIS measurements taken. The measurements below 0s were used to obtain a baseline response, the solution was then spiked to obtain a final concentration of 100 µM BSA, and EIS continually recorded for 3h. The fitted values of R_{ct} are seen to increase rapidly over the course of 25 mins, after which there is a constant rate of increase, presumably caused by aggregation of more BSA onto the fouled film. The experiment was then repeated using hydrogel grown on an MNEE array for 20s at + 100 µA. The fitted values for R_{ct} from this experiment are shown in red in figure 6.16; it is clear that there is no appreciable increase in R_{ct} over time. Thus it can be concluded that this hydrogel, which it had previously been shown was permeable to 15 mer target DNA sequences which can then bind to an underlying probe film, is impermeable to large proteins such as BSA. Thus the hydrogel matrix fulfils the necessary criteria to be an anti-biofouling agent.

6.6. Conclusions and future work

This work was always intended to be a proof of principle to determine if hydrogels could be electrochemically grown on nanoelectrodes. Characterisation of said growth using light microscopy, confocal microscopy, SEM and EIS has been performed. It was found that hydrogels grow evenly across the electrodes at short timescales, progressive growth is enhanced in the corners of the cavities but the hydrogel grows into the centre of the cavity and fills it before any significant growth occurs between neighbouring squares in the array. Once the cavities are filled the hydrogel grows into a hemispherical shape, centred in the middle of the cavity, into the bulk solution. Hydrogel growth becomes more random over longer timescales. Further growth leads to array overlap and the hydrogel proceeds to grow into solution as if the electrode array area were a macro electrode.

The hydrogels have been shown to be permeable to small target molecules whilst impermeable to large fouling biomolecules such as BSA. This coupled with the tuneable porosity of the hydrogels, which was proven by measuring the diffusion coefficient of FFC through hydrogels grown at different currents, displays the ability of the hydrogels to make size selective anti-biofouling membranes the growth and properties of which can be electrochemically controlled.

Future work should encompass the development of hydrogels that gelate over a more biologically friendly pH range so as to allow encapsulation of enzyme probes on the electrode surface. A more in depth analysis of the porosity of the hydrogels grown over a wider range of currents should also be undertaken and should involve imaging and electrochemical techniques. This work was intended to be a proof of principle and further optimisation and characterisation of all the processes involved would be welcome.

The heterogeneity of the hydrogel may affect its function as an anti-biofouling agent, but is in itself a new finding. These hydrogels have until now been grown exclusively on planar macro electrodes, which produce hydrogels of a homogeneous structure.[126] The ability to make heterogeneous hydrogels has, to the best of the authors knowledge at the time of writing, gone unreported in the literature and could be of use to the hydrogels community. Hydrogels have found a wide array of uses and outlining the ability to grow heterogeneous hydrogels may have some benefits in many of these applications. For example, hydrogels are being widely investigated for drug delivery,[137, 138] and the ability to grow hydrogels that release drugs at different rates within the same pill may be possible based on the principle proven herein. Denser hydrogels being formed in the corners of the cavities as a result of a higher current density means that the composition of the hydrogel could in theory be selectively tuned by changing the gelation current density. This was investigated and is discussed in section 6.4.

The nature and form of the imbrication is of interest to the hydrogel community as the multifarious uses of hydrogels may benefit from the properties of hydrogels grown on separate electrodes that merge with one another; again this is not the main purpose of this research so will not be discussed in any great detail but it is interesting to note that the “spindle fibres” of the overlapping xerogels appear to intercalate where they meet. It was thought that where the pH excursions of neighbouring array elements met there might be sufficient pH drop to induce gelation, however this was not observed. That is not to say that no such process occurred and was unable to tether to the silicon nitride. Again, a more in

depth analysis of these processes should be carried out, ideally by an expert in the field of hydrogels rather than an electrochemist.

The pH swing needed to induce gelation is from pH 8 to pH < 4.[139] Most biomolecules will not survive such a large pH swing, so it is important that in the future a gelator should be developed that forms hydrogels over a more biologically friendly pH range.

Analyst

ARTICLE

Characterisation of hydrogels grown on nanoelectrode biosensor arrays for enhanced sensing in biological media

Received 00th January 20xx,
Accepted 00th January 20xx

DOI: 10.1039/x0xx00000x

www.rsc.org/

A. Piper,[a] B. Alston,[b] D. J. Adams[b]† and A. R. Mount[a]*

Nanoelectrodes and nanoelectrode arrays show enhanced diffusion and greater Faradaic current densities and signal-to-noise ratios than macro and microelectrodes, which can lead to enhanced sensing and detection. One example is the microsquare nanoband edge electrode (MNEE) array system, readily formed through microfabrication and whose quantitative response has been established electroanalytically. Hydrogels have been shown to have applications in drug delivery, tissue engineering, and anti-biofouling; some also have the ability to be grown electrochemically. Here, we combine these two emerging technologies to demonstrate the principles of a hydrogel-coated nanoelectrode array biosensor that is resistant to biofouling. We first electrochemically grow and analyze hydrogels on MNEE arrays. The structure of these gels is shown by imaging to be electrochemically controllable, reproducible and structurally hierarchical. This structure is determined by the MNEE array diffusion fields, consistent with the established hydrogel formation reaction, and varies in structural scale from nano (early time, near electrode growth) to micro (for isolated elements in the array) to macro (when there is array overlap) with distance from the electrode. There is also increased hydrogel structural density observed at electrode corners, attributable to enhanced diffusion. The resulting hydrogel structure can be formed and is anchored through/on an established clinically relevant biosensing layer without compromising detection. It also shown, through proof-of-principal model protein studies using Bovine serum albumin (BSA), to prevent protein biofouling whilst enabling smaller molecules such as DNA to pass through the hydrogel matrix and be sensed. Together, this demonstrates a method for developing reproducible, quantitative electrochemical nanoelectrode biosensors able to sense in real-world sample matrices.

Introduction

Nanoelectrodes and hydrogels are each of growing interest in the field of biosensors.[1-5] Hydrogels can be used to encapsulate and support biomolecules on a macroelectrode surface, thereby increasing the shelf life of these biosensor systems whilst not impeding their biomolecular function.[4-9] It has also been shown that hydrogels are permeable to small molecules[10] and can be used to prevent electrode fouling in complex media such as human blood.[11] Nanoelectrodes have been shown to possess enhanced mass transport which, coupled with a relatively small double layer charging current, yields a relatively large detection sensitivity and signal to noise ratio.[12,13]

The use of nanoelectrode arrays containing multiple electrodes also allows the exploitation of the enhanced sensitivity of nanoelectrodes whilst measuring macroelectrode currents.[14] We have recently detailed the reproducible fabrication through photolithographic processing of Microsquare Nanoband Edge Electrode (MNEE) and shown through a combination of experiment and theory that steady-state and quantitative responses can readily and reproducibly be obtained from which electroanalytical parameters can readily be extracted.[12,13,15] MNEE arrays are fabricated by the controlled geometrical etching of an array of square micron dimension cavities of controlled depth through a layer of Pt (of a defined nanometer thickness) sandwiched between two insulators of controlled thickness. This results in an array of micron scale cavities of defined separation, each of which contains a Pt nanoband running around the inside of the cavity at a controlled depth, defined by the etch depth and the thickness of the insulators. These electrode arrays are highly sensitive, but also highly reactive (consistent with the Pt nanoelectrode dimension). This is likely to result in enhanced biofouling in biosensing applications.

In this paper, the potential for combining these technologies through the functionalization of these nanoelectrode systems with hydrogels is therefore investigated, with a view to fabricating electrochemical biosensors which display both enhanced nanoelectrode array performance and the enhanced longevity and resistance to biofouling produced by hydrogels.

[a] EaSTCHEM, School of Chemistry, The University of Edinburgh, Joseph Black Building, King's Building's, David Brewster Road, Edinburgh, EH9 3FJ, U.K.
[b] Department of Chemistry, University of Liverpool, Crown Street, Liverpool, L69 7ZD, U.K..
† School of Chemistry, University of Glasgow, Glasgow, G12 8QQ, UK
*corresponding author
Electronic Supplementary Information (ESI) available: [details of any supplementary information available should be included here]. See DOI: 10.1039/x0xx00000x

To enable localized functionalization of the nanoelectrodes with hydrogels under spatial control, we have used the electrochemically controlled growth of low molecular weight hydrogels on electrodes.[16] We first establish the principal of electrochemical growth of hydrogels on MNEE arrays, then characterize the resulting hydrogel structures and finally determine the potential enhancement in biosensing characteristics of the combined system.

Experimental

MNEE fabrication. The MNEE array design, fabrication procedures and geometries are detailed elsewhere 12,13 (the configuration is shown in Figure S1). All experiments were performed on these MNEE arrays, which consist of 1764 square cavities of 30 µm edge length placed in a square arrangement, with each cavity separated by 90 µm from its neighbors. The cavities were etched to a depth of 560 nm, exposing a nanoband electrode of 50 nm thickness around the perimeter and at the base of each cavity. The total geometrical electrode surface area of the array is therefore 1.0584 x 10-4 cm^2.

Electrochemical Experiments. All electrochemical measurements were made at a constant temperature of 25 °C, controlled by a water bath built in-house. They were performed in a Faraday cage using an Autolab PGSTAT128N with a FRA32 module (supplied by Metrohm Ltd.) controlled by a PC using NOVA 1.10 software. All potentials are reported with respect to the saturated calomel reference electrode (SCE, Accumet® 13-620-61, Fischer Scientific) unless otherwise stated, and the gauze counter electrode was made in house using Pt gauze and wire (Sigma-Aldrich). All solutions were prepared using deionized water (18.2 $M\Omega\,cm^{-1}$, Millipore MilliQ) with sodium chloride (BioXtra ≥99.5%), potassium ferricyanide (ACS reagent ≥99%), potassium ferrocyanide (ACS reagent ≥99%) and hydroquinone (reagentplus® ≥99.5%) all supplied by Sigma Aldrich. All pH measurements were performed using a Fisherbrand Hydrus 400 pH meter with a Mettler Toledo InLab®Routine Pro pH probe. Electrochemical impedance spectroscopy (EIS) measurements were carried out in an aqueous solution of potassium ferrocyanide (1 mM, Sigma Aldrich) and potassium ferricyanide (1 mM, Sigma Aldrich) in KCl (0.1 M, Sigma Aldrich) background electrolyte. EIS was performed by applying a sinusoidal potential of 10 mV rms superimposed on the open circuit potential (OCP), to ensure no overall Faradaic reaction. 50 logarithmically spaced frequencies were applied in the range between 100 kHz and 0.1 Hz. The OCP was measured before each EIS measurement and, as expected for the ferricyanide/ferrocyanide couple was typically between + 165 and + 170 mV with respect to SCE.

Carbazole-alanine synthesis and hydrogel formation. The carbazole-alanine hydrogel was prepared as described previously.[16] A solution of the gelator was prepared by stirring carbazole-alanine (2 mg/mL) in aqueous sodium hydroxide (6.75 mM) at room temperature overnight until it had fully dissolved. Aqueous HCl (1 M) and NaOH (6.75 mM) solutions were used as appropriate to adjust the pH to 8. Hydroquinone (2.88 mg/ml, Sigma Aldrich) and NaCl (0.1 M, Sigma Aldrich) were added as the pH swing inducer and the background electrolyte respectively. Gelation was induced using chronopotentiometry, holding the MNEE array working electrode at +100 µA unless otherwise stated in a three-electrode system using a Pt wire as a pseudo-reference electrode.

Imaging (SEM and confocal microscopy with Nile blue stain). SEM images were obtained using a Hitachi S-4800 FE-SEM at 3 keV. Hydrogels were electrochemically grown on to the MNEE and fixed onto aluminium SEM stubs with carbon tabs and air dried for direct imaging. The MNEE arrays were gold coated for 1.5 minutes at 20 mA using a sputter EMITECH K550X sputter coater prior to imaging.

Confocal microscopy images were obtained on a Zeiss LSM510 and a Plan-Apo 100x (1.4 NA oil) and 63x (1.46 NA oil) objective. The gelator solution was prepared as described previously, with the addition of 0.001 M Nile Blue. Nile Blue fluorescence was excited at 633 nm using a Helium Neon laser and emission detected between 638 and 758 nm using a pinhole diameter of 1 Airy unit (approx. 0.8 μm resolution). The working electrode was placed in an uncoated borosilicate MatTek dish with a 20 mm diameter glass coverslip. Images were analyzed using the Zeiss AIM software (Zeiss, Jena, Germany) and ImageJ software.

PNA SAM formation, DNA target binding and biofouling studies.

PNA SAM formation was carried out using 1.5 nM PNA (Panagene, Daejeon, South Korea), 150 nM tris-2-carboxymethylphosphine (TCEP, Sigma-Aldrich) and 30 nM 6-mercaptohexan-1-ol (MCH, Sigma-Aldrich) in a 50:50 mixture by volume of DMSO and deionized water. 50 µl of this mixture was placed on the MNEE array for 1 hour to form the PNA SAM on the electrode surfaces, followed by growth of the carbazole-alanine hydrogel galvanostatically in gelator solution at +100 µA for 10 s. The functionalized MNEE array was then exposed to a 50 µL droplet of 100µM aqueous solution of 30 mer complementary target DNA (Sigma-Aldrich) sequence:

5'-GTATGCTTTGGTCTTTCTGCATTCCTGGAA-3'

for 30 minutes. Measurement of target binding involved performing EIS as above, using redox buffer (1 mM/1 mM $K+[Fe(CN)_6]^{3-}/K+[Fe(CN)_6]^{4-}$ in aqueous 1x tris-HCl pH 4.3) so as to ensure gel stability. For biofouling kinetic experiments, this redox buffer was also used selected as it has been previously established that bovine serum albumin (BSA) is stable under this pH regime.[17] BSA (Sigma Aldrich, UK) was purchased as a lyophilized powder and made up to a final 100 µM concentration, followed by pH readjustment as required.

RESULTS AND DISCUSSION

The carbazole-alanine forms hydrogels by self-assembling into fibrous structures, induced by a pH decrease. In previous work, the electrochemical oxidation of hydroquinone at a

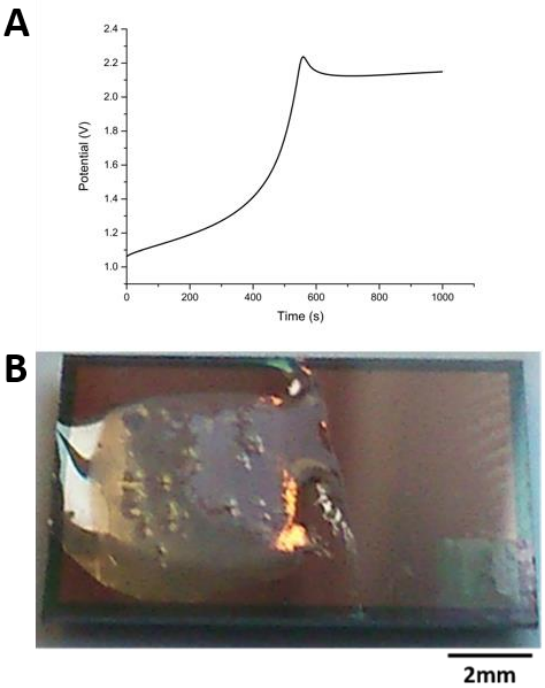

Figure 1 (A) Typical potential-time transient recorded during 15 min of galvanostatic hydrogel growth at +100 μA on an MNEE array and (B) a photograph of the resulting hydrogel. Note that potentials reported are with respect to the platinum pseuodreference.

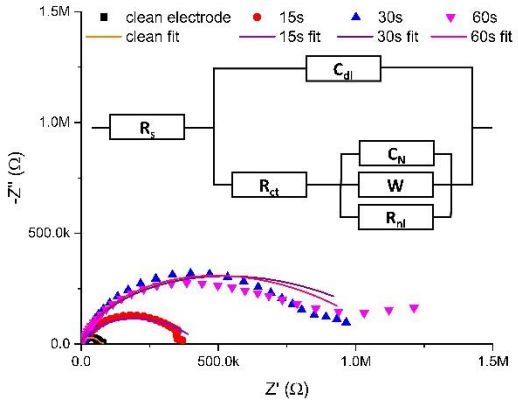

Figure 2 Typical EIS Nyquist data (points) for a clean MNEE and an MNEE after a total of 15 seconds, 30 seconds and 60 seconds of hydrogel growth, along with fits of these data (lines) to the general equivalent circuit (inset); Note that Table S1 in the SI contains the values for the fits of these data to the appropriate limiting case for the general equivalent circuit (inset). Note that this is an extension of the established MNEE equivalent circuit[13], with an additional Warburg element to account for within hydrogel diffusion. All fits give relatively low fit values (with $\chi^2 < 0.156$).

macroelectrode surface has been used to lower the pH locally, so as to grow a hydrogel matrix.[16] The linear diffusion regime established across these electrodes is assumed to produce a relatively homogeneous hydrogel. MNEE arrays have established enhanced steady-state mass transport with a mixture of coupled diffusional regimes (highly enhanced nanoscale diffusion near band electrodes, enhanced microscale diffusion within and immediately outside each cavity and macroscale diffusion where cavity array diffusional fields overlap).[13] This is likely to lead to spatially inhomogeneous pH decrease and hydrogel formation, so the appropriate electrochemical hydrogel growth conditions and resulting hydrogel structures first need to be established for MNEE arrays.

Following the previous electrochemical hydrogel procedure,[16] Figure 1a shows a typical potential time transient for hydrogel formation at the MNEE, along with an image of the resulting hydrogel (Figure 1b). During the gelation process, following the initial establishment of the characteristic hydroquinone oxidation potential above +1.0 V reported previously, over short periods of time (t < 400 s) the potential is seen to increase essentially linearly to around +1.3 V, consistent with the increased overpotential required to deliver this oxidation current through the growing hydrogel. After 400 s, the potential is seen to rise relatively rapidly to over +2.0 V, consistent with mass transfer of hydroquinone to the electrode surface being insufficient to support this current, and the growing importance of solvent oxidation and oxygen gas formation. This gas formation is the most likely cause of the bubbles that can be observed in the hydrogel in Figure 1b. As these oxygen bubbles will compromise the hydrogel structure, growth was limited to times less than 400 s, where bubbles do not form.

To investigate the different stages of electrochemical hydrogel formation, galvanostatic growth using this procedure was carried out for successive 5 second periods, followed by optical (using scanning electron microscopic, confocal microscopic and light microscopic imaging) and electrochemical characterization., Figure 2 shows typical Nyquist plots after these successive growth periods.

It is reassuring that the measured impedance values increased with longer hydrogel formation times, consistent with a progressive increase in surface hydrogel formation. The fits to these EIS data enable quantitative assessment of hydrogel characteristics (*vide infra*). The light microscopy images (Figure 3) also confirm the progressive growth of hydrogel. The magnitude of the galvanostatic current and the potential profile suggest that the hydrogel growth is largely determined by diffusion, with hydroquinone diffusion and reaction at the electrode producing the required local pH decrease for hydrogel formation within the diffusion layer through proton production.16 Under these conditions, the thickness of the diffusion layer, *l*, as a function of time, t, can be estimated by:

$$t \approx l^2/D \qquad \text{(Equation 1)}$$

where D is the diffusion coefficient. This is an estimate, as it is not known whether the gel growth is limited by the flux of hydroquinone to the electrode or by the local pH (controlled by the flux of H_3O^+ away from the electrode). The value of D is also likely to decrease within the hydrogel.

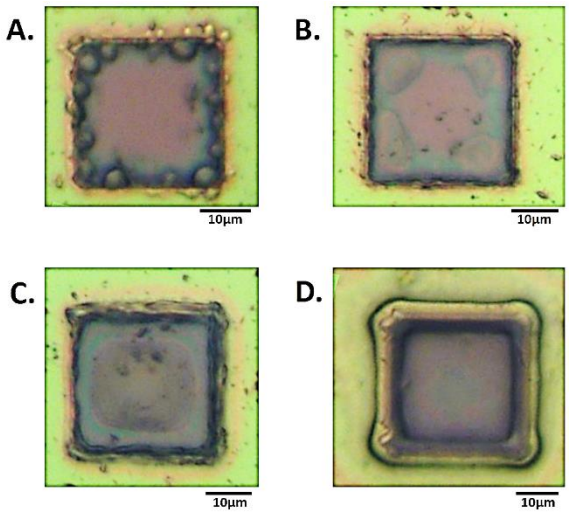

Figure 3 Light microscopy images of a single square in the MNEE array after (A) 5 seconds (B) 10 seconds (C) 15 seconds (D) 20 seconds growth at 50 µA.

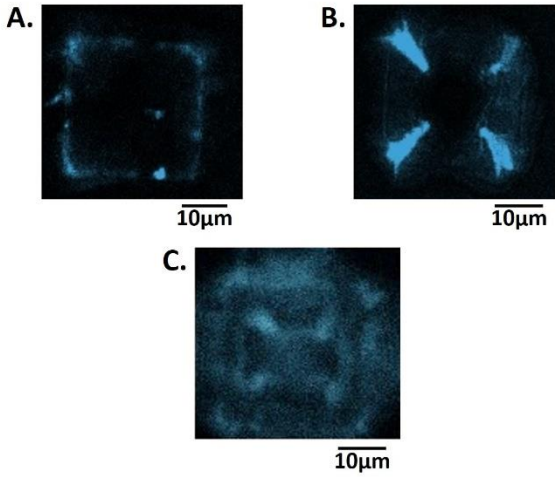

Figure 4 Confocal microscopy images of a single square cavity in the hydrated MNEE array after (A) 5 seconds (B) 10 seconds (C) 20 seconds of hydrogel growth, following staining and imaging with Nile blue.

Characterization of hydrogel growth; spatial determination of the hydrogel structure

t = 5 secs

Taking literature values of D the diffusion coefficient for hydroquinone as 2.7 x 10^{-6} cm^2 s-1,[18] and for H^+ as 4.5 x 10^{-5} cm^2 s^{-1},[19] after 5 seconds, the characteristic diffusion layer thickness for hydroquinone is of the order of 40 µm; for protons it is 225 µm. Given the likely decrease in D and the fact that the pH excursion is likely to be lower, due to buffering by dissolved carbonate species,[19,20] and the dilution caused by the enhanced proton nanoscale diffusion, it is satisfying that the corresponding light microscopy image (Figure 3a) indicates hydrogel growth to a comparable distance of around ten microns.

It is satisfying that the EIS fit values of R_s, R_{ct} and C_{dl} remain relatively constant at 164 ± 5 Ω, 19 ± 6 nF (corresponding to 180 ± 60 µ F cm^{-2} a typical double layer capacitance for an uncoated electrode of these dimensions[21]) and 19 ± 3 kΩ. during hydrogel growth, (Figure S2 and Table S1 in the SI). This confirms that the hydrogel is an open structure which does not hinder significantly the passage of electrolyte ions, and that the electrochemical response at the underlying electrode remains unchanged. However, there is a significant increase in R_{nl} and decrease in Y_0 (obtained from W) compared to the clean MNEE after 5 seconds of hydrogel growth, with the observed mean value of *D* for ferri/ferrocyanide dropping from the accepted literature value[22] of (7.7 ± 0.03) x 10^{-6} cm^2 s^{-1} to (0.89 ± 0.01) x 10^{-6} cm^2 s^{-1} from R_{nl} and (0.26 ± 0.02) x 10^{-6} cm^2 s^{-1} from Y_0 (see equations S1 and S2). This indicates that the progressive growth of the gel matrix does cause a decrease in D. It is interesting that the value derived from Y_0 (due to linear diffusion close to the electrode) is now lower than that derived from R_{nl} hemispherical diffusion across the diffusion layer formed at each cavity), which suggests the inhibition of mass transport due to a relatively dense hydrogel formed at the electrode surface. This is to be expected, as electrochemical hydrogel formation must be localized at the nanoelectrode, where the hydrogel must therefore be of nanodimension. This is confirmed by confocal microscopy (Figure 4a) and SEM (Figure 5a), which show that hydrogel is firmly anchored to, and grows from the entire nanoband.

t = 10 s

The confocal microscopy (Figure 4b) indicates a clear growth in the area of enhanced dye emission, consistent with the expected progressive growth of the hydrogel. It is also interesting that there are areas of markedly enhanced dye emission, emanating from the corners. This indicates increased gelator density, and is consistent with the previously predicted and observed enhanced currents for microsquare versus microdisc electrodes, due to enhanced square corner diffusion and reaction.[13,15] Notwithstanding the expected conversion of hydrogel to collapsed gelator on the electrode surface due to vacuum desiccation, the SEM image (Figure 5b) confirms this increase in gelator.

t = 20 s

After 20 seconds, both the light microscopy and SEM images (Figures 5c and 5d) indicate that hydrogel has grown sufficiently to fills each cavity in the array. This is consistent with the confocal microscopy image (Figure 4c), which is a circular 2D slice of the near hemispherical 3D hydrogel). This image indicates the continuation of spatial heterogeneity in the growing hydrogel structure, built on the observed structure in Figure 4b and consistent with the effects of diffusion to the cavity. This hemispherical hydrogel is consistent with the previous postulation of the origin of C_N in the MNEE equivalent circuit as being due to a relatively rapid reaction of the essentially hemispherical volume above the cavity, brought about by enhanced nanoscale diffusion induced by the nanoband electrode around the cavity edge.[13]

t= 20-30 s and beyond; hemispherical growth to array overlap.

On a timescale of 20-30 seconds, the diffusion fields (and therefore hemispherical hydrogel formation fields) are

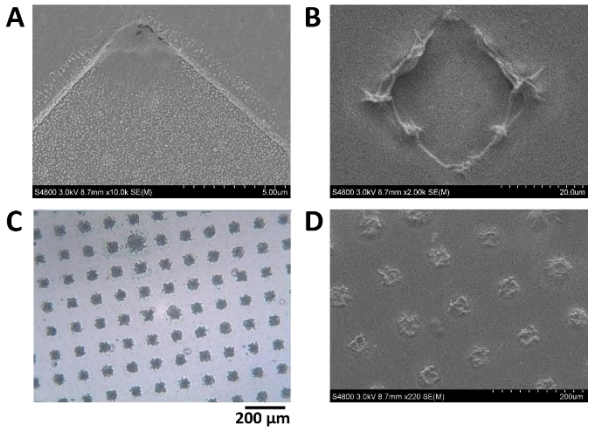

Figure 5 Scanning electron microscopy (SEM) images of the MNEE array after (A) 5 seconds and (B) 10 seconds growth at 50 µA. A close up of the electrode in figure (A) can be found in figure S3 showing that gel is growing across the entire electrode but enhanced growth is clearly occurring in the corners. (C) and (D) are light microscopy and SEM images of collapsed (dehydrated) hydrogel respectively after 20s, which show that hydrogel has completely filled each cavity in the array.

expected to continue to grow outwith each cavity. This is shown by the light microscopy image from a dehydrated hydrogel grown for 30 seconds (Figure 6a), which shows some elements of the growing hydrogel have fused with neighbours, such that their dehydrated, collapsed structure retains the evidence of this fusion.

Further prolonged hydrogel growth leads to progressive fusion of all neighboring hydrogel elements, and the establishment of a hydrogel structure which covers the entire electrode area. This is consistent with the expected elemental diffusion field overlap and the establishment of planar diffusion across the array. Light microscopy of the hydrated hydrogel (Figure 6b) indicates this hydrogel has a relatively open micron-scale structure in comparison to the denser, hemispherical structure imaged at and around each cavity due to the earlier stages of hydrogel formation.

These structural data provide a clear rationale for each of the limiting cases of the global equivalent circuit used to analyse the impedance data (Figure 2). Initially, prior to hydrogel formation, as expected the data fits the established clean MNEE array circuit,[8] with no Warburg impedance ($Y_0 \rightarrow \infty$) and. After initial hydrogel growth, there is a growing contribution from W, which we attribute to the diffusion of redox species within the hydrogel. Finally, on array overlap and continued hydrogel film growth across the entire MNEE array, a further semicircular feature is observed which we attribute to an additional series circuit element of a capacitor and resistor in parallel due to charge transfer into this film. It is satisfying that throughout these different stages of growth the values for R_s, R_{ct} and C_{dl} remain constant, and R_{nl} also remains essentially unchanged. This is consistent with the formation of a spatially heterogeneous hydrogel, whose local structure is determined by the local diffusional characteristics at hydrogel formation.

Global control of the hydrogel structure

In addition to the controlled spatial hydrogel heterogeneity induced by the MNEE diffusion fields, Figure 7 shows the

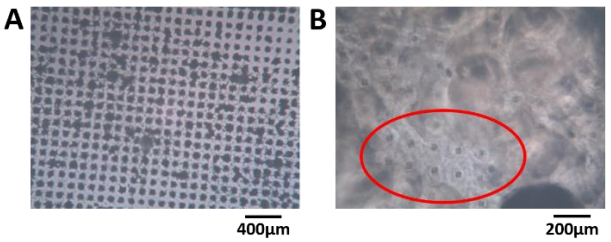

Figure 6 Light microscope images of (A) dehydrated hydrogel after 30 secs growth and (B) hydrated hydrogel after 15 min growth. Note that after 30 seconds there is the start of neighboring hydrogel coalescence. The gel has obscured the majority of the array but thinner patches of gel exist where array elements, and hemispherical shaped hydrogel surrounding them, are observable. Note the black spot in the bottom right is due to a void in the hydrogel arising from growth around a gas bubble (for similar voids, see Figure 1).

current at which the gel is grown also determines the density of the organic scaffold and hence the porosity of the gel formed. These data show a comparison of the EIS spectra of hydrogels grown for 15 seconds at 50 and 100 µA respectively (which should give similar diffusion fields and hydrogel volumes due to the fixed time). It is clear that the impedance values for the reaction and diffusion of ferri/ferrocyanide through the hydrogels formed at the lower current are markedly higher, and that the fit parameters (Table S1) show a statistically significant and marked decrease in Y_0 and a corresponding increase in R_{nl}, attributable to a decrease in the mean diffusion coefficient D of the order of a factor of 4 for ferri/ferrocyanide (from around 2 x 10^{-7} cm^2 s^{-1} at 100 µA to between 4-8 x 10^{-8} cm^2 s^{-1}) at 50 µA, indicating the formation of a denser, less porous hydrogel compared to that formed at the higher current. There is also a small decrease in Cdl, which would be consistent with an increase in the density of the organic scaffold of the nanodimensional hydrogel at the electrode surface. Such an increase in density at lower current would be consistent with an increase in the local concentration of gelator species due to a reduction in the importance of mass transfer.

Feasibility of biosensing through a hydrogel on a MNEE array

The ability to vary the overall density and hence porosity of the gel, combined with the established controlled and reproducible spatial variation in hydrogel structure, could be of value in the tuning of molecular filtration properties of these hydrogels. One potential application would be the production of a surface layer which inhibits or prevents electrode sensor biofouling.[11] Biofouling, especially of nanoelectrodes, is an area of great interest as moves are made towards implantable diagnostic devices.[23,24] All point-of-care diagnostics would benefit from being able to detect analytes in complex media without the need for pre-treatment, which can be expensive and time consuming.[4,23] One potential use of electrochemically produced hydrogels would be if they could be grown over established electrochemical sensing/detection systems, thereby conferring surface anti-biofouling, without compromising target detection. The feasibility of this approach was therefore tested, by using the model system of an

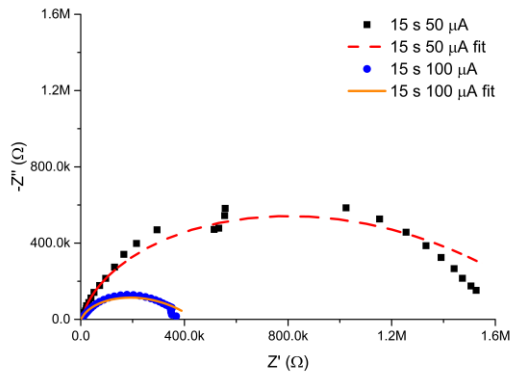

Figure 7 Nyquist plots in redox buffer of hydrogels grown for 15 seconds at 50 and 100 µA, along with their associated fits to the equivalent circuit (with fit parameters given in Table S1).

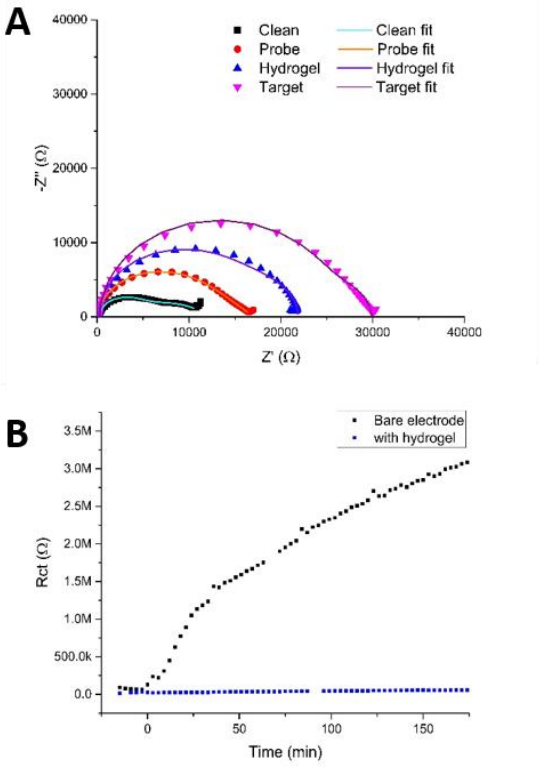

Figure 8 (A) Nyquist plots of a clean MNEE array, an array with a PNA probe SAM layer, with a hydrogel grown over and around the SAM film and after binding of target DNA that has penetrated the hydrogel and bound to the probe. Circuit fits can be found in Table S2. (B) Fitted values of R_{ct} obtained by taking consecutive measurements of an electrode in redox buffer containing 100 µM BSA with and without hydrogel on the electrode surface. The points below 0 min were repeat measurements taken on a clean electrode, prior to exposure to BSA, as a control.

established biomolecular sensing film readily formed through creating a self-assembled monolayer on an electrode.[25] The previously established and clinically relevant DNA sensing protocol for the detection of the MRSA *mecA* cassette was chosen to determine the ability of the electrode to retain its function as a working biosensor following electrochemical hydrogel formation. The protocol involved forming a self-assembled monolayer (SAM) using a peptide nucleic acid (PNA) probe with a sequence homologous to the MRSA *mecA* cassette. A spacer molecule (6-mercaptohexan-1-ol, MCH) was also present in the solution (and film) in a 15:1 ratio with the PNA to optimize surface coverage.[25] The carbazole-alanine hydrogel matrix was then grown through and over this film for 10 seconds at 50 µA as above before being incubated with a 15-mer target DNA (100 µM) for 30 minutes. The electrode was then placed in the redox buffer and hybridization measured as above using EIS. The sensing protocol has previously been shown to not exhibit non-specific binding to mismatched DNA target sequences.[25]

Figure 8a shows the Nyquist plots obtained using this protocol, which show the expected increases in the impedance, first on going from a clean MNEE nanoelectrode array to an array with a blocking PNA SAM probe film, then with an additional layer of hydrogel electrochemically grown on the surface, and finally, when target passes through the hydrogel and binds to the PNA probe. Detailed analysis reveals the expected increase in R_{ct} when going from a clean electrode to one that has a SAM film on the surface, whilst R_{nl} stays constant, which confirms that there is no effect on D (mass transfer to the electrode). Growing the hydrogel over the SAM is then seen to increase R_{nl} significantly, as expected, such that the two near semicircular features are no longer distinguishable by eye. This confirms the growth of the hydrogel matrix, within which there is the corresponding expected in diffusion. It is interesting that is also a significant increase in R_{ct}, since it has been established that this charge transfer response is largely determined by redox reaction through pinhole defects in the SAM layer formed on multicrystalline electrode surfaces.[26-28] This suggests that the local enhanced pH change increases observed the charge transfer resistance through and/or blocking at least some of these pinholes by creating hydrogel anchor points to the underlying electrode. The final sensing step again results in the expected significant increase in R_{ct} (without a change in R_{nl}), due to the formation of the more blocking PNA-DNA duplex SAM film at the electrode surface. It is satisfactory that this relative increase in R_{ct} on target binding is comparable to that observed previously for this biosensor system,[25] which confirms biosensing function is not significantly affected, even after the growth of the surface hydrogel.

To test the ability of this carbazole-alanine hydrogel to prevent biofouling, a clean MNEE was placed in redox buffer containing 1 µM bovine serum albumin (BSA). It has previously been reported that BSA is a ~ 66.5 kDa protein, stable in its wildtype form at the redox buffer pH of 4.3, that has been shown to readily foul a clean electrode surface and is.[17,29] Figure 8b shows the resulting values of R_{ct} obtained from successive EIS measurements as a function of time. These demonstrate the expected and progressive significant increase in R_{ct} due to surface nanoelectrode biofouling. In contrast, after surface hydrogel growth at 100µA for 20 secs the values of R_{ct} are seen to remain low and invariant with time. This stark contrast between the two signals clearly demonstrates the ability of the hydrogel, with its increasingly dense structure from bulk

solution to electrode, to prevent BSA biofouling of the underlying nanoelectrode array.

Conclusions

This work has established that spatially structured hydrogels can be electrochemically grown reproducibly and controllably on the surface of MNEE arrays, and that this growth does not compromise the sensing activity of a biosensing SAM layer. It also demonstrates that the hydrogel can be used to prevent the non-specific binding of the biologically relevant 66 kDa BSA protein. These is the essential proof of principles required to demonstrate the feasibility of electrochemical target detection from complex media, which contain biologically relevant proteins, by using SAM probe-target binding at nanoelectrodes capped with hydrogel. Further work required to develop this system includes the exploitation of the tuning of gelation and the resulting hydrogel structure (as demonstrated by control of the hydrogel current) to enable optimization of protein-target selectivity for the variety of proteins found in such media, and the production of electrochemically generated hydrogels with stability over a wider and clinically relevant pH range.

Acknowledgements

AP would like to thank the University of Edinburgh Schools of Chemistry and Engineering for funding his PhD studentship. DJA thanks the EPSRC for a Fellowship (EP/L021978/1). The Authors would like to acknowledge Dr. A. Bunting and Prof A. Walton from the Scottish Microelectronics Centre for their advice regarding the fabrication of the MNEE devices.

References

1 1. G. Liu, C. Sun, D. Li, S. Song, B. Mao, C. Fan and Z. Tian, *Advanced Materials*, 2010, **22**, 2148-2150.
2 2. M. Silvestrini, L. Fruk and P. Ugo, *Biosensors & Bioelectronics*, 2013, **40**, 265-270.
3 3. A. Guiseppi-Elie, *Biomaterials*, 2010, **31**, 2701-2716.
4 4. W. Yang, H. Xue, L. R. Carr, J. Wang and S. Jiang, *Biosensors & Bioelectronics*, 2011, **26**, 2454-2459.
5 5. M. V. Pishko, A. C. Michael and A. Heller, *Analytical Chemistry*, 1991, **63**, 2268-2272.
6 6. J. A. Rowley, G. Madlambayan and D. J. Mooney, *Biomaterials*, 1999, **20**, 45-53.
7 7. M. M. Dominguez, M. Wathier, M. W. Grinstaff and S. E. Schaus, *Analytical Chemistry*, 2007, **79**, 1064-1066.
8 8. K. Sirkar and M. V. Pishko, *Analytical Chemistry*, 1998, **70**, 2888-2894.
9 9. S. E. Salamifar and R. Y. Lai, *Analytical Chemistry*, 2014, **86**, 2849-2852.
10 10. M. Wallace, D. J. Adams and J. A. Iggo, *Soft Matter*, 2013, **9**, 5483-5491.
11 11. N. Wisniewski and M. Reichert, *Colloids and Surfaces B-Biointerfaces*, 2000, **18**, 197-219.
12 12. J. G. Terry, I. Schmueser, I. Underwood, D. K. Corrigan, N. J. Freeman, A. S. Bunting, A. R. Mount and A. J. Walton, *Iet Nanobiotechnology*, 2013, **7**, 125-134.
13 13. I. Schmueser, A. J. Walton, J. G. Terry, H. L. Woodvine, N. J. Freeman and A. R. Mount, *Faraday Discussions*, 2013, **164**, 295-314.
14 14. Y. H. Lanyon, G. De Marzi, Y. E. Watson, A. J. Quinn, J. P. Gleeson, G. Redmond and D. W. M. Arrigan, *Analytical Chemistry*, 2007, **79**, 3048-3055.
15 15. H. L. Woodvine, J. G. Terry, A. J. Walton and A. R. Mount, *Analyst*, 2010, **135**, 1058-1065.
16 16. J. Raeburn, B. Alston, J. Kroeger, T. O. McDonald, J. R. Howse, P. J. Cameron and D. J. Adams, *Materials Horizons*, 2014, **1**, 241-246.
17 17. A. Michnik, K. Michalik and Z. Drzazga, *Journal of Thermal Analysis and Calorimetry*, 2005, **80**, 399-406.
18 18. X. Ji, C. E. Banks, D. S. Silvester, A. J. Wain and R. G. Compton, *Journal of Physical Chemistry C*, 2007, **111**, 1496-1504.
19 19. W. J. Albery and A. R. Mount, *Journal of the Chemical Society-Faraday Transactions I*, 1989, **85**, 1181-1188.
20 20. W. J. Albery and A. R. Mount, *Journal of the Chemical Society-Faraday Transactions I*, 1989, **85**, 1189-1198.
21 21. A. J. Bard and L. R. Faulkner, *Electrochemical methods : fundamentals and applications*, Wiley, New York ; Chichester, 1980.
22 22. K. Ngamchuea, S. Eloul, K. Tschulik and R. G. Compton, *Journal of Solid State Electrochemistry*, 2014, **18**, 3251-3257.
23 23. N. Wisniewski, F. Moussy and W. M. Reichert, *Fresenius Journal of Analytical Chemistry*, 2000, **366**, 611-621.
24 24. B. Yu, C. Wang, Y. M. Ju, L. West, J. Harmon, Y. Moussy and F. Moussy, *Biosensors & Bioelectronics*, 2008, **23**, 1278-1284.
25 25. D. K. Corrigan, H. Schulze, G. Henihan, A. Hardie, I. Ciani, G. Giraud, J. G. Terry, A. J. Walton, R. Pethig, P. Ghazal, J. Crain, C. J. Campbell, K. E. Templeton, A. R. Mount and T. T. Bachmann, *Analyst*, 2013, **138**, 6997-7005.
26 26. C. M. A. Brett, S. Kresak, T. Hianik and A. M. O. Brett, *Electroanalysis*, 2003, **15**, 557-565.
27 27. P. M. Kosaka, S. Gonzalez, C. M. Dominguez, A. Cebollada, A. San Paulo, M. Calleja and J. Tamayo, *Nanoscale*, 2013, **5**, 7425-7432.
28 28. Z. Novakova, R. Orinakova, A. S. Fedorkova and A. Orinak, *Journal of Solid State Electrochemistry*, 2014, **18**, 2289-2295.
29 29. T. Goda, E. Yamada, Y. Katayama, M. Tabata, A. Matsumoto and Y. Miyahara, *Biosensors & Bioelectronics*, 2016, **77**, 208-214.

7. Global conclusions and future work

The fabrication of MNEE arrays has been greatly investigated in this work, it was found that the photolithography had not been previously optimised. Previously the resist had been spun on too thin, when the cavities were dry etched the milling went through the thin photoresist layer and thinned the silicon nitride insulator. Electrodes fabricated incorrectly in this manner fit to an equivalent circuit with a parasitic capacitance, C_N. Fabricated properly, the nanoelectrode arrays for the same equivalent circuit as micro electrode arrays. This improved fabrication protocol should be used to reproducibly make functioning MNEE arrays for future investigation. It would also be of interest to fabricate the electrodes on glass wafers so as to allow spectroscopic analysis of the MNEE arrays and films formed on them to compliment the electrochemical studies, see figure 7.1.

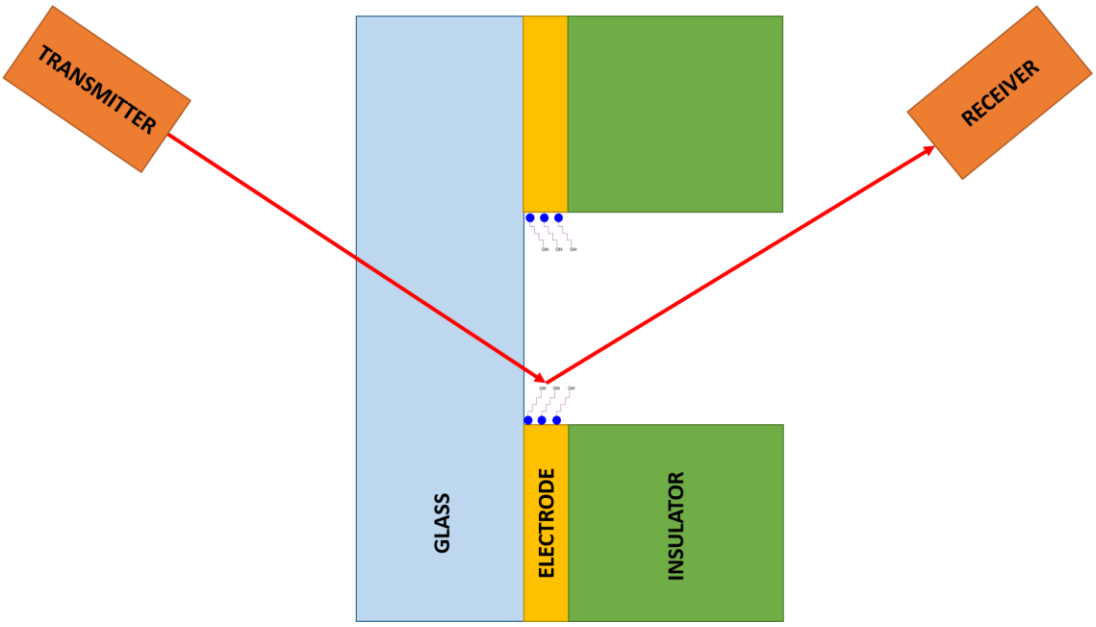

Figure 7.1. Schematic of the proposed MNEE fabricated on glass wafers so as to allow spectroscopic analysis of SAM film formed on the electrode surface.

The increased sensitivities of nanoelectrodes mean that finer control over the experimental conditions in which they are studied is required, chapter 3 of this thesis has outlined the conditions requiring control and simple methods for overcoming them. It is common knowledge that electrode cleanliness is vital for proper electrode function, a method of simultaneously electrochemically cleaning and quantifying the cleanliness of nanoelectrodes by relating their active electrode surface area to their geometrical surface area has been developed as a part of this work. Given the vast array of cleaning protocols for macro electrodes are composed of mechanical, chemical and electrochemical cleaning protocols which are often quite harsh and damage the electrodes; a softer process that does not alter the electrode surface was required for nanoelectrode fabrication where any change to the electrode surface would have a large impact on electrode performance.

The optimised fabrication yielded nano electrodes that have been proven throughout this project to have enhanced biosensing properties compared to macro and micro electrodes. Sub atto molar limits of detection were achieved under idealised conditions. This was achieved with a PNA probe film binding DNA target on the electrode surface. A DNA probe film that bonds the same DNA target sequence was also investigated and comparisons between the two probe films were discussed and investigated in different ionic strength buffers so as to examine the role that charge in a SAM film plays on its sensing performance. It was found that different probes worked best at different ionic strengths, as did the micro and nano electrodes investigated. With nano electrodes and PNA being more sensitive in higher ionic strength media than both micro electrodes and DNA probes. These studies were performed using cyclic voltammetry and electrochemical impedance spectroscopy, analysing the changes in each of the elements in the fitted equivalent circuits allowed a detailed investigation of the different processes at play and how they are affected when different films are formed on different electrodes and how they behave upon target hybridisation.

It was found that DNA target binding caused a decrease in the resistivity of DNA probe film layers, caused by the breaking apart of the film induced by increased stress in the SAM layer by the introduction of more negative charge from the phosphate backbone of the DNA. The PNA probe film on the other hand became more resistive upon DNA target hybridisation as it is more capable of incorporating the negative charge; as well as the introduction of said charge repelling the negatively charged ferri-/ferro-cyanide redox couples used in the measurement buffers. This has gone some way to explaining the literature in which increases and decreases in impedances upon target binding to a probe are both reported.

A collaboration with researchers at the university of Liverpool, wherein carbazole-alanine hydrogels were electrochemically grown on MNEE arrays has also been reported. This work allowed the mapping of the diffusion fields of the MNEE arrays using light, confocal and scanning electron microscopy. The electrochemical analysis of gels grown for different time-periods has led to the development of a novel equivalent circuit, some elements of which are yet to be physically explained and should be investigated further. The ability of these hydrogels to inhibit biofouling was also investigated. It was shown that the hydrogels prevent bovine serum albumin (BSA) from fouling the nanoelectrode surface, whilst being permeable to short ssDNA targets; which bind to a PNA probe SAM layer formed on the electrode prior to hydrogel formation. It was proven that gels grown chronopotentiometrically at higher currents were more permeable than those grown at lower currents grown for the same period of time. This was measured electrochemically by calculating the diffusion coefficient of ferricyanide ions through the hydrogel matrices formed at different potentials. Combining this tunable porosity of the electrochemically triggered hydrogels with their anti-biofouling properties opens the door to developing size selective semi-permeable anti-biofouling hydrogel matrices on MNEE arrays which have huge potential in the diagnostic industry.

This hydrogel work was very much a proof of principle study that, it is hoped, will form the basis for lots of future work. Perhaps most pressingly, gelators need to be developed that function over a much more biologically friendly pH range. Currently having to go from pH8 to pH < 4 will denature the vast majority of biomolecules which severely limits the number of available probes that can be used with this system as it is. Target detection in complex media through a hydrogel matrix should also be prioritised, this was attempted in this work but the results were inconclusive due to non-specific binding of target DNA to BSA.

Both the hydrogel and SAM work has only been performed using DNA and PNA probe films. Using much larger protein or aptamer probes and assessing their SAM structure on nanoelectrodes would be very interesting, when the probe size approaches or even exceeds the size of the electrode what type of SAM layer will form and how sensitive will that sensor be to target binding?

8. REFERENCES

1. Lyandres, O.; Shah, N. C.; Yonzon, C. R.; Walsh, J. T.; Glucksberg, M. R.; Van Duyne, R. P., Real-time glucose sensing by surface-enhanced Raman spectroscopy in bovine plasma facilitated by a mixed decanethiol/mercaptohexanol partition layer. *Analytical Chemistry* **2005,** *77* (19), 6134-6139.
2. Garg, S.; Zisser, H.; Schwartz, S.; Bailey, T.; Kaplan, R.; Ellis, S.; Jovanovic, L., Improvement in glycemic excursions with a transcutaneous, real-time continuous glucose sensor. *Diabetes Care* **2006,** *29* (1), 44-50.
3. Matzeu, G.; Florea, L.; Diamond, D., Advances in wearable chemical sensor design for monitoring biological fluids. *Sensors and Actuators B-Chemical* **2015,** *211*, 403-418.
4. Mozek, M.; Vrtacnik, D.; Resnik, D.; Aljancic, U.; Penic, S.; Amon, S., Digital self-learning calibration system for smart sensors. *Sensors and Actuators a-Physical* **2008,** *141* (1), 101-108.
5. Black, R. D., Recent Advances in Translational Work on Implantable Sensors. *Ieee Sensors Journal* **2011,** *11* (12), 3171-3182.
6. Plicchi, G.; Marcelli, E.; Cercenelli, L., Implantable sensors to assess cardiac function. *Journal of Mechanics in Medicine and Biology* **2006,** *6* (1), 81-89.
7. Wisniewski, N.; Moussy, F.; Reichert, W. M., Characterization of implantable biosensor membrane biofouling. *Fresenius Journal of Analytical Chemistry* **2000,** *366* (6-7), 611-621.
8. Bin, X. M.; Sargent, E. H.; Kelley, S. O., Nanostructuring of Sensors Determines the Efficiency of Biomolecular Capture. *Analytical Chemistry* **2010,** *82* (14), 5928-5931.
9. Lam, B.; Fang, Z. C.; Sargent, E. H.; Kelley, S. O., Polymerase Chain Reaction-Free, Sample-to-Answer Bacterial Detection in 30 Minutes with Integrated Cell Lysis. *Analytical Chemistry* **2012,** *84* (1), 21-25.
10. Kelley, S. O.; Mirkin, C. A.; Walt, D. R.; Ismagilov, R. F.; Toner, M.; Sargent, E. H., Advancing the speed, sensitivity and accuracy of biomolecular detection using multi-length-scale engineering. *Nature Nanotechnology* **2014,** *9* (12), 969-980.
11. Silvestrini, M.; Fruk, L.; Ugo, P., Functionalized ensembles of nanoelectrodes as affinity biosensors for DNA hybridization detection. *Biosensors & Bioelectronics* **2013,** *40* (1), 265-270.
12. Luo, X.; Davis, J. J., Electrical biosensors and the label free detection of protein disease biomarkers. *Chemical Society Reviews* **2013,** *42* (13), 5944-5962.
13. Luo, X.; Xu, M.; Freeman, C.; James, T.; Davis, J. J., Ultrasensitive Label Free Electrical Detection of Insulin in Neat Blood Serum. *Analytical Chemistry* **2013,** *85* (8), 4129-4134.
14. Bedatty Fernandes, F. C.; Goes, M. S.; Davis, J. J.; Bueno, P. R., Label free redox capacitive biosensing. *Biosensors & Bioelectronics* **2013,** *50*, 437-440.
15. Barsoukov, E.; Macdonald, R. J., *Impedance Spectroscopy Theory, Experiment, and Applications*. John Wiley & Sons: Hoboken, New Jersey, 2005.
16. instruments, G. Electrochemical impedance spectroscopy Primer. http://www.gamry.com (accessed 11/2013).
17. Bogomolova, A.; Komarova, E.; Reber, K.; Gerasimov, T.; Yavuz, O.; Bhatt, S.; Aldissi, M., Challenges of Electrochemical Impedance Spectroscopy in Protein Biosensing. *Analytical Chemistry* **2009,** *81* (10), 3944-3949.
18. Corrigan, D. K.; Schulze, H.; Henihan, G.; Hardie, A.; Ciani, I.; Giraud, G.; Terry, J. G.; Walton, A. J.; Pethig, R.; Ghazal, P.; Crain, J.; Campbell, C. J.; Templeton, K. E.; Mount, A. R.; Bachmann, T. T., Development of a PCR-free electrochemical point of care test for clinical detection of methicillin resistant Staphylococcus aureus (MRSA). *Analyst* **2013,** *138* (22), 6997-7005.

19. Whitehead, C. L.; Teh, W. T.; Walker, S. P.; Leung, C.; Larmour, L.; Tong, S., Circulating MicroRNAs in Maternal Blood as Potential Biomarkers for Fetal Hypoxia In-Utero. *Plos One* **2013,** *8* (11).
20. Lo, Y. M. D.; Chan, K. C. A.; Sun, H.; Chen, E. Z.; Jiang, P. Y.; Lun, F. M. F.; Zheng, Y. W.; Leung, T. Y.; Lau, T. K.; Cantor, C. R.; Chiu, R. W. K., Maternal Plasma DNA Sequencing Reveals the Genome-Wide Genetic and Mutational Profile of the Fetus. *Science Translational Medicine* **2010,** *2* (61).
21. Das, J.; Ivanov, I.; Montermini, L.; Rak, J.; Sargent, E. H.; Kelley, S. O., An electrochemical clamp assay for direct, rapid analysis of circulating nucleic acids in serum. *Nature Chemistry* **2015,** *7* (7), 569-575.
22. Terry, J. G.; Schmueser, I.; Underwood, I.; Corrigan, D. K.; Freeman, N. J.; Bunting, A. S.; Mount, A. R.; Walton, A. J., Nanoscale electrode arrays produced with microscale lithographic techniques for use in biomedical sensing applications. *Iet Nanobiotechnology* **2013,** *7* (4), 125-134.
23. Ciani, I.; Schulze, H.; Corrigan, D. K.; Henihan, G.; Giraud, G.; Terry, J. G.; Walton, A. J.; Pethig, R.; Ghazal, P.; Crain, J.; Campbell, C. J.; Bachmann, T. T.; Mount, A. R., Development of immunosensors for direct detection of three wound infection biomarkers at point of care using electrochemical impedance spectroscopy. *Biosensors & Bioelectronics* **2012,** *31* (1), 413-418.
24. Macanovic, A.; Marquette, C.; Polychronakos, C.; Lawrence, M. F., Impedance-based detection of DNA sequences using a silicon transducer with PNA as the probe layer. *Nucleic Acids Research* **2004,** *32* (2).
25. De, A.; Souchelnytskyi, S.; van den Berg, A.; Carlen, E. T., Peptide Nucleic Acid (PNA)-DNA Duplexes: Comparison of Hybridization Affinity between Vertically and Horizontally Tethered PNA Probes. *Acs Applied Materials & Interfaces* **2013,** *5* (11), 4607-4612.
26. Mutyala, S.; Mathiyarasu, J., A reagentless non-enzymatic hydrogen peroxide sensor presented using electrochemically reduced graphene oxide modified glassy carbon electrode. *Materials Science & Engineering C-Materials for Biological Applications* **2016,** *69*, 398-406.
27. Farah, A. M.; Billing, C.; Dikio, C. W.; Dibofori-Orji, A. N.; Oyedeji, O. O.; Wankasi, D.; Mtunzi, F. M.; Dikio, E. D., Synthesis of Prussian Blue and Its Electrochemical Detection of Hydrogen Peroxide Based on Cetyltrimethylammonium Bromide (CTAB) Modified Glassy Carbon Electrode. *International Journal of Electrochemical Science* **2013,** *8* (11), 12132-12146.
28. Fischer, L. M.; Tenje, M.; Heiskanen, A. R.; Masuda, N.; Castillo, J.; Bentien, A.; Emneus, J.; Jakobsen, M. H.; Boisen, A., Gold cleaning methods for electrochemical detection applications. *Microelectronic Engineering* **2009,** *86* (4-6), 1282-1285.
29. Singh, M. B.; Kant, R., Theory of Anomalous Dynamics of Electric Double Layer at Heterogeneous and Rough Electrodes. *Journal of Physical Chemistry C* **2014,** *118* (10), 5122-5133.
30. Schmueser, I.; Walton, A. J.; Terry, J. G.; Woodvine, H. L.; Freeman, N. J.; Mount, A. R., A systematic study of the influence of nanoelectrode dimensions on electrode performance and the implications for electroanalysis and sensing. *Faraday Discussions* **2013,** *164*, 295-314.
31. Bard, A. J.; Faulkner, L. R., *Electrochemical methods : fundamentals and applications*. Wiley: New York ; Chichester, 1980; p xviii, 718 pages.
32. Rasheed, P. A.; Sandhyarani, N., Attomolar detection of BRCA1 gene based on gold nanoparticle assisted signal amplification. *Biosensors & Bioelectronics* **2015,** *65*, 333-340.
33. Loaiza, O. A.; Lamas-Ardisana, P. J.; Jubete, E.; Ochoteco, E.; Loinaz, I.; Cabanero, G.; Garcia, I.; Penades, S., Nanostructured Disposable Impedimetric Sensors as Tools for Specific

Biomolecular Interactions: Sensitive Recognition of Concanavalin A. *Analytical Chemistry* **2011,** *83* (8), 2987-2995.
34. Kumar, B.; Bhalla, V.; Bhadoriya, R. P. S.; Suri, C. R.; Varshney, G. C., Label-free electrochemical detection of malaria-infected red blood cells. *Rsc Advances* **2016,** *6* (79), 75862-75869.
35. Saadaoui, M.; Braiek, M.; Jaffrezic-Renault, N.; Raouafi, N., An ultrasensitive nanobiohybrid platform for glucose electrochemical biosensing based on ferrocenyl iminopropyl-modified silica nanoparticles. *Rsc Advances* **2016,** *6* (52), 46238-46243.
36. Watson, S. M. D.; Pike, A. R.; Pate, J.; Houlton, A.; Horrocks, B. R., DNA-templated nanowires: morphology and electrical conductivity. *Nanoscale* **2014,** *6* (8), 4027-4037.
37. Watson, S. M. D.; Mohamed, H. D. A.; Horrocks, B. R.; Houlton, A., Electrically conductive magnetic nanowires using an electrochemical DNA-templating route. *Nanoscale* **2013,** *5* (12), 5349-5359.
38. Al-Hinai, M. N.; Hassanien, R.; Wright, N. G.; Horsfall, A. B.; Houlton, A.; Horrocks, B. R., Networks of DNA-templated palladium nanowires: structural and electrical characterisation and their use as hydrogen gas sensors. *Faraday Discussions* **2013,** *164*, 71-91.
39. Wang, Z.; Nania, S. L.; Shaw, S. K., Structure of Aqueous Water Films on Textured -OH-Terminated Self-Assembled Monolayers. *Langmuir* **2015,** *31* (8), 2382-2389.
40. Poirier, G. E., Coverage-dependent phases and phase stability of decanethiol on Au(111). *Langmuir* **1999,** *15* (4), 1167-1175.
41. Brett, C. M. A.; Kresak, S.; Hianik, T.; Brett, A. M. O., Studies on self-assembled alkanethiol monolayers formed at applied potential on polycrystalline gold electrodes. *Electroanalysis* **2003,** *15* (5-6), 557-565.
42. Novakova, Z.; Orinakova, R.; Fedorkova, A. S.; Orinak, A., Electrochemical study of self-assembled monolayer adsorption. *Journal of Solid State Electrochemistry* **2014,** *18* (8), 2289-2295.
43. Luo, Y.-R., *Handbook of Bond Dissociation Energies in Organic Compounds*. CRC Press: 2002; p 392.
44. Hakkinen, H., The gold-sulfur interface at the nanoscale. *Nature Chemistry* **2012,** *4* (6), 443-455.
45. Petrovykh, D. Y.; Kimura-Suda, H.; Opdahl, A.; Richter, L. J.; Tarlov, M. J.; Whitman, L. J., Alkanethiols on platinum: Multicomponent self-assembled monolayers. *Langmuir* **2006,** *22* (6), 2578-2587.
46. Chidsey, C. E. D.; Liu, G. Y.; Rowntree, P.; Scoles, G., MOLECULAR ORDER AT THE SURFACE OF AN ORGANIC MONOLAYER STUDIED BY LOW-ENERGY HELIUM DIFFRACTION. *Journal of Chemical Physics* **1989,** *91* (7), 4421-4423.
47. Campina, J. M.; Martins, A.; Silva, F., A new cleaning methodology for efficient Au-SAM removal. *Electrochimica Acta* **2008,** *53* (26), 7681-7689.
48. Kosaka, P. M.; Gonzalez, S.; Dominguez, C. M.; Cebollada, A.; San Paulo, A.; Calleja, M.; Tamayo, J., Atomic force microscopy reveals two phases in single stranded DNA self-assembled monolayers. *Nanoscale* **2013,** *5* (16), 7425-7432.
49. Wu, H.; Sotthewes, K.; Kumar, A.; Vancso, G. J.; Schon, P. M.; Zandvliet, H. J. W., Dynamics of Decanethiol Self-Assembled Monolayers on Au(111) Studied by Time-Resolved Scanning Tunneling Microscopy. *Langmuir* **2013,** *29* (7), 2250-2257.
50. Gebala, M.; Schuhmann, W., Controlled Orientation of DNA in a Binary SAM as a Key for the Successful Determination of DNA Hybridization by Means of Electrochemical Impedance Spectroscopy. *Chemphyschem* **2010,** *11* (13), 2887-2895.
51. Wink, T.; vanZuilen, S. J.; Bult, A.; vanBennekom, W. P., Self-assembled monolayers for biosensors. *Analyst* **1997,** *122* (4), R43-R50.

52. Aoki, H.; Tao, H., Gene sensors based on peptide nucleic acid (PNA) probes: Relationship between sensor sensitivity and probe/target duplex stability. *Analyst* **2005,** *130* (11), 1478-1482.
53. Gileadi, E., *Physical Electrochemistry-Fundamentals, Techniques and Applications*. WILEY-VCH Verlag GmbH & Co. KGaA, Weinheim: Federal Republic of Germany, 2015; p 373.
54. Barsoukov, E., Impedance Spectroscopy Theory, Experiment, and Applications Second Edition Preface. *Impedance Spectroscopy: Theory, Experiment, and Applications, 2nd Edition* **2005**, XII-+.
55. Fisher, A. C.; Royal Society of Chemistry. Electrochemistry Group., *Electrode dynamics*. Oxford University Press: Oxford, 1996; p 83 pages.
56. Barsoukov, E.; Macdonald, J. R., Impedance spectroscopytheory, experiment, and applications. Second edition / ed.; Wiley-Interscience,: Hoboken, N.J., 2005; pp. 1 online resource (xvii, 595 pages).
57. Fletcher, S., TABLES OF DEGENERATE ELECTRICAL NETWORKS FOR USE IN THE EQUIVALENT-CIRCUIT ANALYSIS OF ELECTROCHEMICAL SYSTEMS. *Journal of the Electrochemical Society* **1994,** *141* (7), 1823-1826.
58. Wu, N.-y.; Gao, W.; He, X.-l.; Chang, Z.; Xu, M.-t., Direct electrochemical sensor for label-free DNA detection based on zero current potentiometry. *Biosensors & Bioelectronics* **2013,** *39* (1), 210-214.
59. Woodvine, H. L.; Terry, J. G.; Walton, A. J.; Mount, A. R., The development and characterisation of square microfabricated electrode systems. *Analyst* **2010,** *135* (5), 1058-1065.
60. Atkins, P. W.; De Paula, J., *Atkins' Physical chemistry*. Ninth edition. ed.; Oxford University Press: Oxford, England ; New York, N.Y., 2010; p xxix, 972 pages.
61. Woodvine, H. L. Development and Characterisation of Microelectrode and Nanoelectrode Systems. The University of Edinburgh, 2011.
62. Schmuser, I. Design, fabrication and characterisation of nanoelectrodes for electrochemical sensing. The University of Edinburgh, The University of Edinburgh, 2016.
63. Belaidi, F. S.; Vanhove, E.; Tiddi, W.; Polverel, M.; Lemercier, G.; Lecestre, A.; Dubreuil, P.; Launay, J.; Arbault, S.; Temple-Boyer, P., Integration of ring nanoelectrodes into microwells for the bioelectrochemical analysis in sub-picolitre volumes. *Sensors and Actuators B-Chemical* **2016,** *232*, 345-356.
64. Schmueser, I., Miss. Piper, A., Ed.
65. Berger, T.; Monllor-Satoca, D.; Jankulovska, M.; Lana-Villarreal, T.; Gomez, R., The Electrochemistry of Nanostructured Titanium Dioxide Electrodes. *Chemphyschem* **2012,** *13* (12), 2824-2875.
66. Kavan, L., Electrochemistry of titanium dioxide: some aspects and highlights. *Chemical Record* **2012,** *12* (1), 131-142.
67. Ngamchuea, K.; Eloul, S.; Tschulik, K.; Compton, R. G., Planar diffusion to macro disc electrodes-what electrode size is required for the Cottrell and Randles-Sevcik equations to apply quantitatively? *Journal of Solid State Electrochemistry* **2014,** *18* (12), 3251-3257.
68. Konopka, S. J.; McDuffie, B., DIFFUSION COEFFICIENTS OF FERRICYANIDE AND FERROCYANIDE IONS IN AQUEOUS MEDIA, USING TWIN-ELECTRODE THIN-LAYER ELECTROCHEMISTRY. *Analytical Chemistry* **1970,** *42* (14), 1741-&.
69. Sun, K.; Jiang, B.; Jiang, X., Electrochemical desorption of self-assembled monolayers and its applications in surface chemistry and cell biology. *Journal of Electroanalytical Chemistry* **2011,** *656* (1-2), 223-230.
70. Canaria, C. A.; So, J.; Maloney, J. R.; Yu, C. J.; Smith, J. O.; Roukes, M. L.; Fraser, S. E.; Lansford, R., Formation and removal of alkylthiolate self-assembled monolayers on gold in aqueous solutions. *Lab on a Chip* **2006,** *6* (2), 289-295.

71. Zhou, C.; Trionfi, A.; Jones, J. C.; Hsu, J. W. P.; Walker, A. V., Comparison of Chemical Lithography Using Alkanethiolate Self-Assembled Monolayers on GaAs (001) and Au. *Langmuir* **2010,** *26* (6), 4523-4528.
72. Sun, T.; Blanchard, P.-Y.; Mirkin, M. V., Cleaning Nanoelectrodes with Air Plasma. *Analytical Chemistry* **2015,** *87* (8), 4092-4095.
73. Yajima, T., Electrochemical characteristics of platinum surface treated by RF plasma. *Surface & Coatings Technology* **1999,** *112* (1-3), 80-84.
74. Pavlovic, E.; Lai, R. Y.; Wu, T. T.; Ferguson, B. S.; Sun, R.; Plaxco, K. W.; Soh, H. T., Microfluidic device architecture for electrochemical patterning and detection of multiple DNA sequences. *Langmuir* **2008,** *24* (3), 1102-1107.
75. Yang, D. F.; Wilde, C. P.; Morin, M., Studies of the electrochemical removal and efficient re-formation of a monolayer of hexadecanethiol self-assembled at an Au(111) single crystal in aqueous solutions. *Langmuir* **1997,** *13* (2), 243-249.
76. Kemnade, N.; Chen, Y.; Muglali, M. I.; Erbe, A., Electrochemical reductive desorption of alkyl self-assembled monolayers studied in situ by spectroscopic ellipsometry: evidence for formation of a low refractive index region after desorption. *Physical Chemistry Chemical Physics* **2014,** *16* (32), 17081-17090.
77. Henihan, G.; Schulze, H.; Corrigan, D. K.; Giraud, G.; Terry, J. G.; Hardie, A.; Campbell, C. J.; Walton, A. J.; Crain, J.; Pethig, R.; Templeton, K. E.; Mount, A. R.; Bachmann, T. T., Label- and amplification-free electrochemical detection of bacterial ribosomal RNA. *Biosensors & bioelectronics* **2016,** *81*, 487-94.
78. Keighley, S. D.; Li, P.; Estrela, P.; Mighorato, P., Optimization of DNA immobilization on gold electrodes for label-free detection by electrochemical impedance spectroscopy. *Biosensors & Bioelectronics* **2008,** *23* (8), 1291-1297.
79. Keighley, S. D.; Estrela, P.; Li, P.; Mighorato, P., Optimization of label-free DNA detection with electrochemical impedance spectroscopy using PNA probes. *Biosensors & Bioelectronics* **2008,** *24* (4), 906-911.
80. Clavilier, J.; Rodes, A.; Elachi, K.; Zamakhchari, M. A., ELECTROCHEMISTRY AT PLATINUM SINGLE-CRYSTAL SURFACES IN ACIDIC MEDIA - HYDROGEN AND OXYGEN-ADSORPTION. *Journal De Chimie Physique Et De Physico-Chimie Biologique* **1991,** *88* (7-8), 1291-1337.
81. Clavilier, J.; Faure, R.; Guinet, G.; Durand, R., PREPARATION OF MONO-CRYSTALLINE PT MICROELECTRODES AND ELECTROCHEMICAL STUDY OF THE PLANE SURFACES CUT IN THE DIRECTION OF THE (111) AND (110) PLANES. *Journal of Electroanalytical Chemistry* **1980,** *107* (1), 205-209.
82. Clavilier, J.; Armand, D.; Sun, S. G.; Petit, M., ELECTROCHEMICAL ADSORPTION BEHAVIOR OF PLATINUM STEPPED SURFACES IN SULFURIC-ACID-SOLUTIONS. *Journal of Electroanalytical Chemistry* **1986,** *205* (1-2), 267-277.
83. Biegler, T.; Rand, D. A. J.; Woods, R., LIMITING OXYGEN COVERAGE ON PLATINIZED PLATINUM - RELEVANCE TO DETERMINATION OF REAL PLATINUM AREA BY HYDROGEN ADSORPTION. *Journal of Electroanalytical Chemistry* **1971,** *29* (2), 269-&.
84. Clavilier, J.; Elachi, K.; Rodes, A., INSITU PROBING OF STEP AND TERRACE SITES ON PT(S)- N(111)X(111) ELECTRODES. *Chemical Physics* **1990,** *141* (1), 1-14.
85. Daubinger, P.; Kieninger, J.; Unmuessig, T.; Urban, G. A., Electrochemical characteristics of nanostructured platinum electrodes - a cyclic voltammetry study. *Physical Chemistry Chemical Physics* **2014,** *16* (18), 8392-8399.
86. Sheridan, A. K.; Ngamukot, P.; Bartlett, P. N.; Wilkinson, J. S., Waveguide surface plasmon resonance sensing: Electrochemical desorption of alkane thiol monolayers. *Sensors and Actuators B-Chemical* **2006,** *117* (1), 253-260.

87. Yang, D. F.; AlMaznai, H.; Morin, M., Vibrational study of the fast reductive and the slow oxidative desorptions of a nonanethiol self-assembled monolayer from a Au(111) single crystal electrode. *Journal of Physical Chemistry B* **1997,** *101* (7), 1158-1166.
88. Loglio, F.; Schweizer, M.; Kolb, D. M., In situ characterization of self-assembled butanethiol monolayers on Au(100) electrodes. *Langmuir* **2003,** *19* (3), 830-834.
89. Widrig, C. A.; Chung, C.; Porter, M. D., THE ELECTROCHEMICAL DESORPTION OF N-ALKANETHIOL MONOLAYERS FROM POLYCRYSTALLINE AU AND AG ELECTRODES. *Journal of Electroanalytical Chemistry* **1991,** *310* (1-2), 335-359.
90. Patolsky, F.; Lichtenstein, A.; Willner, I., Electrochemical transduction of liposome-amplified DNA sensing. *Angewandte Chemie-International Edition* **2000,** *39* (5), 940-+.
91. Zuzuarregui, A.; Souto, D.; Perez-Lorenzo, E.; Arizti, F.; Sanchez-Gomez, S.; Martinez de Tejada, G.; Brandenburg, K.; Arana, S.; Mujika, M., Novel integrated and portable endotoxin detection system based on an electrochemical biosensor. *Analyst* **2015,** *140* (2), 654-660.
92. Corrigan, D. K.; Schulze, H.; McDermott, R. A.; Schmueser, I.; Henihan, G.; Henry, J. B.; Bachmann, T. T.; Mount, A. R., Improving electrochemical biosensor performance by understanding the influence of target DNA length on assay sensitivity. *Journal of Electroanalytical Chemistry* **2014,** *732*, 25-29.
93. Paquette, L., *Encyclopedia of Reagents for Organic Synthesis*. 2nd ed.; J. Wiley & Sons: New York., 2004.
94. Vogt, S.; Su, Q.; Gutierrez-Sanchez, C.; Noll, G., Critical View on Electrochemical Impedance Spectroscopy Using the Ferri/Ferrocyanide Redox Couple at Gold Electrodes. *Analytical chemistry* **2016,** *88* (8), 4383-90.
95. Corrigan, D. K.; Gale, N.; Brown, T.; Bartlett, P. N., Analysis of Short Tandem Repeats by Using SERS Monitoring and Electrochemical Melting. *Angewandte Chemie-International Edition* **2010,** *49* (34), 5917-5920.
96. Goda, T.; Singi, A. B.; Maeda, Y.; Matsumoto, A.; Torimura, M.; Aoki, H.; Miyahara, Y., Label-Free Potentiometry for Detecting DNA Hybridization Using Peptide Nucleic Acid and DNA Probes. *Sensors* **2013,** *13* (2), 2267-2278.
97. Silvestrini, M.; Schiavuta, P.; Scopece, P.; Pecchielan, G.; Moretto, L. M.; Ugo, P., Modification of nanoelectrode ensembles by thiols and disulfides to prevent non specific adsorption of proteins. *Electrochimica Acta* **2011,** *56* (22), 7718-7724.
98. Hrapovic, S.; Liu, Y. L.; Male, K. B.; Luong, J. H. T., Electrochemical biosensing platforms using platinum nanoparticles and carbon nanotubes. *Analytical Chemistry* **2004,** *76* (4), 1083-1088.
99. Gutierrez-Sanchez, C.; Olea, D.; Marques, M.; Fernandez, V. M.; Pereira, I. A. C.; Velez, M.; De Lacey, A. L., Oriented Immobilization of a Membrane-Bound Hydrogenase onto an Electrode for Direct Electron Transfer. *Langmuir* **2011,** *27* (10), 6449-6457.
100. Liu, G.; Sun, C.; Li, D.; Song, S.; Mao, B.; Fan, C.; Tian, Z., Gating of Redox Currents at Gold Nanoelectrodes via DNA Hybridization. *Advanced Materials* **2010,** *22* (19), 2148-2150.
101. Rodriguez, M. C.; Kawde, A. N.; Wang, J., Aptamer biosensor for label-free impedance spectroscopy detection of proteins based on recognition-induced switching of the surface charge. *Chemical Communications* **2005,** (34), 4267-4269.
102. Gabrielli, C.; Keddam, M.; Portail, N.; Rousseau, P.; Takenouti, H.; Vivier, V., Electrochemical impedance spectroscopy investigations of a microelectrode behavior in a thin-layer cell: Experimental and theoretical studies. *Journal of Physical Chemistry B* **2006,** *110* (41), 20478-20485.
103. Mount, A., Prof. Piper, A., Ed. 2013.
104. Alexander, C. L.; Tribollet, B.; Orazem, M. E., Contribution of Surface Distributions to Constant-Phase-Element (CPE) Behavior: 1. Influence of Roughness. *Electrochimica Acta* **2015,** *173*, 416-424.

105. Brug, G. J.; Vandeneeden, A. L. G.; Sluytersrehbach, M.; Sluyters, J. H., THE ANALYSIS OF ELECTRODE IMPEDANCES COMPLICATED BY THE PRESENCE OF A CONSTANT PHASE ELEMENT. *Journal of Electroanalytical Chemistry* **1984,** *176* (1-2), 275-295.
106. Davies, T. J.; Ward-Jones, S.; Banks, C. E.; del Campo, J.; Mas, R.; Munoz, F. X.; Compton, R. G., The cyclic and linear sweep voltammetry of regular arrays of microdisc electrodes: Fitting of experimental data. *Journal of Electroanalytical Chemistry* **2005,** *585* (1), 51-62.
107. Ussery, D. W. DNA Structure: A-, B- and Z-DNA Helix Families *Encyclopedia of life sciences* [Online], 2002.
108. Ray, A.; Norden, B., Peptide nucleic acid (PNA): its medical and biotechnical applications and promise for the future. *Faseb Journal* **2000,** *14* (9), 1041-1060.
109. Hill, H. D.; Millstone, J. E.; Banholzer, M. J.; Mirkin, C. A., The Role Radius of Curvature Plays in Thiolated Oligonucleotide Loading on Gold Nanoparticles. *Acs Nano* **2009,** *3* (2), 418-424.
110. Iwasawa, Y.; Onishi, H.; Fukui, K.; Suzuki, S.; Sasaki, T., The selective adsorption and kinetic behaviour of molecules on TiO2(110) observed by STM and NC-AFM. *Faraday Discussions* **1999,** *114*, 259-266.
111. Aoki, H.; Buhlmann, P.; Umezawa, Y., Electrochemical detection of a one-base mismatch in an oligonucleotide using ion-channel sensors with self-assembled PNA monolayers. *Electroanalysis* **2000,** *12* (16), 1272-1276.
112. Ratilainen, T.; Holmen, A.; Tuite, E.; Nielsen, P. E.; Norden, B., Thermodynamics of sequence-specific binding of PNA to DNA. *Biochemistry* **2000,** *39* (26), 7781-7791.
113. Dickinson, E. J. F.; Compton, R. G., Influence of the diffuse double layer on steady-state voltammetry. *Journal of Electroanalytical Chemistry* **2011,** *661* (1), 198-212.
114. Dickinson, E. J. F.; Compton, R. G., Diffuse Double Layer at Nanoelectrodes. *Journal of Physical Chemistry C* **2009,** *113* (41), 17585-17589.
115. Anorga, L.; Rebollo, A.; Herran, J.; Arana, S.; Bandres, E.; Garcia-Foncillas, J., Development of a DNA Microelectrochemical Biosensor for CEACAM5 Detection. *Ieee Sensors Journal* **2010,** *10* (8), 1368-1374.
116. Ruan, C. M.; Li, Y. B., Detection of zeptomolar concentrations of alkaline phosphatase based on a tyrosinase and horse-radish peroxidase bienzyme biosensor. *Talanta* **2001,** *54* (6), 1095-1103.
117. Vijian, D.; Chinni, S. V.; Yin, L. S.; Lertanantawong, B.; Surareungchai, W., Non-protein coding RNA-based genosensor with quantum dots as electrochemical labels for attomolar detection of multiple pathogens. *Biosensors & Bioelectronics* **2016,** *77*, 805-811.
118. Guiseppi-Elie, A., Electroconductive hydrogels: Synthesis, characterization and biomedical applications. *Biomaterials* **2010,** *31* (10), 2701-2716.
119. Yang, W.; Xue, H.; Carr, L. R.; Wang, J.; Jiang, S., Zwitterionic poly(carboxybetaine) hydrogels for glucose biosensors in complex media. *Biosensors & Bioelectronics* **2011,** *26* (5), 2454-2459.
120. Pishko, M. V.; Michael, A. C.; Heller, A., AMPEROMETRIC GLUCOSE MICROELECTRODES PREPARED THROUGH IMMOBILIZATION OF GLUCOSE-OXIDASE IN REDOX HYDROGELS. *Analytical Chemistry* **1991,** *63* (20), 2268-2272.
121. Wallace, M.; Adams, D. J.; Iggo, J. A., Analysis of the mesh size in a supramolecular hydrogel by PFG-NMR spectroscopy. *Soft Matter* **2013,** *9* (22), 5483-5491.
122. Dominguez, M. M.; Wathier, M.; Grinstaff, M. W.; Schaus, S. E., Immobilized hydrogels for screening of molecular interactions. *Analytical Chemistry* **2007,** *79* (3), 1064-1066.
123. Sirkar, K.; Pishko, M. V., Amperometric biosensors based on oxidoreductases immobilized in photopolymerized poly(ethylene glycol) redox polymer hydrogels. *Analytical Chemistry* **1998,** *70* (14), 2888-2894.

124. Salamifar, S. E.; Lai, R. Y., Fabrication of Electrochemical DNA Sensors on Gold-Modified Recessed Platinum Nanoelectrodes. *Analytical Chemistry* **2014,** *86* (6), 2849-2852.
125. Wisniewski, N.; Reichert, M., Methods for reducing biosensor membrane biofouling. *Colloids and Surfaces B-Biointerfaces* **2000,** *18* (3-4), 197-219.
126. Raeburn, J.; Alston, B.; Kroeger, J.; McDonald, T. O.; Howse, J. R.; Cameron, P. J.; Adams, D. J., Electrochemically-triggered spatially and temporally resolved multi-component gels. *Materials Horizons* **2014,** *1* (2), 241-246.
127. Goda, T.; Yamada, E.; Katayama, Y.; Tabata, M.; Matsumoto, A.; Miyahara, Y., Potentiometric responses of ion-selective microelectrode with bovine serum albumin adsorption. *Biosensors & Bioelectronics* **2016,** *77*, 208-214.
128. Michnik, A.; Michalik, K.; Drzazga, Z., Stability of bovine serum albumin at different pH. *Journal of Thermal Analysis and Calorimetry* **2005,** *80* (2), 399-406.
129. Kubiak, P. S.; Awhida, S.; Hotchen, C.; Deng, W.; Alston, B.; McDonald, T. O.; Adams, D. J.; Cameron, P. J., Polymerization of low molecular weight hydrogelators to form electrochromic polymers. *Chemical Communications* **2015,** *51* (52), 10427-10430.
130. Chen, L.; Morris, K.; Laybourn, A.; Elias, D.; Hicks, M. R.; Rodger, A.; Serpell, L.; Adams, D. J., Self-Assembly Mechanism for a Naphthalene-Dipeptide Leading to Hydrogelation. *Langmuir* **2010,** *26* (7), 5232-5242.
131. Raeburn, J.; Chen, L.; Awhida, S.; Deller, R. C.; Vatish, M.; Gibson, M. I.; Adams, D. J., Using molecular rotors to probe gelation. *Soft Matter* **2015,** *11* (18), 3706-3713.
132. Wang, Q.; Mynar, J. L.; Yoshida, M.; Lee, E.; Lee, M.; Okuro, K.; Kinbara, K.; Aida, T., High-water-content mouldable hydrogels by mixing clay and a dendritic molecular binder. *Nature* **2010,** *463* (7279), 339-343.
133. Oh, J. K.; Drumright, R.; Siegwart, D. J.; Matyjaszewski, K., The development of microgels/nanogels for drug delivery applications. *Progress in Polymer Science* **2008,** *33* (4), 448-477.
134. Jackson, N.; Stam, F., Optimization of electrical stimulation parameters for electro-responsive hydrogels for biomedical applications. *Journal of Applied Polymer Science* **2015,** *132* (12).
135. Rowley, J. A.; Madlambayan, G.; Mooney, D. J., Alginate hydrogels as synthetic extracellular matrix materials. *Biomaterials* **1999,** *20* (1), 45-53.
136. Voskerician, G.; Shive, M. S.; Shawgo, R. S.; von Recum, H.; Anderson, J. M.; Cima, M. J.; Langer, R., Biocompatibility and biofouling of MEMS drug delivery devices. *Biomaterials* **2003,** *24* (11), 1959-1967.
137. Qiu, Y.; Park, K., Environment-sensitive hydrogels for drug delivery. *Advanced Drug Delivery Reviews* **2001,** *53* (3), 321-339.
138. Hoare, T. R.; Kohane, D. S., Hydrogels in drug delivery: Progress and challenges. *Polymer* **2008,** *49* (8), 1993-2007.
139. Alston, B., Dr. Piper, A., Ed.

8. Appendix

Appendix 1, equivalent circuits

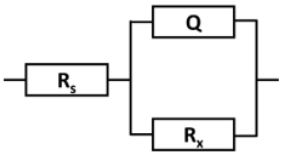

Equivalent circuit 1.1

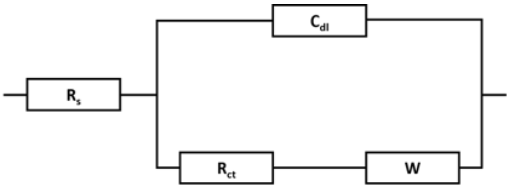

Equivalent circuit 1.2

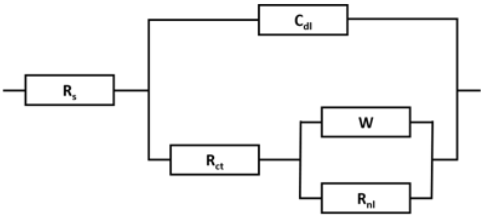

Equivalent circuit 1.3

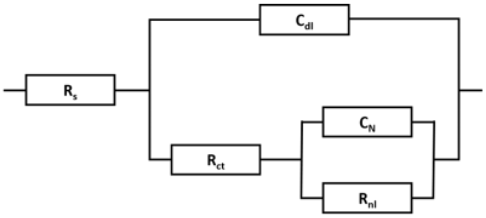

Equivalent circuit 1.4

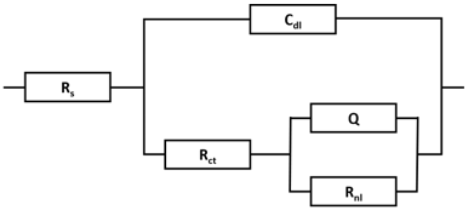

Equivalent circuit 1.5

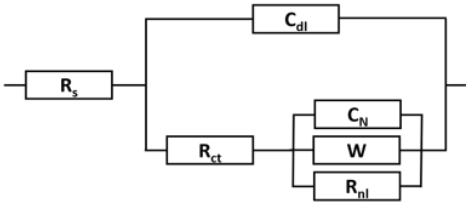

Equivalent circuit 1.6

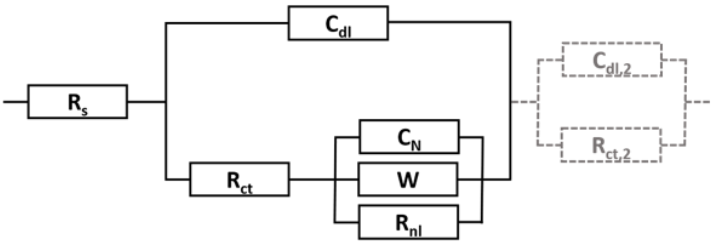

Equivalent circuit 1.7

Appendix 2. Information about different MNEE array configurations

Label	No. of squares in the array	Area ($\times 10^{10}$ nm^2)	Area ($\times 10^{-4}$ cm^2)	Area ($\times 10^{-8}$ m^2)
10-1	62500	12.5	12.5	12.5
20-1	15625	6.25	6.25	6.25
30-1	6889	4.13	4.13	4.13
10-2	27889	5.58	5.58	5.58
20-2	6889	2.76	2.76	2.76
30-2	3136	1.88	1.88	1.88
10-3	15625	3.13	3.13	3.13
20-3	3969	1.59	1.59	1.59
30-3	1764	1.06	1.06	1.06
10-4	10000	2.00	2.00	2.00
20-4	2500	1.00	1.00	1.00
30-4	1165	0.70	0.70	0.70

Appendix 3. Inherited run sheet for MNEE array fabrication

No	Step	Machine	Parameter/Recipe	Notes
1	**Insulate wafers**			
	Thermal Oxidation	F#10 (WETOX 2hr30min)	1000nm	actual=1038.3nm, range=10.9nm
2	**Deposit Metal Layer**			
	- Deposit Titanium	ANS E-Beam Evap	10nm	
	- Deposit Platinum	ANS E-Beam Evap	50nm	
3	**Photolith Platinum Layer**			
	- Coat SPR350	SVG Track System (C)	Recipe 1:2:1	
	- Expose: Caviare (Metal)	KS Contact Aligner	5.0sec	Prox/Spacer
	- Develop	SVG Track System (D)	Recipe 9:1:1	
4	**Etch Platinum Layer**			
	- Etch Platinum	JLS RIE 80	Prog 8 - 9mins	200W (Ar - 25sccm) 9mins
	- Wet Etch Platinum	Wet Bench	60sec	HCl:H2O:HNO3 (3:2:1) @45 degC
5	**Resist Strip**			
	- ACT rinse (1)	Water Bath	15mins	50 degC + sonication
	- ACT rinse (2)	Water Bath	15mins	50 degC + sonication
	- IPA rinse	Wet Deck	10mins	DI rinse and N2 dry
6	**Coat Passivation Nitride**		**Find alignment marks!**	
	- LPCVD SiN	F#3 (SIRNFLAT - 5hr)	300nm	
7	**Photolith Contact**			
	- Coat SPR350	SVG Track System (C)	121	
	- Expose: Caviare (Contact)	KS Contact Aligner	5s	Prox spacer
	- Develop	SVG Track System (D)	911	
8	**Etch Contact**			
	- Etch SiN 2	JLS RIE 80	#25 13min	75W 60mTorr CF4/Ar 60/4
9	**Resist Strip**			
	- ACT rinse (1)	Water Bath	15mins	50 degC + sonication
	- ACT rinse (2)	Water Bath	15mins	50 degC + sonication
	- IPA rinse	Wet Deck	10mins	DI rinse and N2 dry
10	**Photolith Cavity**			
	- Primer	SVG Track System (C)	199	
	- Coat SPR220 3.0	Spinner	60s 2500rpm	3um nominal thickness
	- bake	Hotplate	90s 110deg	
	- Expose: Caviare Cavity	KS Contact Aligner	18s	low vac contact
	- Develop	SVG Track System (D)	911	
11	**Etch Cavity**			
	- Etch Nitride	JLS RIE 80	#25 13min	75W 60mTorr CF4/Ar 60/4
	- Etch Platinum	JLS RIE 80	#8 9min	200W (Ar - 25sccm)
	- Wet Etch Platinum	Wet Bench	60sec	HCl:H2O:HNO3 (3:2:1) @45 degC
	- DI rinse and Dry	Dump Rinse/Marangoni	Standard	5cycle DI / Stand Dry
12	**Resist Strip**			
	- ACT rinse (1)	Water Bath	15mins	50 degC + sonication
	- ACT rinse (2)	Water Bath	15mins	50 degC + sonication
	- IPA rinse	Wet Deck	10mins	DI rinse and N2 dry
13	**Completion**			
	- Coat SPR350	SVG Track System (C)	Recipe 1:1:1	
	- Dice wafers	Disco Saw	Recipe: 39	Ch1: 15.1 / Ch2: 10.1
	- Deliver	Package		COMPLETED

Appendix 4. Run sheet for the fabrication of batches AP1503 and AP1506

Runsheet batch AP1506				
step no.	Step	Machine	Parameter recipe	Notes
1	Insulate wafers			
	Thermal oxidation	F#10 (WETOX 2hr30min)		arrived with 1um oxide on both sides, confirm with nanospec
				Optical inspection
2	Deposit metal layer			
	Deposit titanium	ANS E-Beam Evap	30nm	
	Deposit platinum	ANS E-Beam Evap	100nm	Sheet resistance and thickness check
				Optical inspection/metrology
3	Photolith			
	Barrel Ash	Barrel Asher	1h	
	HMDS primer		10min	
	Coat SPR 350	maual spinner	500rpm for 5s then 3000rpm for 30s	
	Soft bake		90C for 60s	
	Expose: Array metal	KS Contact alligner	7.0 sec (Prox spacer)	
	Develop with MF26A		60s with swirling	wash and dry with DI water and N2
				Optical inspection/metrology
4	Etch Pt layer			
	Etch platinum	JLS RIE 80	Prog 8 for 10min.	Check completion with nanospec
				Optical inspection/Multimeter check
5	Resist strip			
	ACT rinse	Water bath	30min 50C	2 x 15 mins rinse (new solution).
	IPA rinse	Water bath	15min	DI rinse and N2 dry
	Metal step	Dektak		Measure metal step height
6	Coat passivation nitride			
	Coat SiN passivation layer	nitride furnace	overnight for 300nm silicon nitride	
				Optical inspection/metrology
7	Photolith Contact			
	Barrel Ash	Barrel Asher	1h	
	HMDS primer		10min	
	Coat SPR 220	maual spinner	500rpm for 5s then 2500rpm for 60s	
	Soft bake		110C for 90s	
	Expose: Array passivation	KS Contact alligner	18.0 sec (Low vac contact)	
	Develop with MF26A		60s with swirling	wash and dry with DI water and N2
	Cover electrodes with SPR350	paintbrush		
	Soft bake		90C for 60s	Optical inspection/metrology
8	Etch contact			
	- Etch SiN 2	JLS RIE 80	#25 13min	75W 60mTorr CF4/Ar 60/4
	Check etch	nanospec/multimeter	SiN on Pt	etch until completion
				Optical inspection
9	Resist strip			
	ACT rinse	Water bath	30min 50C	Could take longer since the 220 has been baked twice
	IPA rinse	Water bath	15min	DI rinse and N2 dry
				Optical inspection/metrology
10	Photolith cavities			
	Barrel Ash	Barrel Asher	1h	
	HMDS primer		10min	
	Coat SPR 220	maual spinner	500rpm for 5s then 2500rpm for 60s	
	Soft bake		110C for 90s	
	Expose: Array passivation	KS Contact alligner	18.0 sec (low vac contact)	
	Develop with MF26A		60s with swirling	
	Cover bond pads with SPR350	paintbrush		
	Soft bake		90C for 60s	Optical inspection/metrology
11	Etch cavities			
	Etch nitride	JLS RIE 80	#25 13min	75W 60mTorr CF4/Ar 60/4 stop here for MS
	Etch Pt	JLS RIE 80	#8 9min	200W (Ar - 25sccm)
	check etch	Nanospec/multimeter		
12	Resist strip			
	ACT rinse	Water bath	30min 50C	Could take longer since the 220 has been baked twice
	IPA rinse	Water bath	15min	DI rinse and N2 dry
				Optical inspection/metrology
13	Dicing			
	Get wafers diced	Disco saw		

Appendix 5. Run sheet for AP1508

Runsheet batch AP1508				
step no.	**Step**	**Machine**	**Parameter recipe**	**Notes**
1	**Insulate wafers**			
	thermal oxidation	F#10 (WETOX 2hr30min)		confirm with nanospec
				Optical inspection
2	**Deposit metal layer**			
	Deposit titanium	ANS E-Beam Evap	30nm	
	Deposit platinum	ANS E-Beam Evap	100nm	Sheet resistance and thickness check
				Optical inspection/metrology
3	**Photolith**			
	Barrel Ash	Barrel Asher	1h	
	HMDS primer		10min	
	Coat SPR 350	maual spinner	500rpm for 5s then 1800rpm for 60s	This should be checked on a dummy cell prior to each use
	Soft bake		90C for 60s	
	Expose: Array metal	KS Contact alligner	7.0 sec (Prox spacer)	
	Develop with MF26A		60s with swirling	wash and dry with DI water and N2
				Optical inspection/metrology
4	**Etch Pt layer**			
	Etch platinum	JLS RIE 80	Prog 8 for 10min. (Ar mill)	Check completion with nanospec
				Optical inspection/Multimeter check/Metrology
5	**Resist strip**			
	ACT rinse	Water bath	30min 50C	2 x 15 mins rinse (new solution).
	IPA rinse	Water bath	15min	DI rinse and N2 dry
	Metal step	Dektak		Measure metal step height
6	**Coat passivation nitride**			
	Coat SiN passivation layer	nitride furnace	300nm PECVD stoichiometric silicon nitride	
				Optical inspection/metrology
7	**Photolith Contact**			
	Barrel Ash	Barrel Asher	1h	
	HMDS primer		10min	
	Coat SPR 220	maual spinner	500rpm for 5s then 1800rpm for 60s	This should be checked on a dummy cell prior to each use
	Soft bake		110C for 90s	
	Expose: Array passivation	KS Contact alligner	18.0 sec (Low vac contact)	
	Develop with MF26A		60s with swirling	wash and dry with DI water and N2
8	**Etch contact**			
	- Etch SiN 2	JLS RIE 80	#25 13min	75W 60mTorr CF4/Ar 60/4
	Check etch	nanospec/multimeter	SiN on Pt	etch until completion
				Optical inspection
9	**Resist strip**			
	ACT rinse	Water bath	30min 50C	Could take longer since the 220 has been baked twice
	IPA rinse	Water bath	15min	DI rinse and N2 dry
				Optical inspection/metrology
10	**Photolith cavities**			
	Barrel Ash	Barrel Asher	1h	
	HMDS primer		10min	
	Coat SPR 220	maual spinner	500rpm for 5s then 2500rpm for 60s	
	Soft bake		110C for 90s	
	Expose: Array passivation	KS Contact alligner	18.0 sec (low vac contact)	
	Develop with MF26A		60s with swirling	
	Cover bond pads with SPR350	paintbrush		
	Soft bake		90C for 60s	Optical inspection/metrology
11	**Etch cavities**			
	Etch Pt	JLS RIE 80	#8 9min	200W (Ar - 25sccm)
	check etch	Nanospec/multimeter		
12	**Resist strip**			
	ACT rinse	Water bath	30min 50C	Could take longer since the 220 has been baked twice
	IPA rinse	Water bath	15min	DI rinse and N2 dry
				Optical inspection/metrology
13	**Dicing**			
	Get wafers diced	Disco saw		

Appendix 6. Confocal microscopy images received from the University of Liverpool